



Computational Screening of Materials for Water Splitting Applications

Castelli, Ivano Eligio; Jacobsen, Karsten Wedel; Thygesen, Kristian Sommer

Publication date:
2013

Document Version
Publisher's PDF, also known as Version of record

[Link back to DTU Orbit](#)

Citation (APA):
Castelli, I. E., Jacobsen, K. W., & Thygesen, K. S. (2013). Computational Screening of Materials for Water Splitting Applications. Kgs. Lyngby: Technical University of Denmark (DTU).

DTU Library

Technical Information Center of Denmark

General rights

Copyright and moral rights for the publications made accessible in the public portal are retained by the authors and/or other copyright owners and it is a condition of accessing publications that users recognise and abide by the legal requirements associated with these rights.

- Users may download and print one copy of any publication from the public portal for the purpose of private study or research.
- You may not further distribute the material or use it for any profit-making activity or commercial gain
- You may freely distribute the URL identifying the publication in the public portal

If you believe that this document breaches copyright please contact us providing details, and we will remove access to the work immediately and investigate your claim.

Computational Screening of Materials for Water Splitting Applications

Ivano Eligio Castelli

Ph.D. Thesis
May 2013

*Center for Atomic-scale Materials Design
Department of Physics
Technical University of Denmark*

Preface

This thesis is submitted in candidacy for the Ph.D. degree from the Technical University of Denmark (DTU). It is based on the work carried out from June 2010 to May 2013 at the Center for Atomic-scale Material Design (CAMD), Department of Physics, at the Technical University of Denmark, under the supervision of Professor Karsten W. Jacobsen, and Associate Professor Kristian S. Thygesen.

My Ph.D. has been a great experience. This has also been made possible thanks to the people I meet during the last three years that contribute to my growth. I would like to thank all of them and, in particular:

My supervisors Karsten W. Jacobsen and Kristian S. Thygesen for the inspirations, suggestions, and support they gave me during all my Ph.D. I have really appreciate all our discussions regarding physics and life;

Jan Rossmeisl, Vladimir Tripkovic, and Mårten Björketun for explaining electrocatalysis to me;

David D. Landis for the work he did for me on the Computational Materials Repository;

Fabio Dionigi, Peter C.K. Vesborg, Brian Seger, Søren Dahl, and Ib Chorkendorff for the useful discussions necessary for a theoretician to understand what is happening in the real world;

The administrative and computer staff (Marianne Ærsøe, Ole Holm Nielsen, Marcin Dulak, and Jens Jørgen Mortensen) for making my project possible;

All the people at DTU Physics that contributed to the nice environment at work;

Falco Hüser, Jens Jørgen Mortensen, Juan María García-Lastra, Thomas Olsen, Vladimir Tripkovic, Troels Markussen, David D. Landis, Mårten Björketun, Jun Yan, and Marcin Dulak for proofreading my thesis and Kirsten Andersen and Filip A. Rasmussen for translating my abstract in Danish;

The athletic club Trongårdens IF and its members for the good time spent together on the track. A special thanks to my coach, Lars S. Sørensen;

My family; my parents, Ornella e Pietro; my sister Martina; Olga, and Yu-Na for their never ending support.

Ivano E. Castelli
Kgs. Lyngby, 31st May 2013.

Abstract

Design new materials for energy production in a photoelectrochemical cell, where water is split into hydrogen and oxygen by solar light, is one possible solution to the problem of increasing energy demand and storage. A screening procedure based on *ab-initio* density functional theory calculations has been applied to guide the search for new materials. The main descriptors of the properties relevant for the screening are: heat of formation, electronic bandgap, and positions of the band edges with respect to the red-ox levels of water. A recently implemented exchange-correlation functional, called GLLB-SC, has been used for the estimation of the bandgaps.

Firstly, a screening procedure has been applied to 19000 cubic perovskite structures. These are obtained by combining 52 metals together with oxygen, nitrogen, sulfur and fluorine as anions. 32 promising materials have been found for visible light harvesting, 20 for the one-photon and 12 for the two-photon water splitting process. In addition, 16 candidates were suggested for the transparent shielding of the photocatalyst. The problem of corrosion has been addressed for the candidates for the one-photon scheme using Pourbaix diagrams.

Later on, the screening has been extended to more complex structures, like double and layered perovskites and new compounds of interest for the light harvesting problem were found. In addition, the trends in the bandgaps have been studied. The bandgaps can be tuned by an opportune combination of the metal atoms in the B-ion position in the double perovskite, and of the B-metal ion with the thickness of the octahedra in the layered perovskite structure.

In the first part, the crystal structure has been kept fixed. Later, the calculations were done using the structures provided by the Materials Project database, which is based on the experimental ICSD database, and the bandgaps were calculated with focus on finding materials with potential as light harvesters. 24 materials have been proposed for the one-photon water splitting and 23 for the two-photon mechanism.

Another method to obtain energy from Sun is using a photovoltaic cell that converts solar light into electricity. The absorption spectra of 70 experimentally known compounds, that are expected to be useful for light-to-electricity generation, have been calculated. 17 materials have been predicted to be promising for a single-layer solar cell and 11 for a double-layer device.

Resumé

Desig af nye materialer til energiproduktion i en photoelektrokemisk celle, hvor vand spaltes til brint og ilt med sollys, er en mulig løsning på problemet med stigende energifeterspørgsel og krav til opbevaring. En screeningprocedure baseret på beregninger med *ab-initio* tæthedsfunktionalteori blev anvendt i søgningen på nye materialer. Hoveddeskriptorerne for de relevante egenskaber i screeningen er: dannelsesentalpien, det elektroniske båndgab og positionen af båndenes kanter i forhold til red-ox niveauerne for vand. Et nyligt implementeret exchange-korrelations funktionale, kaldet GLLB-SC, er blevet anvendt til at estimere båndgab.

Som det første er en screenings procedure blevet anvendt på 19000 kubiske perovskit-strukturer. Disse opnås ved at kombinere 52 metaller med anionerne ilt, nitrogen, svovl og fluor. Dette resulterede i fund af 32 lovende materialer til høstning af synligt lys; 20 for en-foton og 12 for to-foton processen for spaltning af vand. Desuden blev der foreslået 16 kandidater til transparent skærmning af fotokatalysatoren. Problemet med korrosion er blevet imødekommet for kandidaterne til én-foton mekanismen ved hjælp af Pourbaix-diagrammer.

Senere er screeningen blevet udvidet til mere komplekse strukturer som dobbelte og lagdelte perovskitter, og nye forbindelser af interesse for høst af synlig lys fundet. Derudover er tendenser for båndgab blevet undersøgt. Båndgabene kan justeres ved en belejligt kombination af metalatomerne i B-ion-positionen for dobbelte perovskitter, og i B-metalionen med tykkelsen af oktaeden i den lagdelte perovskitstruktur.

I den første del blev krystalstrukturen fastholdt. Senere blev beregningerne udført under anvendelse af de strukturer der leveres af Materials Projekt databasen, som er baseret på det eksperimentelle ICSD database, og båndgab blev beregnet med fokus på at finde materialer med potentiale til at høste lys. 24 materialer blev foreslået for én-foton spaltning af vand og 23 for to-foton mekanismen.

En anden metode til at høste energi fra Solen er ved hjælp af solceller som omdanner solens lys til elektricitet. Absorptionsspektret af 70 eksperimentelt kendte forbindelser, der forventes at være brugbare for lys-til-el produktion, er blevet beregnet. 17 materialer er blevet forudsagt at være lovende for brug i enkeltlags-solceller og 11 for dobbeltlags-anordningen.

List of Included Papers

Paper I

Computational Screening of Perovskite Metal Oxides for Optimal Solar Light Capture

Ivano E. Castelli, Thomas Olsen, Soumendu Datta, David D. Landis, Søren Dahl, Kristian S. Thygesen, and Karsten W. Jacobsen
Energy Environ. Sci. **5**, 5814-5819, 2012.

Paper II

New Cubic Perovskites for One- and Two-photon Water Splitting Using the Computational Materials Repository

Ivano E. Castelli, David D. Landis, Kristian S. Thygesen, Søren Dahl, Ib Chorkendorff, Thomas F. Jaramillo, and Karsten W. Jacobsen.
Energy Environ. Sci. **5**, 9034-9043, 2012.

Paper III

Bandgap Engineering of Double Perovskites for One- and Two-photon Water Splitting

Ivano E. Castelli, Kristian S. Thygesen, and Karsten W. Jacobsen.
MRS Online Proceedings Library **1523**, 2013.

Paper IV

Performance of Genetic Algorithms in Search for Water Splitting Perovskites

Anubhav Jain, Ivano E. Castelli, Geoffroy Hautier, David H. Bailey, and Karsten W. Jacobsen.
J. Mat. Science Published Online, DOI: 10.1007/s10853-013-7448-9, 2013.

Paper V

Calculated Pourbaix Diagrams of Cubic Perovskites for Water Splitting: Corrosion Against Stability

Ivano E. Castelli, Kristian S. Thygesen, and Karsten W. Jacobsen.
Accepted, 2013.

Paper VI

Stability and Bandgaps of Layered Perovskites for One- and Two-photon Water Splitting

Ivano E. Castelli, Juan María García-Lastra, Falco Hüser, Kristian S. Thygesen, and Karsten W. Jacobsen.

To be submitted, 2013.

Contents

Preface	iii
Abstract	v
Resumé	vii
List of Included Papers	ix
Introduction	1
1 Theory	5
1.1 The Electronic Structure Problem	5
1.2 Density Functional Theory	6
1.2.1 The Kohn-Sham Equations	6
1.2.2 The Exchange-correlation Functionals	7
1.2.3 The Bandgap Problem	8
1.2.4 The Derivative Discontinuity	9
2 Cubic Perovskites for One-photon Water Splitting	13
2.1 One-photon Water Splitting	13
2.2 Computational Screening	14
2.2.1 Stability	14
2.2.2 Evaluation of the Bandgap	15
2.2.3 Calculation of the Band Edges	15
2.2.4 Crystal Periodic Structure	16
2.3 Cubic Perovskite Candidates	19
2.4 The Computational Materials Repository	24
2.5 Summary	24
3 Two-photon Water Splitting and Transparent Protecting Shield	27
3.1 Two-photon Water Splitting	27
3.2 Transparent Shielding	30
3.2.1 Transparent Shielding - Mechanism I	31
3.2.2 Transparent Shielding - Mechanism II	32
3.3 Summary	33
4 Corrosion Analysis of Cubic Perovskites for Water Splitting	35
4.1 The Pourbaix Diagrams	35
4.2 Cubic Perovskites	36
4.3 Candidates for One-photon Water Splitting	37

4.4	Summary	39
5	Statistical Model for Cubic Perovskite Semiconductors	41
5.1	Probability and Dendrogram Analysis	41
5.2	Prediction of ABO_2N Perovskites	46
5.3	Summary	47
6	Evolutionary Algorithms in Search for Water Splitting Perovskites	49
6.1	Evolutionary Algorithm	49
6.2	Results	51
6.3	Summary	54
7	Low Symmetry Perovskites for One- and Two-photon Water Splitting	55
7.1	Double Perovskites	55
7.1.1	Trends in Double Perovskites	55
7.1.2	Candidates in the Double Perovskite Structure	57
7.2	Layered Perovskites	57
7.3	Trends in Stability and Bandgaps	59
7.4	Candidates in the Layered Perovskite Structure	61
7.5	Summary	62
8	Water Splitters from the Materials Project Database	63
8.1	Bandgap Calculations	63
8.2	The Calculated Bandgaps	64
8.3	Materials for Water Splitting Applications	65
8.3.1	One-photon Water Splitting	65
8.3.2	Two-photon Water Splitting	67
8.4	Protective Transparent Shield	71
8.5	Summary	72
9	Thin Film Solar Cells	73
9.1	Theoretical Background	73
9.2	Results	74
9.3	Summary	81
	Final Remarks	83
	Bibliography	85
A	Calculated Bandgaps of the Materials Project Entries	91
B	Theoretical Efficiencies of the Thin Film Solar Cells	107
C	Papers	109

Introduction

One of the most pressing problems of our time is finding an easy and cheap access to sources of energy. Since of the industrial revolution, the consumed energy per person per year has increased constantly. In particular, the energy consumption in these days is more than five times larger than the corresponding consumption in the middle of the last century. This increment is directly related to the increase of the living standards after the Second World War. In the last twenty years, mainly in Europe and in a minor part in North America, the consumption per year is decreasing. The trend is opposite for the developing countries in East Asia and in the Pacific area where the consumption has doubled.¹

The required energy is around 80% obtained from fossil fuels, like petroleum, natural gas, and coal. The remaining is split between nuclear and mainly renewable energy, where the most used sources are biomasses, wind and hydropower. In the future, the fossil fuels will disappear or become too expensive to be used so massively. Indeed, several of the petroleum producer countries have already reached their production peaks. A possible solution is to increase the role of renewable sources in the global energy production next to a more responsible use of the energy. Among all the sources of energy, the Sun is the one with the highest potential.

The massive use of fossil fuels is also related to climate problems. One of the products of their combustion is carbon dioxide that is one of the most present greenhouse gas in the atmosphere and which emission is almost quadrupled in the last twenty years. Even if the effects on the climate of such a large increase of the CO₂ emissions is still uncertain, several scenarios have been studied. Some models predict moderate changes in the climate, whereas others predict dangerous increase in the temperatures, rise of the sea level, and more extreme atmospheric phenomena.² Another effect of the use of fossil fuels is the increase of pollution, particularly in the developing countries, with the related problems for the human health. These and others effects will encourage people to address to other sources of energy and in particular to solar energy since of its enormous potential.

The use of solar energy requires solar harvesting and consequent storage. The capture and conversion of solar light can be accomplished by means of photovoltaic (PV) cells, where the energy from the Sun is converted into electricity, or by photoelectrochemical (PEC) reactions, where the solar energy is converted into chemical energy. The challenge for an efficient PV cell is to reduce the cost of delivery of electricity. Due to the diurnal variation in solar insolation, and without an efficient, cheap, and eco-friendly storage, solar electricity will be hard to be the primary energy source. Solar electricity can be stored in batteries, but they are expensive, and contain dangerous and toxic chemical elements. Electricity can also be converted into thermal or mechanical energy, like pumping water uphill, but it requires for additional and expensive infrastructures (reservoirs, for example).²

In a PEC cell, the chemical bonds are broken and formed to produce fuel in a way similar to a photosynthesis process. The most simple reaction to run in a PEC cell is the electrolysis of water into hydrogen and oxygen. Hydrogen and oxygen can then be stored into tanks, converted into other chemicals, like ammonia, metal hydrides, and hydrocarbons, or stored into fullerenes and carbon nanotubes. A PEC cell requires a semiconductor that absorbs light and the energy from the created electron-hole pair is used to run the chemical reactions.

A semiconductor to be useful in a PEC cell as a light harvester should be (i) chemically and structurally stable under irradiation; have (ii) an appropriate bandgap allowing the utilization of a good part of the solar spectrum; have (iii) band edges well positioned with respect to the red-ox levels of water; and have (iv) high electron-hole mobility so that the electrons and holes reach two different parts of the surface and reduce/oxidize the targets before recombining.^{3,4} In addition, low cost and non-toxicity are also required. Several efforts have been made to design a semiconductor to split water in oxygen and hydrogen using the energy from the Sun starting from more than 40 years ago when Fujishima and Honda⁵ proposed to use TiO_2 as light harvesting material under UV light. More recently, Maeda *et al.*⁶ have found that the solid solution of GaN and ZnO is a promising material for water splitting under visible light. Other materials recently proposed to be used are silver niobate (AgNbO_3)⁷ and few perovskite oxynitrides (BaTaO_2N , SrTaO_2N , CaTaO_2N and LaTiO_2N)⁸. Even if numerous semiconductors have been studied, the ideal material has not been found.

The focus of the present thesis is to find new materials that can be used in a PEC cell under visible light irradiation combining Density Functional Theory (DFT) with a computational screening approach. The development of new materials using *ab-initio* quantum mechanical calculations has been possible thanks to the increase of computational power over the last couple of decades, in combination with methodological improvements. Examples of computational screening include the construction of semiconductor superlattices,⁹ the development of battery cathodes,¹⁰ searching for high stability alloys¹¹ and, more recently, for high performance piezoelectrics,¹² for inorganic scintillators,¹³ and for organic photovoltaics.^{14,15}

In general, computer simulations are faster and cheaper than experiments. It means that the number of materials under investigation can be enormous. Computer simulations can rapidly reduce the number of candidates for a particular application following the desired design criteria based on few descriptors that connect microscopic quantities to macroscopic properties, and then suggest materials for experimental investigation. Experiments and simulations usually work on two different aspect of the same problem: in computer simulations, the atomic and electronic structure can be easily studied but it is difficult to obtain the global picture, including also the external conditions, that instead can be studied by experiments. In the materials design process, experiments and simulations are deeply connected: experiments define the problem and the important parameters to be used in the computer simulations. The screening provides (few) interesting materials to investigate experimentally and wait for feedback on how to improve the results.

In the present study, around 23000 materials have been screened for stability, bandgap, and position of the band edges. An handful number of candidates have potential to be used in a PEC device and as a protecting shield against corrosion. The problem of finding new efficient materials for a thin film solar cell has also been addressed.

Outline of the Thesis

This thesis is organized as follows:

Chapter 1 introduces briefly Density Functional Theory and describes the theoretical methods that have been used during the project.

Chapter 2 presents the screening for new materials in the cubic perovskite structure with general formula ABX_3 , where X_3 is oxygen, nitrogen, sulfur, fluorine, and their possible combinations, for one-photon water splitting. These results are presented in Papers I and II.

Chapter 3 reports the results of the screening for two-photon water splitting device, and transparent shielding of the photocatalyst for the cubic perovskites considered in Chapter 2. This is a summary of the results included in Paper II.

Chapter 4 discusses the problem of stability in water using Pourbaix diagrams and combining theoretical data, like DFT total energies, with experimental information, such as dissolution energies. This chapter is based on Paper V.

Chapter 5 presents trends for stability and bandgap of the cubic perovskites by using simple statistical methods and cluster analysis.

Chapter 6 introduces an evolutionary algorithm used to identify the candidates for one-photon water splitting in the cubic perovskite structures. The results on the effect of different parameters on the efficiency of the algorithm are presented in Paper IV.

Chapter 7 presents the screening for one- and two-photon water splitting for double and layered perovskites. Few suggestions on how to combine different metals, for the double perovskites, and to change the thickness of the layers, for the layered structures, to tune the bandgap are provided. The results are collected in Paper III and VI.

Chapter 8 reports the results of bandgap calculations of experimentally available structures present in the Materials Project database.¹⁶ The screening looks for applications related to the light harvesting problem.

Chapter 9 presents the screening for new thin film solar cell materials. The absorption spectra of 70 experimentally known materials have been calculated.

Most of the results presented in this work are based on first principle (or *ab-initio*) quantum mechanic calculations. First principle means that the only input to a calculation is the information regarding the atoms, like atomic numbers and positions, and the unit cell. No additional empirical parameters are needed. The methodological improvements and the increase of computational powers in the last decades has made it possible to study more realistic systems and to enable a direct comparison with experimental results. It has also been possible to search for new, more efficient materials by using only first principle techniques. The goal of this chapter is to provide a general introduction of the theory used in this thesis. Atomic units are used in this section, $e = \hbar = m_e = 1$.

1.1 The Electronic Structure Problem

Condensed matter systems are composed of interacting electrons and nuclei. All their ground state properties can be described using the time independent Schrödinger equation:

$$\hat{H}\Psi = \epsilon\Psi, \quad (1.1)$$

where \hat{H} is the Hamilton operator that describes the system, Ψ the many-body wavefunction, and ϵ the total energy. The non-relativistic hamiltonian of N electrons and M nuclei of charge $Z_K > 0$ and mass m_K is given by the sum of the kinetic energies, T , of the electrons and nuclei, the attractive interaction between the electrons and nuclei, V_{en} , and the Coulomb repulsion between the electrons, V_{ee} , and between the nuclei, V_{nn} :

$$\begin{aligned} H &= T + V_{en} + V_{ee} + V_{nn} \\ &= -\frac{1}{2} \sum_{i=1}^N \nabla_i^2 - \frac{1}{2} \sum_{K=1}^M \frac{1}{m_K} \nabla_K^2 \\ &\quad - \sum_{i=1}^N \sum_{K=1}^M \frac{Z_K}{|\mathbf{r}_i - \mathbf{R}_K|} + \sum_{i<j}^N \frac{1}{|\mathbf{r}_i - \mathbf{r}_j|} + \sum_{K<L}^M \frac{Z_K Z_L}{|\mathbf{R}_K - \mathbf{R}_L|}, \end{aligned} \quad (1.2)$$

where the lower- (upper-)case letters indicate electrons (nuclei). The hamiltonian depends on both electrons and nuclei. V_{en} can be replaced by v_{ext} to include also other possible static force fields than those created by the nuclear charges. Due to the large difference in mass between the electrons and nuclei, the hamiltonian can be decoupled

into nuclear and electron systems (Born-Oppenheimer approximation¹⁷). Electrons, that are around 2000 times lighter than the hydrogen nucleus, respond instantaneously to the change in the positions of the nuclei, while nuclei are assumed to be fixed. The kinetic term of the nuclei and the repulsive Coulomb interaction between them can thus be added to the hamiltonian as constants.

Eq. 1.2 can be solved in different ways depending on the system under investigation and the level of approximation. In the *Hartree-Fock* method,¹⁸ the many-body wavefunction is approximated by a single Slater determinant. More sophisticated methods, as for example Configuration Interaction¹⁹ and variational Quantum Monte Carlo,²⁰ have been developed to provide more accurate results, but with an increase of the computational cost. Eq. 1.2 can also be calculated in terms of one-particle Green's functions to obtain the ground state energies (Random Phase Approximation²¹) or the quasi-particle energies (GW method²²).

Density Functional Theory (DFT) is one of the most used and powerful methods to calculate ground state properties. Instead of using the many-body wavefunctions or the one-particle green's functions, the many-body problem is solved in terms of the non-interacting electron density, $n(\mathbf{r})$. The next section gives an introduction to the DFT method.

1.2 Density Functional Theory

DFT is based on the work by Hohenberg and Kohn:²³

Theorem 1.1. (Hohenberg-Kohn 1, 1964) *There is a one-to-one correspondence between the ground state electron density $n(\mathbf{r})$ and the external potential v_{ext} acting on the system.*

This means that two ground state densities are different if their external potentials differ by more than a constant. All the physical ground state properties of a system are determined uniquely by the electron density $n(\mathbf{r})$. The ground state energy E , depending on v_{ext} , is a functional of the ground state density:

$$E[n(\mathbf{r})] = \langle \Psi[n(\mathbf{r})] | T + V_{ee} | \Psi[n(\mathbf{r})] \rangle + \int v_{ext}(\mathbf{r})n(\mathbf{r})d\mathbf{r} . \quad (1.3)$$

The ground state energy is obtained through a variational principle which is a consequence of the Hohenberg-Kohn Theorem.

Theorem 1.2. (Hohenberg-Kohn 2, 1964) *For any density $n'(\mathbf{r})$, the ground state energy, E_0 , is the minimum value of the energy functional, $E[n'(\mathbf{r})]$.*

So, the energy functional $E[n'(\mathbf{r})]$, that is uniquely defined by v_{ext} , is minimal at the ground state density and the minimum is:

$$E_0 = \min_{n'(\mathbf{r})} E[n'(\mathbf{r})] . \quad (1.4)$$

The two theorems provide the basis for DFT, but they do not explain how to solve the many-body problem in a simple way.

1.2.1 The Kohn-Sham Equations

The work by Kohn and Sham²⁴ gives a simple scheme in which the system of interacting electrons is mapped onto a system of non-interacting electrons. Kohn and Sham proved that for a given interacting ground state density, $n_0(\mathbf{r})$, there exists an effective potential,

V_s , where the non-interacting hamiltonian $H = T + V_s$ gives a ground state density, $n(\mathbf{r})$, equal to $n_0(\mathbf{r})$. The Schrödinger equation (Eq. 1.1) can now be written in terms of the single-particle wavefunctions $\phi_i(\mathbf{r})$:

$$\widehat{H}_{\text{KS}}\phi_i(\mathbf{r}) = \epsilon_i\phi_i(\mathbf{r}) , \quad (1.5)$$

where \widehat{H}_{KS} is the one-electron hamiltonian.

Since the Hohenberg-Kohn theorem 1.1 is valid for any system of electrons, v_s is determined in a unique way by the density n and the density functional 1.3 can be written as:

$$E_{KS}[n(\mathbf{r})] = T_s[n(\mathbf{r})] + \int v_s(\mathbf{r})n(\mathbf{r})d\mathbf{r} , \quad (1.6)$$

where T_s is the kinetic energy of the independent particles.

The Kohn-Sham effective potential, v_s , is the sum of the Hartree potential v_H , the external potential v_{ext} and the exchange-correlation potential v_{xc} :

$$v_s(\mathbf{r}) = v_H(\mathbf{r}) + v_{ext}(\mathbf{r}) + v_{xc}(\mathbf{r}) . \quad (1.7)$$

The Hartree potential accounts for the Coulomb interaction between the electrons:

$$v_H = \frac{1}{2} \iint \frac{n(\mathbf{r})n(\mathbf{r}')}{|\mathbf{r} - \mathbf{r}'|} d\mathbf{r}d\mathbf{r}' , \quad (1.8)$$

and v_{ext} includes the interactions due to the nuclei and other external potentials. The many-body interactions (exchange and correlation) are collected in v_{xc} .

The exchange-correlation functional $E_{xc}[n]$ is defined as:

$$E_{xc}[n] = T[n] - T_s[n] + V_{ee}[n] - V_H[n] , \quad (1.9)$$

where $T[n] - T_s[n]$ reproduces the correlation contribution to the kinetic energy and $V_{ee}[n] - V_H[n]$ the interactions between electrons beyond the Hartree energy. v_{xc} is the functional derivative of $E_{xc}[n]$ with respect to the density. The Kohn-Sham hamiltonian is exact, and only v_{xc} needs to be approximated. The Kohn-Sham equation (Eq. 1.5) is usually solved numerically through a self-consistency procedure: at first an initial density is chosen, the corresponding effective potential is calculated, and, then, the Kohn-Sham equation is solved. A new density is constructed and the iterative cycle starts again until the desired convergence is reached.

1.2.2 The Exchange-correlation Functionals

The exchange-correlation functional can be approximated in several ways with different computational cost and accuracy. The most common functionals are the Local Density Approximation (LDA) and the Generalized Gradient Approximation (GGA).

The Local Density Approximation (LDA)

Since the Kohn-Sham equations separate the independent-particle kinetic energy and the long range Hartree potential, the remaining term can be approximated by a local functional of the density. In the Local Density Approximation,²⁴ the xc-energy density is approximated by the xc-energy density of the homogeneous electron gas of density $n(\mathbf{r})$, $\epsilon_{xc}^{\text{HEG}}(n(\mathbf{r}))$:

$$E_{xc}^{\text{LDA}} = \int n(\mathbf{r})\epsilon_{xc}^{\text{HEG}}(n(\mathbf{r}))d\mathbf{r} . \quad (1.10)$$

The exchange term of $\epsilon_{xc}^{\text{HEG}}(n(\mathbf{r}))$ is known exactly, while the correlation part is calculated by quantum Monte-Carlo methods. In principle, LDA should be used only for slowly varying densities but it has success for a larger class of systems even if it overbinds the atoms in molecules and solids, and underbinds the core electrons.²⁵ For example, LDA fails to reproduce strongly correlated systems, where the approximation of independent particles breaks down.

The Generalized Gradient Approximation (GGA)

The Generalized Gradient Approximation is an improvement of the Local Density Approximation. Since the exchange-correlation functional also depends on the gradient of the density in addition to the density, GGA is more suitable for in-homogeneous systems. The exchange-correlation functional assumes the form:

$$E_{xc}^{\text{GGA}} = \int f(n(\mathbf{r}), \nabla n(\mathbf{r})) d\mathbf{r} . \quad (1.11)$$

Compared to LDA functionals, GGAs usually give better results in terms of total and atomization energies, structural energy differences and energy barriers. GGA corrects (and sometimes overcorrects) the length of bonds by making them longer than for LDA.²⁶ While the $\epsilon_{xc}^{\text{HEG}}$ in LDA is a well defined function, several forms of the GGAs $f(n(\mathbf{r}), \nabla n(\mathbf{r}))$ are available and lead to different implementations, like Perdew-Wang (PW91),²⁵ and Perdew-Burke-Enzerhof (PBE).²⁶ A revised PBE, called RPBE,²⁷ that gives better results for atomization energies, has been used for optimizing the structures and for calculating the total energies throughout this work.

1.2.3 The Bandgap Problem

One of the biggest failures of standard DFT is the evaluation of bandgaps. In comparison with experimental values, DFT bandgaps are seriously underestimated. DFT calculates the bandgap as the difference between the lowest unoccupied (LUMO) and the highest occupied molecular orbital (HOMO). In reality, the quasi-particle or fundamental bandgap, $E_{\text{gap}}^{\text{QS}}$, is given by the difference between the ionization energy, I , and the electron affinity, A . The ionization energy is defined as the energy required to remove an electron from the system, the electron affinity as the energy released from a neutral system when an electron is added:

$$E_{\text{gap}}^{\text{QS}} = I - A = E_{N-1} - E_N + E_{N+1} - E_N = E_{N+1} + E_{N-1} - 2E_N , \quad (1.12)$$

where E_N is the energy of the N -electron system and E_{N+1} and E_{N-1} are the energies of the system when one electron is added and removed, respectively.

The work by Janak²⁸ provides a relation between the energy functional and the Kohn-Sham eigenvalues:

Theorem 1.3. (Janak, 1978) *The eigenvalue, ϵ_i , of a system is the derivative of the total energy with respect to the orbital occupation number of the state, n_i :*

$$\epsilon_i = \frac{\partial E}{\partial n_i} . \quad (1.13)$$

For a non-interacting system, the theorem is always valid. For an interacting system, the only eigenvalue that is exact is the energy of the highest occupied state, because the ground state density is exact.²⁹ This eigenvalue corresponds to minus the ionization energy, $-I$. The lowest unoccupied state is, instead, different from the electron affinity, because the density changes when this state becomes occupied. As a result, the bandgaps turn out to be underestimated.

Another source of error is the so-called self-interaction error: in the expression of the Hartree potential (Eq. 1.8), each electron feels the electrostatic repulsion from all the electrons in the system including itself.

The bandgap problem is not intrinsic in DFT, but is related to the exchange-correlation functional chosen. All the functionals that do not include the calculation of the derivative discontinuity show a failure in the evaluation of the bandgap.³⁰ There are several methods to overcome the problem. Since Hartree-Fock (HF) does not suffer from the self-interaction error and does not contain any correlation term, the bandgap

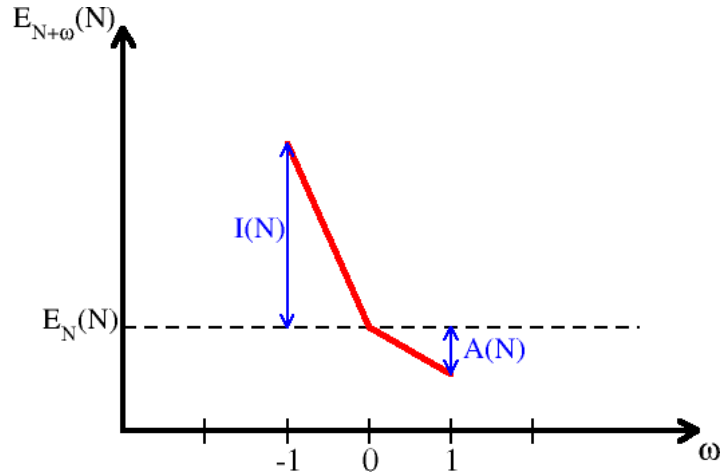


Figure 1.1: Ground state energy of an atom with N charges in the nucleus and $N + \omega$ electrons.

is overestimated. Hybrid functionals combine a portion of exact exchange present in HF with exchange and correlation from DFT and gives more reliable bandgaps. There are several hybrid functionals available. The most popular functionals are Becke, Lee-Yang-Parr (B3LYP),³¹ and Heyd-Scuseria-Ernzerhof (HSE).³² Another approach is to use many-body methods, like the GW approximation.²² These methods give more accurate results for the bandgap than standard DFT with an increase of the computational cost. A third way is to use a functional that includes the derivative discontinuity.

1.2.4 The Derivative Discontinuity

The chemical potential, μ , for a system is defined as:

$$\mu = \frac{\delta E}{\delta n(\mathbf{r})} . \quad (1.14)$$

For a N -electron system in the ground state with energy E_N , the chemical potential $\mu(N)$ takes the form

$$\mu(N) = \frac{\partial E_N}{\partial N} . \quad (1.15)$$

The concept of derivative discontinuity becomes clear when a system with non-integer number of particles is considered* The total ground state energy, E_{tot} , of two well-separated neutral atoms, X and Y , is:

$$E_{tot} = E_X + E_Y , \quad (1.16)$$

where E_X (E_Y) is the ground state energy of X (Y). $\mu(N)$ is assumed to be continuous and, in addition, $\mu(X) < \mu(Y)$, so that there is a fraction of electrons, δN_y , that moves from Y to X . This lowers the total energy by $(\mu(X) - \mu(Y))\delta N_y < 0$. The energy is thus minimized with a negative charge on X and a positive charge on Y and this is a paradox to Eq. 1.16.

Following Perdew *et al.*,³³ for an open system with fractional electron number, the minimizing density is

$$n(\mathbf{r}) = (1 - \omega)n_N(\mathbf{r}) + \omega n_{N+1}(\mathbf{r}) , \quad (1.17)$$

*In 1982, Perdew *et al.*³³ extended Density Functional Theory to densities with fractional particle numbers.

where n_N and n_{N+1} are the densities of the N and $N+1$ -particle systems, and ω is the fraction of electron. The energy minimum for a fractional electron ω is given by:

$$E_{N+\omega} = (1 - \omega)E_N + \omega E_{N+1} , \quad (1.18)$$

where E_N and E_{N+1} are the energies of the N and $N+1$ -particle systems, respectively. The total energy E_N as a function of the particle number N is composed of straight lines with possible derivative discontinuities at N , as shown in Fig. 1.1. The first ionization potential, $I(N)$, and the electron affinity, $A(N)$, are defined as:

$$I(N) = E_{N-1}(N) - E_N(N) \quad (1.19)$$

$$A(N) = E_N(N) - E_{N+1}(N) . \quad (1.20)$$

The chemical potential is equal to $I(N)$ for $1 < \omega < 0$ and to $A(N)$ for $0 < \omega < 1$. The paradox is solved using these definitions. In fact, the total energy of the two separated atoms is:

$$E_{tot} = E_{X-\omega} + E_{Y+\omega} , \quad (1.21)$$

and is minimized at $\omega = 0$ since for real systems the largest electron affinity is still smaller than the smallest first ionization potential.³⁴

With the concept of fractional number of electrons, the bandgap of a solid can be written as:

$$E_{\text{gap}} = I - A = -\mu(N - \delta) + \mu(N + \delta) = \left. \frac{\delta E}{\delta n(\mathbf{r})} \right|_{N+\delta} - \left. \frac{\delta E}{\delta n(\mathbf{r})} \right|_{N-\delta} , \quad (1.22)$$

with $\delta \rightarrow 0$. The Hartree and the external potential give no contribution to the bandgap and do not contain a discontinuity. For a non interacting system, the bandgap is given by the Kohn-Sham bandgap, $E_{\text{gap}}^{\text{KS}}$, through the kinetic term:

$$E_{\text{gap}}^{\text{KS}} = \left. \frac{\delta T_s}{\delta n(\mathbf{r})} \right|_{N+\delta} - \left. \frac{\delta T_s}{\delta n(\mathbf{r})} \right|_{N-\delta} = \epsilon_{\text{lumo}} - \epsilon_{\text{homo}} , \quad (1.23)$$

and for the interacting system, the bandgap is equal to:

$$E_{\text{gap}} = \left. \frac{\delta T_s}{\delta n(\mathbf{r})} \right|_{N+\delta} - \left. \frac{\delta T_s}{\delta n(\mathbf{r})} \right|_{N-\delta} + \left. \frac{\delta E_{xc}}{\delta n(\mathbf{r})} \right|_{N+\delta} - \left. \frac{\delta E_{xc}}{\delta n(\mathbf{r})} \right|_{N-\delta} = E_{\text{gap}}^{\text{KS}} + \Delta_{\text{gap}}^{xc} , \quad (1.24)$$

where Δ_{gap}^{xc} is derivative discontinuity. This term is missing by construction in the most common exchange-correlation functionals, and the segments of Fig. 1.1 are approximated by a continuous function with continuous derivative. At least for common semiconductors, the lack of the derivative discontinuity is considered responsible for the discrepancy between the calculated and experimental bandgaps.

The Gritsenko-van Leeuwen-van Lenthe-Baerends Potential (GLLB)

The potential proposed by Gritsenko, van Leeuwen, van Lenthe, and Baerends³⁵ contains by construction the derivative discontinuity. The good results with respect to the evaluation of the bandgaps of semiconductors is one of the reasons why this potential has been chosen during this work. The following section will give a brief introduction to the potential.

The original GLLB potential is a further approximation to the KLI approximation to the exact exchange optimized effective potential (EXX-OEP)[†]. The exchange correlation potential, v_{xc} , contains a screening part, $v_{xc,scr}$, and a response term, $v_{xc,resp}$. The

[†]The Optimized Effective Potential method³⁶ is an improvement to the common exchange-correlation functionals. It has the advantages of including the derivative discontinuity and it does not require any assumption about the homogeneity of the system.³⁷ It is also more time consuming than standard functionals, like LDA, and it requires further approximations, like the one proposed by Krüger, Li, and Iafate (KLI).³⁸

Compound	LDA	GLLB	GLLB-SC	GW	Exp.
C ^a	4.09	5.70	5.41	5.33	5.48
Si ^a	0.44	1.13	1.00	1.24	1.17
Ge ^a	0.00	0.00	0.27	n.a.	0.74
AlAs ^a	1.34	2.72	2.49	2.18	2.32
GaAs ^a	0.36	0.69	1.04	1.58	1.63
LiF ^a	8.78	15.38	14.96	13.5	14.2
Ar ^a	8.18	14.46	14.97	13.1	14.2
InP ^b	0.61	n.a.	1.63	1.32	1.42
MgO ^b	4.63	n.a.	8.32	7.25	7.83
MAE	2.28	0.54	0.41	0.36	

^aReference.⁴⁰

^bReference.⁴²

Table 1.1: Comparison between different methods for calculating the bandgaps and their experimental values. The Mean Absolute Error (MAE) is also indicated. All units are in eV.

screening term contains the Coulomb potential of the exchange-correlation hole and is attractive. The response term depends on the pair correlation response to variations of the density. It is repulsive and a short-range term. These two terms are approximated using a GGA functional. In the original GLLB potential, B88 was used³⁹ with good results for small systems because of the asymptotic behavior $-1/r$ and a single parameter that fits with a variety of atomic systems. A revised version of the GLLB potential, called GLLB-SC⁴⁰ (where SC stands for solid, correlation), uses the PBEsol functional⁴¹ which performs better in case of solids. The screening term is written as

$$v_{xc,scr}(\mathbf{r}) = 2\epsilon_{xc}^{\text{PBEsol}}(\mathbf{r}) . \quad (1.25)$$

Using the KLI approximation, the response term is written as

$$v_{xc,resp}(\mathbf{r}) = \sum_i^{\text{occ}} \omega_i \frac{|\psi_i(\mathbf{r})|^2}{n(\mathbf{r})} , \quad (1.26)$$

where the coefficients ω_i are determined self-consistently. ω_i is expensive to calculate because it includes the Fock-operator. The GLLB potential simplifies this expression to a function that depends only on the differences of the Kohn-Sham eigenvalues:

$$\omega_i = f(\epsilon_r - \epsilon_i) = K_x \sqrt{\epsilon_r - \epsilon_i} , \quad (1.27)$$

where $K_x \approx 0.382$ is a parameter to reproduce the exchange potential for the uniform electron gas and ϵ_r is a reference energy corresponding to the highest occupied eigenvalue. The final form for the exchange-correlation potential is:

$$v_{xc}^{\text{GLLB-SC}}(\mathbf{r}) = 2\epsilon_{xc}^{\text{PBEsol}}(\mathbf{r}) + \sum_i^{\text{occ}} \kappa_x \sqrt{\epsilon_r - \epsilon_i} \frac{|\psi_i(\mathbf{r})|^2}{n(\mathbf{r})} + v_{c,resp}^{\text{PBEsol}}(\mathbf{r}) , \quad (1.28)$$

The correlation in the response part is taken from the PBEsol functional, $v_{c,resp}^{\text{PBEsol}}$.

The discontinuity is included in the exchange response part and in particular in the calculation of the coefficients ω_i . ω_i depends explicitly on the reference energy ϵ_r . For an integer occupation J , ϵ_r is equal to:

$$\epsilon_r = \begin{cases} \epsilon_J & \text{if } N \leq J \\ \epsilon_{J+1} & \text{if } N > J . \end{cases} \quad (1.29)$$

ϵ_r is the HOMO when the particle number, N , is smaller than the J . As soon as N exceeds the occupation, the LUMO becomes now the highest occupied state and it is the

new reference. Due to the change in the reference energy, the discontinuity, at $N = J$, has the form:

$$\Delta_{x,resp} = \sum_i^N \kappa_x (\sqrt{\epsilon_{N+1} - \epsilon_i} - \sqrt{\epsilon_N - \epsilon_i}) \frac{|\psi_i(\mathbf{r})|^2}{n(\mathbf{r})}. \quad (1.30)$$

$\Delta_{x,resp}$ depends on the spatial coordinates. The discontinuity, that is unique for each system, is evaluated using first order perturbation theory:

$$\Delta_{xc} = \langle \psi_{N+1} | \Delta_{x,resp} | \psi_{N+1} \rangle. \quad (1.31)$$

The dominant term in the discontinuity comes from a region close to the Fermi level. In fact, the contribution to $\Delta_{x,resp}$ is vanishing for $\epsilon_i \rightarrow -\infty$.

The quasi-particle bandgap, $E_{\text{gap}}^{\text{QS}}$, is then obtained adding the discontinuity to the Kohn-Sham gap:

$$E_{\text{gap}}^{\text{QS}} = E_{\text{gap}}^{\text{KS}} + \Delta_{xc} = \epsilon_{\text{lumo}} - \epsilon_{\text{homo}} + \Delta_{xc}. \quad (1.32)$$

Kuisma *et al.*⁴⁰ have calculated the bandgaps of semiconductors and insulators using different methods, like LDA, GLLB(-SC), and GW, and compared the results with experimental values. All the values are reported in Table 1.1. As indicated by the Mean Absolute Errors, the GLLB(-SC) performs much better than standard LDA and gives bandgaps very close to the ones obtained by GW.

The GLLB-SC potential has been widely used in this work. Since it is not a functional, but only a potential, the total energy is not calculated. The GLLB-SC has been used to calculate the bandgaps while the crystal structures have been optimized using RPBE. GPAW^{43,44} is the DFT code used throughout this thesis.

Chapter 2

Cubic Perovskites for One-photon Water Splitting

This chapter describes the screening scheme and discusses the results of the screening of around 19000 cubic perovskites for the one-photon water splitting application. In order to have an easy access to the data and to favor their sharing and analysis, the development of a database, called Computational Materials Repository (CMR), has been necessary. The chapter is based mainly on Paper I and, in a minor part, on Paper II.

2.1 One-photon Water Splitting

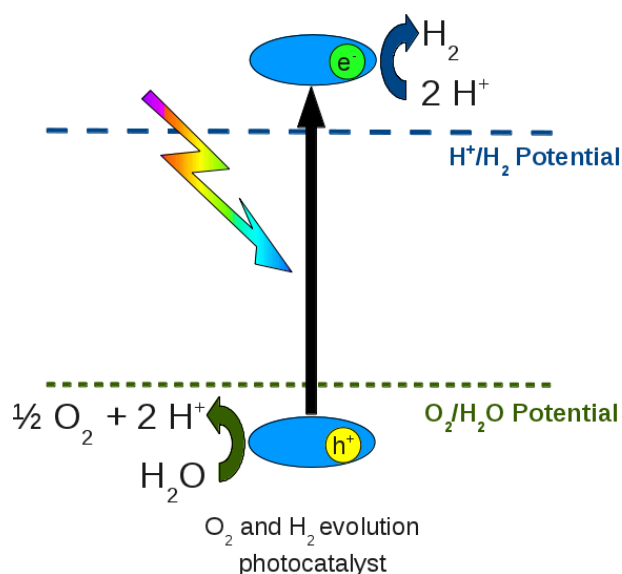


Figure 2.1: One-photon water splitting scheme. One photon creates an electron-hole pair that evolves oxygen and hydrogen from water.

Since the discovery of TiO_2 as a light harvesting material and its use in a photo-electrochemical (PEC) cell,⁵ several devices for water splitting have been studied. The

basic PEC device uses a single material to collect the light and to run the reactions that simultaneously produce hydrogen and oxygen from water. Since only one photon is required, this process is usually called one-photon (or overall) water splitting.

The one-photon water splitting process is schematized in Fig. 2.1: firstly a single photon creates an electron-hole pair. Subsequently the electron and the hole reach two different regions of the surface, and then evolve hydrogen and oxygen, respectively. An ideal material to carry out this process should fulfill several requisites, namely (i) chemical and structural stability, (ii) bandgap that allows a significant use of the solar spectrum, (iii) band edges straddling with the oxygen and hydrogen evolution potentials, and (iv) high mobility to avoid recombination.

A light harvester with a large bandgap, for example in the UV part of the solar spectrum, like TiO_2 , will collect only few percents of the spectrum corresponding to the photons at a higher energy. Thus, it does not fulfill criterion (ii) from above. The theoretical efficiency, given by the amount of photon collected and considering that each photon generates an electron-hole pair, is further reduced during the process because of the engineering of the device. It is thus natural to look for a smaller bandgap, typically in the visible range, that provides a higher theoretical efficiency. In fact, the bandgap should not be too small: the lower limit is defined by the bare energy required to split water (1.23 eV) plus an additional energy required to overcome the overpotential for the oxygen and hydrogen evolution processes⁴⁵ and to compensate for the positions of the quasi Fermi levels within the bandgaps.⁴⁶ In summary, the bandgap should be large enough to run the water splitting reactions and in the same time small enough to provide a good efficiency. This can be mainly accomplished in the visible part of the solar spectrum between 1.5 and 3 eV.

2.2 Computational Screening

The screening for new materials is based on properties (i), (ii), and (iii) mentioned above, namely the search for stable materials with optimal, well positioned, bandgaps. From the theoretical point of view, each material under investigation requires a stability analysis, the evaluation of the size of the bandgap, and of the position of the band edges. The method described in the following sections is used for the screenings throughout all this thesis.

2.2.1 Stability

Each material investigated in the screening is fully optimized. The optimization has been done in three steps: (i) a relaxation of the lattice parameters, (ii) an optimization of the internal degrees of freedom and (iii) a second relaxation of the lattices. At this point, most of the structures do not require further iterations. The optimized structures have a level of accuracy good enough compared to the available experimental data to be used for calculating the energy and the bandgap. For the relaxations and the calculation of the stabilities, a standard DFT-GGA exchange-correlation functional (RPBE-approximation²⁷) has been used.

The simplest way to evaluate the stability of a compound is to calculate its atomization energy, i.e. the energy difference between the material and its constituents in their standard state. In the screening process, the stability is obtained using a more accurate scheme. In fact, the total energy of each compound is compared, using a linear programming algorithm (LP), with a pool of reference systems, rather than the standard states, to determine whether the material is stable or not. This method has been used for example for obtaining effective cluster interactions,⁴⁷ and for prediction of thermodynamically reversible hydrogen storage reactions.⁴⁸ For each chemical element, M, the pool of references include the most stable, single-metal bulk (M_x), oxide (M_xO_y), nitride (M_xN_y), sulfide (M_xS_y), fluoride (M_xF_y), oxynitride ($\text{M}_x\text{N}_y\text{O}_z$),

oxysulfide ($M_xS_yO_z$), and oxyfluoride ($M_xF_yO_z$), and the most stable, bi-metal oxide ($M_x^1M_y^2O_z$), nitride ($M_x^1M_y^2N_z$), sulfide ($M_x^1M_y^2S_z$), fluoride ($M_x^1M_y^2F_z$), oxynitride ($M_x^1M_y^2N_zO_k$), and oxyfluoride ($M_x^1M_y^2F_zO_k$) as available in the experimental ICSD database⁴⁹ and from the Materials Project database¹⁶ for a total of around 500 reference systems. The chemical potentials for nitrogen, sulfur and fluorine have been taken from the standard references in the gas phase (N_2 , S_8 , and F_2). The chemical potential for oxygen refers to water in the gas phase, and the oxygen reference has been calculated as the energy difference between water and hydrogen molecule (H_2O-H_2) in the gas phase. This choice is also supported by the fact that the candidate has to work in an aqueous environment since the presence of a water film is a necessary condition to run the water splitting reaction because it increases the mobility of the H^+ ions.⁵⁰

For example, the $ABON_2$ cubic perovskite is considered stable when the difference between its DFT energy and the most favorable outcome from the LP, ΔE , is below 0.2 eV/atom. There are two main reasons to take this positive threshold for the stability: (i) DFT accuracy is around this value,⁵¹ and (ii) some materials can be metastable. The energy difference, ΔE is

$$\begin{aligned} \Delta E = & ABON_2(s) + \\ & - \min_{c_i} (c_1A(s) + c_2B(s) + c_3A_{a_3}O_{o_3}(s) + c_4B_{b_4}O_{o_4}(s) + \\ & + c_5A_{a_5}N_{n_5}O_{o_5}(s) + c_6B_{b_6}N_{n_6}O_{o_6}(s) + c_7A_{a_7}N_{n_7}(s) + \\ & + c_8B_{b_8}N_{n_8}(s) + c_9A_{a_9}B_{b_9}O_{o_9}(s) + c_{10}A_{a_{10}}B_{b_{10}}N_{n_{11}}(s) + \\ & + c_{11}O + c_{12}N_2) , \end{aligned} \quad (2.1)$$

with the condition

$$c_i \geq 0 , \quad (2.2)$$

that ensures that only the references containing A, B, N, or O are used as references. The correct stoichiometry of $ABON_2$ is obtained by imposing the following constrains:

$$\begin{aligned} \sum_i c_i a_i = 1 , \quad \sum_i c_i b_i = 1 , \\ \sum_i c_i o_i = 1 , \quad \sum_i c_i n_i = 2 . \end{aligned} \quad (2.3)$$

2.2.2 Evaluation of the Bandgap

As described in the previous chapter, reliable calculations of the bandgaps require a density functional beyond GGA. The GLLB-SC potential^{35,40} has been used for calculating the bandgaps once the structures have been optimized.

The bandgaps obtained using the GLLB-SC potential have been compared with other methods, like LDA, GW, and experiments, for semiconductors and insulators^{40,42} (Table 1.1) and for molecules.⁵² Fig. 2.2 compares the magnitudes of the GLLB-SC bandgaps of a selection of non-magnetic metal oxides with different structures with the experimental values. The obtained absolute deviation of 0.5 eV is sufficiently accurate for the screening study. A similar result has been obtained also in the cases of bi-metal bulk systems, while for molecules GW gives significantly better results. The GLLB-SC gives results comparable to the one obtained with many-body perturbation techniques such as the GW approximation, but with a significantly lower computational cost. This is very important in a screening project that involves several thousands of calculations where the optimal balance between accuracy and computational cost should be pursued.

2.2.3 Calculation of the Band Edges

To evolve hydrogen and oxygen, the band edges of the compound have to straddle with the red-ox levels of water. Although some methods have been proposed,^{53,54} it

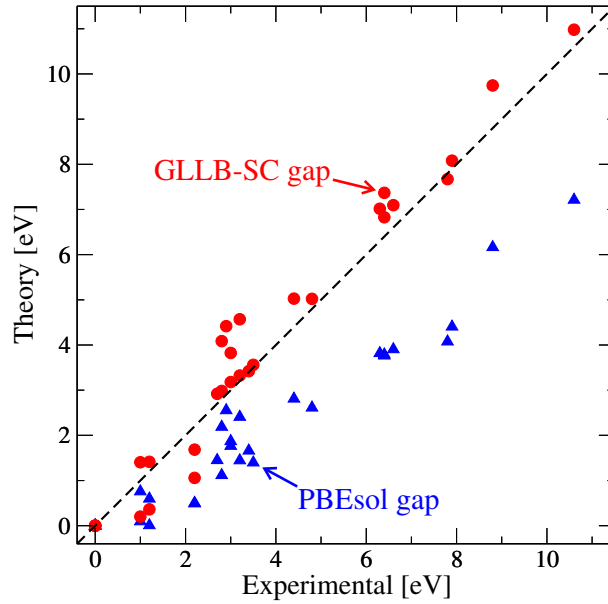


Figure 2.2: Comparison between the calculated and experimental bandgap of non-magnetic metal oxides in their most stable structure. The gaps are calculated using both the standard PBEsol (blue triangles) and the GLLB-SC functional (red circles). The dashed line represent the perfect matching between experiments and theory.

is theoretically complicated and computationally expensive, especially for a screening study, to calculate the positions of the band edges using DFT because it requires the investigation of one or more surfaces, and of the role of the pH of the environment and of the water molecules present on the surface. The estimation of the positions of the band edges has been done using an empirical formula based on the electronegativity of the chemical elements and on the size of the bandgap.^{55,56}

According to this formula the center of the bandgap for a material is given by the geometrical average of the electronegativities in the Mulliken scale*, χ_{M_i} , of its constituent atoms, M_i ; the positions of the valence and conduction band edges, E_{VB} , E_{CB} , are then obtained adding or subtracting half of the gap. This approximation does not include the effects due to the interactions between the atoms and any surface effect. For example, for the $ABON_2$ perovskite, the positions of the valence and conduction band are given by

$$E_{VB, CB} = E_0 + (\chi_A \chi_B \chi_O \chi_N^2)^{1/5} \pm E_{gap}/2, \quad (2.4)$$

where E_0 is the difference between the normal hydrogen electrode (NHE) and the vacuum ($E_0 = -4.5$ eV). Fig. 2.3 shows the comparison between the calculated and measured conduction band edge potential for a set of metal oxides and sulfides.⁵⁶ The calculated edges are usually within an error of 0.5 eV compared with the experimental values.

2.2.4 Crystal Periodic Structure

In nature there are countless known crystal structures with different stoichiometries and chemical elements. Thus, it is necessary to choose an appropriate structure to investigate

*In the scale proposed by Mulliken, the tendency of an atom to attract electrons, χ , is calculated as the arithmetic average between the electron affinity, A , and the first ionization potential, I :

$$\chi = (A + I)/2.$$

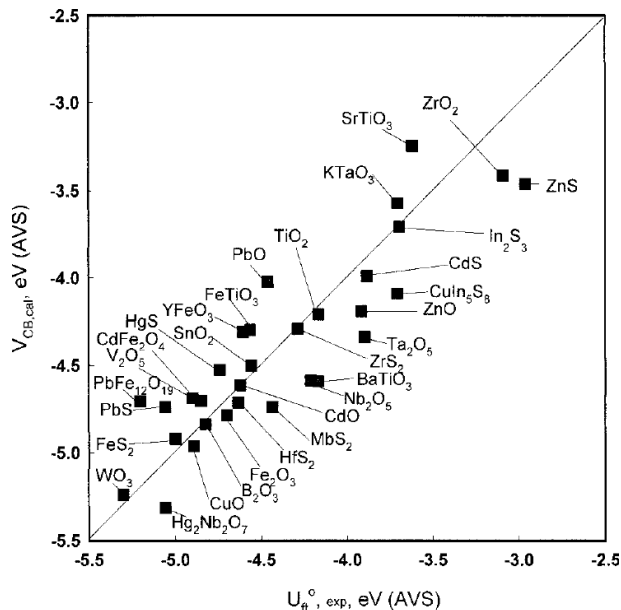


Figure 2.3: Comparison between the empirical and experimental conduction band edges. The solid line represent the perfect agreement between experiments and theory. Figure taken from Xu *et al.*⁵⁶

and a set of chemical elements to use. Within the class of mixed oxides, the perovskite structure has been chosen for the screening procedure described in this chapter. Perovskites are experimentally well known for their variety of chemical compositions, and properties, like magnetism, ferroelectricity, superconductivity, and as (photo-)catalytic materials.⁵⁷ The ideal perovskite has a cubic structure with general formula ABO_3 (space group $Pm\bar{3}m$), shown in Fig. 2.4C. It has the highest symmetry among all the existing perovskites and it can be described with a 5 atoms unit cell. There are also perovskites of lower symmetries (e.g. tetragonal, orthorhombic or monoclinic). A lower symmetry structure requires a more complex description of the unit cell (20 atoms for the tetragonal and the orthorhombic phase and 40 for the monoclinic). A change in the symmetry is also correlated to a change of the electronic and optical properties. Perovskite is a very flexible structure because almost all the metals of the periodic table can occupy one of the its sites. All these reasons make the perovskite one of the ideal structures to be used in the screening project.

The cubic perovskite, shown in Fig. 2.4C, contains 3 anions and 2 metals, a large 12-coordinated cation in the A site and a small 6-coordinated cation at the B site. All the angles of the unit cell are 90° and all the lattice vectors are equal. Many different combination of cation charges, e.g. $1 + 5$, $2 + 4$, and $3 + 3$, are experimentally known to form a perovskite. Around 19000 materials have been studied in the screening by combining 52 non-radioactive metals of the periodic table with various anions, namely O_3 , O_2N , ON_2 , N_3 , O_2S , O_2F , and ONF . The screening can also be guided using the tolerance and octahedral factors. These empirical factors are based on the size of the ionic radii, and indicate the degree of stability and distortion of structures. The tolerance, or Goldschmidt's factor, t , for the ABO_3 structure is defined as

$$t = \frac{r_A + r_O}{\sqrt{2}(r_B + r_O)}, \quad (2.5)$$

where r_A , r_B , and r_O are respectively the ionic radius of the A- and B-ion and oxygen. For other stoichiometries, r_O is replaced by the weighted average of the ionic radii of the 3 anions. The perovskite-like compounds have, in general, a tolerance factor in a

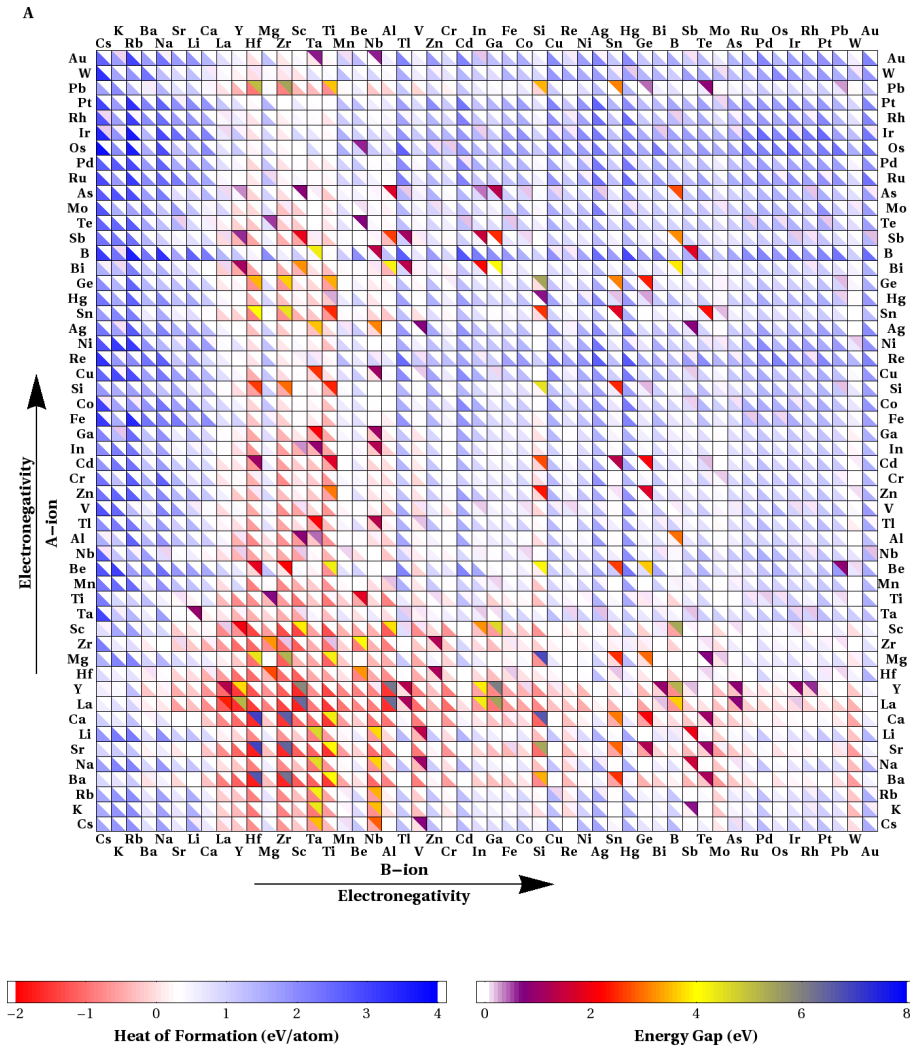


Figure 2.4: (A) Calculated heat of formations following the definitions in Eqs. 2.1 - 2.3 (in eV/atom) and bandgaps (in eV) of perovskite binary metal oxides. (B) Each square represents an ABO_3 combination with the lower, left triangle showing the formation energy with red indicating stability (and blue instability) while the upper, right triangle showing the bandgap with red indicating an advantageous bandgap in the visible light range 1.5-3.0 eV. The chemical elements are sorted for increasing electronegativity. The unit cell of the cubic perovskite structure is shown in (C).

range between 0.8 and 1.1, and the cubic between 0.9 and 1.0 (some exceptions have been found⁵⁷). The octahedral factor is defined as the ratio between r_B and r_O and for

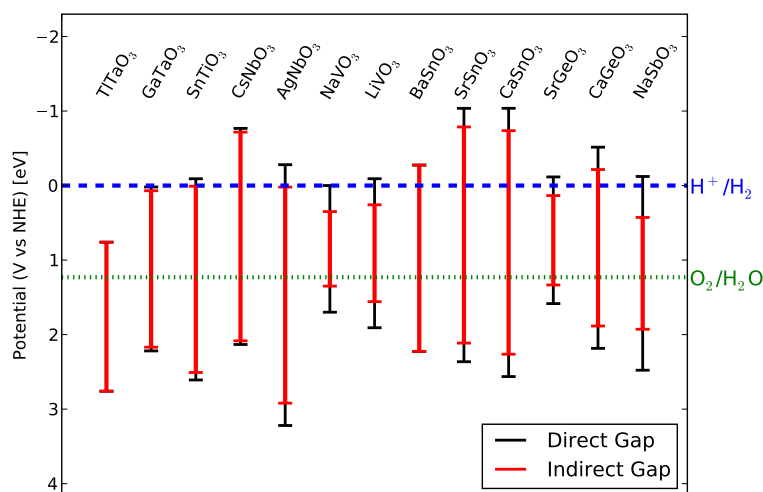


Figure 2.5: Band edge position evaluated for the ABO_3 stable perovskites showing a bandgap between 1.5 and 3.0 eV. In the figure, the band edge position for the indirect and direct gap are indicated in red and black, respectively. The red-ox levels of water are also included.

the cubic perovskite is close to $\sqrt{2}$. Although these factors are useful to reduce the vast space of possible combinations and thus to reduce the computational time, they have not been used in the screening. The tolerance factor will be used in Chapter 6 combined with an evolutionary algorithm to guide the search for new materials.

2.3 Cubic Perovskite Candidates

Fig. 2.4A reports the formation energies and bandgaps for the investigated oxides, each square correspond to an ABO_3 combination. As shown in Fig. 2.4B, the square is split into two triangles, the lower-left indicates the stability (red is stable); the upper-right the bandgap. The pure chemical elements are sorted according to their electronegativity (increasing order).

The factors determining the stability of a compound are three: (i) the radii of the A- and B-ion have to be in reasonable proportions, following the tolerance and the octahedral factors, (ii) the sum of the possible oxidation numbers of the two metals has to match with the sum of the ones coming from the anions, 6 in the particular case of oxo-perovskites, i.e. with formula ABO_3 , (iii) low-electronegativity elements form more stable bonds with oxygen, especially in the case of the A-ion since of the nonequivalence of the two ions position and of their different coordination numbers.

The second important designing criterion is the size of the bandgap, which is required to be between 1.5 and 3.0 eV. The bandgaps range from 0 to almost 8 eV. When the bandgap is in the desired region the corresponding triangle is colored in red. The combinations fulfilling both the criteria about stability and bandgap are thus indicated with red squares. The bandgap can be tuned by substituting the elements in the composition. In fact, by adjusting the size of the A-ion and thus increasing the crystallographic symmetry or by increasing the electronegativity of the B-ion, it is possible to decrease the size the bandgap.⁵⁸

Fig. 2.5 shows the positions of the band edges, calculated using Eq. 2.4, for the ABO_3 stable combinations with a bandgap (direct or indirect) in the visible range. Ten

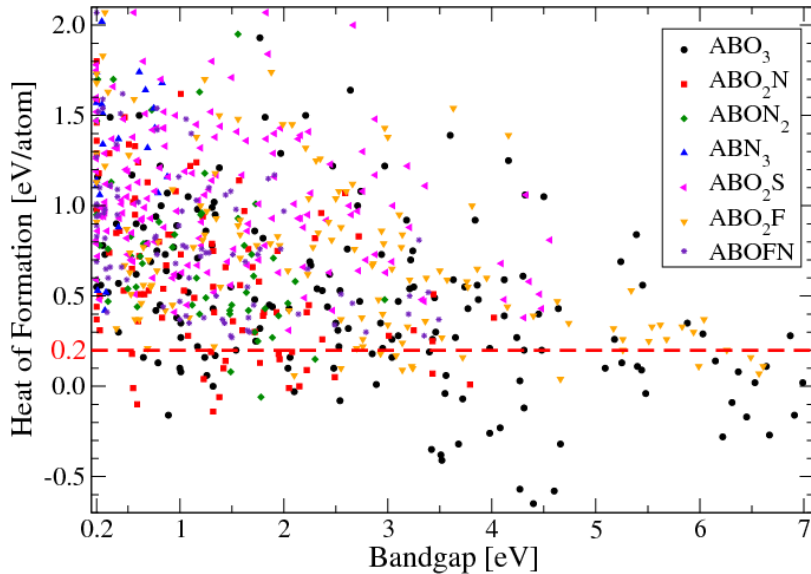


Figure 2.6: Correlation between bandgap and heat of formation for the cubic perovskites under investigation. The figure includes only the compounds with a gap (> 0.2 eV). The threshold of 0.2 eV/atom for the heat of formation is also displayed.

of these materials have the band edges that match with the red-ox levels of water and are thus suitable for being used in a water splitting device. Although the screening predicts some of the cubic perovskites to be stable, there are experiments revealing that they exist in other crystallographic phases. This is the case of SrSnO_3 and CaSnO_3 that are known in the orthorhombic perovskite phase and have a bandgap in the UV region in their most stable structure. By contrast, AgNbO_3 and BaSnO_3 have been synthesized experimentally in the cubic phase and are the only two compounds of the list to exist, at the moment, in the cubic perovskite structure. AgNbO_3 is well-known in the water splitting community to split water in visible light in the presence of sacrificial reagents⁷ while BaSnO_3 does not work due to defect-assisted recombination.⁵⁹ No experimental data are available for the other 6 compounds.

Relaxing the criterion on the bandgap, the screening finds ten materials, like AgTaO_3 and SrTiO_3 , that have a bandgap between 3 and 4 eV and that can be used to split water in UV light.

Because of the large quantity of experimental data, the oxo-perovskites work like a test-ground for the screening. The screening has pointed out the only two cubic perovskites known in the water splitting community (AgNbO_3 and BaSnO_3). Thus, the screening process performs well in the case of the oxo-perovskites, and can be extended to other perovskites with different anions.

One of the major issues with the oxides is that the bandgaps are usually large, outside the visible range region, and the band edges are too deep in position with respect to the red-ox levels of water. On the other side, the oxides are well known for their stability and this is a crucial criterion for design new materials.

The correlation between the formation energies and the bandgaps for the datasets under investigation is shown in Fig. 2.6. A wider bandgap is seen to correspond to a higher stability for all the sets of data even if stable zero-gap compound has been synthesized.

Nitrogen is the most natural element for replacing oxygen because of the similar atomic radii. For the screening criteria, the reduction in stability, more evident with the increase of the nitrogen/oxygen ratio, is balanced by a general reduction in the width of the bandgaps and a shifting up in the valence band positions both due to the

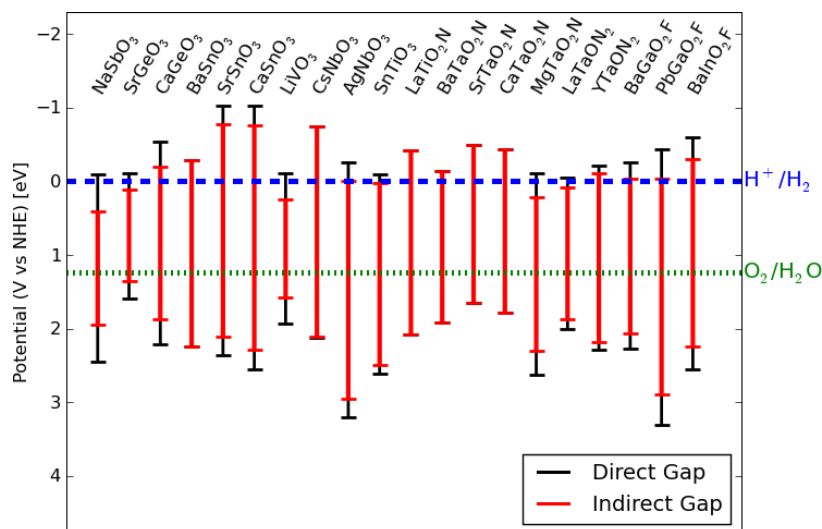


Figure 2.7: Materials identified as candidates for the photocatalytic water splitting device. The calculated band edges are in black for the direct and in red for the indirect gap. The levels for hydrogen and oxygen evolution are also included.

lower electronegativity of nitrogen compared with oxygen. In fact, the valence band (VB) edge of the oxynitrides is usually dominated by N p -orbitals which are higher in energy than the O p -orbitals, that mainly compose the VB of the oxides.

Sulfur has an electronegativity similar to the one of nitrogen, and has the same charge of oxygen, although it has a larger radius. The bandgaps have a similar size of the ones for the oxynitrides and they are well positioned compared to the red-ox levels of water, but the larger radius has a detrimental effect of reducing the stabilities because of distortions introduced into the structures. No stable oxysulfides have been found, as shown in Fig. 2.6.

Fluorine is more electronegative than oxygen with a slightly smaller radius. The former has the effect of increasing the bandgaps relative to the ones for the oxides (Fig. 2.6) and the latter of reducing the stability.

Inspired by a nitrogen and fluorine co-doping in TiO_2 that is effective for water oxidation,⁶⁰ the ABONF class has been studied. The bandgaps are comparable with ones of the oxynitrides, but the cell is highly distorted and the heats of formation are above 0.2 eV.

The candidates for one-photon water splitting in the cubic perovskite structure are shown in Fig. 2.7. 20 materials have been found. 10 of those are oxides and have been described previously. Out of the remaining 10, 7 are oxynitrides (5 with general formula ABO_2N and 2 with ABON_2 stoichiometry) and 3 oxyfluorides (ABO_2F). Five oxynitrides are already experimentally known (BaTaO_2N , SrTaO_2N , CaTaO_2N , LaTiO_2N , and LaTaON_2) with a good performance for hydrogen evolution.^{8,61} No other oxynitrides are known to be able to split water. MgTaO_2N , YTaON_2 , and all the oxyfluorides have not yet been synthesized and are susceptible to be experimentally investigated.

The materials identified as candidates have also been investigated using a many-body method.⁵² G_0W_0 calculations within the plasmon pole approximation⁶² have been performed starting from the electron densities obtained using LDA. Fig. 2.8 shows the values of the bandgaps calculated with different methods (LDA, GLLB-SC, and G_0W_0). As expected, LDA seriously underestimates the bandgaps, while the agreement

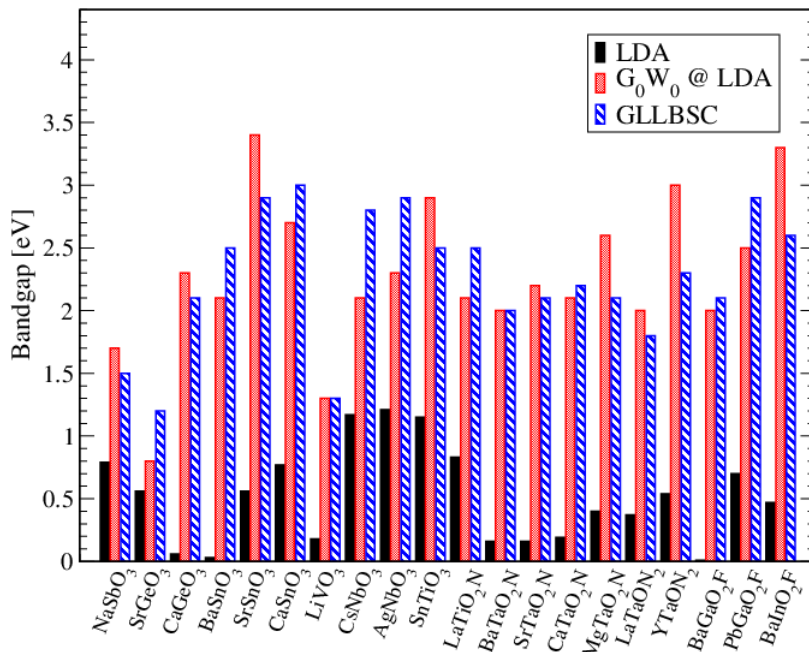


Figure 2.8: The bandgaps of the identified materials of Fig. 2.7 calculated with LDA (in black), GLLB-SC (in blue) and G_0W_0 (in red). The figure shows a good agreement between the bandgaps calculated with the GLLB-SC functional and G_0W_0 . The agreement is perfect for LiVO_3 and BaTaO_2N .

between GLLB-SC and G_0W_0 @LDA is fairly good. The mean absolute error[†] of GLLB-SC compared with G_0W_0 is around 0.35 eV. The computational cost of a GLLB-SC calculation is significantly smaller compared to the one required by G_0W_0 (at least one order of magnitude). Even if G_0W_0 is considered more reliable in evaluating the bandgaps, its high cost makes it unaffordable for a computational screening. On the other hand, it can be used in a more exhaustive study of selected materials.

A parameter not taken into account in the screening is the electron-hole mobility. After the electron-hole pair is formed, the electron and the hole need to reach the surface to evolve hydrogen and oxygen. This depends on the mobility and is correlated to the effective masses of the electron and of the hole. Only *a posteriori* investigation of the effective masses for the materials resulting from the screening have been performed since, at the moment, there is no clear indication of when the mass is considered too heavy.

The effective mass m^* is the inverse of the second derivative of the energy band with respect to two orientation, i and j in reciprocal space evaluated at the LUMO (HOMO)

[†]The Mean Absolute Error (MAE) is defined as:

$$\text{MAE} = \frac{1}{n} \sum_n |E_{\text{gap}}^{\text{GLLB-SC}} - E_{\text{gap}}^{\text{G}_0\text{W}_0}|. \quad (2.6)$$

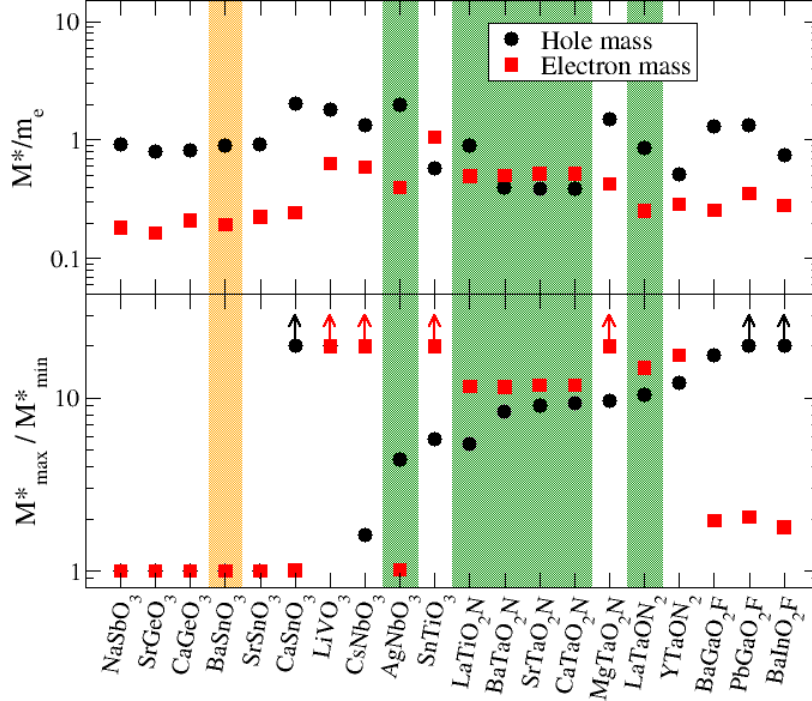


Figure 2.9: Average effective masses obtained using Eq. 2.7 (upper panel) and ratio between the highest and lowest effective masses for the candidates for one-photon water splitting of Fig. 2.7. A very high anisotropy between the masses in different directions is indicated by an upper arrow. The materials known to be able to split water are shown in the green area, while in the orange area the material known to not work as photocatalyst.

for the electron (hole)[‡]. Mathematically, it is written as:

$$m^* = \hbar^2 \left(\frac{\partial^2 \epsilon}{\partial k_i \partial k_j} \right)^{-1}, \quad (2.7)$$

Because of the similar character of the conduction bands, the LUMO of all the candidates is at the Gamma-point, $\Gamma = (0, 0, 0)$. The HOMO depends strongly on the different metals and anions in the material. The HOMO can be at different high symmetry points: $R = (1/2, 1/2, 1/2)$ and at $M_{xz} = (1/2, 0, 1/2)$ or $M_{xy} = (1/2, 1/2, 0)$ for the oxides, Γ and R for the oxynitrides and oxyfluorides.

The effective masses are shown in Fig. 2.9. The oxides have, in general, a very light electron mass, while the hole masses are one order of magnitude heavier, i.e. above $1 m_e$. The two masses are more similar, with values between 0.5 and $1 m_e$, for the oxynitrides (the hole masses are lighter than the ones of the oxides). The electron masses of the oxyfluorides are of the same order of magnitude as the ones of the oxynitrides, but the holes are heavier. The materials known to work in a photocatalytic device are shown, in the figure, in the green region. For these materials, in general, the electron and hole masses are similar. It might be that two very different masses are not a good

[‡]The effective mass is a 3×3 matrix with eigenvalues depending on the coordinate system, but the trace of the mass matrix, used in the upper panel of Fig. 2.9, defined as

$$\frac{1}{M^*} = \frac{1}{3} \left(\frac{1}{m_x^*} + \frac{1}{m_y^*} + \frac{1}{m_z^*} \right),$$

is a unique number independent of the orientation

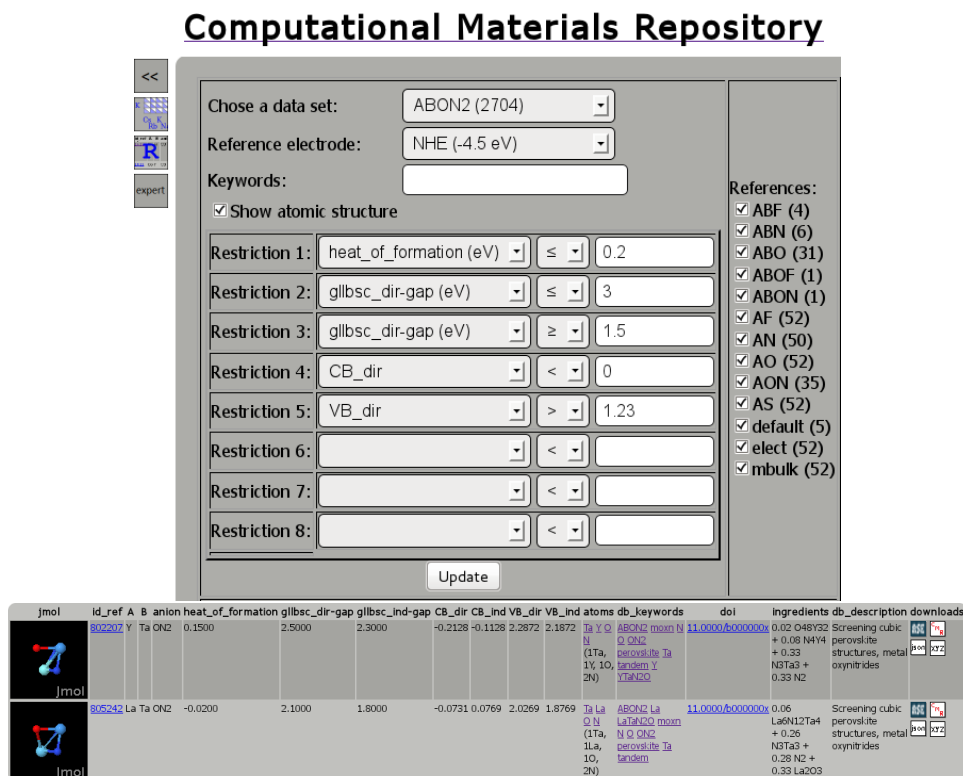


Figure 2.10: Example of a search in CMR for ABON₂ perovskites able to split water.

combination because it would be difficult to avoid a fast electron-hole recombination and to keep the neutral charge of the compound when the holes work as a trap.

The ratio between the highest and lowest values of the electron and hole masses is shown in the lower panel of Fig. 2.9. Mainly the masses are anisotropic except for the oxides with the HOMO at the R-point. The anisotropy has its origin in a flatband in at least one direction at the HOMO (LUMO). This properties could be potentially used for designing water splitting devices. In a pillared photocatalytic device, for example, the “long” direction can be used for efficient harvesting of the light and the “short” one by the electrons and holes to reach the surfaces.

2.4 The Computational Materials Repository

When an enormous amount of data is generated, it is crucial to have an efficient way to store and to analyze the data. The Computational Materials Repository (CMR)^{63,64} has been developed for these reasons.

An example of a search in the CMR database for a ABON₂ perovskite working in photocatalytic water splitting device is shown in Fig. 2.10. LaTaON₂ and YTaON₂, as also indicated in Fig. 2.7, are the only two materials fulfilling the designing criteria.

2.5 Summary

A screening technique is an efficient way to discover new materials. This approach has been applied to around 19000 cubic perovskites with the goal of finding new light harvesters for water splitting. The method is based on the calculation of the bandgaps using

a recently implemented exchange-correlation functional that gives reliable results at low computational cost. 20 materials result from the screening: 10 oxides, 7 oxynitrides, and 3 oxyfluorides. Few of them are already known in the water splitting community while the others require a more detailed theoretical and experimental investigation.

It has been necessary to develop a database, called Computational Materials Repository, to have an easy access to the data.

The testing of the proposed materials is also desirable. Dionigi *et al.* have recently used μ -reactors to investigate the one-photon water splitting activity in water vapor of GaN:ZnO, loaded with $\text{Rh}_{2-y}\text{Cr}_y\text{O}_3$ as co-catalyst.⁵⁰ The μ -reactor consist of a silicon chip with a reaction chamber of 240 nl where the powder of the material to test is deposited. The evolution of O_2 and H_2 is then detected. This approach allows the study of new materials in a reasonable time and with low expenses, once that the candidate has been synthesized.

A limitation of the study is the focus on only one single crystal structure. In the future, it might be necessary to combine the screening approach with structure prediction techniques to overcome the limitations imposed by the selection of a crystal structure. Only a part of the problems related to the water splitting device has been taken into account here. For example, the role of the electron-hole mobility or the use of a co-catalyst to minimize the overpotentials and thus the energy loss in the reactions⁶⁵ have not been investigated.

Chapter 3

Two-photon Water Splitting and Transparent Protecting Shield

In this chapter, based on Paper II, the screening approach has been applied to find new materials to split water using two photons and for designing a protecting transparent layer against corrosion for the photoanode and photocathode. The crystal structure under investigation is still the cubic perovskite, already subject of the previous chapter.

3.1 Two-photon Water Splitting

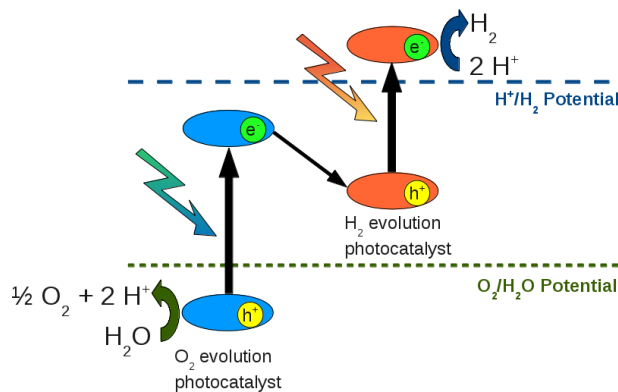


Figure 3.1: Two-photon water splitting scheme. Two photons and two semiconductors are required to run the water splitting reactions.

A good conversion efficiency is required to use a material in the daily life to transform solar light into energy. Unfortunately, the one-photon water splitting process, described in Chapter 2, can accomplish an ideal efficiency of only 7%.⁴⁶ This efficiency is comparable with the efficiency of the dye-sensitized and organic solar cell, that is around 10% including all the losses, but it is way lower than the efficiency for the latest multi-junction photovoltaic cells that have an efficiency of around 45%. This fact reduces the possibility of a massive use of a one-photon water splitting device to produce energy. The same idea behind the multi-junction cells, where several materials are used to collect different ranges of the solar spectrum, can be also used for a multi-photon

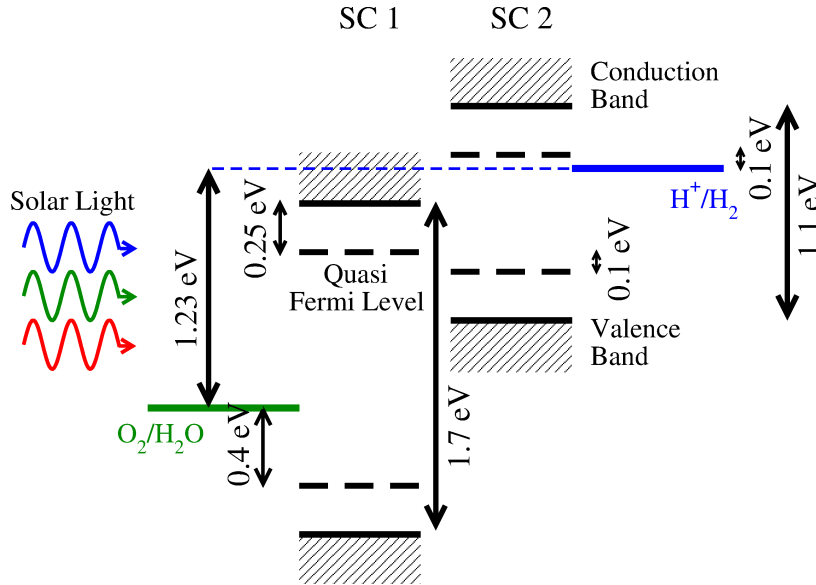


Figure 3.2: Sketch of the electronic levels in the two-photon water splitting device. Due to the required overpotentials and of the positions of the quasi Fermi levels the minimal requirement for the sum of the two bandgaps is 2.8 eV.

water splitting device. In this cell, two photons and two different semiconductors are required and the water splitting is divided into the two-step mechanism^{66,67} shown in Fig. 3.1: the solar light meets first the larger bandgap semiconductor that absorbs the part of the spectrum at higher energy, while the one at lower energy goes through and is partially absorbed by the second semiconductor with a smaller bandgap. One material works as a photoanode and evolves hydrogen and the other as a photocathode and evolves oxygen.

The requirements for this device are similar to the ones for the one-photon water splitting, namely the materials should be stable with appropriate bandgaps well positioned with respect to the red-ox levels of water. In addition to these, to keep the charge neutrality of the two photocatalysts, the electron generated by the anode that oxidizes water should be higher in energy than the hole generated by the cathode where the reduction of $2H^+$ to H_2 takes place.

In the one-photon water splitting device, the lower limit in the size of the bandgaps has been set to 1.5 eV, considering the bare energy required to split water (1.23 eV) plus an additional 0.3 eV to account for the overpotentials. In the two-photon device, it is necessary to include also other effects, shown in Fig. 3.2: starting from the minimum energy required to split water, an additional energy of 0.5 eV is required to overcome the overpotential (0.1 and 0.4 eV for the hydrogen and oxygen evolution, respectively⁶⁸). Other 0.5 eV per semiconductor are required to compensate for the positions of the quasi Fermi levels within the bandgaps. When the process is running, the electrons and holes are in a non-equilibrium distribution described by quasi Fermi levels that correspond to the work that the electrons and holes can do. 0.1 eV is required for electron transfer between the semiconductors. This brings the lower limit for the sum of the two bandgaps to 2.8 eV. This does not take into consideration the problem related to the band bending necessary for the separation of electrons and holes that, for example, can be solved by doping of the semiconductors and by the pn-junction.⁴⁵

There are infinite ways to combine two bandgaps to obtain the lower limit of 2.8 eV. The ideal efficiency of the two-photon water splitting device as a function of the size of the two bandgaps is shown in Fig. 3.3. The maximum efficiency (in purple in the figure) is obtained when the two semiconductors absorb the same amount of photons.

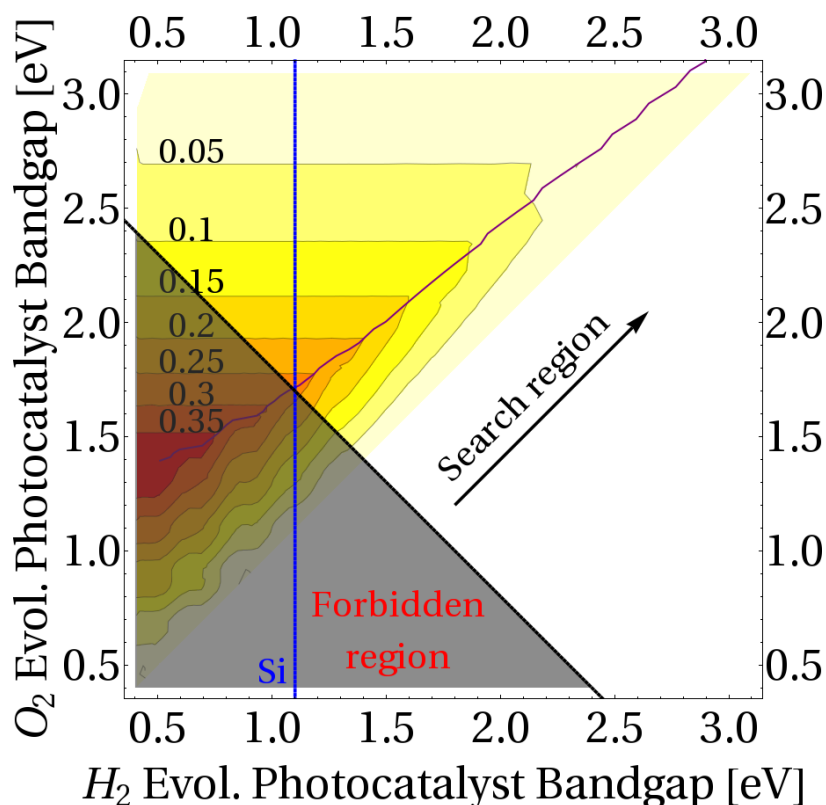


Figure 3.3: Ideal efficiency of the two-photon water splitting without any losses using the spectral distribution of the solar photon flux at AM1.5G. The black line is the minimum combination of gap for running the reactions and the purple line corresponds to the highest efficiency achievable once the H_2 photocatalyst is chosen. The blue line corresponds to the experimental bandgap of silicon. The numbers in the contour plot indicate the ideal efficiency.

The 2.8 eV limit is indicated by a black line. The maximum efficiency, around 27%, is obtained combining two bandgaps with sizes 1.7 and 1.1 eV. Silicon is a perfect candidate to be used for the hydrogen evolution. It is a 1.1 eV semiconductor (the bandgap calculated using the GLLB-SC potential is 1.2 eV), with the conduction band edge well positioned with respect to the hydrogen potential. It is also a well known material with an advanced fabrication technology and it works well with non-noble hydrogen evolution catalysts.⁶⁹

The screening criteria are:

Screening parameters	Two-photon WS
Chemical/structural stability (ΔE)	$\Delta E \leq 0.2$ eV
Bandgap (E_{gap})	$1.3 \leq E_{\text{gap}} \leq 3.0$ eV
Band edges ($VB_{\text{edge}}, CB_{\text{edge}}$)	$VB_{\text{edge}}^{\text{cathode}} > 1.23$ eV w.r.t. NHE $CB_{\text{edge}}^{\text{anode}} < 0$ eV w.r.t. NHE $VB_{\text{edge}}^{\text{anode}} < CB_{\text{edge}}^{\text{cathode}}$

where the search window for the bandgaps has been broadened from 1.7 to 1.3 eV to account for inaccuracy of the GLLB-SC bandgap calculations.

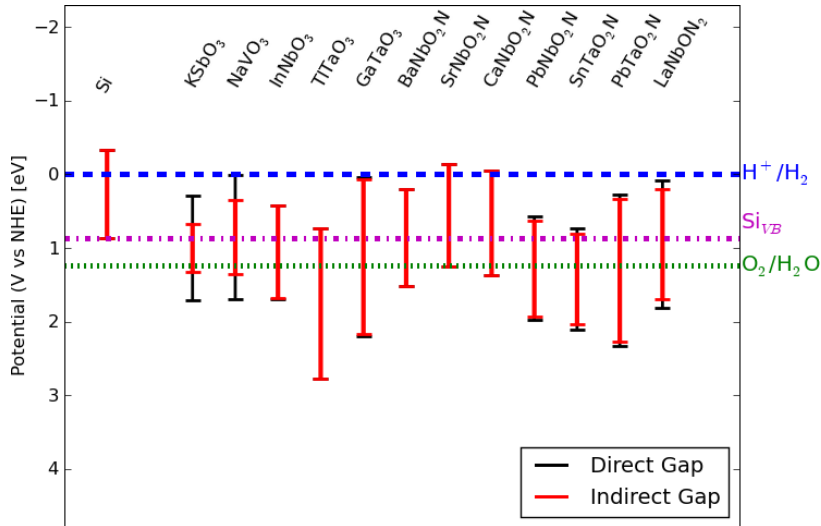


Figure 3.4: The candidates for the two-photon water splitting device not yet included in Fig. 2.7. The band edges for the direct (black) and indirect (red) gaps are indicated. The calculated valence band for silicon is also included.

All the compositions shown in Fig. 2.7 for the one-photon water splitting device can also be used in the two-photon device. The oxynitrides, that are seen to evolve hydrogen or oxygen in the presence of a sacrificial agent,⁸ can be used instead of silicon for the hydrogen evolution. In this case, due to the bandgaps that are way larger than 1.1 eV, the best performance is obtained by swapping the two semiconductors of Fig. 3.1: the part of the solar spectrum at higher energy is absorbed by the hydrogen evolution photocatalyst and the part at lower energy goes through and is absorbed by the oxygen evolution photocatalyst.

The 12 additional candidates for oxygen evolution are presented in Fig. 3.4. Some of the niobates oxynitride (CaNbO_2N , SrNbO_2N , BaNbO_2N , and LaNbON_2) have recently been synthesized.⁷⁰ CaNbO_2N gives the best performance both in terms of water oxidation and reduction with sacrificial agents. SrNbO_2N is seen to evolve O_2 , while no activity has been detected for the other two oxynitrides, where the bandgap is probably too small to overcome the overpotentials. The other proposed materials have not been experimentally investigated.

TiNbO_3 is the only material that could potentially be used for oxygen evolution in combination with a hydrogen evolution photocatalyst with a lower valence band than silicon (like the tantalate or niobate oxynitrides). Because of the positions of the band edges, no candidates for H_2 evolution have been found. In fact, all the materials found for H_2 evolution can be also used for O_2 evolution.

3.2 Transparent Shielding

Photocorrosion is a common issue related to the use of materials for oxygen and hydrogen production. A solution is to find a high stable material to cover the photocatalyst as a protecting shield. The correlation between large bandgap and high stability, shown in Fig. 2.6, can help in finding a solution to this problem. In fact, the thin protecting film has to be transparent to let the light go through without reducing the efficiency of the photocatalyst. A bandgap larger than 3 eV is thus one of the screening criteria. Excluding tunneling mechanisms,⁷¹ the shielding can be obtained in two ways.

3.2.1 Transparent Shielding - Mechanism I

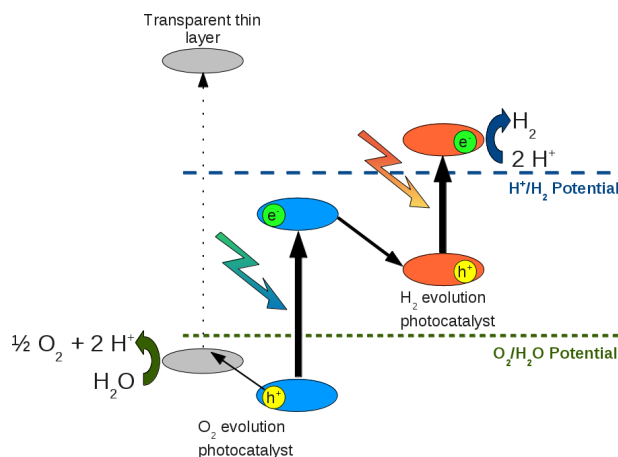


Figure 3.5: Scheme of the transparent shielding of the photoanode in a two-photon water splitting cell.

Fig. 3.5 illustrates the shielding of the photoanode in a two-photon water splitting device, but the principle is also valid for the one-photon scheme. The thin film is transparent to the visible light that goes through and is later collected by the two photocatalysts. Hydrogen is then evolved by the electron at higher energy, and the hole at lower energy moves to the transparent film valence band and evolves oxygen. The valence band of the shield needs to be between the valence band of the photocatalyst and the oxygen evolution potential. The same idea can be used to develop a shield to protect the photocathode, where now the electron at higher energy has to move to the conduction band of the shield before evolving hydrogen.⁷² This mechanism has some losses due to the energy, usually < 0.5 eV, required by the electrons or by the holes to reach the reacting regions.

The parameters used in the screening are:

Screening parameters	Transparent Shield (TS)
Chemical/structural stability (ΔE)	$\Delta E \leq 0.2$ eV
Bandgap (E_{gap})	$E_{\text{gap}}^{\text{dir}} > 3$ eV
Band edges (VB_{edge} , CB_{edge})	Photoanode TS: $1.7 < \text{VB}_{\text{edge}} < 2.5$ eV w.r.t NHE Photocathode TS: $-0.7 < \text{CB}_{\text{edge}} < 0$ eV w.r.t. NHE

where the criteria on the positions of the band edges take into account the inaccuracy both in the bandgaps and in the positions of the band edges.

Eight compounds have been screened for a possible use as transparent shield of the photoanode (Fig. 3.6a). Only oxides and oxyfluorides have been found due to the large bandgap required. SrSnO_3 , CaSnO_3 are experimentally known in a distorted perovskite structure with bandgaps larger than the ones predicted. SrTiO_3 is well known in the cubic perovskite structure, is a material used for water splitting under UV light, and has all the requirements for being used as a transparent shield in a visible-light device.

Nine candidates have been proposed for protecting the cathode (Fig. 3.6b). AgNbO_3 is already known as a good photocatalyst and it can also be used as a protecting shield because of its direct bandgap larger than 3 eV, while its indirect bandgap is in the visible part of the solar spectrum. AgTaO_3 and KTiO_2F are already experimentally known in

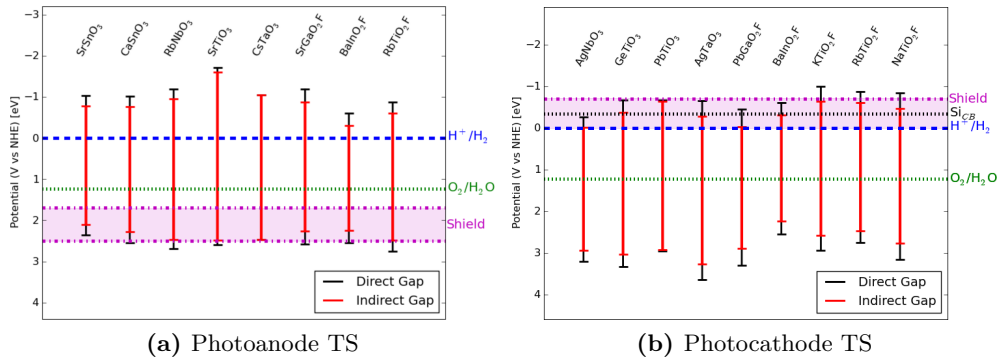


Figure 3.6: The materials proposed to be used as protecting shield for the (a) photoanode and for the (b) photocathode.

the perovskite structure. RbTiO_2F and BaInO_2F can be used as a transparent shield for both the cathode and the anode.

All the other compounds (5 for the anode and 6 for the cathode) are currently unknown.

3.2.2 Transparent Shielding - Mechanism II

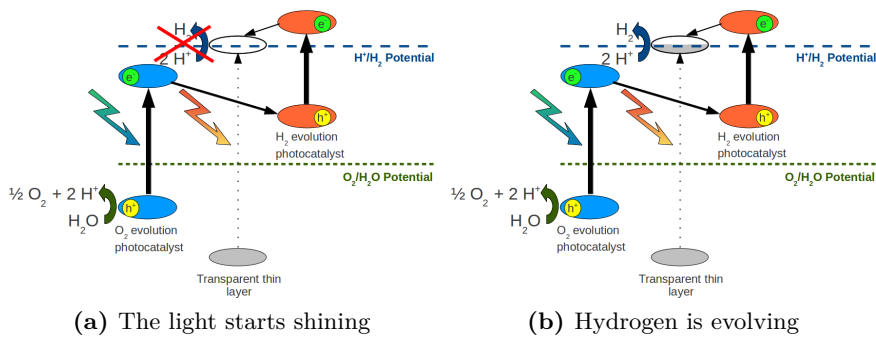


Figure 3.7: Scheme of the transparent shielding of the photocathode in a two-photon water splitting cell. (a): The energy of the electrons in the conduction band of the thin film is below the hydrogen evolution potential. (b): Once that the bottom of the conduction band of the shield is filled, the electrons are at an higher energy than the hydrogen potential and thus H_2 is evolved.

Another way of protecting the photocatalyst is shown in Fig. 3.7 for the shield of the photocathode. The conduction band of the transparent film is below the hydrogen evolution potential. When the light start shining, the generated electrons move from the photocatalyst to the thin film at an energy below the hydrogen evolution potential and no hydrogen is produced (Fig. 3.7a). After some time, the bottom of the conduction band of the thin film is filled and the new electrons moving from the cathode to the film have enough energy to run the reaction (Fig. 3.7b). In this mechanics there are less losses compared to the one proposed before where the conduction band of the shield was placed between the conduction band of the cathode and the hydrogen evolution potential to have the electrons moving from the place where they are generated (photocathode) to where they react (shield). On the other hand, the hydrogen evolution requires some time before it starts, since it is required that the bottom of the conduction band of the thin film is filled up to the hydrogen evolution potential.

The criteria on the stability and on the bandgap are the same as in the mechanism I. The criterion on the position of the conduction band is:

$$-0.2 < \text{CB}_{\text{edge}} < 0.5 \text{ eV w.r.t. NHE ,}$$

where the lower limit of -0.2 eV takes into account the overpotential for hydrogen.

Only three materials fulfill the screening criteria: AgNbO_3 , PbGaO_2F , and AgTiO_2F . The first two can also be used in the mechanism I and have already been described. AgTiO_2F has the indirect conduction band edge placed below the hydrogen evolution potential and is experimentally unknown.

The same idea can be applied to the photoanode and to its shield. Mainly due to the presence of oxygen in the composition of the material and in the desired large bandgap, the valence band edges of the investigated compounds are too deep in energy and no candidates are found.

3.3 Summary

The screening approach has been applied to the problem of the two-photon water splitting and transparent shielding of the photocatalyst. 12 perovskites, plus 20 found for the one-photon water splitting device, can be used in combination with silicon to split water using two photons. 9 plus 9 materials have the potential to be used as protecting shield against corrosion for the oxygen and the hydrogen evolution reactions, respectively. Few of these materials are already known in the water splitting community, but several comprise new suggestions that require further investigation.

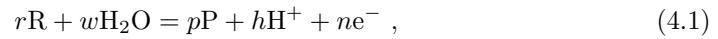
Chapter 4

Corrosion Analysis of Cubic Perovskites for Water Splitting

The first, most important requirement for a material to be used in real life is stability. The stability requirements depend on the application and might be more or less restrictive depending on the conditions under which a material has to work. This chapter, based on Paper V, analyses the (photo-)corrosion problem for the materials previously screened with potential for the one-photon water splitting device.

4.1 The Pourbaix Diagrams

In Chapters 2 and 3, the stability of a material has been investigated with respect to experimentally known solid substances. In practice, a material was considered stable if the difference between its total energy and the energetically most favorable linear combination of the energies of its possible constituents was below 0.2 eV/atom. The dissolution of materials in aqueous solutions was not included in the analysis. The dissolution is, in general, described by the reaction:



where R and P indicate reactants and products, and H^+ , and e^- a dissolved proton and a free electron at the Fermi level of the material, respectively. The equilibrium of (4.1) is calculated using the Nernst equation:

$$nU = \Delta G + 0.0591 \log \frac{(a_P)^p (a_{H^+})^h}{(a_R)^r (a_{H_2O})^w} , \quad (4.2)$$

where U is the electrochemical potential, ΔG the standard free energy of the reaction (in eV), and a_i the concentration of the involved species. The coefficient 0.0591 equals $RT \ln(10)$ at room temperature ($T = 25^\circ C$). For diluted solutions, $a_{H_2O} = 1$ and, by definition, $pH = -\log a_{H^+}$, and Eq. 4.2 becomes:

$$nU = \Delta G + 0.0591 \log \frac{(a_P)^p}{(a_R)^r} - 0.0591h \text{ pH} . \quad (4.3)$$

This equation is used to draw stability diagrams, so-called Pourbaix diagrams, of materials as a function of the concentration of ions H^+ (pH, on the x -axis) and of the

potential U (along the y -axis). The concentrations of all other involved ions are usually assumed to be 10^{-6} M.

Each region in a Pourbaix diagram is delimited by straight lines representing different equilibrium reactions. There are three kinds of lines:⁷³

- Vertical lines: the equilibrium is independent of the potential and the reaction involves solid and dissolved substances with hydrogen ions but without free electrons.
- Horizontal lines: the equilibrium is independent of the pH and the reaction involves solid and dissolved substances with free electrons but without hydrogen ions.
- Straight lines with a slope equal to $0.0591h/n$: the reaction involves solid and dissolved substances with free electrons and hydrogen ions as in reaction 4.1.

A calculated Pourbaix diagram combines computational and experimental information. The computational data are provided through DFT in the form of total energies of bulk materials, and the experimental data are usually dissolution energies.^{74,75} A similar scheme has recently been used by Persson *et al.*⁷⁶ to calculate the Pourbaix diagrams of several oxides and nitrides. In Chapters. 2 and 3, the reference energy for oxygen was given at the chemical potential of water. Here, the chemical potential of oxygen is defined to be at oxygen standard state, i.e. the oxygen molecule in the gas phase. This choice is supported by the fact that the photo-generated oxygen will be at the chemical potential of water only if hydrogen is present at high enough pressure that it can react with oxygen and form water. The formation of water can be suppressed by the use of a co-catalyst⁷⁷ that helps in separating the charges, so that the oxygen and hydrogen evolution happens in two different regions of a semiconductor. In addition, by convention, the Pourbaix diagrams are drawn with all the chemical elements in their standard states. With this choice, 23 cubic perovskites are found to be candidates for one-photon water splitting (MgSnO₃, LiSbO₃, and SrInO₂F in addition to the 20 described earlier).

4.2 Cubic Perovskites

The method of combining experimental and calculated data in Pourbaix diagrams has been validated for TiO₂ and ZnO in Paper V. Only Pourbaix diagrams for the cubic perovskites are reported in the present chapter.

Very limited information are available about Pourbaix diagrams of ternary compounds. SrTiO₃ and KTaO₃ are, for example, two well known cubic perovskites. They are stable in water and they are used for water splitting under the UV light. Their Pourbaix diagrams are shown in Figs. 4.1a and 4.1b, respectively. The two diagrams conserve some of the characteristics of the diagrams of the constituent chemical elements.⁷⁵

Figs. 4.1c and 4.1d show the energy difference, ΔE , between the cubic perovskite structure and the most stable phase into which the perovskite can separate as a function of the pH and potential for SrTiO₃ and KTaO₃. The energy difference defines a convex surface, called convex hull. SrTiO₃ and KTaO₃ are less stable at higher and lower potentials as well as under more acidic conditions. In fact, the amount of oxygen in the solid substance is increasing with the pH, and an increase in the potential favors the dissolution of the solid into positive ions and free electrons. The region where the two perovskites are more stable (colored in green in the figure) is around the red-ox levels of water. The stability is, in general, more affected by changes in the potential compared to variations in the pH. This is because, the pH, in Nernst equation (Eq. 4.3) scales with the small number 0.0591 eV/pH.

Fig. 4.2 shows the formation energy of nine experimentally known cubic perovskites compared with the most stable linear combination of known solid and aqueous phases

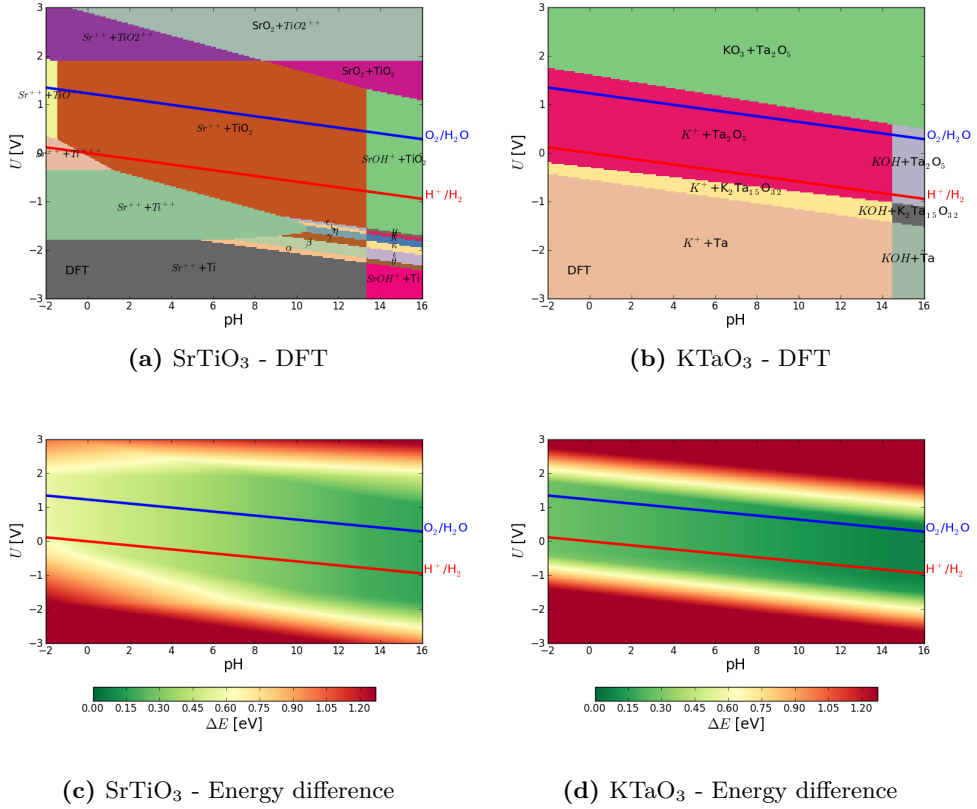


Figure 4.1: Pourbaix diagrams for the cubic perovskites SrTiO₃ (a) and KTaO₃ (b), drawn at a concentration of 10^{-6} M and at 25°C. The compounds in aqueous solution are indicated in *italic*. The Greek letters in (a) stand for the different phases in which SrTiO₃ splits (α : $Sr^{++}+Ti_6O$; β : $Sr^{++}+Ti_3O$; γ : $Sr^{++}+Ti_2O$; ϵ : $Sr^{++}+Ti_3O_5$; ζ : $Sr^{++}+Ti_2O_3$; η : $Sr^{++}+TiO$; θ : $SrOH^++Ti_6O$; ν : $SrOH^++Ti_3O$; κ : $SrOH^++Ti_2O$; λ : $SrOH^++TiO$; μ : $SrOH^++Ti_2O_3$; ν : $SrOH^++Ti_3O_5$). (c) and (d) show the energy differences between the cubic perovskite phases and the most favorable phases for SrTiO₃ and KTaO₃, respectively.

at pH = 7 and for four chosen values of the potential (−1, 0, 1, and 2 V) in which the perovskite can separate. Although most of these materials have been used for water splitting under UV light and have not been found to corrode in contact with water, only KTaO₃ is seen to be stable at zero potential, with an energy threshold of 0.2 eV/atom. The disagreement between experiment and theory might be that the Pourbaix diagrams include only the thermodynamic stability while the reaction kinetics are not considered. These materials might, thus, be metastable with large barriers separating the phases. More compounds become stable if the increased energy threshold is set to 0.5 eV/atom.

4.3 Candidates for One-photon Water Splitting

In the ideal conditions, a material for water splitting should be stable at pH \approx 7 and in a potential range between −1 V and 2 V covering the red-ox potentials of water and the reaction overpotentials. Fig. 4.3 shows the energy difference between the cubic perovskites and the most stable phases of the 23 identified candidates for water splitting. For all the materials, there is a potential where the candidate is stable, with an energy threshold of 0.5 eV/atom to account for metastability and energy barriers between the

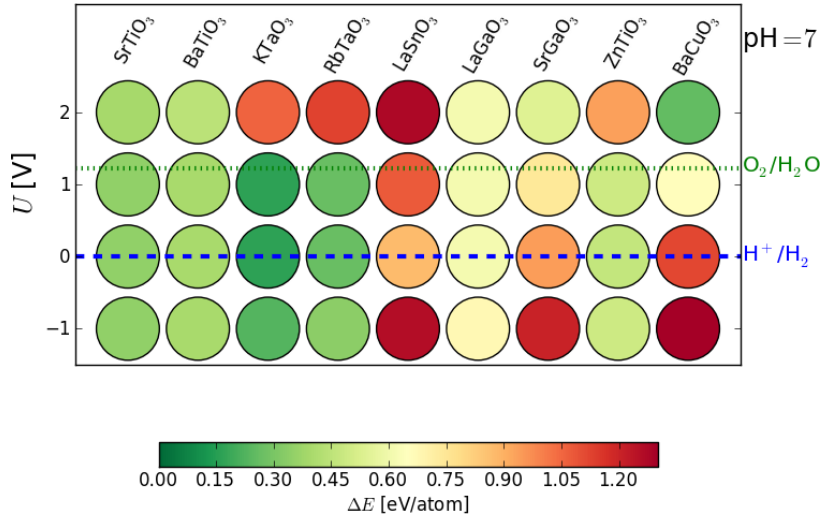


Figure 4.2: Energy differences between nine cubic perovskite known to be stable and the most stable phases in which each material can separate calculated at pH = 7 and at a potential equal to -1, 0, 1, and 2 V, respectively.

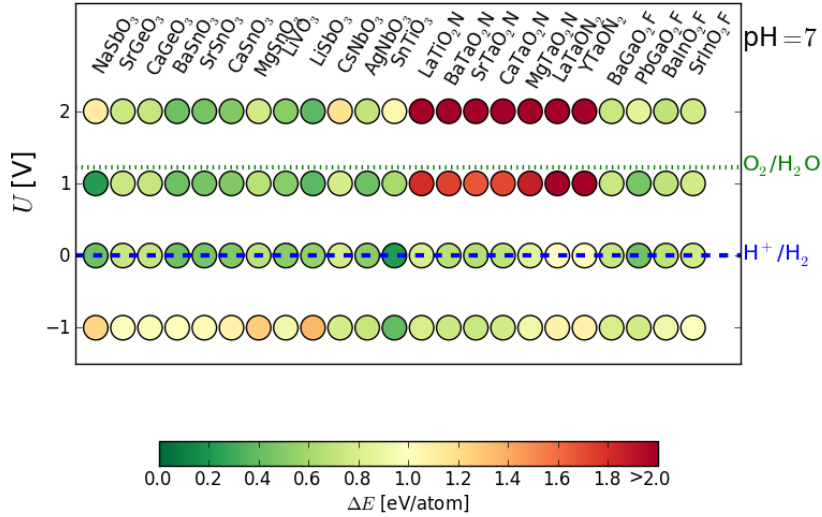
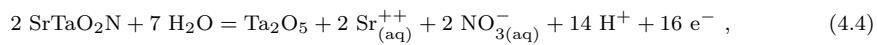


Figure 4.3: Energy differences between the candidates for one-photon water splitting in cubic perovskite phases and the most favorable phases in which each material can separate calculated at pH = 7 and for potentials equal to -1, 0, 1, and 2 V.

structures. The highest stability is usually achieved at zero potential. The oxides and oxyfluorides are also stable at higher potential, while the oxynitrides become unstable due to a large number of free electrons present in the reactions which become more stable with at higher potential.*

The problem of stability against photocorrosion can be investigated considering the stability of the material at pH = 7 and potentials -1 V and 2 V, corresponding to the conduction and valence band edges: under high light intensity, the photo-excited electrons and holes might induce other chemical reactions different from the water oxidation

*For instance, the reaction for SrTaO₂N at pH = 7 and $U = 2$ V, is



with 16 free electrons involved.

and hydrogen reduction. All the candidates are less stable at lower and higher potentials. The oxides are less stable at potential of -1 V, while they remain stable at higher potential. The oxynitrides, instead, are less stable at high potential, due to the large number of electrons involved in the relevant reactions. In the case of the oxyfluorides, the variation in the stability due to a change in the potential is weak.

4.4 Summary

The problem of corrosion and photocorrosion has been investigated for the candidate materials for one-photon water splitting. The proposed method combines experimental and theoretical information to draw Pourbaix diagram of each compound. The stability threshold of 0.2 eV/atom used before for separation into solid substances might be too strict when aqueous solutions are included in the pool of reference systems. It might thus be necessary to increase the threshold to 0.5 eV/atom to take into account non thermodynamics terms, like metastability, inaccuracy in the calculations, and reaction kinetics.

With this threshold, the oxides at $\text{pH} = 7$ are usually stable at positive potential potentials, while they are less stable at negative potentials. The situation is opposite for the oxynitrides, due to a large number of electrons involved in the dissolution reactions. For the oxyfluorides, the effects of a change in the potential are rather weak.

The problem of photocorrosion has also been investigated by considering the stability at the potentials corresponding to the valence and conduction band edges where all the candidates are seen to be less stable.

Chapter 5

Statistical Model for Cubic Perovskite Semiconductors

The structures presented in Chapters 2 and 3 are the results of the calculations obtained by combining two metals from a set of 52 interesting elements of the periodic table, and seven different combinations of anions for a total of around 19000 cubic perovskites. This has been possible mainly because of the small crystal structure under investigation (only 5 atoms in the unit cell), while for larger structures, like the double and layered perovskites proposed in Chapter 7, this is not affordable. It is thus convenient to find general rules based on the experimental data and on the experience gained so far to reduce the space of investigation. In data mining methods, for example, machine learning techniques are used to extract rules to design new structures starting from data present in experimental databases.⁷⁸

In this chapter, some basic statistical methods have been applied to the cubic perovskite data to investigate the trends behind the stability and the bandgap. The results and the figures shown here are, for simplicity, for the ABO_3 cubic perovskites, but the same information can be obtained by considering the other anions. Most of the analysis done here has been made using the Wolfram Mathematica 8 software.⁷⁹

5.1 Probability and Dendrogram Analysis

A very simple analysis is based on counting how often a chemical element is found either in the A- or B-ion position to form a perovskite that is stable and/or that shows a bandgap. The cubic perovskite has two nonequivalent sites and the chemicals are chosen on the basis of their ionic radii and of their oxidation states to be either the A- or the B-ion. The A-ion is usually larger than the B-ion with cation charges of +1, +2, and +3. The B-ion has usually oxidation states +3, +4, and +5.

Fig. 5.1 shows the probability to form a stable perovskite for all the 52 chemicals considered. As in the previous chapters, the stability is evaluated with respect to a pool of reference systems in which the perovskite can separate. A compound is considered stable if its heat of formation is below the energy threshold of 0.2 eV/atom. Due to the size of the ionic radii and to the cation charges, the alkali and alkaline-earth elements, as well as the d^{10} metals, prefers to occupy the A-ion position. With some exception (yttrium and lanthanum than works well in the A-position), d-metals with $d \leq 5$ are generally good for being used as B-ion, even if few of them (vanadium, chromium, and manganese) can be used in both the positions. Post transition metals are found to be

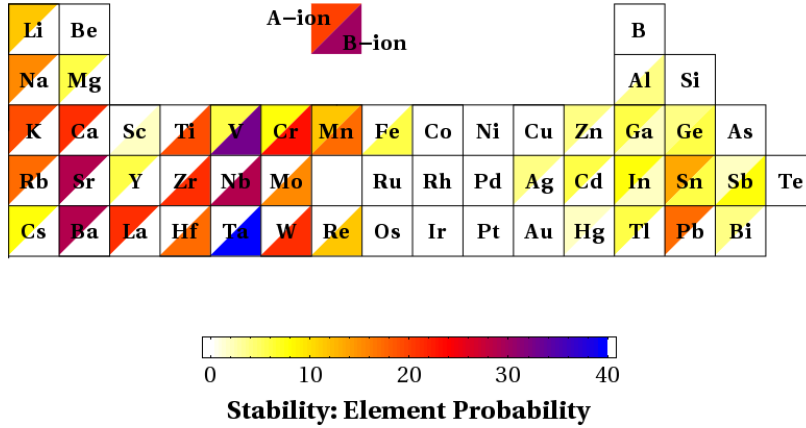


Figure 5.1: Probability (in %) to form a stable perovskite when the element occupies the A- (upper triangle) or the B-ion position (lower triangle). The probability of a metal M is calculated as the number of successful (stable) combinations that include M divided by 52, the total number of possible materials formed by M.

stable in both the A- and B-ion site. The most successful elements, with a rate of success larger than 30%, are strontium and barium for the A-ion and tantalum and niobium for the B site. Few metals never produce stable perovskites mainly because of their radii that can not fit in the cubic perovskite structure and they thus prefer to form other crystal structures.

The electronic properties of the constituent chemical elements are more important if the resulting material has to be a semiconductor. In fact for showing a bandgap, a material should fulfill two rules:

1. Even-odd electrons rule: a semiconductor has completely-occupied bands at the Fermi level. A compound with an odd number of electrons has partially-occupied eigenstates at the Fermi level so it is a zero-gap material.
2. Valence balance rule: the sum of the possible oxidation states of its elements must be zero, so that the compound is valence-neutral.

These conditions are fulfilled if the total number of electrons in the unit cell is an even number (1) and if the sum of the possible oxidation states of the atoms is zero (2). For example, the compound $\text{Ca}^{+2}\text{Ta}^{+5}\text{O}_3^{-2}$ is a metal because there are an odd number of electrons in the cell and the oxidation states sum up to +1. Only the condition (1) is fulfilled by $\text{Sc}^{+3}\text{Ta}^{+5}\text{O}_3^{-2}$, while $\text{K}^{+1}\text{Ta}^{+5}\text{O}_3^{-2}$ is expected to be a semiconductor. The configurations allowed by the two rules are shown in Fig. 5.2. The number of compounds that require to be calculated is thus reduced to around 40%. Because of the condition 1, there are no couple of elements A and B that can be successful for both the ABO_3 and ABO_2N perovskites. In fact, oxygen has 8 electrons and the sum of the electrons from the A- and B-ion has to be an even number, while the anions O_2N have, in total, 23 electrons and thus, the sum of the electrons of the A- and B-metal must be an odd number. The situation is different for the ABO_3 and ABON_2 perovskites: both requires an even number of electrons from the two metals and the sums of valences equal to 6 and 8, respectively. The two conditions give no information about the position that a metal occupies in the crystal structure. An indication can be provided by Fig. 5.1 and by the Goldschmidt's tolerance factor (Eq. 2.5).

Fig. 5.3 shows the probability to generate a stable perovskite with a bandgap for a chemical that occupies the A- (upper triangle) or B-ion position (lower triangle). The probability for a metal M is calculated as the ratio between the number of stable combinations with a bandgap that include M and the total number of allowed configuration.

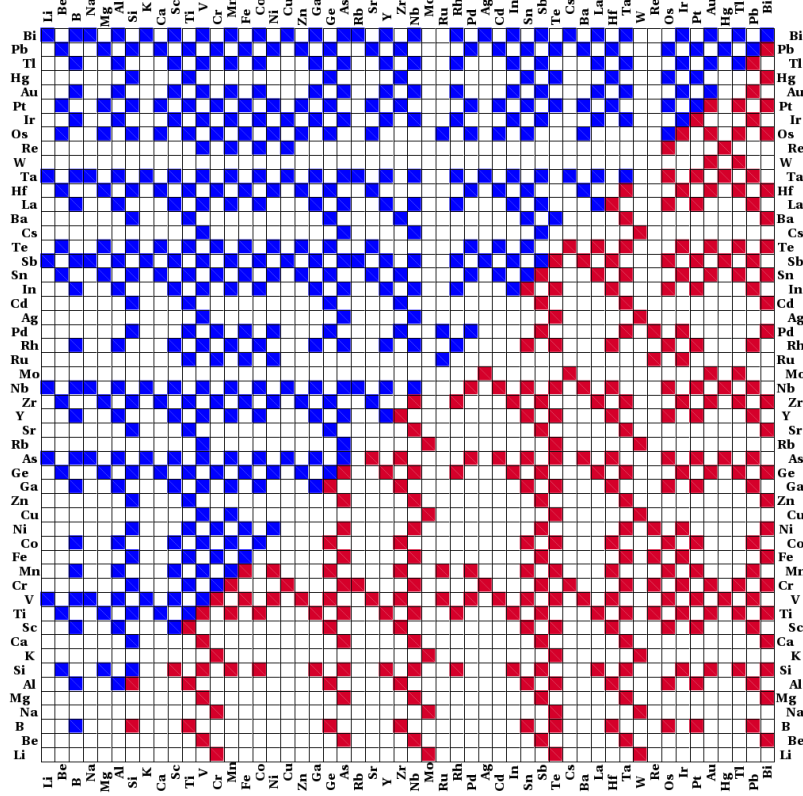


Figure 5.2: Combinations allowed including the chemical-based on counting electrons and oxidation states of the pure chemicals. The blue squares in the upper matrix indicate combinations permitted for the ABO_3 perovskite while red squares in the lower matrix combinations allowed for the ABO_2N .

Alkali and alkaline earth metals have a very large probability ($\geq 50\%$, as shown in Table 5.1) to generate a stable structure with a bandgap when they are used as A-ion. Early transition metals, instead, form stable semiconductors with a probability larger than 25% when they occupy the B-ion position. Metalloids and post-transition metals are equally good to be used as A- and B-ion. In fact, the ionic radii of both metalloids and post-transition metals fit, in general, with both the positions. The metalloids with an oxidation state of +3 can be easily combined with another +3 metal to form a 3 + 3 perovskite. The post-transition metals (that have valences of +2 or +4) can be used either as an A-ion with oxidation state +2 or as +4 metal and be placed in the B-ion position. Almost half of the chemicals considered do not produce perovskites that are at the same time stable and have a bandgap. Table 5.1 shows, in parenthesis, the probability for each metal to generate a semiconductor when the rules 1 and 2 are not used. The calculated probabilities are drastically reduced. This indicates that few chemical-based rules can have a high impact on the performances of the screening.

The information about stability and bandgap can also be studied using cluster analysis and dendrogram plots. A dendrogram is a tree diagram used to draw the clusters produced by hierarchical clustering. The distance $d(A_1, A_2)$ between two elements A_1 and A_2 is defined as:

$$d(A_1, A_2) = \frac{1}{N_B} \sum_B (E_{A_1BO_3}^{\text{gap}} - E_{A_2BO_3}^{\text{gap}})^2, \quad (5.1)$$

where N_B is the number of possible combinations. The same distance can be defined between B_1 and B_2 , where the sum now runs over all the possible elements in the A-

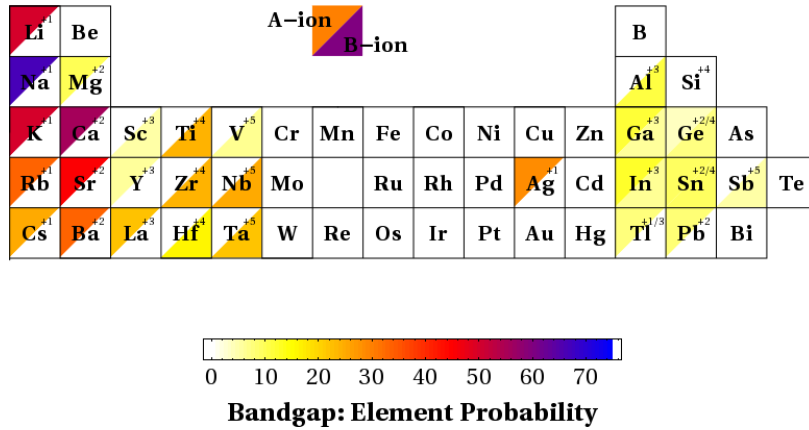


Figure 5.3: A- and B-ion probabilities (in %) for the stable combinations showing a bandgap. The probabilities are calculated taking into consideration the two conditions of counting electrons and oxidation states, i.e. as the number of successful (stable and showing a bandgap) combinations that include M divided by the total number of allowed materials formed by that element. The most common oxidation states are also indicated for the metals with a probability different from zero.

A-ion	Probability [%]	B-ion	Probability [%]
Na	60.0 (7.7)	Ta, Nb	34.6 (17.3)
Ca, Sr	50.0 (9.6)	Zr	33.3 (11.5)
K, Li	50.0 (5.8)	Hf	27.8 (9.7)
Ba	40.0 (7.7)	Ti	26.1 (11.5)
Rb, Cs, Ag	33.3 (3.8)	Sn	13.6 (5.8)
La	21.1 (7.7)	Al	10.5 (3.8)
Sn, Pb	13.6 (5.8)	Ge	9.1 (3.8)
Ga, In, Tl	10.5 (3.8)	Sb	7.7 (3.8)
Mg	10.0 (1.9)	V	7.4 (3.8)
Y	5.3 (1.9)	Sc, Ga, In	5.2 (1.9)
Ge	4.5 (1.9)		

Table 5.1: Probability for an element to occupy the A- or the B-ion position when the resulting combination is stable with a bandgap. In parenthesis the probability when the chemical-based rules 1 and 2 are not used on the selection of the chemical elements.

position. At a large cutoff distance, all the elements are grouped together. At a smaller distance, the clustering starts until each individual is found. In general, two data points belong to the same cluster if there is a chain of data points, with distances d less than the cutoff, that connect them. For the current problem, two A- (or B-) elements are close to each other, when the resulting perovskites show similar bandgaps for all the possible B- (or A-) atoms.

The cluster analysis and the dendrogram plots have recently been used to study the interleukin interactions between different heterocycles and to guide the search in the crystal structure prediction.⁸⁰

Figure 5.4 shows the dendrogram plots calculated using the bandgaps of the stable combinations (49 observables). α and β collects all the elements where no stable configurations with gap have been found for the A- and B-ion, respectively. The elements are grouped mainly following the different valences of the chemical elements: Cs, Ag, Rb, K, Na, Li, Tl, Ga, and In (valence 1); Ge, Mg, Sn, Pb, Ba, Sr, and Ca (2); Y, and La (3) for the A-site, and In, Ga, Sc, and Al (3); Hf, Zr, Ti, Sn, and Ge (4); Sb, V, Nb, and Ta (5) for the B-ion. At a smaller cutoff distance, the clusters are divided

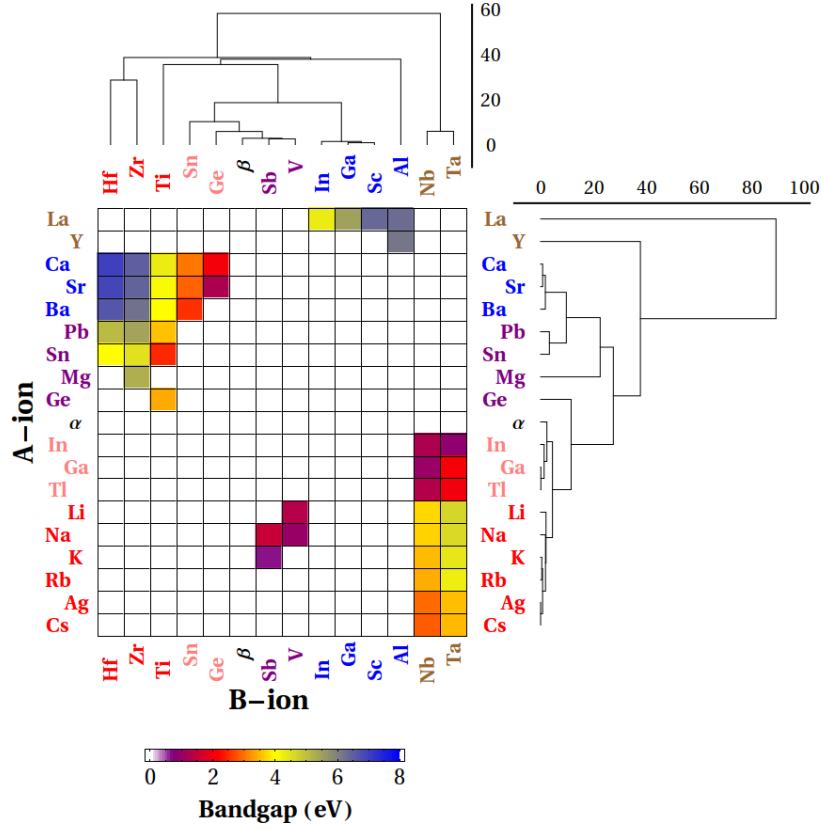


Figure 5.4: Dendrogram trees for the A- and B-ion positions for the stable perovskites showing a bandgap. The size of the bandgaps are indicated in the colored map where the elements are sorted accordingly to the dendrogram analysis. Only the 49 stable materials with bandgap are considered in the diagrams. The elements that do not contribute to any stable semiconductor are grouped together and are indicated with α and β for the A- and B-ion, respectively. The numbered scales indicate the distances between the clusters.

in sub-groups depending on the position of the element in the periodic table (s-, p-, or d-metal), as shown by the different color fonts in Fig. 5.4. The dendrogram analysis also orders the elements in each cluster as a function of the size of the gap. The bandgap increases going from left to right and from the bottom to the top of the periodic table. In fact, the size of the bandgap is strictly correlated to the size of the atoms and to the character of the chemical bonds.⁵⁸ The dendrogram analysis can give suggestions on the possible substitution that can be done to tune the bandgap to the desired size.

The heats of formation and the bandgaps are combined in the dendrograms of Fig. 5.5. More combinations are now included with respect to Fig. 5.4 since also the non stable compounds are considered. The distance between two A-ions is now defined as:

$$d(A_1, A_2) = \frac{1}{N_B} \sum_B \left[(E_{A_1BO_3}^{\text{gap}} - E_{A_2BO_3}^{\text{gap}})^2 + (\Delta E_{A_1BO_3} - \Delta E_{A_2BO_3})^2 \right], \quad (5.2)$$

that includes both the difference between the bandgaps (E^{gap}) and between the heats of formation (ΔE) with the same weight. The division in clusters is again dominated by the oxidation states and by the position of the elements in the periodic table.

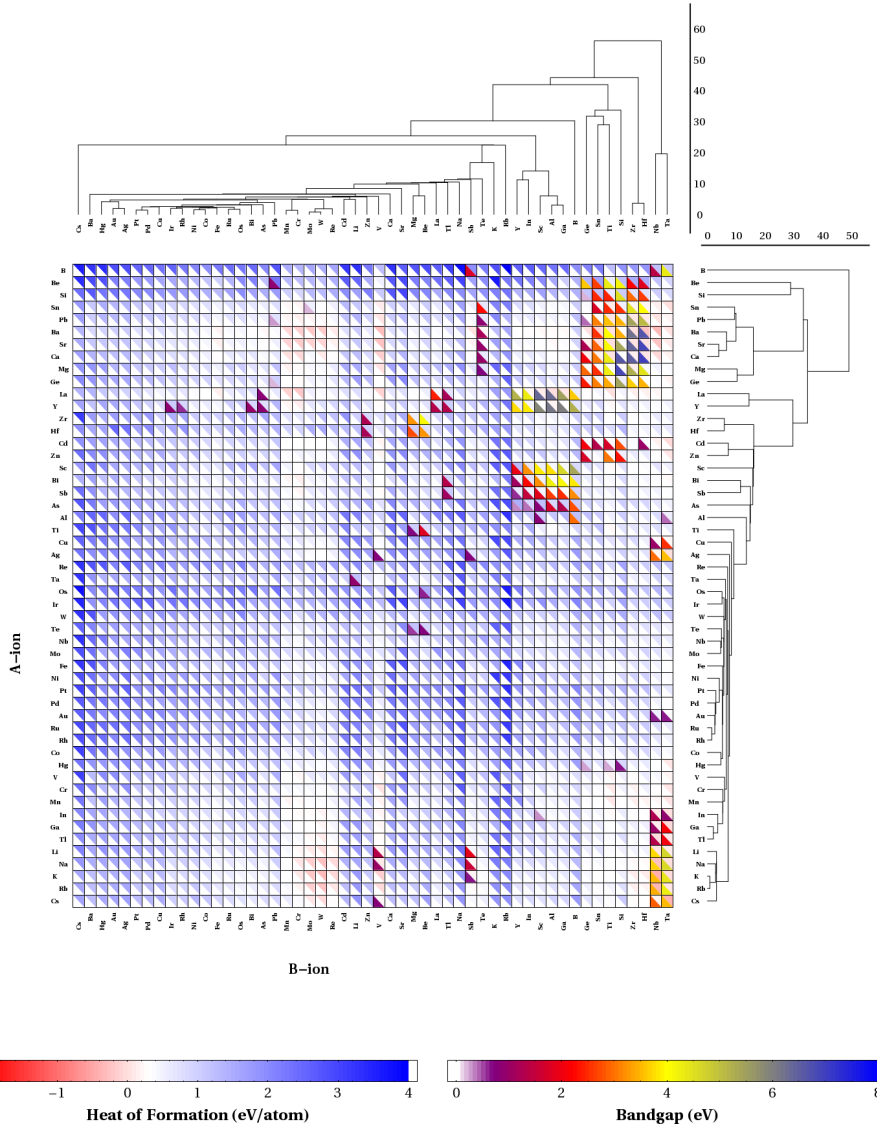


Figure 5.5: Dendrogram trees for the A- and B-ion positions for all the ABO_3 perovskites. The heats of formation and the size of the bandgaps are indicated in the colored map ordered following the dendrogram analysis. This map differs from the one of Fig. 2.4A because of a different order in the chemical elements.

5.2 Prediction of ABO_2N Perovskites

The information obtained by the probabilities of Figs. 5.1 and 5.3 can be used to predict new materials in a class of compounds different from the ABO_3 perovskite, like the ABO_2N perovskites.

Table 5.2 shows the possible ABO_2N cubic perovskites obtained by combining the elements from Table 5.1 in the A- and B-site. The chemical-based rules 1 and 2, described before, have also been used to reduce the list of possible combinations. The stabilities and bandgaps of those materials have been checked with the results obtained by DFT and described in Chapter 2. 14 of the 16 stable ABO_2N perovskites with a bandgap are found. The two missing compounds are KWO_2N and $RbWO_2N$ because tungsten generates no stable ABO_3 perovskites due to its oxidation state (6) that makes one of the chemical rules to fail. The first 13 combinations are all stable with a bandgap and

A-ion	B-ion	Stable?	Gap [eV]	A-ion	B-ion	Stable?	Gap [eV]
Ca	Ta	✓	2.2	(cont.)			
Sr	Ta	✓	2.1	In	Hf		0
Ca	Nb	✓	1.4	La	Sn		1.8
Sr	Nb	✓	1.4	In	Ti		0
Ba	Ta	✓	2.0	La	Ge		0
Ba	Nb	✓	1.3	Y	Zr		3.3
La	Zr	✓	3.4	Ge	Ta		1.8
La	Hf	✓	3.8	Ge	Nb		1.1
La	Ti	✓	2.5	Y	Hf		3.4
Sn	Ta	✓	1.2	In	Sn		0
Sn	Nb	✓	0.5	Y	Ti		2.4
Pb	Ta	✓	2.0	Sn	Sb		0
Pb	Nb	✓	1.3	Pb	Sb		0
Sr	Sb		0	Sn	V		0
Ca	Sb		0	Pb	V		0
Sr	V		0	In	Ge		0
Ca	V		0	Mg	Sb		0
In	Zr		0	Mg	V		0
Mg	Ta	✓	2.1	Y	Sn		2.7
Mg	Nb		1.5	Y	Ge		1.3
Ba	Sb		0	Ge	Sb		0
Ba	V		0	Ge	V		0

Table 5.2: Possible combinations in the ABO_2N stoichiometry using the elements with a non-zero probability to generate a stable semiconductor in the ABO_3 structure after that the chemical-based rules have been applied. The stability check and the size of the obtained bandgap is included. The combinations are sorted for decreasing probability defined as the product of the probabilities of the two constituent metals.

no more than 20 simulations are needed to find the 14 stable bandgap materials. All the stable ABO_2N with a bandgap and the related dendrograms are shown in Figure 5.6. As in Figure 5.4, the elements are clustered following the different oxidation states and the positions in the periodic table.

The high rate of success of this simple method is determined by the similarity between the two investigated structure. In fact, oxygen and nitrogen have similar properties, like electronegativity and ionic radius that make the oxynitride perovskites not too different from the oxides. More sophisticated methods, like evolutionary algorithms and/or data mining, might be necessary for investigating structures very different from the ABO_3 cubic perovskite.

In the following chapter, an evolutionary algorithm will be introduced to make the search of new materials more efficient. It will also be shown that the chemical-based rules are still valid and useful for the large set of data of 19000 cubic perovskites.

5.3 Summary

A statistical analysis has been applied to the ABO_3 cubic perovskites. Simple chemical-based rules have been found useful to reduce the space of investigation of around 40% of the total when the goal is to find stable semiconductors. In particular, atoms with equal oxidation states, behave in a similar way in generating stable structures with a bandgap, as shown by the dendrogram plots where the atoms are grouped depending mainly on the valences and on their position in the periodic table. This can be used to suggest how to substitute chemicals to tune the size of the bandgap. The information

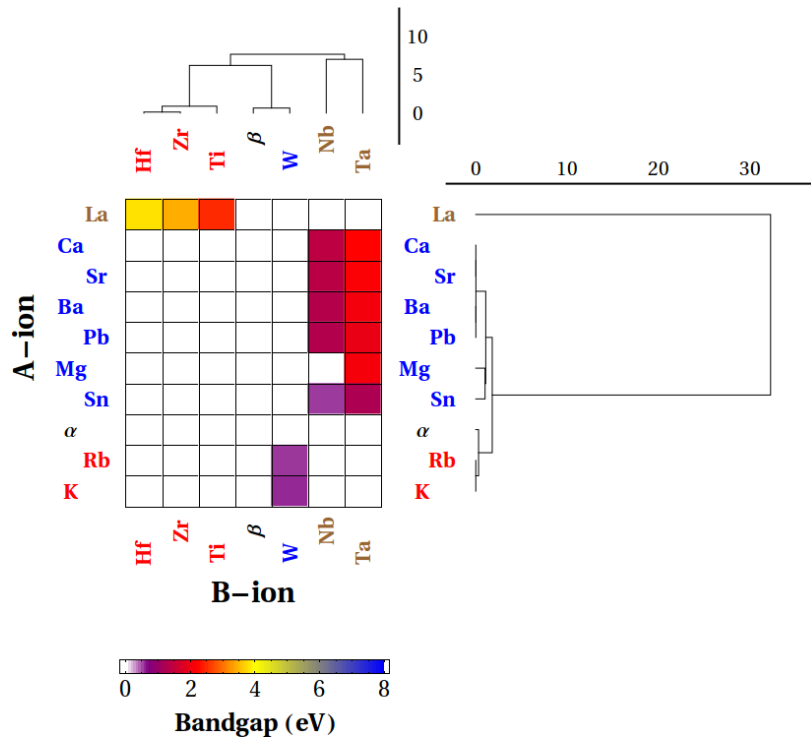


Figure 5.6: Dendrogram trees for the A- and B-ion positions for the stable perovskites showing a bandgap. The size of the bandgaps are indicated in the colored map where the elements are sorted accordingly to the dendrogram analysis. The elements that do not contribute to any stable semiconductor are grouped together and are indicated with α and β for the A- and B-ion, respectively.

obtained for the ABO_3 perovskites can be used to predict new ABO_2N materials with a very good success rate.

Evolutionary Algorithms in Search for Water Splitting Perovskites

The search for new materials can be guided using sophisticated methods like data mining⁷⁸ or evolutionary (or genetic) algorithms and combine them with *ab-initio* quantum mechanics simulations. In a data mining approach, the starting point is provided by nature and new materials are obtained by combining the already known crystal structures following the chemical/structural rules suggested by experience. In a genetic algorithm, no *a priori* knowledge is needed and the best materials are found using an evolutionary technique similar to nature where only the strongest individuals survive.

It is a challenge to find the best parameters to achieve the highest efficiency in a genetic algorithm. In the present chapter, the role of different parameters has been investigated. The algorithm works in the chemical and structural space of the cubic perovskites and searches for the new water splitting materials already described in Chap. 2 and 3.

This chapter is the result of a collaboration with Dr. Anubhav Jain and Dr. David H. Bailey (Lawrence Berkeley National Laboratory, Berkeley, California, USA), and Dr. Geoffroy Hautier (Université Catholique de Louvain, Louvain-la-Neuve, Belgium).

6.1 Evolutionary Algorithm

An evolutionary algorithm runs through three main steps: (i) definition of the initial population; (ii) calculation of the fitness function of each individual, that determines the probability of the individual to be used to make the following generation; (iii) creation of the next generation of individuals starting from the best-fit individuals using mixing operations like mutation and crossover. The algorithm then continues from point (ii) until a sufficient fitness is achieved.

The efficiency of the algorithm highly depends highly on the definition of the fitness function. In the case under investigation, the ranking of the individuals must depend on the three screening criteria described earlier and there is no unique way to rank the materials. Fig. 6.1 shows the three different fitness functions used: (i) the fitness function (called *discontinuous*) is obtained by a sum of the scores for the stability, bandgap, and band edges and no points are given unless the screening properties are fully met; (ii) called *smooth*, the fitness function is given by the sum of the three scores

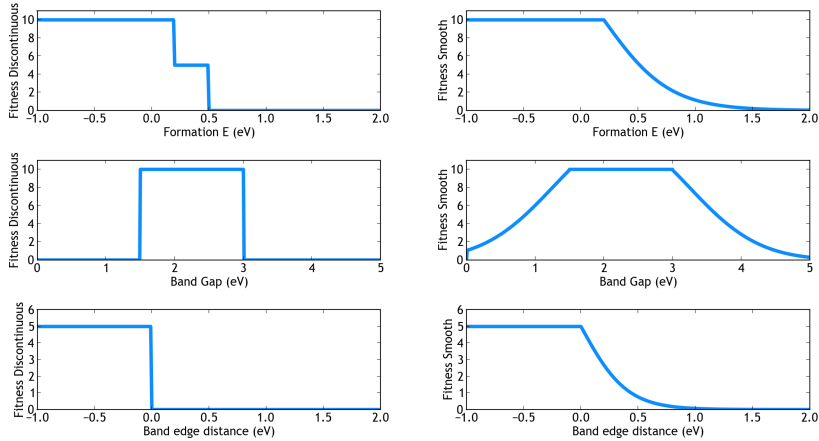


Figure 6.1: The *discontinuous* (left column) and the *smooth* (right column) strategies. The overall fitness function is obtained by either sums or products of the fitness functions of each criterion.

as in (i), but the fitness score increases as an individual becomes closer to the target properties; (iii) called *smooth product*, similar to (ii) but the fitness function takes the product of the stability fitness with the sum of the band gap and band edge position fitness, rather than the sum. This assigns higher fitness to compounds that balance stability and desired electronic structure.

Three methods are used to select the parents for the next generation: (i) uniform, where the individuals are selected randomly; (ii) roulette wheel, where the fitness function determines the probability of an individual to be selected; (iii) tournament wheel, where the individuals are grouped randomly and, in each group, only the individual with the highest fitness is selected.

Crossover functions and mutations are then used to generate the children population from the parents. Three crossovers are tested (Fig. 6.2: (i) single-point, the children are generated by swapping either the A or B cation (but not both); (ii) two-point, the generated children swap the anion (X_3); (iii) uniform, A, B, and X_3 are randomly swapped between the parents. To explore a region far away for the parents, a mutation is necessary. The mutation used here replaces randomly an element of the individual. The performance can be improved by promoting some of the fittest individual to the next generation and replacing the least fit individuals. This procedure is called elitism.

The selection of the individuals can be guided by empirical knowledge and scientific principles. The rules applied here are:

1. Even-odd electrons rule: a material with an odd number of electrons has partially-occupied eigenstates at the Fermi level so it has a bandgap equal to zero.
2. Valence balance rule: in a realistic material, the sum of the possible oxidation states of its elements must be zero, so that the compound is neutral.
3. Goldschmidt's tolerance factor ranking: the materials are ranked using the absolute deviation between their Goldschmidt's tolerance factor (Eq. 2.5) and the ideal value ($t_{\text{ideal}}=1$). In the case of multiple known ionic radii, the unweighted average of the radii has been used. The weighted average of the individual ionic radii is used when the anion X_3 contains different elements, for example like O_2N .

Materials not fulfilling the rules 1 and 2 are excluded from the search. In fact, as shown in Chapter 5, combinations not fulfilling one of the two rules, fail in producing stable semiconductors. Rule 3 gives an additional ranking of the compounds so that the ones with a smaller deviation from the ideal value are calculated first.

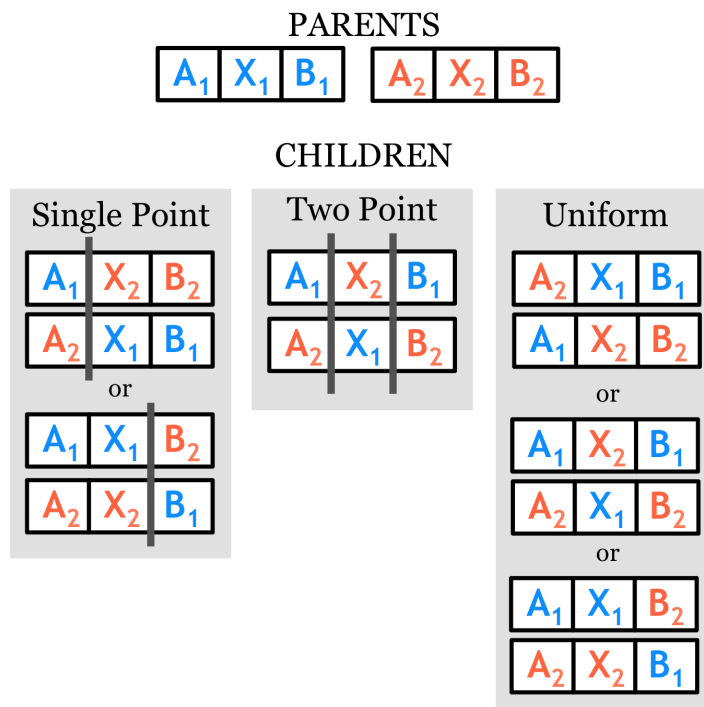


Figure 6.2: The crossover functions used in the algorithm to produce two children from a pair of parents.

Parameter set	20 solutions	10 solutions
Chemical rules	4.5	9.2
Best GA	5.8	9.8
Best GA + chemical rules	11.7	16.9

Table 6.1: Efficiency of the best GA and chemical rules to find 20 and 10 candidates for the one-photon water splitting. The efficiency of the random search is defined to be equal to 1.

6.2 Results

The robustness or efficiency of both genetic algorithms and chemical rules has been tested for the problem of the one-photon water splitting and transparent shielding of the photoanode. The descriptor of the robustness is given by the expected number of computations needed to produce a given number of solutions. The robustness is then defined as the ratio between the average number of calculations needed for a random search and for the genetic algorithm to produce the same number of solutions.

The average number of calculations needed to find a given number of solutions for the one-photon water splitting problem is shown in Fig. 6.3 and summarized in Table 6.1. On average, the best genetic algorithm (in blue) requires around 3100 calculations to find all the 20 candidates with an efficiency 5.8 times higher than a random search (in black). The chemical rules described above, reduce the space of investigation of around 60%, and a random search based on the chemical rules (in orange) performs as good as the best genetic algorithm without any *a priori* knowledge. The genetic algorithm benefits from the knowledge provided by the chemical rules. Excluding the combinations not fulfilling the chemical rules and rerunning the best genetic algorithm (in green), the efficiency improves of 11.7 times with respect to the random search and of more than 2 compared with the best genetic algorithm and the search using only the chemical rules.

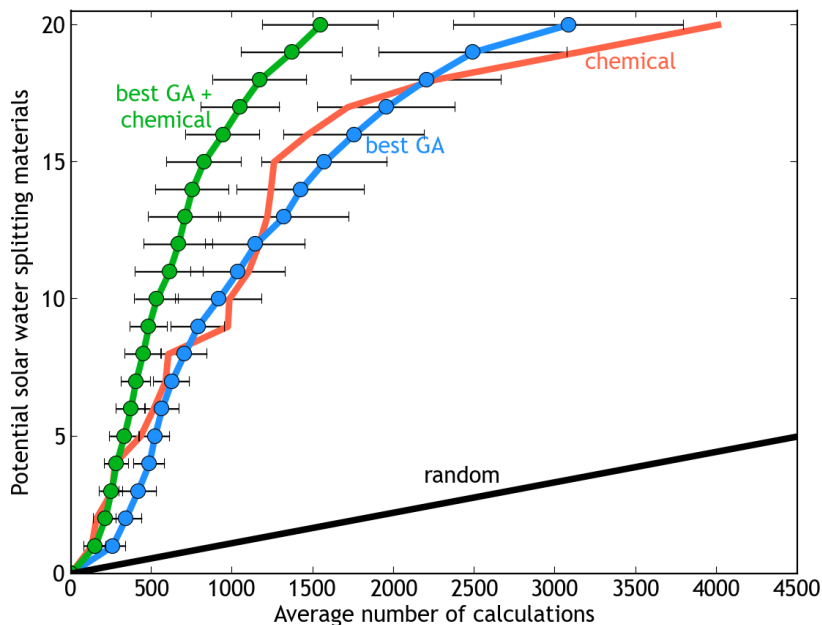


Figure 6.3: The average number of simulations needed to produce a given number of solutions for the one-photon water splitting problem. The best genetic algorithm (in blue) requires fewer calculations than a random strategy (in black), but performs similarly to a random search based only on the chemical rules (in orange). A significantly improvement is obtained by applying the chemical rules to the genetic algorithm (in green). One standard deviation from the average performance over 20 independent runs of the genetic algorithm is indicated by the error bars.

Fig. 6.4 shows the effects of the different parameters on the efficiency of the algorithm (listed here in order of importance):

- Elitism is crucial even if it saturates after a rate of 50%.
- The *smooth product* fitness function gives higher performance than the *smooth* and the *discontinuous* functions. Both give partial points for partial solutions and multiply the individual fitness functions are beneficial in the definition of multi-objective functions.
- A small population size is preferable to large population sizes where a large portion of the search space has to be investigated before the selection and crossover functions are able to narrow down the genes.
- Single-point and uniform crossover perform almost equally better than the two-point one. In the two-point crossover the anions X_3 are swapped, but the problem contains only seven different anions. Since many parents have the same anions, the children will then be identical to the parents. This prevent to have enough diversity in the population and thus the two-point crossover is not appropriate.
- The roulette and the tournament selection types perform in a similar way and better than the uniform selection. A weak roulette selection that prefers the population diversity instead of the stronger individuals gives results comparable to the uniform selection.

The role of various parameters has been tested also for two other problems: (i) finding 10 solutions out of the 20 candidates for one-photon water splitting, and (ii) finding the 8 materials suitable for protecting the photoanode from photocorrosion, listed in Fig. 3.6a.

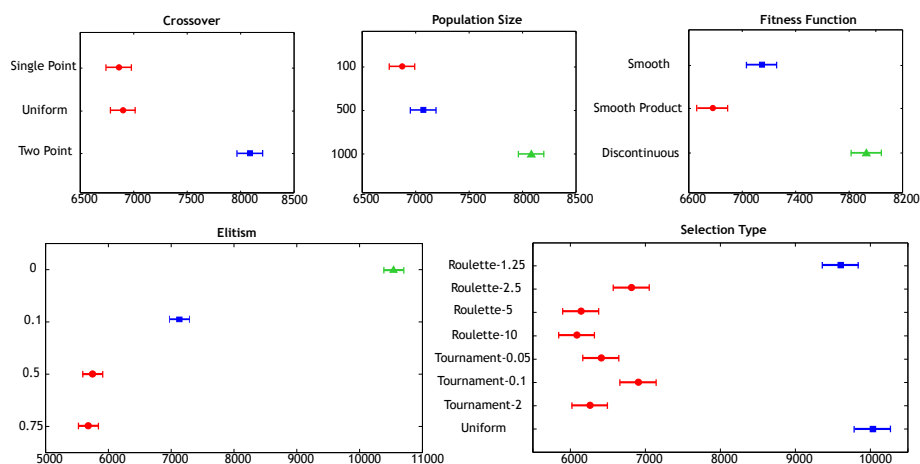


Figure 6.4: Effects of the choice of the various parameters in the genetic algorithm.

The benefits of a smaller population is more pronounced in the problem of finding 10 materials for water splitting compared with the full solution. In fact, smaller populations learn the rules to find a few good candidates faster than a larger population, but their advantage disappears as more candidates must be found because of a lower diversity in the population. The efficiencies in finding 10 candidates for the best GA and chemical rules are shown in Table 6.1.

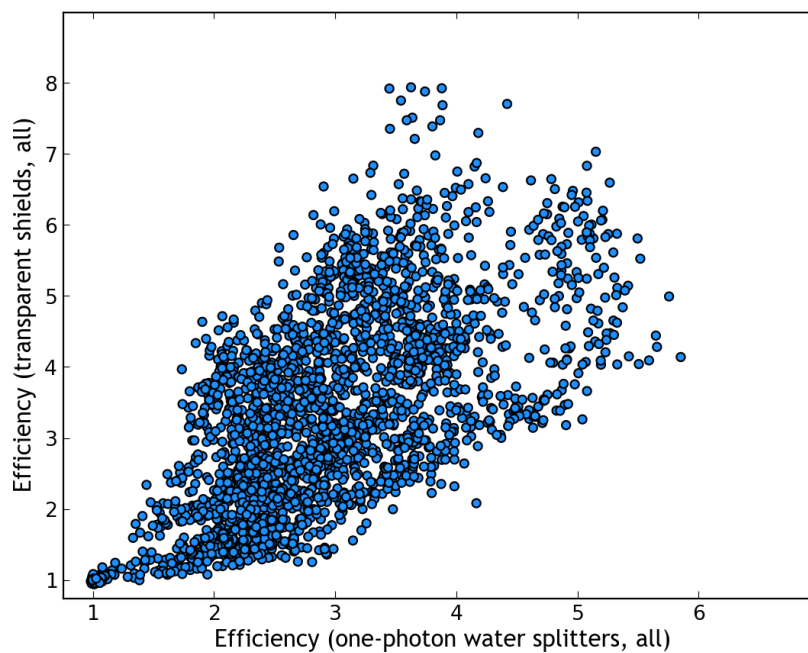


Figure 6.5: Correlation between the efficiencies of various set of parameters in finding the 20 perovskites for one-photon water splitting (x -axis) and the 8 materials to protect the photoanode (y -axis).

The best genetic algorithm for finding the solutions to the transparent shielding problem is 8 times more efficient than a random search, but even if there is a correlation between the transparent shielding and water splitting problems, the best set of parameters for one-photon problem do not give the best efficiency for the other. In particular, the set of parameters giving the highest efficiency (around 6 times better than random

search) for the water splitting problem, gives an improvement of 4 times with respect to the random search for the transparent shield, and the one giving the highest improvement (8 times) for the transparent shield problem, gives an improvement of around 3.5 for the water splitting (Fig. 6.5). In this case, a chemical-based search performs even better than the best genetic algorithm (13.4 times better than random search). This indicates that the chemical rules might be better than a genetic algorithm in finding fewer solutions, while a genetic algorithm is preferable to search for more. The role of the various parameters is similar to the results presented for the water splitting problem (Fig. 6.4).

In general, the parameters with the largest effects on the robustness of the algorithm are elitism, selection method, and population size.

6.3 Summary

A genetic algorithm is useful to improve the search for materials to use in a photoelectrochemical cell. The algorithm quickly finds half of the solutions for the one-photon water splitting problem and the full set of solutions with an efficiency 5.8 times higher than the random search. The algorithm can become more efficient by applying a set of chemical rules that filters and ranks the perovskites under investigation. The efficiencies of the combined genetic algorithm and chemical rules are 16.9 and 11.7 times better for half and all the solutions, respectively.

The study suggests few guidelines: the elitism should be set high, around 50% of the population; a strong roulette or tournament selection method are recommended. In addition, a uniform or single point crossover, a small population size (around 0.5% of the search space) and the *smooth product* fitness function should be preferable.

Chapter 7

Low Symmetry Perovskites for One- and Two-photon Water Splitting

The success in the screening of cubic perovskites leads to the search of more complex materials. The screening approach has been applied to low symmetry perovskites obtained by combining two cubic perovskites in a structure called *double perovskite* or combining a cubic perovskite with different motif to form the so-called *layered perovskite*. The screening is applied to the problem of finding new materials for one- and two-photon water splitting. This chapter is based on Papers III and VI.

7.1 Double Perovskites

The double perovskite structure is composed of two cubic perovskites as shown in Fig. 7.1A. The general formula is $A_1A_2B_1B_2O_6$, where A_1 and A_2 are in the A-ion position of the cubic perovskite and B_1 and B_2 are in the B-ion position. The double perovskite requires a unit cell of 20 atoms. The four-metal space is too vast to be investigated completely as it has been done for the cubic perovskite materials. For this reason, the double perovskites studied here, are obtained by combining two of the 46 stable cubic perovskites with a non-zero bandgap resulting from the previous screening. Double perovskites have been first synthesized in 1998⁸¹ and they have been investigated theoretically because of their various properties, like ferroelectricity and high magnetic Curie temperature or small bandgap.

7.1.1 Trends in Double Perovskites

The bandgaps of 1100 combinations investigated are summarized in Fig. 7.1B. The bandgaps span over a region from 0 to 7 eV; most of the combinations have a bandgap larger than 4 eV and only few have a bandgap between 1.5 and 3 eV corresponding to the visible light range. Compared to the oxides in the cubic perovskite structure, the bandgaps are generally larger. The reason might be related to the octahedral distortion that leads by itself to an increase of the bandgap and that cannot be studied in the 5 atoms unit cell used for the cubic perovskites.

The difference between the bandgaps of the double perovskites and of the average of the two bandgaps of the constituents ABO_3 is shown in Fig. 7.2A. Usually, the double

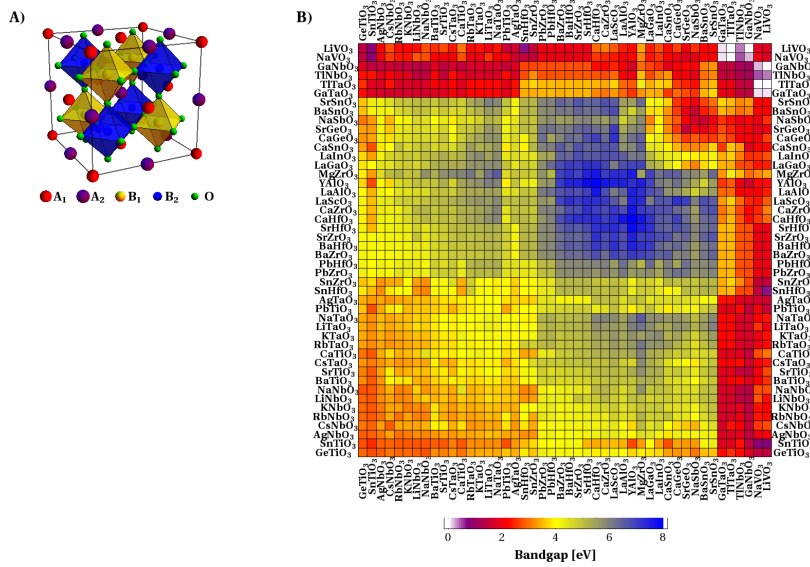


Figure 7.1: (A) Double perovskite crystal structure. (B) Calculated bandgaps for the possible combinations. In red the materials with an ideal bandgap for one-photon water splitting. The cubic perovskites along the two axes of the plot are sorted using a cluster analysis similar to the one described in Chapter 5.

perovskites have a bandgap similar to the average gap of the two cubic perovskites (in white). When one of the two constituents has a small bandgap (below 1.5 eV), the corresponding double perovskites show a general reduction of the bandgap (in blue) compared to the average gap of the two corresponding cubic structures. However, there are also combinations, where a d-metal is combined with a p-metal in the two B-ion positions, for which there is a significant increase of the bandgap (up to 3 eV, in red). By contrast, the bandgap is not significantly affected by the elements in the A-ion positions.

A strong hybridization between the p- and d-metals in the B-ion positions causes the opening of the bandgap. Fig. 7.3 shows the projected density of states (DOS) for

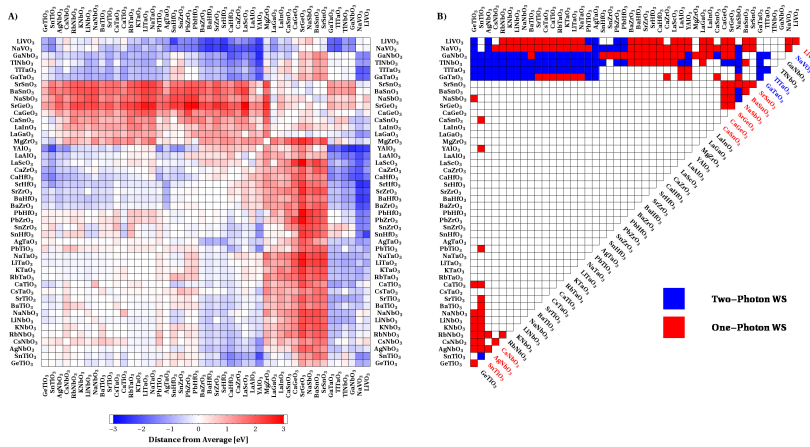


Figure 7.2: (A) Difference between the double perovskite bandgap and the average gaps of the constituent perovskites calculated for the 20 atoms unit cell. (B) Candidates for one- and two-photon water splitting. The colored font for the name of the structure indicates that the cubic perovskite has been previously proposed as a candidate for one- or two-photon water splitting.

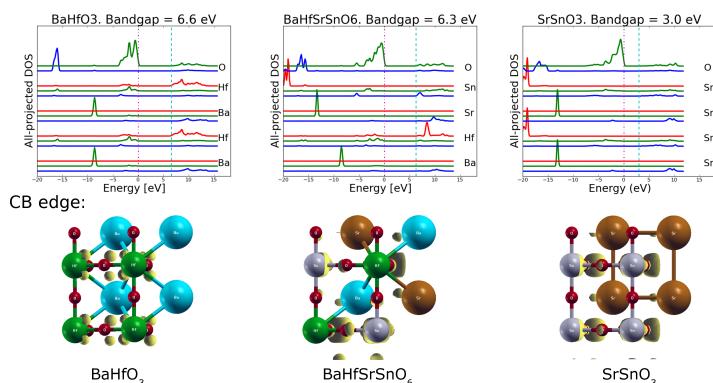


Figure 7.3: Projected density of states for BaHfO_3 , BaHfSrSnO_6 , and SrSnO_3 . The s, p, and d orbitals are drawn in blue, green, and red, respectively. The zero energy is set to the HOMO level (in magenta). The LUMO level is indicated by a cyan line. A strong hybridization between the p- and d-metals in the B-ion positions causes the increase in the bandgap for the double perovskite. The wavefunctions of the conduction band (CB) edge states of the three materials are also shown.

BaHfO_3 , SrSnO_3 , and their combination BaHfSrSnO_6 . The projected density of states of Hf-d and Sn-s/p show peaks in the double perovskite that are not present in the cubic ones. The conduction band wavefunctions follow the densities: the d-like wavefunction of Hf in the BaHfO_3 disappears for the more intense s-like wavefunction of Sn in the BaHfSrSnO_6 .

7.1.2 Candidates in the Double Perovskite Structure

The same parameters used in the screening for the cubic perovskite are applied also here. Fig. 7.2B shows the candidates for one-photon water splitting (150 combinations, in red) and two-photon (100, in blue) mechanism. 6 cubic perovskites are particularly promising to generate candidates. Some of the candidates in the cubic perovskite, like CaGeO_3 or CaSnO_3 , shown with colored fonts in the diagonal of Fig. 7.2B, now fall in or out of the bandgap region for the one- or two-photon water splitting because of distortions or changes in the lattice parameters of the structure with consequent increase or reduction in the bandgap.

7.2 Layered Perovskites

A layered perovskite is formed by 2D slabs of ABO_3 cubic perovskite separated by some motifs. Several phases of layered perovskite are known, depending on the relative displacement and of the thickness of the slabs of cubic perovskite and of the motif. This section shows the results for the Ruddleson-Popper phase (Fig. 7.4) with general formula $\text{A}_{n-1}\text{B}_n\text{O}_{3n+1}$, where n is the number of BO_6 octahedra forming the 2D slabs. The cases of $n = 1$ (A_2BO_4 and $\text{A}_2\text{BO}_3\text{N}$, where the case of one oxygen replaced by one nitrogen is studied because of the beneficial effect that this has on the level alignment⁵⁸) and of $n = 2$ ($\text{A}_3\text{B}_2\text{O}_7$) are considered. The $n = 1$ phase is composed of slabs of cubic perovskite ABO_3 offset by a translation of $(1/2, 1/2)$ with respect to each other and separated by a layer of A_2 . The $n = 2$ is similar except that each slab of perovskite is formed by two octahedra BO_6 . The unit cells are composed of 14 and 24 atoms, respectively.

As shown before, the search for new materials can be guided by chemical-based rules (Chapter 5 and 6). Those rules can reduce the number of calculations to perform since only the combinations that fulfill them will be calculated for the screening. The

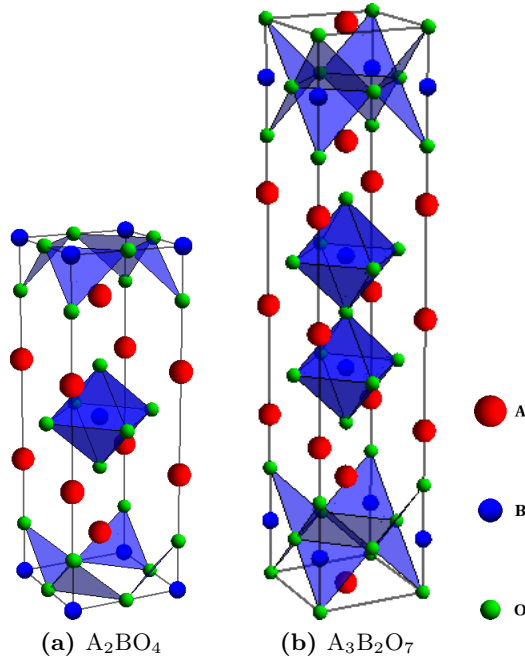


Figure 7.4: Crystal structure of the Ruddlesden-Popper phase with $n = 1$ (a) and $n = 2$ (b).

Goldsmith's tolerance factor (Eq. 2.5) selects which metals can occupy the A- and B-ion positions*. With these constraints, 300 combinations will be screened.

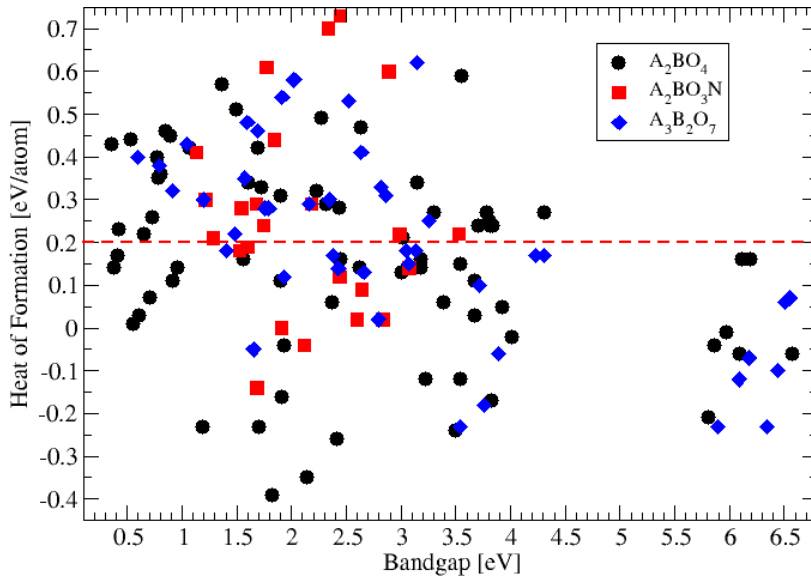


Figure 7.5: Heats of formation as a function of the bandgaps for the A_2BO_4 (black circles), A_2BO_3N (red squares), and $A_3B_2O_7$ (blue diamonds). The oxides show high stability and a wide range of bandgaps. The oxynitrides are slightly less stable and show a general reduction in the size of the gaps compared to the oxides.

*The metals used in the A-ion position are: Li, Na, Mg, K, Ca, Ga, Ge, Rb, Sr, Y, Ag, Cd, In, Sn, Cs, Ba, La, Tl, and Pb. The B-metals are Al, Sc, Ti, V, Cr, Mn, Fe, Co, Ni, Cu, Zn, Ga, Ge, Zr, Nb, Mo, Ru, Rh, Pd, In, Sn, Sb, Te, Hf, Ta, W, Re, Os, Ir, Pt, and Bi.

7.3 Trends in Stability and Bandgaps

The heats of formation and the bandgaps are calculated for the A_2BO_4 , $A_3B_2O_7$, and A_2BO_3N layered perovskites using the linear programming analysis described in Chapter 2. Fig. 7.5 shows the heat of formation as a function of the bandgap. The bandgaps of the oxides range from zero to more than 6 eV, but no materials with a gap between 4.5 and 5.5 eV have been found. The oxides are usually very stable and the stability increases with the bandgap. The oxynitrides show lower stabilities and smaller bandgaps. In fact, nitrogen is slightly less electronegative than oxygen and the valence band edges are formed by the nitrogen 2p orbitals hybridized with the oxygen 2p. The nitrogen 2p are higher in energy than the oxygen 2p with the consequence of making the gaps smaller and shifting up the band edges to have a better matching with the red-ox levels of water. On the other side, nitrogen breaks the symmetry of the cubic perovskite octahedron. This leads to a reduction in the stability, as shown in Fig. 7.5. Further nitrogen replacements will result in even smaller bandgaps and to an additional reduction in the stability of the compounds (Fig. 2.6), so this is not investigated here.

The bandgaps of the stable A_2BO_4 layered perovskites are shown in Fig. 7.6. The chemical elements are sorted using a dendrogram analysis and atoms that generate structures with similar gaps are next to each other. The elements are grouped depending on their valences and their positions in the periodic table. For the B-ion position, Hf

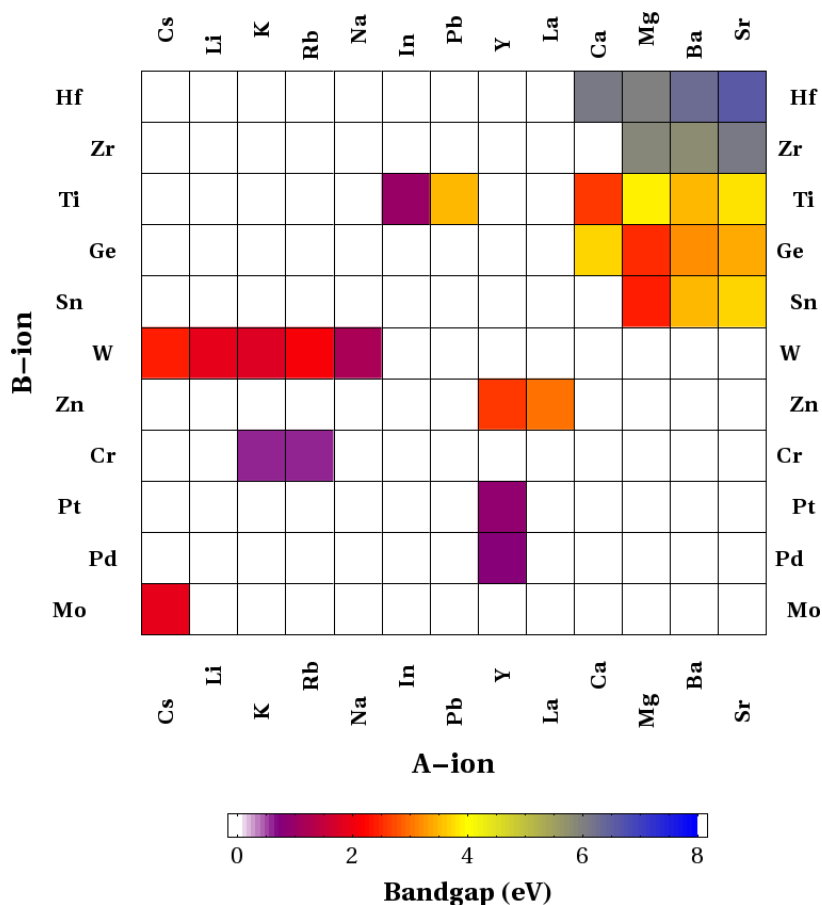


Figure 7.6: Bandgaps of the stable compounds in the A_2BO_4 structure. The gaps range from zero to more than 6 eV. The chemical elements are sorted using a dendrogram analysis, so that elements with similar size of the bandgaps are next to each other.

B-ion	In vacuum	V_R	Bandgap		
			Ca ₂ BO ₄	Sr ₂ BO ₄	Cd ₂ BO ₄
Ti ⁴⁺ (d)	-56.13	-3.35	4.01	3.82	0.78
Zr ⁴⁺ (d)	-42.30	-1.24	6.19	6.09	1.90
Hf ⁴⁺ (d)	-39.90	-1.10	6.11	6.57	1.60
Ge ⁴⁺ (s)	-52.28	-3.64	3.67	3.39	0.36
Sn ⁴⁺ (s)	-45.45	-3.82	3.70	3.67	0.54

Table 7.1: LUMO energies (in eV) of B⁴⁺ ions in vacuum and under the effect of V_R . V_R is calculated for the A²⁺ in the ASnO₄ structures and for the B⁴⁺ in the CaBO₄, but similar results are obtained for other lattices. The LUMO energies of the A²⁺ in vacuum and under the effect of V_R are for Ca²⁺ (s): -14.65 and -0.58; for Sr²⁺ (s): -13.58 and -1.02; for Cd²⁺ (s): -20.35 and -4.91. The bandgaps of the compounds containing these ions are also shown for comparison.

and Zr generate very large bandgap insulators with a gap above 6 eV and Ti, Ge, and Sn give structures with gaps above 3 eV even if few combinations have gaps in the visible range. Only minor changes in the size of the gaps are seen with changes of the atom in the A-ion position. W and Zn as A-ion seem to be particularly good for visible light absorption since the stable structures have a gap in the visible range.

The valence bands of most of the oxides are formed by the 2p levels of the O²⁻ ions and, in a first approximation, the top of the valence band energy is constant for all of them[†]. The trends in the bandgaps can be analyzed by looking at the energy of the LUMO levels of the A- and B-ions. In general, the lower the energy of the most stable LUMO from A- and B-cations the smaller will be the bandgap. The energies of the LUMOs are calculated taking into account the electrostatic field from the rest of lattice, V_R . This is done following an Ewald-Evjen scheme, assuming that all the ions keep their nominal charges.⁸²

The LUMO energies change dramatically passing from the free cations to the cations under the effect of V_R (Table 7.1). Because of the shorter distance between the O²⁻ and A-ions in comparison to the B-O²⁻ distances, V_R has the effect of destabilizing much more the LUMO energies of the B site ions than the ones of A-site ions. The correlation between the lowest LUMO energy out of A- and B- (under the effect of V_R) ions and the bandgap is shown in the table. The LUMO of the B⁴⁺ ions has lower energy than the LUMO of the A²⁺ ions when the A-position is occupied by an alkaline-earth ion and the bandgap depends on the LUMO energy of the B ion. Zr⁴⁺ and Hf⁴⁺ compounds have similar V_R and thus similar gaps, while Ti⁴⁺ shows a smaller gap. This could be understood even just by looking at the energies of the ions in vacuum, since the d-levels of Ti⁴⁺ are much deeper in energy than those of Zr⁴⁺ and Hf⁴⁺. Ge⁴⁺ and Sn⁴⁺ compounds have similar bandgaps due to a compensation of effects: the Ge⁴⁺ s level in vacuum is lower in energy than the Sn⁴⁺ s level (by ≈ 7 eV), but Ge⁴⁺ ionic radii is 16 pm smaller than that of Sn⁴⁺. Cd²⁺, contrary to the alkaline-earth elements, has the LUMO more stable than the LUMO of B⁴⁺ ion and its compounds have the conduction band dominated by the Cd²⁺ s level and consequently have a smaller bandgap.

The same results are found for the A₃B₂O₇ layered perovskites and are not reported here. These considerations are expected to be valid also in the case of a nitrogen replacement since the electronegativity of nitrogen is not too different from the one of oxygen. The main difference will be that the valence band is now formed by a hybridization of the oxygen and nitrogen 2p orbitals.

[†]This is because the ions are usually in their most favorable oxidation state that is a closed shell structure and the bonds are highly ionic. Few exceptions are for those compounds that contain carbon group ions (Ge²⁺, Sn²⁺ and Pb²⁺), in which the valence band is an hybridization between the 2p levels of the O²⁻ ions and the s levels of the carbon group ion.

Criterion	One-photon WS	Two-photon WS
Stability (ΔE)	0.2 eV/atom	0.2 eV/atom
Bandgap (E_{gap})	$1.7 \leq E_{\text{gap}} \leq 3$	$1.3 \leq E_{\text{gap}} \leq 3$
Band edges	$\text{VB}_{\text{edge}} > 1.6$	$\text{VB}_{\text{edge}}^{\text{anode}} > 1.6$
($\text{VB}_{\text{edge}}, \text{CB}_{\text{edge}}$)	$\text{CB}_{\text{edge}} < -0.1$	$\text{CB}_{\text{edge}}^{\text{cathode}} < -0.1$
		$\text{CB}_{\text{edge}}^{\text{anode}} < \text{VB}_{\text{edge}}^{\text{cathode}}$

Table 7.2: Screening parameters (in eV) used for the one- and two-photon water splitting devices. The red-ox levels of water with respect to the Normal Hydrogen Electrode (NHE) are 0 and 1.23 eV for the hydrogen and oxygen evolution, respectively. The criterion for the position of the band edges include also the overpotentials for hydrogen (0.1 eV) and for oxygen (0.4 eV).⁶⁸ Silicon is used as cathode in the two-photon water splitting device ($\text{VB}_{\text{edge}}^{\text{Si}} = 0.86$ eV).

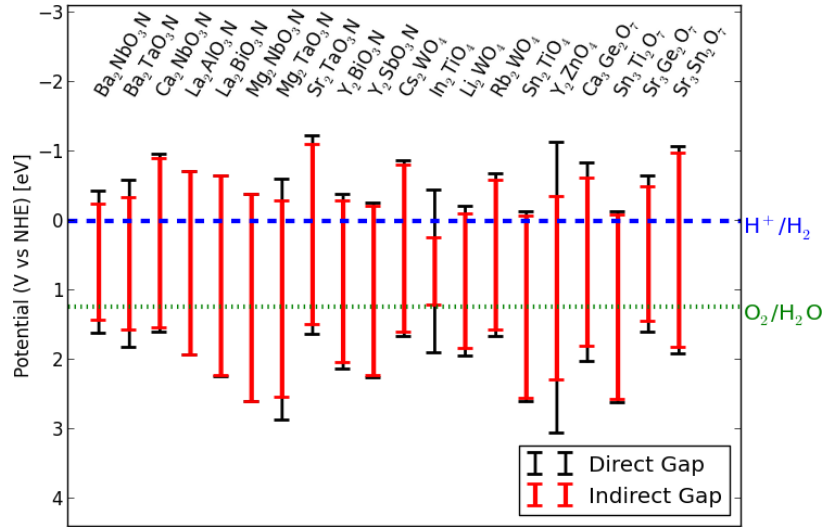


Figure 7.7: The candidates identified for one-photon water splitting. The figure shows the red-ox levels of water and the calculated band edges for the indirect (red) and direct (black) bandgaps.

Few couples of A- and B-ions can be used for both the A_2BO_4 and $\text{A}_3\text{B}_2\text{O}_7$ perovskites. There is a weak trend that correlates the bandgaps to the B-ions and to the thickness of the 2D cubic slab: if the B-ion position is occupied by a p-metal (Ge, and Sn), the gaps decrease with the thickness of the octahedra, while when a d-metal, like Ti, Zr, and Hf, is used as a B-ion, the gaps increase. This can be used to tune the bandgap to the desired region by increasing or reducing the number of octahedra in the structure.

7.4 Candidates in the Layered Perovskite Structure

The screening parameters for the one- and two-photon water splitting device are summarized in Table 7.2. In addition to stability and a bandgap in the visible range, the band edges should straddle the red-ox levels of water plus the required overpotentials to run the reactions (0.1 eV for hydrogen and 0.4 eV for oxygen.⁶⁸ Previously the criterion on the position of the band edges did not consider the overpotentials).

20 materials are identified to be used in the one-photon water splitting device and are shown in Fig. 7.7. $\text{Ba}_2\text{TaO}_3\text{N}$ and $\text{Sr}_3\text{Sn}_2\text{O}_7$ are already known in the layered perovskite

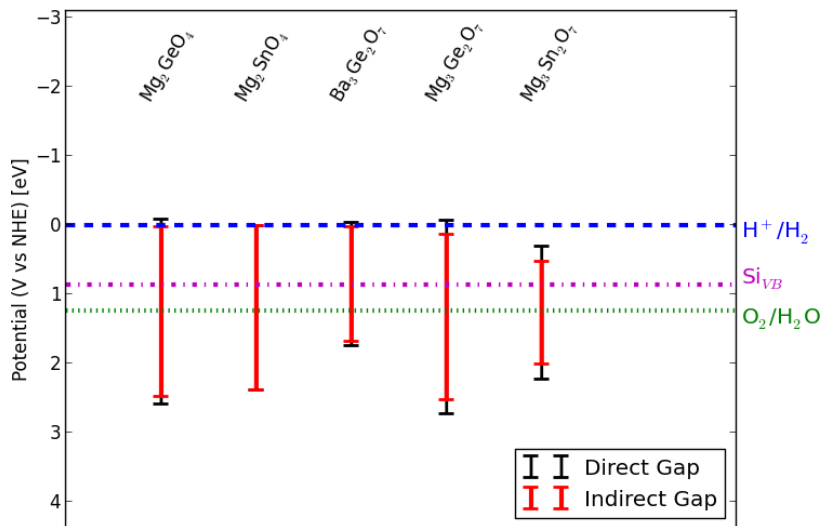


Figure 7.8: The candidates identified for a two-photon water splitting device.

structure. Ba₂TaO₃N has recently been suggested as a water splitting material.⁸³ Some of the proposed materials are experimentally known in other stoichiometries or crystal structures. 8 perovskites are unknown. The oxynitrides seem to be interesting for water splitting. In fact, the cubic perovskites ABO₂N with A = Ba, Sr, and Ca, and B = Ta, and Nb are known in the water splitting community to evolve hydrogen and/or oxygen in presence of sacrificial reagent^{8,70} and the layered perovskites generated by these elements are expected to conserve the good properties in terms of activity already present in the cubic phase.

5 layered perovskites are identified as candidates to split water in the two-photon device in combination with silicon as photocathode (Fig. 7.8) in addition to the ones already proposed for the one-photon mechanism. They are all experimentally known in other structures/stoichiometry, but none of them has been used as photocatalyst so far.

7.5 Summary

The screening procedure has been applied to low symmetry perovskites with focus on the problem of light harvesting and of solar light conversion and on finding general rules for tuning the bandgap. A double perovskite obtained by combining two cubic perovskites with only p- or d-metals in the B-ion positions shows a bandgap close to the average gaps of its constituents. When it is formed by the combination of a p- and a d-metal, its bandgap increases. For the layered perovskite, a p-metal in the B-ion position, generates structures with bandgaps that decrease with the thickness of the 2D slab of cubic perovskite, while a d-metal in the B-position has the effect of opening the gaps with the thickness of the octahedra. The A-ion has only a minor effect on the gaps.

Many low symmetry perovskites are known. A screening of these and other crystal structures will be performed in the future.

Water Splitters from the Materials Project Database

Several databases have been established in the last decade to collect experimental and theoretical results. The Inorganic Crystal Structure Database (ICSD)⁴⁹ contains more than 150000 experimentally known compounds. The Materials Project database¹⁶ and the AflowLib consortium⁸⁴ have collected respectively around 31000 and 17000 materials from DFT simulations.

In this chapter, the GLLB-SC potential has been applied to a subset of the Materials Project database to calculate the bandgaps of known stable compounds. In addition, the screening procedure selects the candidates for one- and two-photon water splitting and transparent shielding of the photocatalysts, as presented for the cubic perovskite structures in Chapter 2 and 3.

This project is carried out in collaboration with Dr. Anubhav Jain and Dr. Kristin Persson (Lawrence Berkeley National Laboratory, Berkeley, California, USA), and Prof. Gerbrand Ceder (Massachusetts Institute of Technology, Cambridge, Massachusetts, USA).

8.1 Bandgap Calculations

So far, the screening for new materials has proceeded by selecting a crystal structure and then by calculating possible combinations of chemical elements that occupy the different sites of the structure. This approach favors the discovery of materials still experimentally unknown. On the other hand, it has the drawback that the candidate can be extremely difficult or impossible to synthesize.

Nature can help in the search for optimal materials. There are hundreds of thousands of known materials, with different stoichiometries, structures, and compositions. A good part of them are collected in databases, like the already cited ICSD.⁴⁹ These databases collect mainly crystal structures while electronic data, like bandgaps and band structures, are not present. It is thus possible to complete the missing information using computational methods and to use the additional pieces of information as descriptors for the screening. The main advantage of this approach is that the potential candidates have already been synthesized, while it excludes the possibility of finding new materials still experimentally unknown. The two methods can be combined in several ways, like using data mining⁷⁸ or genetic algorithms.⁸⁵

Several people have applied *ab-initio* methods to experimental databases, relaxing

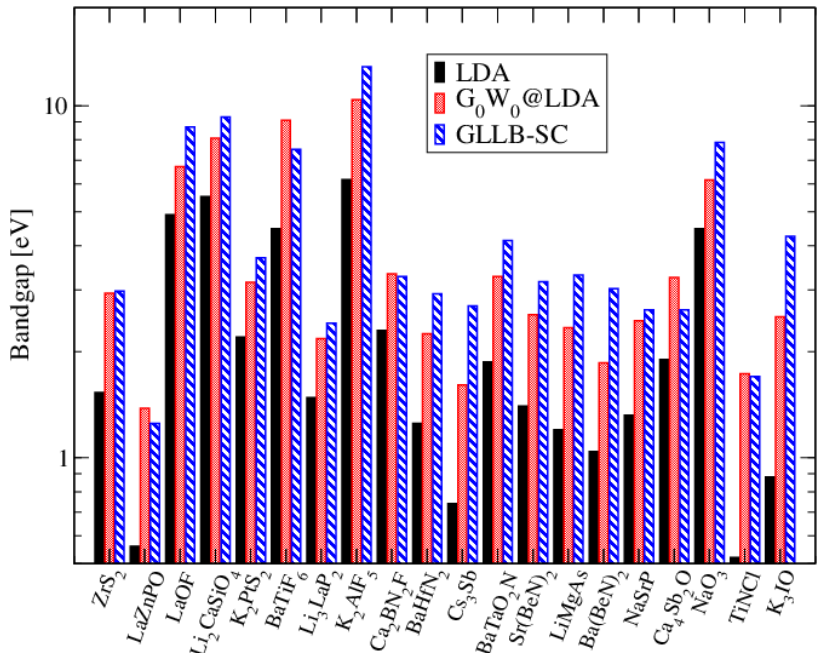


Figure 8.1: Comparison of direct Γ -point bandgaps calculated with LDA (in black), GLLB-SC (in blue) and $G_0W_0@LDA$ (in red). The figure shows a good agreement between the bandgaps calculated with the GLLB-SC functional and the G_0W_0 method.

the structures and afterwards calculating the properties relevant for the screening. Here, the input compounds are provided by the already optimized structures as present in the Materials Project database¹⁶ (where the optimization has been performed using the DFT-code VASP, and PBE and PBE+U as exchange-correlation functional).

As described in Chapter 2, one of the descriptors for designing new absorbers is the size of the bandgap. Thus, the GLLB-SC potential is used to calculate the bandgaps of a subset of the stable* relaxed structures present in the Materials Project database. The positions of the band edges are evaluated using the empirical formula proposed by Butler and Ginley.⁵⁵

8.2 The Calculated Bandgaps

The bandgaps of around 2200 structures are calculated. The gaps range from 0 to 16 eV. All the calculated bandgaps are listed in Appendix A.

The quality of the GLLB-SC bandgaps is tested once more, with respect to the gaps obtained using the $G_0W_0@LDA$ method within the plasmon pole approximation, for 20 materials shown in Fig. 8.1. As shown before for the candidates for one-photon water splitting (Fig. 2.8), the agreement between the bandgaps obtained with the GLLB-SC functional and the G_0W_0 method is good, especially when compared with other methods, like LDA, that seriously underestimates the size of the bandgaps, or Hartree-Fock, where the bandgaps are overestimated. The agreement between GLLB-SC and G_0W_0 is not perfect and the latter is considered more reliable. The mean absolute error, as defined in Eq. 2.6, between the two methods is around 0.9 eV. Because of the wide range of gaps considered, it is more appropriate to look at the relative errors between

*The stability analysis has been made using a linear programming approach and the database might also contain structures that are metastable or that are not stable because of inaccuracy in the calculations.

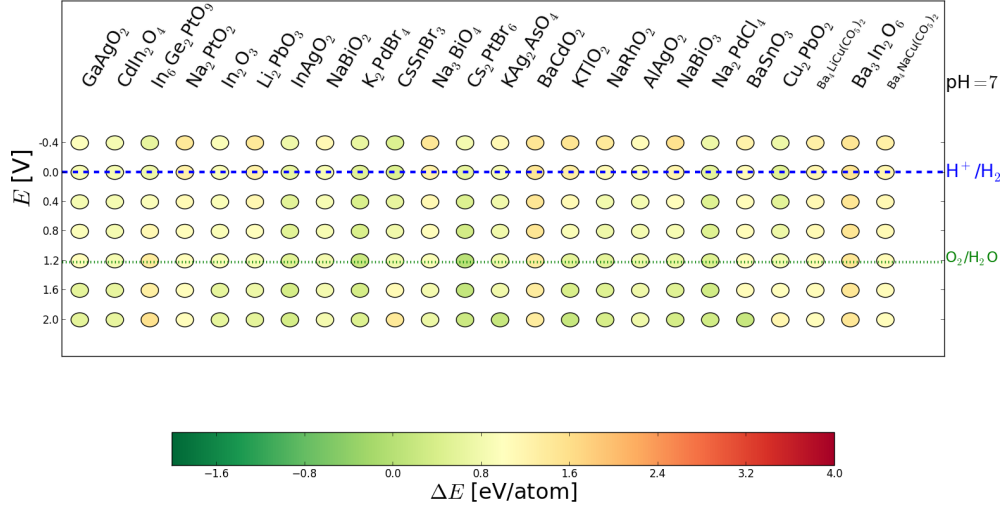


Figure 8.2: The most stable materials with potential for one-photon water splitting. Each colored spot indicates the energy difference between the material and the most stable phases (solid and aqueous) in which it can separate. The stability calculations are performed at pH = 7 and in the potential range where the device has to work.

GLLB-SC and G_0W_0 . The mean relative error[†] is around 0.25. By contrast, the G_0W_0 is, at least, one order of magnitude more computationally expensive than GLLB-SC, making it too costly to be used in a screening project. G_0W_0 can thus be used on selected interesting materials to refine the results.

8.3 Materials for Water Splitting Applications

In this section, different screening criteria will be applied to find materials for water splitting applications. In Chapters 2 and 3, the usefulness of a material was determined based on its stability, and the size and position of the bandgap. Here the stability issue can be neglected since the investigated materials are already experimentally known. Due to the large number of available data/structures, the criteria on the bandgap and on the positions of the band edges can be more strict than the ones used previously. In particular, the overpotentials will now be included among the design criteria. The applications considered are one- and two-photon water splitting and transparent shielding of the photocatalyst.

8.3.1 One-photon Water Splitting

The screening criteria to find new materials for light harvesting and water splitting using one photon are:

- Bandgap: $1.7 \leq E_{\text{gap}} \leq 3.0$ eV;
- Band edges: CB < -0.1 eV and VB > 1.6 eV w.r.t. RHE.

More than one hundred compounds survive to these screening criteria. Thus it is necessary to reduce the number of candidates even more. One possibility is to look at the

[†]The Mean Relative Error (MRE) is defined as:

$$\text{MRE} = \frac{1}{n} \sum_n \left| \frac{E_{\text{gap}}^{\text{GLLB-SC}} - E_{\text{gap}}^{\text{G}_0\text{W}_0}}{E_{\text{gap}}^{\text{G}_0\text{W}_0}} \right|. \quad (8.1)$$

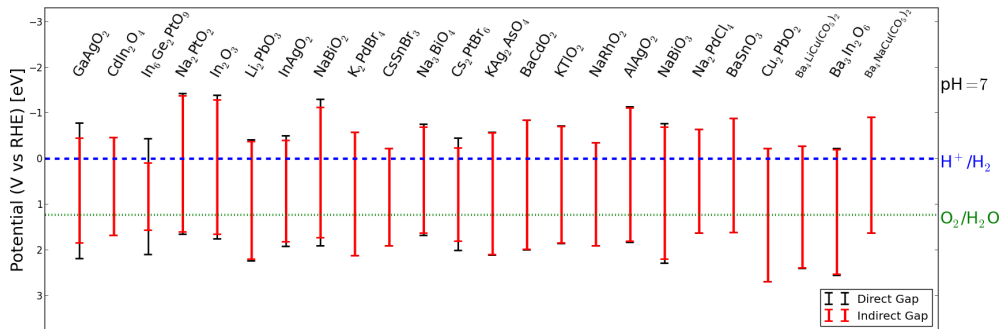


Figure 8.3: The positions of the band edges for the candidates for the one-photon water splitting identified in Fig. 8.2.

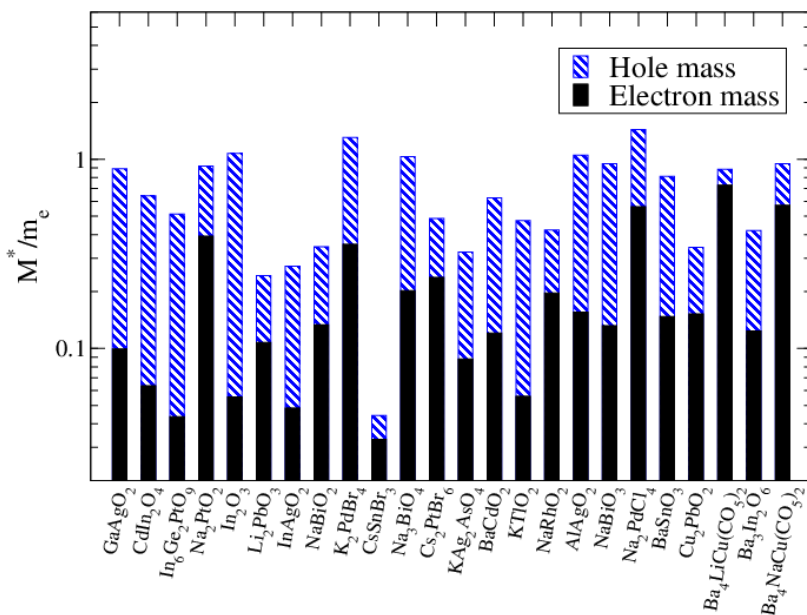


Figure 8.4: Electron and hole masses the candidates for one-photon water splitting, identified in Fig. 8.2.

world global production of the pure chemical species. This might be useful in order to reduce the cost of the device, but might also remove some interesting materials that will become technologically available and cheap in the future. Another possibility is to use Pourbaix diagrams (Chapter 4) to investigate the stability against dissolution of the candidate materials. In fact, the compounds selected by the screening are stable with respect to solid structures, but no information are available regarding their stability against corrosion. It is still a challenge to define the energy threshold below which a material can be considered stable since the Pourbaix diagrams do not include the reaction kinetics but only the thermodynamics of the reactions. No threshold is thus set here, but the materials are ranked depending on their stability and only the best 20/25 are proposed as candidates. The Pourbaix diagrams are calculated in a potential range covering a region where the device has to work (between -0.4 and 2.0 eV) and at $\text{pH} = 7$, which is not harmful to environment and not corrosive.

Fig. 8.2 shows the most stable materials with respect to solid and aqueous substances identified by the screening, and Fig. 8.3 reports the positions of the band edges, for the indirect (in red) and direct bandgap (in black) with respect to the reversible hydrogen

electrode (RHE[‡]). Most of these materials are oxides. This indicates that the oxides have in general a good matching regarding stability, bandgap, and band edge positions. In particular, the Pourbaix analysis has removed most of the bromides, iodides, and chlorides for which it is more energetically favorable to decompose into ions instead of forming the solid compound. BaSnO₃ is the only material that comes out as a candidate both from this screening and from the one of the cubic perovskites (Chapter 2). As mentioned before, BaSnO₃ has been used for water splitting but it does not evolve hydrogen or oxygen because of defect-assisted electron-hole recombination.⁵⁹ The other known material from the cubic perovskite screening is AgNbO₃. It is not included among the candidates of Fig. 8.2 because its CB position does not match with the design criterion that includes the hydrogen overpotential. The other materials have not yet been tested as water splitting photocatalyst.

The mobility of the photogenerated charges is another crucial issue and it can be estimated looking at the hole and electron effective masses (Chapter 2). As shown for the cubic perovskites (Fig. 2.9), the hole masses are heavy because the valence band at the HOMO is almost flat, and, thus, the mobility is expected to be low. This is usually an issue for the device because the electrons and holes might recombine before reaching the surface and splitting water. This is the case, for instance, of hematite (Fe₂O₃) which has optimal bandgap and band edge positions, but a low photo-catalytic activity due to a low hole mobility.⁸⁶ The electrons, on the other hand, are lighter and they seem not to be an issue for the device. In general, the limiting factor is the hole mass rather than the electron mass.

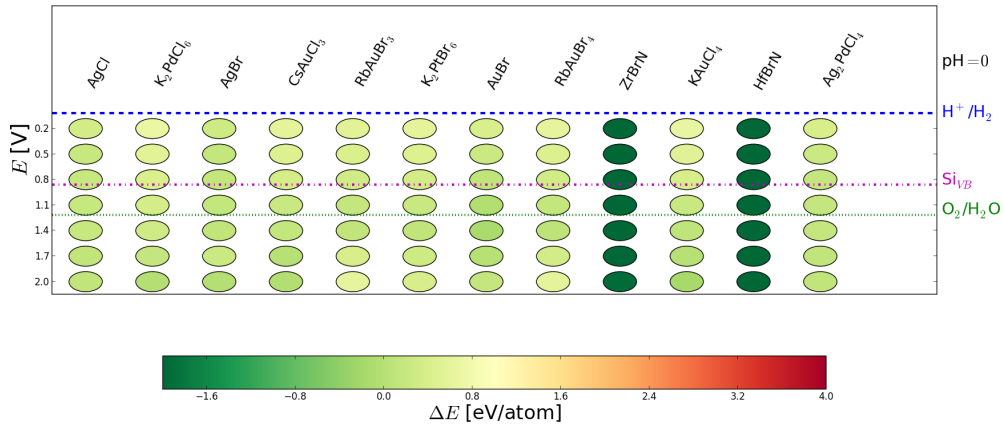
The effective masses of the proposed materials of Fig. 8.3 are shown in Fig. 8.4. The electron masses are in general one order of magnitude smaller than the hole ones. Both the electrons and holes of these compounds are lighter than the ones of the candidates in the cubic perovskite structure. The cubic perovskite might have intrinsically poor mobility. In fact, in the cubic perovskite the valence band is mainly formed by oxygen 2p orbitals with very little hybridization with the A- and B-ions, leading to flat shape of the band and thus to a low electrons and holes mobility. This poor hybridization is due to the highly ionic character of A and B ions since their most favorable oxidation state usually is a closed shell structure. The structures investigated here are different from the cubic perovskite; they might show a less ionic character and a higher degree of hybridization, resulting in less flat bands at the HOMO and LUMO. All the proposed materials have a smaller hole mass compared to hematite, which hole mass is around 1.8 m_e. The hole mobilities might, thus, be high enough to overcome the problems related to recombination present in hematite.

8.3.2 Two-photon Water Splitting

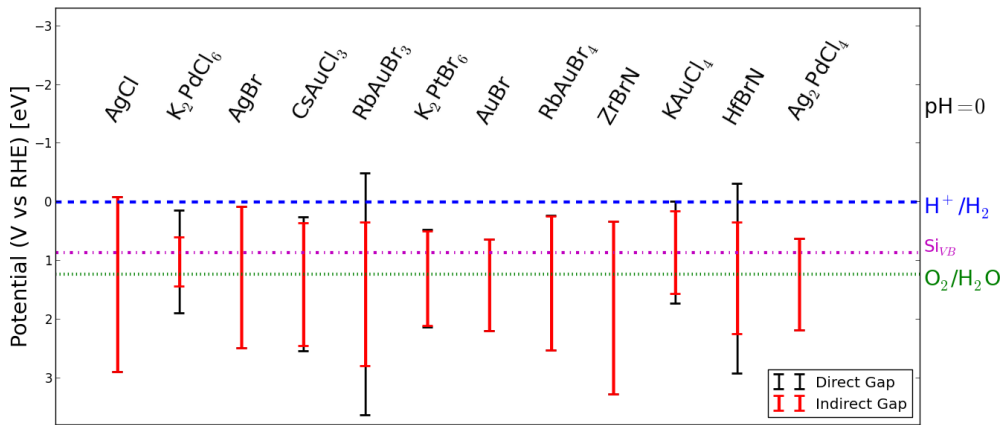
In the more complex two-photon mechanism, two materials with perfect matching of their bandgaps are required. A detailed explanation of the device is available in Chapter 3. The screening looks for an optimal material to combine with silicon, which results in the following requirements:

- Bandgap: $1.3 \leq E_{\text{gap}} \leq 3.0$ eV;
- Band edges: CB < 0.86 eV (corresponding to the VB of silicon) and VB > 1.6 eV w.r.t. RHE.

[‡]The reversible hydrogen electrode (RHE) and the normal hydrogen electrode (NHE) differs because the former includes the effect of the pH in its definition, while the latter is defined at pH = 0. In the previous chapters the effect of the pH was not included, but now, with the calculations of the Pourbaix diagrams, the pH becomes a new variable. Despite of this the red-ox levels of water and the band edges of the material will suffer from the same shift due to a change in the concentration of H⁺-ions. In fact, a change in the pH is followed by a change in the surface dipole in order to keep the $\frac{1}{2}\text{H}_2 \leftrightarrow \text{H}^+ + \text{e}^-$ equilibrium, and so effectively the Fermi level is shifted relative to vacuum. All electronic levels, including the band edges, will respond in the same way to the altered dipole field, and hence the identical shift and the fixed distance between the red-ox levels and the band edges



(a) Two-photon WS, pH = 0 - Stability



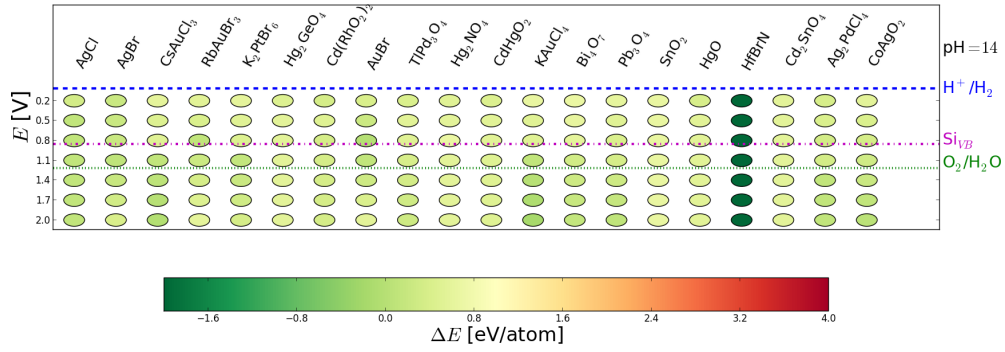
(b) Two-photon WS, pH = 0 - Band Edge Positions

Figure 8.5: The most stable materials to be used in the two-photon water splitting device. (a) Each colored spot indicates the energy difference between the material and the most stable phases (solid and aqueous) in which it can separate. The Pourbaix diagrams are calculated at pH = 0 and for potentials in the working range of the device. (b) Shows the positions of the band edges.

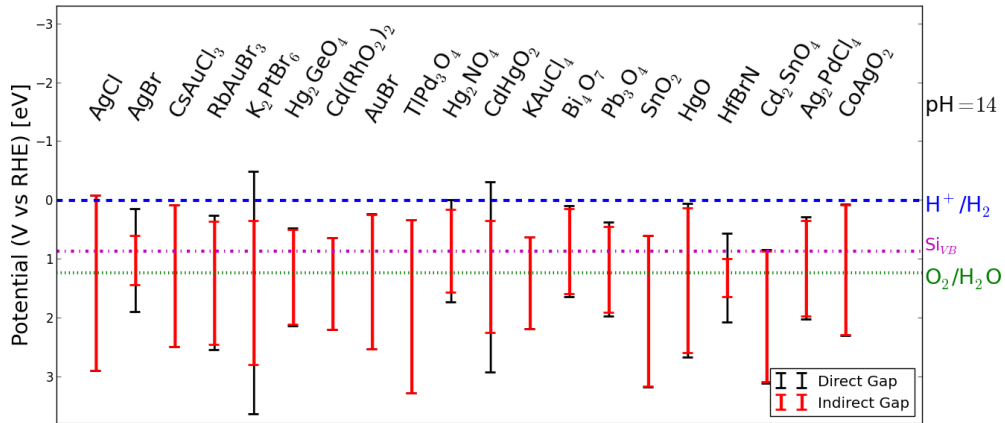
The Pourbaix diagrams of the resulting candidates are calculated for potentials in the working region of the device and at pH = 0 and pH = 14. Acidic conditions are, in fact, required to favor the drift of H^+ from the photoanode to the photocathode where H_2 is produced. Basic conditions can be, instead, used to enhance the movement of OH^- ions.

Fig. 8.5 shows the Pourbaix analysis and the positions of the band edges for the materials with the higher ranking in stability for the two-photon water splitting device under acidic conditions. Under these conditions, the oxides are unstable in water where they dissolve. The bromides, chlorides, and nitrides seem, instead, to be stable. It has been shown that some of the candidates, like $AgCl$ and $AgBr$ dissolve in water, but they can still be used as light harvesters if protected. Other materials, like $AuBr$, exhibit only a low stability in water.

In a basic environment, the oxides become stable. Fig. 8.6 reports the Pourbaix analysis and the band edge positions of the candidates for the two-photon device at pH = 14. A few chlorides, bromides, and nitrides are found promising for the process. Out of these materials, only SnO_2 has been used as photoanode. Recently, it has been used in a multilayer structure with $BiVO_4$ and WO_3 with an efficiency of around 1%.⁸⁷



(a) Two-photon WS, pH = 14 - Stability



(b) Two-photon WS, pH = 14 - Band Edge Positions

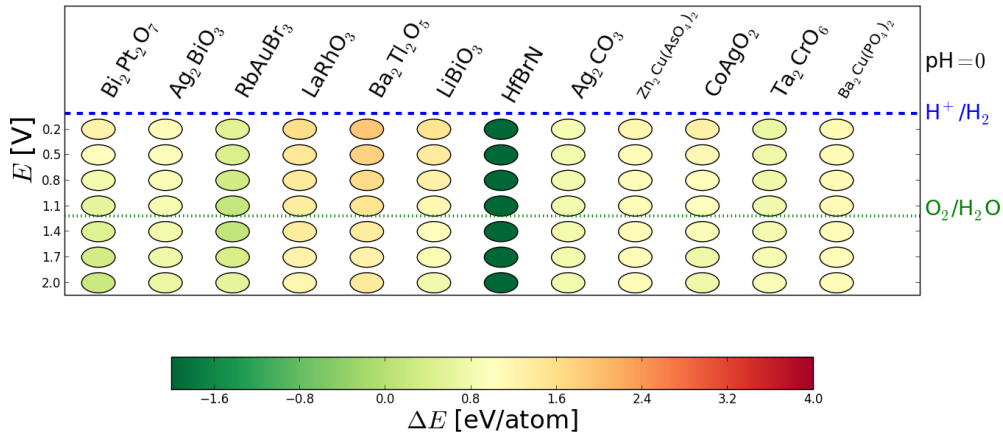
Figure 8.6: The most stable materials to be used in the two-photon water splitting device. (a) Each colored spot indicates the energy difference between the material and the most stable phases (solids and aqueous) in which it can separate. The Pourbaix diagrams are calculated at pH = 14 and for potentials in the working range of the device. (b) Shows the positions of the band edges.

All the materials proposed for the one-photon process can be also used for the two-photon device, but with a loss in efficiency because of the too large bandgap compared to the optimal value of 1.7 eV.

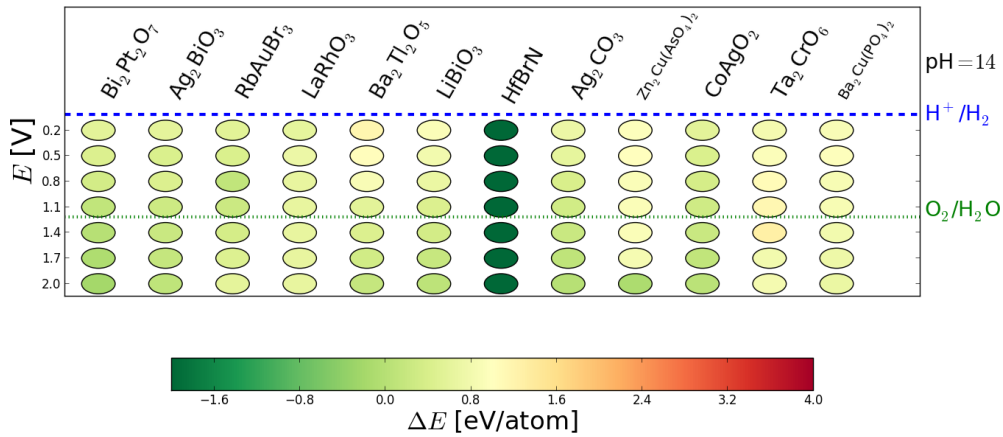
In the two-photon device described so far, the light first illuminates the oxygen evolution photocatalyst where the high-energy part is absorbed. The low-energy light continues to the hydrogen evolution photocatalyst where much of it is absorbed. The situation can be reversed so that the light first hits the hydrogen catalyst (a large bandgap material in this case) and the remaining will partially be absorbed by the oxygen catalyst, with a smaller bandgap. The perfect matching for the size of the bandgaps is still 1.7 and 1.1 eV, as shown in Fig. 3.3. The advantages of this scheme with respect to the one previously described are: (i) there are already successful materials for hydrogen evolution with a bandgap of around 2 eV (the oxynitrides in the cubic perovskite structure,⁸ for example); (ii) a protective layer for the photoanode can now be metallic, since the light is coming from the opposite direction and has already been absorbed by the photocatalyst.

The design criteria for an oxygen evolution photocatalyst that works, for instance, with one of the oxynitrides, can be summarized at:

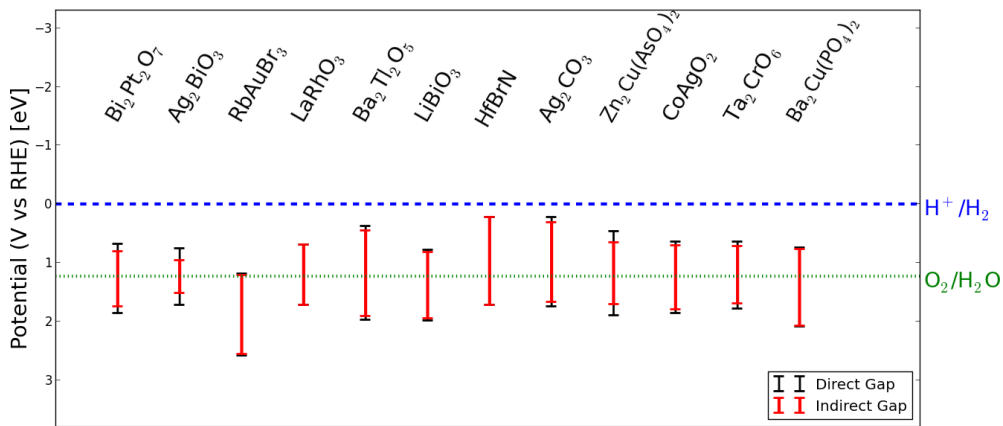
- Bandgap: $0.8 \leq E_{\text{gap}} \leq 1.5$ eV;
- Band edges: CB < 1.2 eV and VB > 1.6 eV w.r.t. RHE.



(a) Two-photon WS, pH = 0 - Stability



(b) Two-photon WS, pH = 14 - Stability



(c) Two-photon WS - Band Edge Positions

Figure 8.7: The most stable materials to be used in the two-photon water splitting device. (a) and (b) Each colored spot indicates the energy difference between the material and the most stable phases (solid and aqueous) in which it can separate. The Pourbaix diagrams are calculated at pH = 0 and pH = 14. The same materials are identified as candidates for the two investigated pH. (c) Shows the positions of the band edges.

The Pourbaix diagrams at pH = 0 and pH = 14 and the positions of the band edges for the identified materials are shown in Fig. 8.7. The identified materials are the same

at both $\text{pH} = 0$ and $\text{pH} = 14$ (Figs. 8.7a and 8.7b, respectively). None of the proposed materials has so far been used for water splitting. This process is optimal for obtaining high efficiency in the case of a large bandgap material used as a photocathode. In addition, a few transparent protecting layers for the photocathode, like TiO_2 ,⁷² have recently been developed. If needed, the protective shield for the photoanode does not have to be a large bandgap semiconductor because the solar radiation has already been absorbed, but it has to be just a highly stable material with activity for oxygen evolution. Silicon can be used for evolving oxygen, with an appropriate pn-doping that shifts its band edges. Silicon, with an appropriate pn-doping that shifts the band edges, can now be used for oxygen evolution.

With this mechanism, a hydrogen evolution photocatalyst should have the following properties:

- Bandgap: $1.4 \leq E_{\text{gap}} \leq 3.0 \text{ eV}$;
- Band edges: $\text{CB} < -0.1 \text{ eV}$ and $\text{VB} > 1.3 \text{ eV}$ w.r.t. RHE.

No materials are found with these parameters and an energy threshold of 0.8 eV/atom once that the Pourbaix analysis is applied.

8.4 Protective Transparent Shield

A transparent protective layer is necessary when the photocatalyst corrodes in presence of water. Here, the two shielding mechanisms described in Chapter 3 are considered together. The screening criteria for the protective layer of the photoanode and photocathode are:

- Photoanode TS:
 - Bandgap: $E_{\text{gap}} > 3.0 \text{ eV}$;
 - Band edges: $1.3 < \text{VB} < 2.0 \text{ eV}$ w.r.t. RHE.
- Photocathode TS:
 - Bandgap: $E_{\text{gap}} > 3.0 \text{ eV}$;
 - Band edges: $-0.4 < \text{CB} < 0.3 \text{ eV}$ w.r.t. RHE.

The Pourbaix diagrams are calculated at $\text{pH} = 0$ and $\text{pH} = 14$ and for potentials in the working region of the device, i.e. covering the window for the criterion on the valence or conduction band. The shield usually has to work under very acidic or basic conditions, needed to enhance the drift of H^+ or OH^- ions. A ranking of the candidates is not enough here, and an energy threshold of 0.5 eV/atom has been set to account for metastability, inaccuracy in the calculations, and reaction kinetics.

No materials are stable for the shielding of the photoanode. If the energy threshold is increased to 0.8 eV/atom, four materials (CsAuO , RbAuO , Rb_2PbO_3 , and Li_4PbO_4) are stable against dissolution at $\text{pH} = 14$, but they all dissolve at $\text{pH} = 0$. The positions of the band edges for the stable materials, at $\text{pH} = 0$, to be used as transparent shielding of the photocathode are shown in Fig. 8.8. Only PbBrF , HgBr , and HgCl are stable at $\text{pH} = 14$. None of the proposed materials has so far been used as a transparent layer. TiO_2 is not in the list because it does not fulfill the criterion on the positions of the band edges. It seems that oxides are more interesting for the shielding of the photoanode, and alogenates are promising for the shielding of the photocathode. In general, a deeper investigation on the (photo-)corrosion problem is necessary and will be performed in the future.

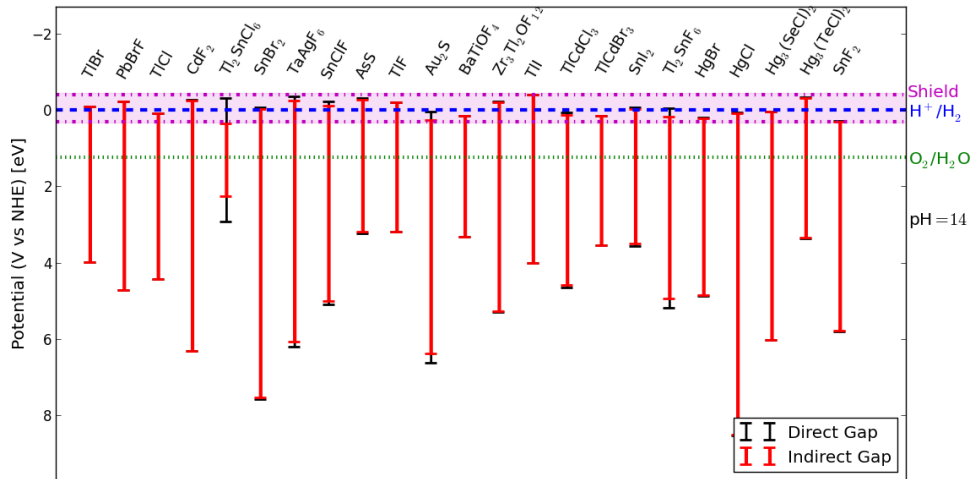


Figure 8.8: The positions of the band edges for the candidates for the transparent shielding of the photocathode at pH = 0.

8.5 Summary

In the present chapter, the focus has been moved from designing new materials to provide the missing information of experimentally known crystals. The bandgaps of around 2200 structures present in the Materials Project database¹⁶ have been calculated using the GLLB-SC potential. For 20 materials, the bandgaps obtained with the GLLB-SC potential and $G_0W_0@LDA$ have been compared and show a reasonable agreement.

The bandgaps can then be combined with a stability analysis based on the calculation of Pourbaix diagrams and with the evaluation of the positions of the band edges to screen for materials to be used for one- and two-photon water splitting and for the transparent shielding of the photocatalysts. In total, around 80 materials have been proposed for the different applications. Stability remains a crucial point for the design and the use of new materials.

This chapter is based on an open project and more structures will be calculated in the future. In addition, a deeper investigation of the present and future technological use of the different materials is required.

Thin Film Solar Cells

Another method to obtain energy directly from Sun is through a photovoltaic cell, that converts solar light into electricity. There are several ways to build such a device: single- and multi- junctions, single- and multi- crystals, thin films and organic cells. The highest efficiency achieved in these days is 44% and was obtained using a three-junction cell.

In the present chapter, new materials for thin film solar cells will be investigated. The main reason to choose a thin film PV cell to a standard PV cell is to reduce the amount of material in the device and thus to reduce the cost. All the materials studied here are already experimentally known and available in the ICSD database.⁴⁹ The structures have been optimized using DFT simulations.¹⁶

The bandgap is again a starting point for selecting interesting materials, but alone it is not a sufficient descriptor for the efficiency of a photovoltaic cell.⁸⁸ There are, in fact, other optical properties, for instance the type of the bandgap (direct or indirect), the shape of the absorption spectrum, and the existence of forbidden transitions, that must be taken into account in evaluating the theoretical efficiency of a cell. Most of these information are available once the absorption spectrum is known. The absorption spectra of around 70 materials with a bandgap between 0.5 and 2.5 eV have been calculated*.

9.1 Theoretical Background

Time-dependent Density Functional Theory (TDDFT) is used to calculate the absorption spectra. In TDDFT, the electronic properties, such as excitation energies and oscillator strengths, are obtained through the density response function, $\chi(\mathbf{r}, \mathbf{r}', \omega)$, which is defined as $\delta n(\mathbf{r}, \omega) = \int d\mathbf{r}' \chi(\mathbf{r}, \mathbf{r}', \omega) \delta V_{\text{ext}}(\mathbf{r}', \omega)$.

With planewave expansion, χ can be written as:

$$\chi(\mathbf{r}, \mathbf{r}', \omega) = \frac{1}{N_q \Omega} \sum_{\mathbf{q}} \sum_{\mathbf{G} \mathbf{G}'}^{BZ} e^{i(\mathbf{q}+\mathbf{G})\cdot\mathbf{r}} \chi_{\mathbf{G} \mathbf{G}'}(\mathbf{q}, \omega) e^{-i(\mathbf{q}+\mathbf{G}')\cdot\mathbf{r}'}, \quad (9.1)$$

where N_q is the number of \mathbf{q} vectors in the Brillouin Zone (BZ), Ω is the volume of the real space unit cell, and \mathbf{G} and \mathbf{G}' are reciprocal lattice vectors.

*The calculations of the absorption spectra are computationally expensive. For this and other reasons, the set of the calculated materials is around half of the amount of the structures of interest for the screening. The missing compounds will be calculated in the future.

For interacting systems, the density response function can be calculated by solving the Dyson-like equation

$$\chi_{\mathbf{G}\mathbf{G}'}(\mathbf{q}, \omega) = \chi_{\mathbf{G}\mathbf{G}'}^0(\mathbf{q}, \omega) + \sum_{\mathbf{G}_1\mathbf{G}_2} \chi_{\mathbf{G}\mathbf{G}_1}^0(\mathbf{q}, \omega) K_{\mathbf{G}_1\mathbf{G}_2}(\mathbf{q}) \chi_{\mathbf{G}_2\mathbf{G}'}(\mathbf{q}, \omega), \quad (9.2)$$

starting from the non-interacting density response function of the Kohn-Sham system, χ^0 , and the electron-electron interactions described by a kernel, K . The off-diagonal terms of $\chi_{\mathbf{G}\mathbf{G}'}^0$ represent the response of the electrons for \mathbf{q} different from the external perturbing field and thus describe the inhomogeneity of the response (local field effect⁸⁹). K can be divided into a Coulomb and an exchange-correlation term:

$$K_{\mathbf{G}_1\mathbf{G}_2}^C(\mathbf{q}) = \frac{4\pi}{|\mathbf{q} + \mathbf{G}_1|^2} \delta_{\mathbf{G}_1\mathbf{G}_2}, \quad (9.3)$$

for the Coulomb part and

$$K_{\mathbf{G}_1\mathbf{G}_2}^{\text{xc-ALDA}}(\mathbf{q}) = \frac{1}{\Omega} \int dr f_{xc}[n(\mathbf{r})] e^{-i(\mathbf{G}_1 - \mathbf{G}_2) \cdot \mathbf{r}}, \quad (9.4)$$

and

$$f_{xc}[n(\mathbf{r})] = \left. \frac{\partial^2 E_{xc}[n]}{\partial n^2} \right|_{n_0(\mathbf{r})} \quad (9.5)$$

for the exchange-correlation (xc) part in the Adiabatic Local Density Approximation (ALDA).

The microscopic dielectric matrix is defined as:

$$\epsilon_{\mathbf{G}\mathbf{G}'}^{-1}(\mathbf{q}, \omega) = \delta_{\mathbf{G}\mathbf{G}'} + \frac{4\pi}{|\mathbf{q} + \mathbf{G}|^2} \chi_{\mathbf{G}\mathbf{G}'}(\mathbf{q}, \omega). \quad (9.6)$$

Many properties like the absorption spectrum and the energy loss spectrum are described by the macroscopic dielectric function:

$$\epsilon_M(\mathbf{q}, \omega) = \frac{1}{\epsilon_{00}^{-1}(\mathbf{q}, \omega)}. \quad (9.7)$$

The absorption spectrum that is used as a descriptor for the efficiency of a thin film cell is given by $\text{Im}\epsilon_M(\mathbf{q} \rightarrow 0, \omega)$. A more detailed description of how the linear response function is defined and implemented in GPAW is provided in Ref.⁹⁰

9.2 Results

A good absorber shall have a bandgap in the visible range. As shown by Shockley and Queisser,⁹¹ the ideal maximum efficiency per photon achievable by a PV device is around 33% and above 10% in a range between 0.5 and 2.5 eV (the maximum efficiency as a function of the bandgap is indicated by the red curve in Fig 9.1). Despite of this, the bandgap is not a sufficient descriptor for the efficiency, since it does not include relevant features of the absorption spectrum. For example, silicon has a bandgap of 1.1 eV, which is perfect to achieve the highest efficiency, but it is an indirect gap semiconductor (with a direct gap of around 3 eV) and, thus, a thick material is required to absorb a relevant part of the solar spectrum since phonons are required to conserve the momentum. An efficiency of only around 1% can be obtained with a silicon thin film of thickness 0.5 μm . Amorphous silicon is used in a thin film cell because of the random orientation of the crystals inside the material and creates phonons that permit the absorption of the indirect transitions. Thick crystal silicon is instead a standard material for conventional solar cells (with a thickness of 5 μm , the theoretical efficiency gets above 32%).

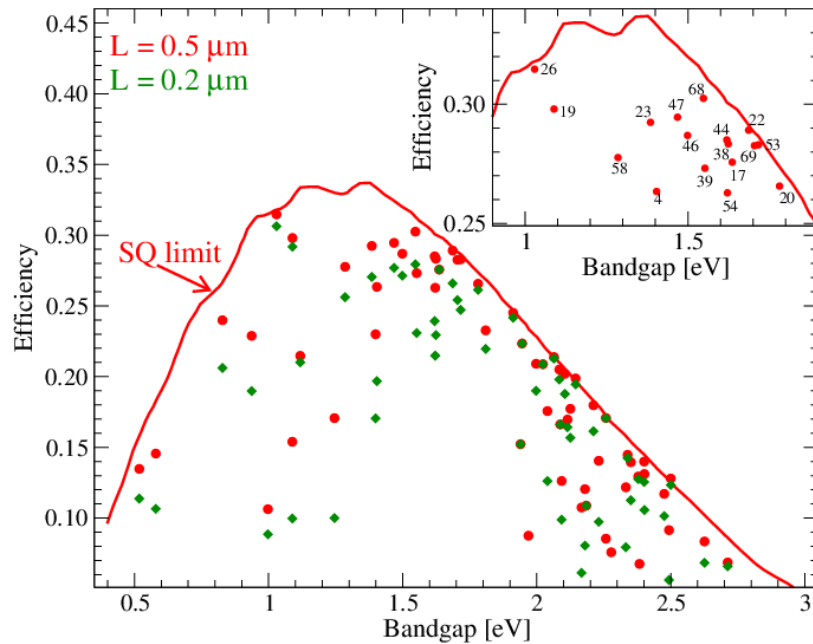


Figure 9.1: Calculated efficiency as a function of the bandgap for a single-layer cell of thickness $L = 0.5\mu\text{m}$ (red circles) and $0.2\mu\text{m}$ (green diamonds). The highest efficiency is around 33% and is obtained with a bandgap of 1.3 eV. The inset shows the materials with an efficiency of more than 25%. The labels correspond to the id of the materials in Table. 9.1. The SQ limit is shown in red.

In the Materials Project database there are several hundreds of materials with bandgaps in the window 0.5 – 2.5 eV. Since the calculation of the absorption spectrum is in general more expensive than the calculation of the bandgap, only the materials formed by cheap and technologically interesting chemical elements have been considered. These elements have a world production of, at least, 33 kton/year and are in the greenish region of Fig. 9.2. This criterion reduces the number of materials to investigate to around 120. The other compounds might be of interest, especially in the case of a thin film cell which does not require much materials. This additional investigation is left for future work. The absorption spectra of around 70 materials have been calculated so far using the ALDA approximation and including the local field effects.

A photovoltaic cell works in a three-step process: (i) absorption of light and generation of electron-hole pairs, (ii) separation of charge carriers, and (iii) extraction of the carriers to an external circuit. The focus here is on property (i), i.e. finding an efficient light absorber. The separation of charges is usually obtained using a pn-doping inside the semiconductor.

The efficiency of a PV device, η , is the ratio between the output power, P_{out} , and the incident solar power, $P_{\text{in}} \approx 1000 \text{ kW/m}^2$:

$$\eta = \frac{P_{\text{out}}}{P_{\text{in}}} . \quad (9.8)$$

The output power is given by the product between the current density and the output voltage (or photovoltage). The current is simply the short current density and the output voltage is the indirect bandgap of the material corresponding to the energy difference between the extracted electron and hole. The losses that occur in a cell are taken into account by looking at the difference between the Shockley-Queisser (SQ) limit without losses (maximum efficiency around 48%) and with. This gives an estimation of the losses as a function of the bandgap that is used to reduce the estimated efficiency

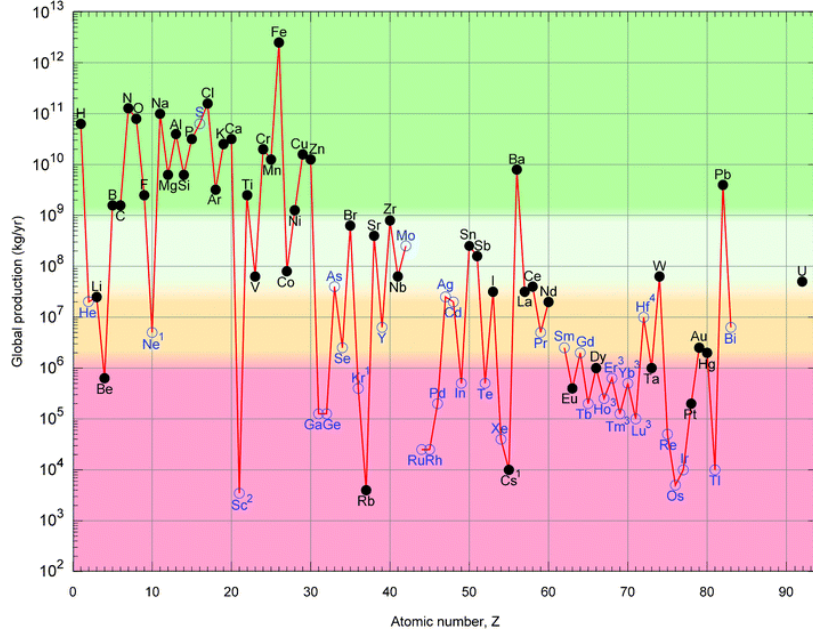


Figure 9.2: World production of the chemical elements in 2010. Solid circles indicate an atom which is a main economic product, while open circles indicates atoms which are by-products of other elements. Figure from Ref. [92].

of each candidate. The short circuit current density, J_{sc} , is given by:

$$J_{sc} = e \int_{E_{gap}}^{\infty} a(E) I_{sun}(E) dE, \quad (9.9)$$

where e is the elementary charge, $a(E)$ is the photon absorptivity, and $I_{sun}(E)$ is the solar photon flux (at standard AM1.5G) and E_{gap} is the bandgap. In a thin film cell, only the photons above the direct bandgap are absorbed since the indirect transitions contribute to the absorption only through phonons which are very weak in a thin film. E_{gap} is thus the direct bandgap. For a thick material, it is assumed that all the photons above the indirect gap are absorbed because the phonons are stronger.

The photon absorptivity depends on the absorption coefficient, $\alpha(E)$, and on the thickness, L , of the absorber:

$$a(E) = 1 - e^{-2\alpha(E)L}. \quad (9.10)$$

$\alpha(E)$ is then obtained from the calculated absorption spectrum:

$$\alpha(E) = \frac{2E}{\hbar c} k(E), \quad (9.11)$$

where c is the speed of light, and $k^2 = \frac{-\epsilon_1 + \sqrt{\epsilon_1^2 + \epsilon_2^2}}{2}$ (ϵ_1 and ϵ_2 are the real and imaginary part of the dielectric constant, respectively).

Fig. 9.1 shows the calculated efficiencies as a function of the bandgaps for a single-layer thin film solar cell of thickness $0.5\mu\text{m}$ (red circles) and $0.2\mu\text{m}$ (green diamonds)[†]. The efficiencies increase with the thickness. 17 materials have an efficiency larger than 25% (shown in the inset and listed in Table 9.1). Crystal silicon has a very weak absorption (efficiency of around 1%), because even though it has the optimal bandgap,

[†]The absorption spectra are calculated for a single unit cell. The thickness enters only in the equation for the photon absorptivity (Eq. 9.10).

Id	Formula	Materials Project Id	Bandgap [eV]	Efficiency
4	Sr(ZnP) ₂	8276	1.4	26.3%
17	ZrCl ₂	23162	1.6	27.6%
19	MnP ₄	487	1.1	29.8%
20	WBr ₆	504993	1.8	26.6%
22	TiBrN	27849	1.7	28.9%
23	MgP ₄	384	1.4	29.2%
26	Cu ₂ O	361	1.0	31.5%
38	Sr ₃ SbN	7752	1.6	28.3%
39	CuP ₂	927	1.6	27.3%
44	ZnSiAs ₂	3595	1.6	28.5%
46	K(MoS) ₃	8116	1.5	28.7%
47	Ba ₂ Cu(PO ₄) ₂	9372	1.5	29.5%
53	KZrCuS ₃	9317	1.7	28.3%
54	BaP ₃	7808	1.6	26.3%
58	TiNb ₃ O ₆	29699	1.3	27.8%
68	K ₂ NiAs ₂	9673	1.5	30.2%
69	TiNCl	27850	1.7	28.3%

Table 9.1: The identified materials to use in a thin film solar cell with an ideal efficiency above 25%. The full list of the calculated materials is included in Appendix B.

its gap is indirect and thus is not used in the thin film technology. Nowadays, silicon seems still to be one of the most convenient material for common photovoltaics with respect to the other materials proposed here. The silicon fabrication technology is mature and the cost of the energy obtained through a solar cell is competitive compared to the energy generated by fossil fuels.

Cu₂O has recently been used with ZnO to form a cheap solar cell with an efficiency of less than 2%;⁹³ MgP₄ and CuP₂ have also been used⁹⁴ and ZnSiAs₂ has been proposed in the late 70s to use with silicon with an efficiency above 23%. None of the other materials listed in Table 9.1 have been used so far in a thin film solar cell.

One of the approximations made is that the output voltage is equal to the indirect bandgap. In a real device, this value is reduced by around 0.5 V. For silicon, the highest output voltage so far obtained is 707 mV,⁹⁵ around 0.4 V lower than its bandgap.

As for the water splitting process, the efficiency of a photovoltaic cell can be increased by combining thin film layers in the so-called tandem cell. The simplest tandem cell is composed of two layers each absorbing a photon. The diagram of a tandem cell is shown in Fig. 9.3. Part of the solar light, coming from the left, is absorbed by the top-cell with a larger bandgap and an electron-hole pair is created. The rest of the light goes through the top-layer, and is partially absorbed by the bottom-cell. Both of the cells are designed using a pn-doping of the semiconductors, so that there is a driving force that moves the electrons and holes in the right place to facilitate their extraction from the cell to the circuit (properties (ii) and (iii) listed above). In fact the electrons need to go from left to right in the figure, and opposite for the holes. The connection between the two cells is usually made by using a tunnel junction. The tunnel junction prevents that the p-doped region of the top cell is directly connected with the n-doped region of the bottom-cell. Without it, the photovoltage would be lower because of the pn-junction with opposite direction to the others would be created in the region of contact.

Since the two cells are connected in series, it is required that the output currents from the two cells are equal and so their mismatch has to be minimized to achieve a high efficiency. In the most favorable case, where the quasi Fermi levels are not included

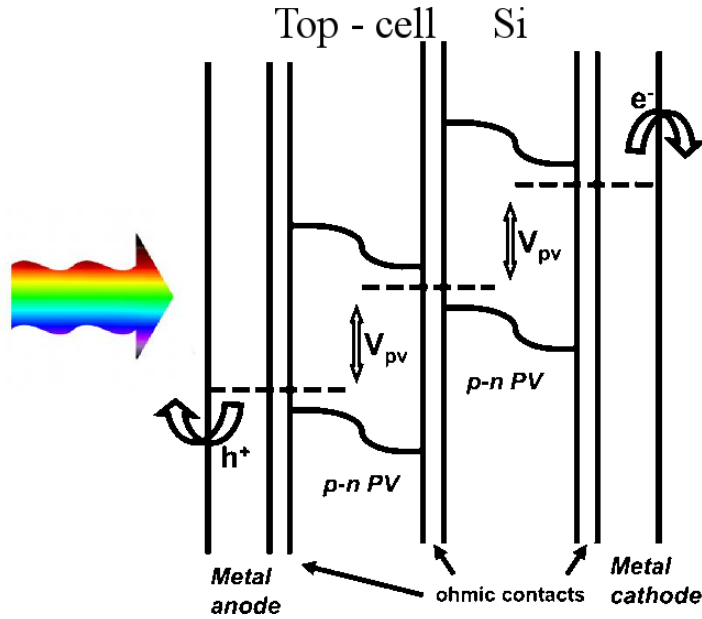


Figure 9.3: Band energy diagram of a tandem photovoltaic cell. Silicon is the bottom-cell. Figure adapted from Ref. [45].

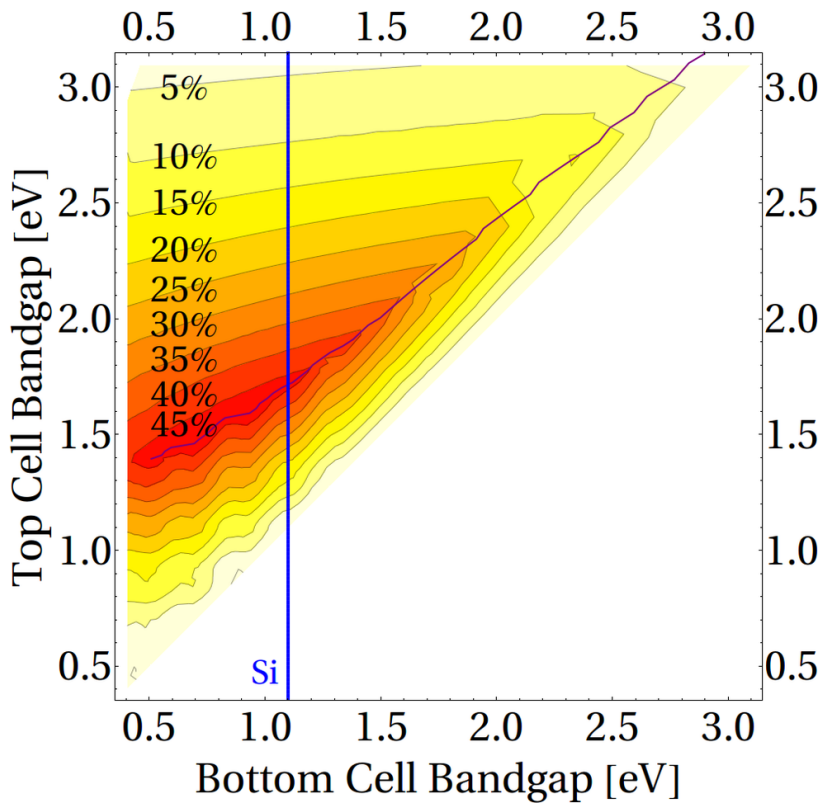


Figure 9.4: Theoretical efficiency of the tandem cell in a thin film device using the spectral distribution of the solar photon flux at AM1.5G. The purple line corresponds to the highest efficiency achievable once the bottom cell is chosen. The blue line corresponds to the experimental bandgap of silicon. The numbers in the contour plot indicate the ideal efficiency.

in the calculation of the efficiency, the output voltage is simply the sum of the two bandgaps, where the correct level alignment can be pursued by means of an appropriate pn-doping. In a tandem cell, the output current is lower than in a single-layer cell but the photovoltage is higher and the maximum theoretical efficiency can overcome 45%, as shown in Fig. 9.4. Several semiconductors can then be grown together to form a multi-layered cell. The ideal maximum efficiency increases with the number of layers (46% for two, 52% for three, 55% for four layers,⁹⁶ and up to 68% in the ideal case of infinity-layer cell⁹⁷).

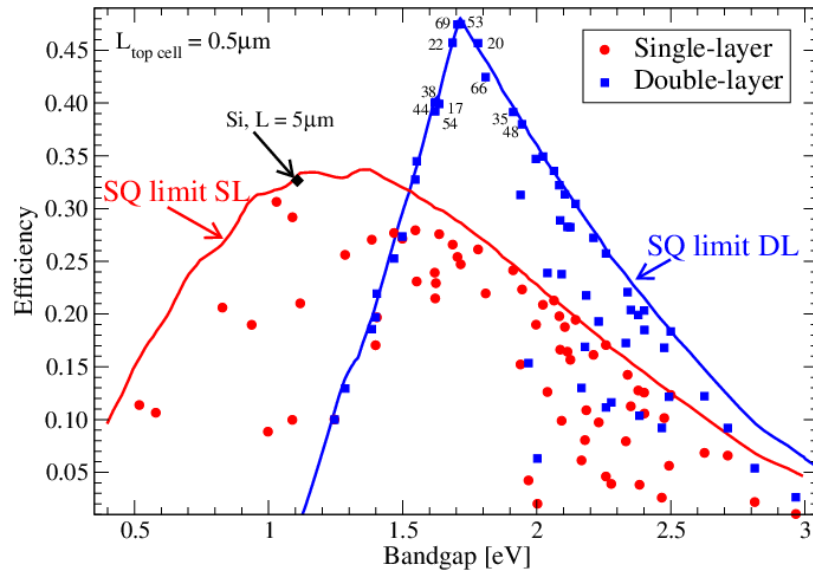


Figure 9.5: Efficiency as a function of the bandgap for the single- (red circles) and double-layer cell (blue squares). The thickness of the candidate layer is $0.5\mu\text{m}$, and the one of the bottom layer of silicon is $5\mu\text{m}$. The efficiency of a single-layer of silicon with thickness of $5\mu\text{m}$ is indicated with a black diamond. The SQ limits for the single- (SL, in red) and double-layer (DL, in blue) are drawn too. The labels correspond to the id of the materials in Table. 9.2.

Id	Formula	Materials Project Id	Bandgap [eV]	Efficiency	
				Single-layer	Double-layer
17	ZrCl ₂	23162	1.6	27.6%	39.9%
20	WBr ₆	504993	1.8	26.6%	45.7%
22	TiBrN	27849	1.7	28.9%	45.7%
35	K ₂ P ₃	8262	1.9	24.5%	39.1%
38	Sr ₃ SbN	7752	1.6	28.3%	40.1%
44	ZnSiAs ₂	3595	1.6	28.5%	40.0%
48	NaSbS ₂	5414	1.9	15.4%	38.0%
53	KZrCuS ₃	9317	1.7	28.3%	47.5%
54	BaP ₃	7808	1.6	26.3%	39.2%
66	SnS	2231	1.8	23.3%	42.5%
69	TiNCl	27850	1.7	28.3%	47.5%

Table 9.2: The identified materials to use in a thin film solar cell with an ideal efficiency above 35%. The full list of the calculated materials is included in Appendix B.

In the present chapter, only the case of two layers is considered. A thick layer of silicon (thickness equal to $5\mu\text{m}$) is one of the best semiconductor to use as a bottom

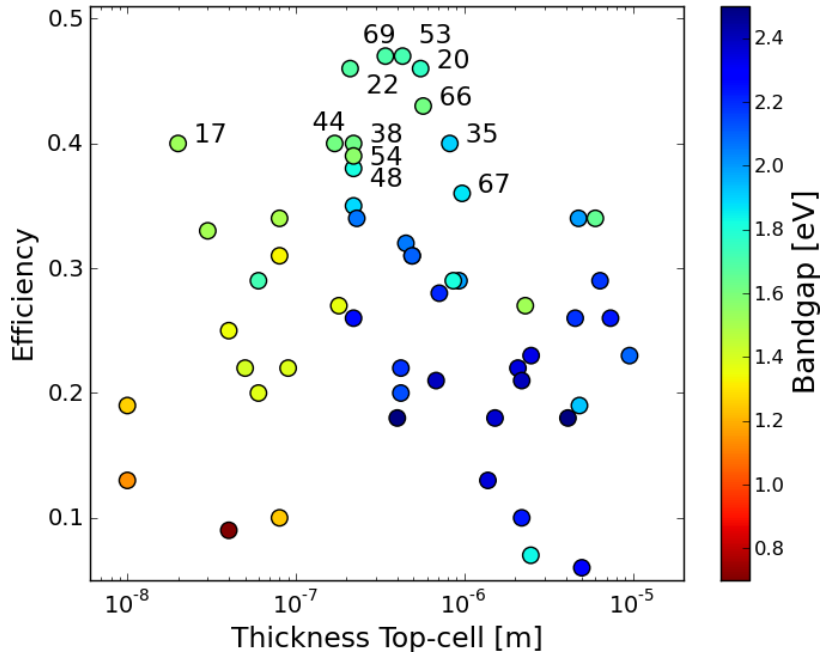


Figure 9.6: Efficiency as a function of the thickness of the top-cell. The bottom-cell is composed of a layer of $5\mu\text{m}$ of silicon. The color of the dots indicates the size of the bandgap. The ids of the materials with an efficiency larger than 35% are indicated.

cell for the same reasons as in a two-photon water splitting device, namely because of the optimal bandgap and the advanced fabrication technology. The screening searches for the optimal material to use as the top cell, with a thickness of $0.5\mu\text{m}$.

Fig. 9.5 shows the efficiencies for the double-layer cell (the ones for the single-layer are also indicated for completeness). 11 materials have an efficiency of more than 35%. The best performances are obtained from materials with a bandgap of around 1.7 eV. 4 compounds (WBr₆ (indicated by the id 20 in the figure), TiBrN(22), KZrCuS₃ (53), and TiNCl(69)) have an efficiency of more than 35%. As in the case of a single-layer, the real output voltage achievable is lowered by around 0.4 V per semiconductor, and, thus, the efficiency will be reduced.

Apart from the already mentioned ZnSiAs₂,⁹⁸ SnS has already been used in a one-layer thin film solar cell with an conversion efficiency of 1.3%.⁹⁹ Except ZnSiAs₂ that has been used in a layer with silicon, none of the other proposed materials has been used in a tandem cell. Some of the problems related to these materials might be the possibility of an efficient pn-doping to enhance the charge separation, the presence of defects in the crystal, and a fast recombination of the generated electrons and holes. All these issues have not been investigated here.

As described before, the theoretical output power of a multi-layer cell is given as the product of the sum of the bandgaps with the minimum output current. The excess current produced by one or more semiconductors is thus wasted. The photon absorptivity (Eq. 9.10), can be tuned by optimizing the thickness of the top-cell to pursuit the highest possible efficiency. Due to the indirect bandgap of silicon, it is not possible to optimize its thickness since the absorption spectrum does not take into consideration the phonon contributions to the absorption. The thickness of silicon is $5\mu\text{m}$, when all the photons above the indirect bandgap are absorbed.

Fig. 9.6 shows the efficiency as a function of the thickness for the considered materials. The bandgaps are indicated by the color of the dots. 12 materials have an efficiency of more than 35% (11 are the same of Table 9.2, and Sr₃P₄). 4 of them have

the highest achievable efficiency for a thickness of more than $0.5\mu\text{m}$ used in Fig. 9.5. The thickness of the others can be reduced with respect to $0.5\mu\text{m}$ because of the high absorption properties. The reduction of the thickness is directly related to a lower cost in the production of the cell.

9.3 Summary

The absorption spectra of 70 potential materials for applications as thin film solar cells have been investigated. 17 compounds have been proposed to be used in a single-layer solar cell, and 11 have potential to achieve high efficiencies when used in a double-layer device with silicon. The possibility of reducing the cost of the cell by an optimization of the thickness of the top-cell has been investigated.

In the future, the absorption spectra of the other structures available from the Materials Project database will be calculated. A more detailed investigation of the different technological applications for the studied materials will be also performed.

Final Remarks

In this work, 23000 materials have been screened for water splitting applications: 2000 in their experimental crystal structure and other 21000 in their *potential* structure (cubic, double, and layered). The criteria determining the usefulness of a material have been based on stability, size of the bandgap and positions of the band edges. A compound has been considered stable looking at the possible experimental materials in which it could decompose. The bandgap evaluation has been performed using the GLLB-SC potential that gives reliable results for bandgaps at a low computational cost. The band edge positions have been calculated using an empirical formula. The problem of corrosion has been studied using Pourbaix diagrams and combining DFT with experimental information.

The screening has been able to identify the already known compounds used for one- and two-photon water splitting. In particular, for the cubic perovskite structure, 20 materials (of which 7 are already known) have been proposed for the one-photon device, and 12 (4 are known) for the two-photon mechanism. The problem of finding new materials for transparent shielding of the photocatalyst has been addressed. The cubic perovskite has also been the test ground for an evolutionary algorithm in order to investigate which are the most important parameters to obtain the best performance from the algorithm. The performance has been defined as the number of simulations needed to find all (or a subset) of the identified candidates. A good elitism and fitness functions are fundamental to get the highest performances from the algorithm.

Low symmetry perovskites, like double and layered perovskite, have been studied with focus on how to tune the bandgap. For the double perovskites, the bandgaps can be tuned by an opportune combination of the metal atoms in the B-ion position, and for the layered structure, by the B-metal ion and the thickness of the octahedra.

One of the limitations of this study is the focus on few crystal structures. However, this has been partially overcome by considering already experimentally known materials from the Materials Project database. The descriptors used in the screening are stability with respect to solid and aqueous substances, calculated using the Pourbaix diagrams, bandgap size and position. Considering all the different applications, around 150 materials have been proposed for further theoretical and experimental investigation.

A photoelectrochemical cell is promising for the future. Nowadays, photovoltaics is the standard technology for solar cell. The problem of finding new materials for thin film solar cells has also been addressed calculating the absorption spectra of 70 relevant compounds. 17 materials have potential to be used in a single-layer device, 11 in a more complex double-layer cell.

A good part of the data used for this thesis is available in the Computational Materials Repository. It is, in fact, crucial to have a fast and an easy sharing of the data to contribute to a development of new technologies.

In future work it would be natural to combine the approach proposed here with struc-

Final Remarks

ture prediction tools to widen the scope of the materials search even further. There are, in fact, many low symmetry structures that can be investigated for the different applications. The layered perovskite, in particular, seems to be a very promising structure because of the possibility of combining different layers to obtain the desired properties.

Other aspects will be investigated in more details. For instance, the evaluation of the band edge positions can be done with more sophisticated methods than using an empirical formula. The role of the mobility of electrons and holes can also be studied more in details. The crucial descriptor remains the stability: a more deep investigation of the corrosion and photocorrosion problem will be performed.

Bibliography

- ¹ The World Bank - Working for a World Free of Poverty, <http://www.worldbank.org/>.
- ² N. Lewis and D. Nocera, *Proceedings of the National Academy of Sciences*, 15729 (2006).
- ³ A. Kudo and Y. Miseki, *Chemical Society Reviews* **38**, 253 (2009).
- ⁴ X. Chen, S. Shen, L. Guo, and S. S. Mao, *Chemical Reviews* **110**, 6503 (2010).
- ⁵ A. Fujishima and K. Honda, *Nature* **238**, 37 (1972).
- ⁶ K. Maeda, K. Teramura, D. Lu, T. Takata, N. Saito, Y. Inoue, and K. Domen, *Nature* **440**, 295 (2006).
- ⁷ H. Kato, H. Kobayashi, and A. Kudo, *The Journal of Physical Chemistry B* **106**, 12441 (2002).
- ⁸ D. Yamasita, T. Takata, M. Hara, J. Kondo, and K. Domen, *Solid State Ionics* **172**, 591 (2004).
- ⁹ A. Franceschetti and A. Zunger, *Nature* **402**, 60 (1999).
- ¹⁰ G. Ceder, Y. M. Chiang, D. R. Sadoway, M. K. Aydinol, Y-I. Jang, and B. Huang, *Nature* **392**, 694 (1998).
- ¹¹ G. H. Johannesson, T. Bligaard, A. V. Ruban, H. L. Skriver, K. W. Jacobsen, and J. K. Nørskov, *Physical Review Letters* **88**, 255506 (2002).
- ¹² R. Armiento, B. Kozinsky, M. Fornari, and G. Ceder, *Physical Review B* **84**, 014103 (2011).
- ¹³ W. Setyawan, R. M. Gaume, S. Lam, R. S. Feigelson, and S. Curtarolo, *ACS Combinatorial Science* **13**, 382 (2011).
- ¹⁴ N. M. O'Boyle, C. M. Campbell, and G. R. Hutchison, *Journal of Physical Chemistry C* **115**, 16200 (2011).
- ¹⁵ J. Hachmann, R. Olivares-Amaya, S. Atahan-Evrenk, C. Amador-Bedolla, R. S. Sanchez-Carrera, A. Gold-Parker, L. Vogt, A. M. Brockway, and A. Aspuru-Guzik, *The Journal of Physical Chemistry Letters* **2**, 2241 (2011).
- ¹⁶ Materials Project - A Materials Genome Approach, <http://materialsproject.org/>.

- ¹⁷ G. Grosso and G. P. Parravicini, *Solid state physics*, Academic Press, San Diego, CA, 2000.
- ¹⁸ V. Fock, *Zeitschrift für Physik* **61**, 126 (1930).
- ¹⁹ C. D. Sherrill and H. F. Schaefer III, *The configuration interaction method: Advances in highly correlated approaches*, volume 34 of *Advances in Quantum Chemistry*, pages 143 – 269, Academic Press, 1999.
- ²⁰ W. L. McMillan, *Physical Review* **138**, A442 (1965).
- ²¹ H. Ehrenreich and M. H. Cohen, *Physical Review* **115**, 786 (1959).
- ²² L. Hedin, *Physical Review* **139**, A796 (1965).
- ²³ P. Hohenberg and W. Kohn, *Physical Review* **136**, 864 (1964).
- ²⁴ W. Kohn and L. J. Sham, *Physical Review* **140**, 1133 (1965).
- ²⁵ J. P. Perdew, J. A. Chevary, S. H. Vosko, K. A. Jackson, M. R. Pederson, D. J. Singh, and C. Fiolhais, *Physical Review B* **46**, 6671 (1992).
- ²⁶ J. P. Perdew, K. Burke, and M. Ernzerhof, *Physical Review Letters* **77**, 3865 (1996).
- ²⁷ B. Hammer, L. B. Hansen, and J. K. Nørskov, *Physical Review B* **59**, 7413 (1999).
- ²⁸ J. F. Janak, *Physical Review B* **18**, 7165 (1978).
- ²⁹ M. Levy, J. P. Perdew, and V. Sahni, *Physical Review A* **30**, 2745 (1984).
- ³⁰ R. W. Godby, M. Schlüter, and L. J. Sham, *Physical Review Letters* **56**, 2415 (1986).
- ³¹ K. Kim and K. D. Jordan, *The Journal of Physical Chemistry* **98**, 10089 (1994).
- ³² J. Heyd, G. E. Scuseria, and M. Ernzerhof, *The Journal of Chemical Physics* **118**, 8207 (2003).
- ³³ J. P. Perdew, R. G. Parr, M. Levy, and J. L. Balduz, *Physical Review Letters* **49**, 1691 (1982).
- ³⁴ E. Gross and R. Dreizler, *Density Functional Theory*, Springer, 1995.
- ³⁵ O. Gritsenko, R. van Leeuwen, E. van Lenthe, and E. J. Baerends, *Physical Review A* **51**, 1944 (1995).
- ³⁶ J. D. Talman and W. F. Shadwick, *Physical Review A* **14**, 36 (1976).
- ³⁷ T. Fukazawa and H. Akai, *Journal of Physics: Condensed Matter* **22**, 405501 (2010).
- ³⁸ J. Krieger, Y. Li, and G. Iafate, *Physics Letters A* **146**, 256 (1990).
- ³⁹ A. D. Becke, *Physical Review A* **38**, 3098 (1988).
- ⁴⁰ M. Kuisma, J. Ojanen, J. Enkovaara, and T. T. Rantala, *Physical Review B* **82**, 115106 (2010).
- ⁴¹ J. P. Perdew, A. Ruzsinszky, G. I. Csonka, O. A. Vydrov, G. E. Scuseria, L. A. Constantin, X. Zhou, and K. Burke, *Physical Review Letters* **100**, 136406 (2008).
- ⁴² J. Yan, K. W. Jacobsen, and K. S. Thygesen, *Physical Review B* **86**, 045208 (2012).
- ⁴³ J. J. Mortensen, L. B. Hansen, and K. W. Jacobsen, *Physical Review B* **71**, 35109 (2005).

- ⁴⁴ J. Enkovaara, C. Rostgaard, J. J. Mortensen, J. Chen, M. Dulak, L. Ferrighi, J. Gavnholt, C. Glinsvad, V. Haikola, H. A. Hansen, H. H. Kristoffersen, M. Kuisma, A. H. Larsen, L. Lehtovaara, M. Ljungberg, O. Lopez-Acevedo, P. G. Moses, J. Ojanen, T. Olsen, V. Petzold, N. A. Romero, J. Stausholm-Møller, M. Strange, G. A. Tritsarlis, M. Vanin, M. Walter, B. Hammer, H. Hakkinen, G. K. H. Madsen, R. M. Nieminen, J. K. Nørskov, M. Puska, T. T. Rantala, J. Schiøtz, K. S. Thygesen, and K. W. Jacobsen, *Journal of Physics Condensed Matter* **22**, 253202 (2010).
- ⁴⁵ M. G. Walter, E. L. Warren, J. R. McKone, S. W. Boettcher, Q. Mi, E. A. Santori, and N. S. Lewis, *Chemical reviews* **110**, 6446 (2010).
- ⁴⁶ M. R. Weber and M. J. Dignam, *Int. J. Hydrogen Energy* **11**, 225 (1986).
- ⁴⁷ G. D. Garbulsky and G. Ceder, *Physical Review B* **51**, 67 (1995).
- ⁴⁸ V. Ozolins, E. H. Majzoub, and C. Wolverton, *Journal of the American Chemical Society* **131**, 230 (2009).
- ⁴⁹ ICSDWeb, http://www.fiz-karlsruhe.de/icsd_web.html.
- ⁵⁰ F. Dionigi, P. C. K. Vesborg, T. Pedersen, O. Hansen, S. Dahl, A. Xiong, K. Maeda, K. Domen, and I. Chorkendorff, *Energy Environ. Sci.* **4**, 2937 (2011).
- ⁵¹ K. Honkala, A. Hellman, I. N. Remediakis, A. Logadottir, A. Carlsson, S. Dahl, C. H. Christensen, and J. K. Nørskov, *Science* **307**, 555 (2005).
- ⁵² F. Hüser, T. Olsen, and K. S. Thygesen, *PrePrint* (2013).
- ⁵³ Y. Wu, M. K. Y. Chan, and G. Ceder, *Physical Review B* **83**, 235301 (2011).
- ⁵⁴ P. G. Moses and C. G. Van de Walle, *Applied Physics Letters* **96**, 021908 (2010).
- ⁵⁵ M. A. Butler and D. S. Ginley, *Journal of The Electrochemical Society* **125**, 228 (1978).
- ⁵⁶ Y. Xu and M. A. Schoonen, *American Mineralogist* **85**, 543 (2000).
- ⁵⁷ T. Ishihara, *Perovskite Oxide for Solid Oxide Fuel Cells*, Springer Verlag, 2009.
- ⁵⁸ R. Aguiar, D. Logvinovich, A. Weidenkaff, A. Rachel, A. Reller, and S. G. Ebbinghaus, *Dyes and Pigments* **76**, 70 (2008).
- ⁵⁹ W. Zhang, J. Tang, and J. Ye, *Journal of Materials Research* **22**, 1859 (2007).
- ⁶⁰ K. Nukumizu, J. Nunoshige, T. Takata, J. N. Kondo, M. Hara, H. Kobayashi, and K. Domen, *Chemistry Letters* **32**, 196 (2003).
- ⁶¹ M. Liu, W. You, Z. Lei, T. Takata, K. Domen, and C. Li, *Chinese Journal of Catalysis* **27**, 556 (2006).
- ⁶² R. W. Godby and R. J. Needs, *Physical Review Letters* **62**, 1169 (1989).
- ⁶³ D. D. Landis, J. S. Hummelshøj, S. Nestorov, J. Greeley, M. Dulak, T. Bligaard, J. K. Nørskov, and K. W. Jacobsen, *Computing in Science and Engineering* **14**, 51 (2012).
- ⁶⁴ Computational Materials Repository, <https://wiki.fysik.dtu.dk/cmr/> (Documentation) and <https://cmr.fysik.dtu.dk/> (Database).
- ⁶⁵ L. Duan, L. Tong, Y. Xu, and L. Sun, *Energy Environ. Sci.* **4**, 3296 (2011).
- ⁶⁶ M. Grätzel, *Nature* **414**, 338 (2001).

- ⁶⁷ M. Grätzel, *Chemistry Letters* **34**, 8 (2005).
- ⁶⁸ S. Trasatti, *Croat. Chem. Acta* **63**, 313 (1990).
- ⁶⁹ Y. Hou, B. L. Abrams, P. C. K. Vesborg, M. E. Björketun, K. Herbst, L. Bech, A. M. Setti, C. D. Damsgaard, T. Pedersen, O. Hansen, J. Rossmeisl, S. Dahl, J. K. Nørskov, and I. Chorkendorff, *Nature Materials* **10**, 434 (2011).
- ⁷⁰ B. Siritanaratkul, K. Maeda, T. Hisatomi, and K. Domen, *ChemSusChem* **4**, 74 (2011).
- ⁷¹ Y. W. Chen, J. D. Prange, S. Dühnen, Y. Park, M. Gunji, C. E. D. Chidsey, and P. C. McIntyre, *Nature Materials* **10**, 539 (2011).
- ⁷² B. Seger, A. B. Laursen, P. C. K. Vesborg, T. Pedersen, O. Hansen, S. Dahl, and I. Chorkendorff, *Angewandte Chemie International Edition* **51**, 9128 (2012).
- ⁷³ E. D. Verink, *Simplified Procedure for Constructing Pourbaix Diagrams*, pages 93–101, John Wiley & Sons, Inc., 2011.
- ⁷⁴ J. W. Johnson, E. H. Oelkers, and H. C. Helgeson, *Computers & Geosciences* **18**, 899 (1992).
- ⁷⁵ M. Pourbaix, *Atlas of electrochemical equilibria in aqueous solutions*, Number v. 1 in Atlas of Electrochemical Equilibria in Aqueous Solutions, Pergamon Press, 1966.
- ⁷⁶ K. A. Persson, B. Waldwick, P. Lazic, and G. Ceder, *Physical Review B* **85**, 235438 (2012).
- ⁷⁷ F. Dionigi, P. C. K. Vesborg, T. Pedersen, O. Hansen, S. Dahl, A. Xiong, K. Maeda, K. Domen, and I. Chorkendorff, *Journal of Catalysis* **292**, 26 (2012).
- ⁷⁸ G. Hautier, C. C. Fischer, A. Jain, T. Mueller, and G. Ceder, *Chemistry of Materials* **22**, 3762 (2010).
- ⁷⁹ I. Wolfram Research, Mathematica edition: Version 8.0, 2010.
- ⁸⁰ A. Collins, C. C. Wilson, and C. J. Gilmore, *CrystEngComm* **12**, 810 (2010).
- ⁸¹ K.-I. Kobayashi, T. Kimura, H. Sawada, K. Terakura, and Y. Tokura, *Nature* **395**, 677 (1998).
- ⁸² A. G. Piken and W. Van Gool, Ewald Program v1.1 (v3.4 modified by J A Aramburu) (1968).
- ⁸³ Y. Wu, P. Lazic, G. Hautier, K. Persson, and G. Ceder, *Energy Environ. Sci.* **6**, 157 (2013).
- ⁸⁴ AFLOWLIB.ORG: a distributed materials genome properties repository from high-throughput ab-initio calculation, <http://aflowlib.org/>.
- ⁸⁵ B. Meredig and C. Wolverton, *Nature Materials* **12**, 123 (2012).
- ⁸⁶ M. J. Katz, S. C. Riha, N. C. Jeong, A. B. F. Martinson, O. K. Farha, and J. T. Hupp, *Coordination Chemistry Reviews* **256**, 2521 (2012),
- ⁸⁷ R. Saito, Y. Miseki, and K. Sayama, *Chem. Commun.* **48**, 3833 (2012).
- ⁸⁸ L. Yu, R. S. Kokenyesi, D. A. Keszler, and A. Zunger, *Advanced Energy Materials* **3**, 43 (2013).
- ⁸⁹ M. S. Hybertsen and S. G. Louie, *Physical Review B* **35**, 5585 (1987).

-
- ⁹⁰ J. Yan, J. J. Mortensen, K. W. Jacobsen, and K. S. Thygesen, *Physical Review B* **83**, 245122 (2011).
- ⁹¹ W. Shockley and H. J. Queisser, *Journal of Applied Physics* **32**, 510 (1961).
- ⁹² P. C. K. Vesborg and T. F. Jaramillo, *RSC Adv.* **2**, 7933 (2012).
- ⁹³ T. Gershon, K. P. Musselman, A. Marin, R. H. Friend, and J. L. MacManus-Driscoll, *Solar Energy Materials and Solar Cells* **96**, 148 (2012).
- ⁹⁴ T. Mowles, High efficiency solar photovoltaic cells produced with inexpensive materials by processes suitable for large volume production, 1994.
- ⁹⁵ J. Zhao, *Solar Energy Materials and Solar Cells* **82**, 53 (2004),
- ⁹⁶ S. P. Bremner, M. Y. Levy, and C. B. Honsberg, *Progress in Photovoltaics: Research and Applications* **16**, 225 (2008).
- ⁹⁷ A. D. Vos, *Journal of Physics D: Applied Physics* **13**, 839 (1980).
- ⁹⁸ J. E. Andrews, *Development of high-efficiency, low-cost ZnSiAs₂ solar cells*, 1980.
- ⁹⁹ K. R. Reddy, N. K. Reddy, and R. Miles, *Solar Energy Materials and Solar Cells* **90**, 3041 (2006),

Appendix **A**

Calculated Bandgaps of the Materials Project Entries

This Appendix contains the values of the bandgaps of the calculated structures from the Materials Project database¹⁶ and already described in Chapter 8. The additional information available in the table are: chemical formula, id of the structure in the Materials Project database, and indirect and direct bandgap.

Appendix A. Calculated Bandgaps of the Materials Project Entries

Formula	Id	Gap	Formula	Id	Gap	Formula	Id	Gap	Formula	Id	Gap
NaCuSe	7433	0.1 (0.1)	K ₂ PtBr ₆	27691	2.2 (2.2)	KInP ₂ S ₇	22583	3.7 (3.7)	Li ₂ ZnGeO ₄	8184	5.8 (5.8)
SrMgSi	15642	0.1 (0.1)	KLi ₂ As	28994	2.2 (2.2)	NbAlCl ₈	28358	3.7 (3.7)	BaPbF ₆	19799	5.8 (5.8)
SrMgGe	15643	0.1 (0.1)	Hf(Te ₂ Cl ₃) ₂	29419	2.2 (2.2)	Rb ₂ CdO ₂	28364	3.7 (3.7)	K ₂ NaAlH ₆	24412	5.8 (5.8)
Rh ₂ S ₃	17173	0.1 (0.1)	GaSe	1943	2.2 (2.2)	K ₂ Zn ₃ O ₄	504936	3.7 (3.7)	All ₃	30930	5.8 (5.8)
Sr ₂ Pb	30828	0.1 (0.1)	HgPSe ₃	7293	2.2 (2.2)	Ba ₂ SnS ₄	541832	3.7 (3.7)	KNaS	504938	5.8 (5.8)
V ₄ As ₂ O ₁₃	32447	0.1 (0.1)	Na ₃ SbSe ₄	8703	2.2 (2.2)	Cd(Ga ₂ S ₂) ₂	4452	3.7 (3.7)	RbTaO ₃	3033	5.8 (5.8)
K ₂ MnSe ₂	8716	0.1 (0.2)	Sr ₂ ZnN ₂	9306	2.2 (2.2)	AlAgS ₂	5782	3.7 (3.7)	BaMoO ₄	19276	5.8 (5.8)
Li ₂ MnO ₃	18988	0.1 (0.2)	Sr ₂ CdS ₄	10953	2.2 (2.2)	SrPSe ₃	7198	3.7 (3.7)	RbIn(MoO ₄) ₂	504506	5.8 (5.8)
CoAs ₂	2715	0.1 (0.3)	VNCl ₄	27868	2.2 (2.2)	CsYCdSe ₃	11116	3.7 (3.7)	ScBrO	546279	5.8 (5.8)
CaAgP	12277	0.1 (0.3)	BaHgS ₂	28007	2.2 (2.2)	K ₂ NaRhF ₆	14039	3.7 (3.7)	TlF	720	5.8 (5.9)
TaAgS ₃	5821	0.1 (0.4)	Sr ₅ Mo ₂ N ₇	31231	2.2 (2.2)	Sr ₃ ScRhO ₆	18247	3.7 (3.7)	PbBrCl	22997	5.8 (5.9)
Sr ₂ Sn	978	0.2 (0.2)	KPt ₂ S ₃	510130	2.2 (2.2)	KAlTe ₂	18347	3.7 (3.7)	Ba(IO ₃) ₂	30991	5.8 (5.9)
YSbPt	4964	0.2 (0.2)	WS ₂	224	2.2 (2.3)	PCl ₅	23228	3.7 (3.7)	Pb ₂ CO ₄	505702	5.8 (5.9)
Cu ₂ GeS ₃	15252	0.2 (0.2)	NaTiO ₂	3056	2.2 (2.3)	NClO ₆	27774	3.7 (3.7)	Tl ₂ F ₆	10402	5.8 (5.9)
Tl ₄ Te ₃ Pb	20740	0.2 (0.2)	Sr ₃ GaN ₃	7191	2.2 (2.3)	CsPS ₃	504838	3.7 (3.7)	ZnCN ₂	29826	5.8 (6.1)
InAgTe ₂	22386	0.2 (0.2)	Ca ₂ ZnN ₂	8818	2.2 (2.3)	Ba ₄ Li(SbO ₄) ₃	7971	3.7 (3.8)	Ca(AsO ₃) ₂	4555	5.8 (6.1)
Na ₄ CoO ₄	31593	0.2 (0.2)	K ₂ VAgS ₄	8900	2.2 (2.3)	BaPSe ₃	11008	3.7 (3.8)	LiN ₃	2659	5.8 (6.2)
Cs ₂ K ₄ Fe ₂ O ₅	541234	0.2 (0.2)	NaSe ₂	15514	2.2 (2.3)	LaI ₃	27979	3.7 (3.8)	BaH ₂	23715	5.8 (6.3)
CoSb ₃	1317	0.2 (0.2)	Ca ₂ NCl	22936	2.2 (2.3)	Cs ₂ HfI ₆	29398	3.7 (3.8)	SnB ₄ O ₇	13252	5.8 (6.3)
Li ₂ AgSb	16238	0.2 (0.2)	Te ₃ Cl ₂	27628	2.2 (2.3)	Na ₄ SeO ₅	29871	3.7 (3.8)	CaH ₂	23713	5.8 (6.6)
CaAgAs	5615	0.2 (0.3)	K ₄ CdAs ₂	29585	2.2 (2.3)	InBrO	504656	3.7 (3.8)	LiGaO ₂	3338	5.9 (5.9)
RbMnBr ₃	505596	0.2 (0.3)	PtS ₂	762	2.2 (2.3)	AgNO ₃	552185	3.7 (4.0)	RbLiS	8751	5.9 (5.9)
CsMnBr ₃	23048	0.2 (0.3)	ZrS ₃	9921	2.2 (2.3)	B ₆ As	624	3.8 (3.8)	K ₂ TiO ₃	13133	5.9 (5.9)
CsMnI ₃	540609	0.2 (0.3)	RhBr ₃	504719	2.2 (2.3)	Sb ₂ O ₃	2136	3.8 (3.8)	Rb ₃ GaO ₃	13744	5.9 (5.9)
CdSb	1321	0.2 (0.5)	In ₆ Ge ₂ PtO ₉	22186	2.2 (2.4)	AlCuS ₂	4979	3.8 (3.8)	K ₄ Zr ₅ O ₁₂	27377	5.9 (5.9)
P ₃ Ir	13853	0.2 (0.5)	K(SnSe ₂) ₂	28769	2.2 (2.4)	CsRb ₂ PdF ₅	8202	3.8 (3.8)	AsClF ₈	27926	5.9 (5.9)
ZnSb	753	0.2 (0.5)	BaP ₁₀	504809	2.2 (2.4)	K ₃ AsSe ₃	18594	3.8 (3.8)	Na ₃ ScBr ₆	29417	5.9 (5.9)
Li ₃ LaSb ₂	8405	0.2 (1.0)	Ca ₄ Sb ₂ O	13660	2.2 (2.5)	Ba ₂ ZnGe ₂ S ₆ O	17244	3.8 (3.8)	Sr ₃ Ga ₄ O ₉	30158	5.9 (5.9)
ScNiSb	3432	0.2 (1.3)	RbInTe ₂	22255	2.2 (2.5)	Ba ₂ YBiO ₆	23137	3.8 (3.8)	NaGaBr ₄	505084	5.9 (5.9)
YNiSb	11520	0.2 (1.3)	HgAsO ₃	30284	2.2 (2.6)	TiCl ₂	27205	3.8 (3.8)	GaAsO ₄	3996	5.9 (5.9)
MoCl ₃	22853	0.3 (0.3)	Ba ₄ NaCu(CO ₅) ₂	6841	2.2 (2.7)	K ₂ CdO ₂	27742	3.8 (3.8)	As ₂ O ₃	1581	5.9 (6.0)
Ge ₃ Ru ₂	21945	0.3 (0.3)	NaLi ₂ Sb	5077	2.2 (3.0)	PICl ₆	27824	3.8 (3.8)	TaInO ₄	8979	5.9 (6.0)
Cs ₆ Fe ₂ O ₅	541385	0.3 (0.3)	ZnSiP ₂	4763	2.3 (2.3)	BiClF ₈	28194	3.8 (3.8)	CsMgI ₃	505586	5.9 (6.0)
Sr(As ₃ Pt ₂) ₂	14500	0.3 (0.4)	K ₂ Cd ₂ O ₃	7534	2.3 (2.3)	Ba ₂ Bi ₂ O ₅	28670	3.8 (3.8)	CaBiClO ₂	553025	5.9 (6.0)
As ₂ Rh	15954	0.3 (0.4)	AlCuTe ₂	8017	2.3 (2.3)	KBiO ₂	30988	3.8 (3.8)	Li ₃ BN ₂	5001	5.9 (6.2)
SiRu	189	0.3 (0.5)	CaPdF ₄	8161	2.3 (2.3)	KAgCO ₃	541966	3.8 (3.8)	Mg ₂ PN ₃	3933	5.9 (6.6)
Ba ₃ CrN ₃	12905	0.3 (0.5)	K ₂ PAu	9687	2.3 (2.3)	SrCrO ₄	542885	3.8 (3.8)			

Sb ₂ Ru	20928	0.3 (0.6)	Hf ₃ N ₄	11660	2.3 (2.3)	K ₃ Nb ₃ (BO ₆) ₂	15248	3.8 (3.8)	SrSeO ₃	3395	6.0 (6.0)
Ba(ZnP) ₂	7426	0.3 (0.8)	NaAg ₃ S ₂	16992	2.3 (2.3)	BiPbClO ₂	23084	3.8 (3.8)	KNaLaNbO ₅	10942	6.0 (6.0)
YIr	30746	0.3 (1.1)	KGaTe ₂	17965	2.3 (2.3)	CsBr ₃	504635	3.8 (3.8)	Li ₁₆ Ta ₂ N ₈ O	14871	6.0 (6.0)
HfSnPd	11869	0.3 (1.3)	K ₂ PdCl ₆	23067	2.3 (2.3)	LiInI ₄	541001	3.8 (3.8)	Sr ₂ ZnGe ₂ O ₇	17392	6.0 (6.0)
C	48	0.4 (0.4)	SbI ₃ Cl ₈	23536	2.3 (2.3)	K ₂ NaAlP ₂	9068	3.8 (3.9)	CdCl ₂	22881	6.0 (6.0)
K ₃ FeO ₃	504570	0.4 (0.4)	CsSnBr ₃	27214	2.3 (2.3)	CdMoO ₄	19039	3.8 (3.9)	SnI ₂ O	28406	6.0 (6.0)
HfCu ₂ Te ₃	3650	0.4 (0.6)	CsGel ₃	28377	2.3 (2.3)	K ₂ TeBr ₆	22963	3.8 (3.9)	SrN ₆	2131	6.0 (6.0)
TlTe ₃ Pt ₂	9251	0.4 (0.6)	K ₂ TlS ₃	28766	2.3 (2.3)	SBr	28099	3.8 (3.9)	CsPbF ₃	20282	6.0 (6.0)
CaAgSb	11214	0.4 (0.6)	PdSO ₄	28952	2.3 (2.3)	CdI ₂	28248	3.8 (3.9)	Zn ₃ S ₂ O ₉	30986	6.0 (6.0)
ReTeS	5222	0.4 (0.8)	AsSeI	505373	2.3 (2.3)	RbS	9062	3.8 (3.9)	GeO ₂	733	6.0 (6.1)
LiAlGe	5920	0.4 (1.7)	Cd ₂ GaAgS ₄	6356	2.3 (2.3)	K ₃ BP ₂	9664	3.8 (3.9)	Na ₃ In ₂ (PO ₄) ₃	17349	6.0 (6.1)
Sr(ZnAs) ₂	7770	0.5 (0.5)	KP	7441	2.3 (2.3)	TlI	22858	3.8 (3.9)	SbCl ₃	22872	6.0 (6.1)
La ₃ MnGaS ₇	504891	0.5 (0.6)	Ag ₂ HgI ₄	23485	2.3 (2.3)	Rb ₂ TaCuS ₄	11923	3.8 (4.0)	NaIO ₃	22989	6.0 (6.1)
Sb ₂ Ir	1247	0.5 (0.8)	BaZrS ₃	540771	2.3 (2.3)	B ₆ P	28395	3.8 (4.0)	K ₂ S	1022	6.0 (6.1)
P ₂ Rh	15953	0.5 (0.9)	Cs ₂ VAgS ₄	8684	2.3 (2.4)	SrTiO ₃	4651	3.9 (3.9)	Li ₂ TeO ₃	27231	6.0 (6.2)
CdAs ₂	471	0.5 (1.0)	Rb ₂ VAgS ₄	8901	2.3 (2.4)	KAuF ₄	5309	3.9 (3.9)	K ₂ TeO ₃	8724	6.0 (6.2)
MgB ₄	365	0.5 (1.0)	K ₅ P ₂ Au	14624	2.3 (2.4)	K ₂ SO ₂	10417	3.9 (3.9)	Zn(ReO ₄) ₂	10326	6.1 (6.1)
GePtSe	20817	0.5 (1.1)	BiTeI	22965	2.3 (2.4)	Sr ₂ SnS ₃ F ₂	17676	3.9 (3.9)	Ba ₂ YTaO ₆	12385	6.1 (6.1)
Te ₂ Ru	267	0.5 (1.3)	Rb ₂ SnAs ₂	8931	2.3 (2.4)	Ba ₂ CdS ₃	18309	3.9 (3.9)	LiAlGeO ₄	16947	6.1 (6.1)
ReO ₃	190	0.5 (1.4)	Li ₂ PbO ₃	22450	2.3 (2.4)	Sr(InS ₂) ₂	21781	3.9 (3.9)	BaI ₂	23260	6.1 (6.1)
LiAlSi	3161	0.5 (2.2)	Cs ₂ SnAs ₂	8934	2.3 (2.5)	CsGeCl ₃	22988	3.9 (3.9)	LaBr ₃	23263	6.1 (6.1)
P	157	0.6 (0.6)	K ₃ Sb ₂ Au ₃	9273	2.3 (2.5)	SbCl ₅	23176	3.9 (3.9)	Na ₃ NbO ₄	27247	6.1 (6.1)
GaAs	2534	0.6 (0.6)	Tl ₂ TeS ₃	17172	2.3 (2.5)	Pl ₃	27529	3.9 (3.9)	Sr ₂ I ₂ O	551203	6.1 (6.1)
Cd(PtO ₂) ₃	8212	0.6 (0.6)	Ba ₅ P ₄	17566	2.3 (2.5)	Rb ₂ TiCl ₆	27827	3.9 (3.9)	HfTe ₃ O ₈	18352	6.1 (6.1)
LaTeAs	10383	0.6 (0.6)	NalnSe ₂	22473	2.3 (2.5)	BrNO ₃	29526	3.9 (3.9)	Ta ₂ Zn ₃ O ₈	28251	6.1 (6.1)
Sr(PIr) ₂	15074	0.6 (0.6)	PAuS ₄	30938	2.3 (2.5)	MgV ₂ O ₆	504510	3.9 (3.9)	BaZrO ₃	3834	6.1 (6.2)
Si ₃ Ru ₂	22192	0.6 (0.6)	LiBeP	9915	2.3 (2.6)	LiBiO ₃	504893	3.9 (3.9)	KSO ₄	7622	6.1 (6.2)
YB ₄ Mo	7691	0.6 (0.7)	Ag ₃ AsS ₃	4431	2.3 (2.7)	TaTi ₃ Se ₄	10644	3.9 (3.9)	PbCO ₃	19893	6.1 (6.2)
CoP ₂	14285	0.6 (0.7)	KSe	9268	2.3 (2.7)	Rb ₂ Cr ₂ O ₇	19658	3.9 (3.9)	KCdCl ₃	23442	6.1 (6.2)
Si ₃ Ag ₃ (SnP ₃) ₂	18310	0.6 (0.8)	NbCu ₃ Se ₄	4043	2.3 (2.7)	AlICl ₆	27935	3.9 (3.9)	Li ₂ TiGeO ₅	13182	6.1 (6.2)
BaP ₃ Pt ₂	28373	0.6 (0.8)	ZrS ₂	1186	2.3 (3.0)	Cs ₂ PtCl ₄	29216	3.9 (3.9)	K ₂ MoO ₄	18914	6.1 (6.2)
RbGa ₃	31493	0.6 (0.8)	ZnO	2133	2.4 (2.4)	Hf(PS ₃) ₂	14444	3.9 (4.0)	Ba ₂ LaTaO ₆	13055	6.1 (6.3)
Zr ₃ Ni ₃ Sb ₄	17926	0.6 (0.9)	Cd(GaSe ₂) ₂	3772	2.4 (2.4)	MoPbO ₄	25054	3.9 (4.0)	RbMgH ₃	23738	6.1 (6.3)
Sb ₂ Os	2695	0.6 (1.0)	Cu ₃ PS ₄	3934	2.4 (2.4)	Na ₃ TlO ₂	29454	3.9 (4.1)	CdF ₂	241	6.1 (6.6)
OsS ₂	20905	0.6 (1.0)	NaAs ₂	5942	2.4 (2.4)	Cd(AsO ₃) ₂	7128	3.9 (4.2)	Li ₂ S	1153	6.1 (7.0)
AuSe	2793	0.6 (1.5)	KNb(CuSe ₂) ₂	6599	2.4 (2.4)	HgPb ₂ (ClO) ₂	546862	3.9 (4.3)	KReO ₄	4757	6.2 (6.2)
Mg ₂ Ge	408	0.6 (1.6)	AlCuSe ₂	8016	2.4 (2.4)	RbAuF ₄	3419	4.0 (4.0)	NaLiS	8452	6.2 (6.2)
ScSbPt	7173	0.7 (0.7)	K ₂ NaGaAs ₂	9676	2.4 (2.4)	Al ₂ ZnS ₄	4842	4.0 (4.0)	Na ₅ TaO ₅	8957	6.2 (6.2)
GaCuTe ₂	3839	0.7 (0.7)	SiP ₂	9996	2.4 (2.4)	Ba ₂ ZnS ₃	5587	4.0 (4.0)	MgPbF ₆	19734	6.2 (6.2)

Ca(ZnAs) ₂	9571	0.7	(0.7)	BaLiP	13277	2.4	(2.4)	CaMg ₂ N ₂	5795	4.0	(4.0)	KBrO ₃	22958	6.2	(6.2)
LiZnSb	9919	0.7	(0.7)	AlAgSe ₂	14091	2.4	(2.4)	Li ₂ PtF ₆	13986	4.0	(4.0)	Rb ₂ ZrCl ₆	27831	6.2	(6.2)
KAg ₃ Se ₂	9782	0.7	(0.8)	CsGaTe ₂	17688	2.4	(2.4)	K ₃ Nb ₃ Si ₂ O ₁₃	17059	4.0	(4.0)	Sr ₄ I ₆ O	29910	6.2	(6.2)
Ba(GeAs) ₂	27810	0.7	(0.9)	Na ₅ SiAs ₃	18139	2.4	(2.4)	SrTiPS ₄	17090	4.0	(4.0)	SrWO ₄	19163	6.2	(6.2)
FeAs ₂	2008	0.7	(1.0)	CrHgO ₄	19380	2.4	(2.4)	SeVO ₄	19247	4.0	(4.0)	PbClF	22964	6.2	(6.2)
As ₂ Ru	766	0.7	(1.2)	K ₂ In ₃ AgSe ₆	21705	2.4	(2.4)	BaCrO ₄	19662	4.0	(4.0)	BeAlH ₅	23719	6.2	(6.2)
YP ₅	9854	0.7	(1.2)	K ₄ HgAs ₂	29484	2.4	(2.4)	Ba(ImS ₂) ₂	21943	4.0	(4.0)	LaNbO ₄	5295	6.2	(6.3)
Al ₂ Os	7188	0.7	(1.5)	InGaSe ₃	504952	2.4	(2.4)	CsCu ₂ Br ₃	23017	4.0	(4.0)	Na ₂ CN ₂	541989	6.2	(6.3)
Mg ₂ Si	1367	0.7	(2.5)	CdS	672	2.4	(2.4)	SCl ₂	28128	4.0	(4.0)	SrH ₂	23714	6.2	(6.9)
Te	19	0.8	(0.8)	LaCuS ₂	4841	2.4	(2.4)	Gal ₃	30954	4.0	(4.0)	KMgH ₃	23737	6.2	(7.9)
KSnSb	3486	0.8	(0.8)	Tl ₂ B ₂ Se ₇	16183	2.4	(2.4)	Rb ₂ PbO ₂	504598	4.0	(4.0)	BaN ₆	1707	6.3	(6.3)
Ca(CdAs) ₂	7067	0.8	(0.8)	LiInTe ₂	20782	2.4	(2.4)	VCl ₃ O	504820	4.0	(4.0)	Ca ₄ Al ₆ TeO ₁₂	15312	6.3	(6.3)
K ₂ Ag ₄ S ₃	7494	0.8	(0.8)	HgI ₂	23192	2.4	(2.4)	RbLiZn ₂ O ₃	18422	4.0	(4.0)	ScAsO ₄	546125	6.3	(6.3)
TiS ₃	9920	0.8	(0.8)	Tl ₂ Au ₄ S ₃	29898	2.4	(2.4)	Tl ₃ VO ₄	32479	4.0	(4.0)	RbReO ₄	4035	6.3	(6.3)
SrCaPb	21166	0.8	(0.8)	MoS ₂ Cl ₃	504716	2.4	(2.4)	Sr ₂ GeS ₄	4578	4.0	(4.1)	KLiS	8430	6.3	(6.3)
TiBiSe ₂	29662	0.8	(0.8)	Cs ₂ TiS ₃	3247	2.4	(2.5)	CsCu ₃ S ₂	7786	4.0	(4.1)	CaTaAlO ₅	15733	6.3	(6.3)
KGa ₃	181	0.8	(0.9)	Nb ₂ SnO ₆	3324	2.4	(2.5)	Rb ₃ BP ₂	9720	4.0	(4.1)	Rb ₂ MoO ₄	19212	6.3	(6.3)
TaTe ₄ I	28691	0.8	(0.9)	Cs ₂ Pt ₃ Se ₄	14338	2.4	(2.5)	AsPO ₅	14367	4.0	(4.1)	MgSn(BO ₃) ₂	11715	6.3	(6.4)
Si ₃ NiP ₄	8311	0.8	(0.9)	Ga ₂ PdI ₈	30946	2.4	(2.5)	Mg ₂ GeS ₄	17441	4.0	(4.1)	MgI ₂	23205	6.3	(6.4)
KSb ₂	29055	0.8	(1.1)	Cs ₃ LazCuSe ₄	505815	2.4	(2.5)	Sr ₂ NbN ₃	17701	4.0	(4.1)	CsSrN ₉	29228	6.3	(6.4)
P ₂ Ir	10155	0.8	(1.8)	Cs ₂ Pd ₃ S ₄	510268	2.4	(2.5)	RbLiCrO ₄	18741	4.0	(4.1)	KAsO ₂	30298	6.3	(6.4)
KZnAs	7421	0.9	(0.9)	BaSnO ₃	3163	2.4	(2.6)	Li ₂ GePbS ₄	19896	4.0	(4.1)	MgSeO ₃	12271	6.3	(6.5)
BaCaSi	16253	0.9	(0.9)	InBr	22870	2.4	(2.6)	CsI ₂	22990	4.0	(4.1)	PbCl ₂	23291	6.3	(6.5)
Na ₄ FeO ₃	19026	0.9	(0.9)	Tl ₃ BSe ₃	28490	2.4	(2.6)	CaV ₂ O ₆	32526	4.0	(4.1)	TaAlO ₄	14333	6.3	(6.5)
SrCaSn	20726	0.9	(0.9)	Li ₂ PdO ₂	7608	2.4	(2.7)	GeS ₂	542613	4.0	(4.1)	CsMgH ₃	23751	6.3	(6.6)
Na ₂ Pd ₃ O ₄	27562	0.9	(0.9)	Cs ₃ Sb	10378	2.4	(2.7)	Sr(BeN) ₂	11919	4.0	(4.1)	AsCl ₃	23280	6.3	(6.6)
Ta ₂ CrO ₆	31629	0.9	(0.9)	HgO	1224	2.4	(2.8)	RbAuS	9010	4.0	(4.2)	AlN	661	6.4	(6.4)
GaAgSe ₂	5518	0.9	(0.9)	Ba(MgAs) ₂	8280	2.4	(2.8)	K ₂ LiAlP ₂	6450	4.0	(4.2)	Ba ₃ NaTaO ₆	8961	6.4	(6.4)
KZnSb	7438	0.9	(0.9)	Na ₂ PtS ₂	10246	2.4	(2.8)	CsS	29266	4.0	(4.2)	Rb ₃ AlO ₃	14951	6.4	(6.4)
BaCaSn	11265	0.9	(0.9)	Li ₂ PdO ₂	545750	2.4	(2.8)	CsAgBr ₂	23454	4.0	(4.3)	Rb ₆ Ge ₂ O ₇	18224	6.4	(6.4)
BaCaGe	16252	0.9	(0.9)	Cs ₂ O	7988	2.4	(3.1)	Sc ₂ SO ₂	7288	4.0	(4.4)	BaSeO ₃	6989	6.4	(6.5)
Tl(MoSe) ₃	3411	0.9	(1.0)	AgCl	22922	2.4	(4.1)	RbLaSe ₂	7176	4.0	(4.4)	BaSeO ₃	6989	6.4	(6.5)
Y ₃ Sb ₄ Au ₃	13654	0.9	(1.0)	Al ₂ HgSe ₄	3038	2.5	(2.5)	K ₂ PtF ₆	3821	4.1	(4.1)	Si ₃ (BiO ₃) ₄	23331	6.4	(6.5)
CoPSe	10368	0.9	(1.1)	BaZrN ₂	3104	2.5	(2.5)	LiAlTe ₂	4586	4.1	(4.1)	NaGe ₂ (PO ₄) ₃	542919	6.4	(6.5)
NaNiO ₂	19149	0.9	(1.1)	CdSiP ₂	4666	2.5	(2.5)	Na ₅ ReO ₆	8253	4.1	(4.1)	Na ₂ GeO ₃	5784	6.4	(6.6)
P ₂ Pd	28266	0.9	(1.1)	PtF ₄	8943	2.5	(2.5)	Ba ₂ SiSe ₄	14447	4.1	(4.1)	YTaO ₄	5377	6.4	(6.7)
Rb ₂ Te ₅	31002	0.9	(1.1)	RbTeAu	9008	2.5	(2.5)	Ba ₂ TeAgS ₄	15217	4.1	(4.1)	GeF ₂	7595	6.4	(6.8)
Ba ₂ CuClO ₂	551456	0.9	(1.1)	Ba(AuO ₂) ₂	9297	2.5	(2.5)	Ba ₂ Nb ₆ Te ₂ O ₂₁	16998	4.1	(4.1)	SrSn(BO ₃) ₂	8000	6.4	(6.8)
PtSe ₂	1115	0.9	(1.2)	Ca ₃ PN	11824	2.5	(2.5)	Sr ₃ (AlN ₂) ₂	17129	4.1	(4.1)	SrCN ₂	12317	6.4	(7.1)
												CsCdF ₃	8399	6.4	(7.3)

AuSeBr	27199	0.9 (1.3)	Tl(PS ₃) ₂	13666	2.5 (2.5)	Li ₄ MoO ₅	19117	4.1 (4.1)	ZrO ₂	2858	6.5 (6.5)
FeSe ₂	760	0.9 (1.5)	Sr ₃ TaAs ₃ O	18199	2.5 (2.5)	SiSe ₂	22142	4.1 (4.1)	Al ₂ ZnO ₄	2908	6.5 (6.5)
Si ₃ P ₂ Pt	29157	0.9 (1.5)	CuCl	22914	2.5 (2.5)	GaPS ₄	30979	4.1 (4.1)	NaSc(GeO ₃) ₂	8054	6.5 (6.5)
Ca ₂ Ge	304	1.0 (1.0)	AgI	22925	2.5 (2.5)	Ca ₂ Ta ₂ O ₇	14026	4.1 (4.1)	K ₂ CN ₂	10408	6.5 (6.5)
Cu ₂ O	361	1.0 (1.0)	P ₂ PtO ₇	29282	2.5 (2.5)	K ₃ GeS ₃	14434	4.1 (4.1)	SrCdP ₂ O ₇	17693	6.5 (6.5)
Te ₃ As ₂	484	1.0 (1.0)	RbIn ₃ S ₅	542654	2.5 (2.5)	Ba ₂ Ta ₂ N ₃	17400	4.1 (4.1)	Cu ₃ Se ₂ (GeO ₄) ₃	21989	6.5 (6.5)
TaCuS ₃	3102	1.0 (1.0)	Sc ₂ S ₃	401	2.5 (2.5)	TlTl ₂ O ₃	17986	4.1 (4.1)	K ₂ ZnBr ₄	23535	6.5 (6.5)
Hg ₂ GeSe ₄	3167	1.0 (1.0)	MgSiP ₂	2961	2.5 (2.5)	TlBr	22875	4.1 (4.1)	Na ₃ AlH ₆	23705	6.5 (6.5)
KSnAs	3481	1.0 (1.0)	Ba ₂ GeSe ₄	11902	2.5 (2.5)	BaZnSO	548469	4.1 (4.1)	RbAsO ₂	30299	6.5 (6.5)
RbAg ₃ Te ₂	10481	1.0 (1.0)	CdP ₂	913	2.5 (2.6)	Tl ₂ SiS ₃	8190	4.1 (4.2)	RbBrO ₃	28872	6.5 (6.5)
TlBiTe ₂	27438	1.0 (1.0)	SiAs	1863	2.5 (2.6)	InPS ₄	20790	4.1 (4.2)	GeP ₂ O ₇	28883	6.5 (6.5)
BaAs ₂	31243	1.0 (1.0)	Si ₄ P ₄ Ru	14983	2.5 (2.6)	Bi ₃ BrO ₄	29447	4.1 (4.2)	Na ₂ ZnSiO ₄	6391	6.5 (6.6)
Ca ₂ Si	2517	1.0 (1.0)	Ca ₆ GaN ₅	17875	2.5 (2.6)	KAuS	7077	4.1 (4.2)	ZrGeO ₄	8042	6.5 (6.6)
CdSiAs ₂	3078	1.0 (1.0)	SbSeI	22996	2.5 (2.6)	Li ₆ MoN ₄	8804	4.1 (4.2)	SrGeO ₃	17464	6.5 (6.6)
CsAg ₃ Se ₂	16234	1.0 (1.0)	K ₂ PdBr ₄	27138	2.5 (2.6)	NaGe ₂ N ₃	14433	4.1 (4.2)	CaGeO ₃	17761	6.5 (6.6)
Ca ₃ GeO	17193	1.0 (1.0)	Na ₄ HgP ₂	28591	2.5 (2.6)	BrF ₃	23297	4.1 (4.3)	PCl ₃	23230	6.5 (6.6)
Ag ₂ BiO ₃	23558	1.0 (1.0)	RbAuBr ₄	510267	2.5 (2.6)	KSn ₂ Br ₅	23541	4.1 (4.3)	Zn ₄ P ₆ Sn ₁₂	15833	6.5 (6.7)
Cs ₂ SnI ₆	27636	1.0 (1.0)	K ₂ PdO ₂	540584	2.5 (2.6)	Tl ₂ TeCl ₆	27833	4.1 (4.3)	SbPO ₄	3439	6.5 (6.8)
PtI ₃	28268	1.0 (1.0)	BaCdO ₂	7899	2.5 (2.6)	Bi ₃ ClO ₄	29558	4.1 (4.3)	MgSiN ₂	3677	6.5 (6.8)
Bi ₄ RuI ₂	541771	1.0 (1.0)	Ta ₃ N ₅	27488	2.5 (2.6)	Nb ₂ O ₅	1595	4.1 (4.6)	KSO ₂ F	6560	6.6 (6.6)
MnP ₄	487	1.0 (1.1)	As ₂ Se ₃	909	2.5 (2.7)	Ba ₂ InO ₃ F	19956	4.1 (4.6)	BaWO ₄	19048	6.6 (6.6)
NbTeI ₃	540924	1.0 (1.1)	GaP	2490	2.5 (2.7)	KTaO ₃	3614	4.1 (4.6)	SeOF ₂	27367	6.6 (6.6)
TlPt ₂ Se ₃	541487	1.0 (1.1)	Rb ₃ Sb ₂ Au ₃	9274	2.5 (2.7)	Li ₂ O ₂	841	4.2 (4.2)	SeF ₄	29172	6.6 (6.6)
Sr(GaTe ₂) ₂	6987	1.0 (1.2)	SrLi ₄ N ₂	15845	2.5 (2.7)	ReAgO ₄	7094	4.2 (4.2)	Zr ₃ Cd(PO ₄) ₆	541299	6.6 (6.6)
Ag ₃ Ge ₅ P ₆	17862	1.0 (1.2)	InS	20094	2.5 (2.7)	Rb ₂ PtF ₆	8192	4.2 (4.2)	Na ₄ GeO ₄	2970	6.6 (6.6)
Ta ₂ Pd ₃ Se ₈	18010	1.0 (1.2)	Rb ₂ SiAs ₂	6960	2.5 (2.8)	NbBO ₄	8615	4.2 (4.2)	YAsO ₄	8058	6.6 (6.6)
HfSe ₃	15622	1.0 (1.3)	K ₂ SiAs ₂	6984	2.5 (2.8)	BaLa ₂ PtO ₅	8809	4.2 (4.2)	KCdF ₃	9628	6.6 (6.6)
FeP ₂	20027	1.0 (1.3)	Si ₂ Hg ₆ O ₇	28712	2.5 (2.8)	K ₃ SbS ₄	9781	4.2 (4.2)	MgO ₂	2589	6.6 (6.7)
PdSe ₂	2418	1.0 (1.5)	Rb ₂ PtS ₂	7929	2.5 (2.9)	ZnPtF ₆	13610	4.2 (4.2)	Na ₂ SeO ₄	5141	6.6 (6.7)
ZrTiCuSe ₃	7050	1.1 (1.1)	LiAlB ₁₄	8204	2.5 (2.9)	Cs ₂ TaAgS ₄	15218	4.2 (4.2)	Sr ₂ YSbO ₆	12878	6.6 (6.7)
KZrCuSe ₃	9318	1.1 (1.1)	K ₂ PtS ₂	7928	2.5 (3.0)	Ba ₂ SnS ₃ F ₂	17918	4.2 (4.2)	TlZnPO ₄	18168	6.6 (6.7)
TaTiS ₃	10795	1.1 (1.1)	Ba ₂ PbO ₄	20098	2.5 (3.0)	CaIn ₂ O ₄	22766	4.2 (4.2)	NaScCl ₄	29432	6.6 (6.7)
Ca ₃ SiO	11649	1.1 (1.1)	Na ₂ W ₄ O ₁₃	32533	2.5 (3.0)	BiI ₃	22849	4.2 (4.2)	SnF ₄	2706	6.6 (6.8)
Si ₃ Os ₂	16608	1.1 (1.1)	Ba(MgF) ₂	8278	2.5 (3.1)	KBiP ₂ S ₇	23572	4.2 (4.2)	BBr ₃	23225	6.6 (6.8)
Na ₃ InAs ₂	21622	1.1 (1.1)	KAg ₂ PS ₄	12532	2.5 (3.3)	Ca ₃ PI ₃	27272	4.2 (4.2)	NaN ₃	22003	6.6 (7.0)
Ta ₂ AgF ₁₂	28375	1.1 (1.1)	AlAgO ₂	9631	2.5 (3.4)	Te ₆ Br ₂ O ₁₁	29251	4.2 (4.2)	CaCN ₂	4124	6.6 (7.3)
Sb ₂ WO ₆	541435	1.1 (1.1)	SnO ₂	856	2.6 (2.6)	RbBiO ₂	29521	4.2 (4.2)	RbSO ₂ F	6384	6.7 (6.7)
Bi ₄ RuBr ₂	541772	1.1 (1.1)	Ca ₃ AsN	4192	2.6 (2.6)	Cd ₄ OF ₆	505174	4.2 (4.2)	KCSN	6511	6.7 (6.7)
LaZnAsO	549589	1.1 (1.1)	KHgF ₃	7483	2.6 (2.6)	Ca ₂ O ₃	886	4.2 (4.2)	HfGeO ₄	9755	6.7 (6.7)

Appendix A. Calculated Bandgaps of the Materials Project Entries

S ₄ C ₃	15661	1.1 (1.1)	Rb ₂ Sn ₂ O ₃	7863	2.6 (2.6)	CaPtF ₆	8255	4.2 (4.2)	Li ₂ ZnSiO ₄	17288	6.7 (6.7)
SiCu ₂ Se ₃	15896	1.1 (1.1)	CsYHgSe ₃	11123	2.6 (2.6)	CdCN ₂	10969	4.2 (4.2)	ScCl ₃	23300	6.7 (6.7)
In ₂ HgTe ₄	19765	1.1 (1.1)	Rb ₃ AsSe ₄	18305	2.6 (2.6)	SbS ₂ NF ₆	12368	4.2 (4.2)	S(ClO) ₂	28405	6.7 (6.7)
GeTe	938	1.1 (1.2)	Na ₅ SnP ₃	18317	2.6 (2.6)	LiVO ₃	19440	4.2 (4.2)	Na ₂ Li ₃ GaO ₄	540945	6.7 (6.7)
GeAs	9548	1.1 (1.2)	Nb(SCl) ₂	27362	2.6 (2.6)	RbPbI ₃	23517	4.2 (4.2)	K ₂ NaTlF ₆	13798	6.7 (6.7)
LiAuI ₄	505462	1.1 (1.2)	Sr ₅ (AuO ₄) ₂	28796	2.6 (2.6)	Na ₃ PS ₄	28782	4.2 (4.2)	BaGeO ₃	13863	6.7 (6.7)
PtS	288	1.1 (1.2)	CdSi(CuS ₂) ₂	6449	2.6 (2.6)	Ga ₄ GeO ₈	29455	4.2 (4.2)	NaMgH ₃	23730	6.7 (6.7)
As ₂ Ir	15649	1.1 (1.2)	SrPdF ₄	12622	2.6 (2.6)	K ₂ TeS ₃	505556	4.2 (4.2)	HfCl ₄	29422	6.7 (6.7)
CdP ₄	7904	1.1 (1.3)	ZrBrN	541912	2.6 (2.6)	ZnO ₂	8484	4.2 (4.3)	SrZrO ₃	4387	6.7 (6.8)
LiAs	7943	1.1 (1.3)	Li ₃ N	2251	2.6 (2.7)	RbSbO ₂	10418	4.2 (4.3)	Se ₂ (SeO ₃) ₃	31065	6.7 (6.8)
RbS ₅ Te ₈	13336	1.1 (1.3)	AgSbS ₂	3922	2.6 (2.7)	PbI ₂	22883	4.2 (4.3)	BaSeO ₄	12010	6.7 (6.8)
TiNb ₃ O ₆	29699	1.1 (1.3)	Rb ₂ Pt ₃ S ₄	4030	2.6 (2.7)	Rb ₂ TeCl ₆	22975	4.2 (4.3)	TlSbF ₆	8348	6.7 (6.9)
Ba ₂ GeAs ₂	8195	1.1 (1.3)	SnGeS ₃	5045	2.6 (2.7)	SnBr ₂	29862	4.2 (4.3)	RbNa ₂ BO ₃	8872	6.7 (6.9)
TlSe	1836	1.1 (1.4)	NaAgF ₄	7386	2.6 (2.7)	Sr ₃ (BS ₃) ₂	30239	4.2 (4.3)	KNa ₂ BO ₃	8263	6.7 (6.9)
LaAs ₂	505640	1.1 (1.4)	CdIn ₂ O ₄	21047	2.6 (2.7)	LaBN ₂	505493	4.2 (4.3)	RbScO ₂	7650	6.7 (7.1)
PtO ₂	1285	1.1 (1.4)	IrBr ₃	27397	2.6 (2.7)	Li ₄ GeS ₄	510033	4.2 (4.3)	Mg(BeN) ₂	11917	6.7 (7.3)
NaNbSe ₂	7939	1.1 (1.5)	AuCl ₃	27647	2.6 (2.7)	TaTeCl ₉	541877	4.2 (4.3)	KN ₃	827	6.8 (6.8)
Li ₃ LaP ₂	8407	1.1 (1.5)	Sc ₂ PbSe ₄	542826	2.6 (2.7)	BaSe	1253	4.2 (4.4)	Na ₂ SeO ₃	5416	6.8 (6.8)
ZrSe ₂	2076	1.1 (1.9)	NaRhO ₂	8830	2.6 (2.7)	CsAu ₃ Se ₂	9386	4.2 (4.4)	NaCSN	6633	6.8 (6.8)
Mg ₃ Sb ₂	2646	1.1 (1.9)	Sr(AuO ₂) ₂	9298	2.6 (2.7)	Rb ₂ SeCl ₆	27829	4.2 (4.4)	RbLaO ₂	7972	6.8 (6.8)
NbSbRu	505297	1.1 (2.0)	CsIn ₅ S ₈	22007	2.6 (2.7)	YAgO ₂	510034	4.2 (4.4)	KAsOF ₄	17539	6.8 (6.8)
Si	149	1.1 (3.1)	RbSe	9063	2.6 (2.8)	Sr ₃ BPO ₃	9702	4.2 (4.4)	K ₂ Li ₃ GaO ₄	17774	6.8 (6.8)
CdTe	406	1.2 (1.2)	Tl ₃ AsS ₃	9791	2.6 (2.8)	K ₃ AlTe ₃	18378	4.2 (4.4)	CsBrO ₃	28873	6.8 (6.8)
Sr ₂ Ge	2576	1.2 (1.2)	Ag ₂ S	31053	2.6 (2.8)	TiO ₂	390	4.2 (4.5)	Ba ₄ I ₆ O	29909	6.8 (6.8)
LaZnPO	7060	1.2 (1.2)	Cu ₂ PbO ₂	29396	2.6 (2.8)	K ₂ SrTa ₂ O ₇	7148	4.2 (4.5)	Mg ₃ NF ₃	7604	6.8 (6.8)
CsZrCuSe ₃	7152	1.2 (1.2)	Cs ₂ Tel ₆	540957	2.6 (2.9)	BiBrO	23072	4.2 (4.5)	Mg ₄ Ta ₂ O ₉	17481	6.8 (6.8)
LaCuTeS	10288	1.2 (1.2)	NaAuO ₂	20343	2.6 (2.9)	KAs ₄ IO ₆	23126	4.2 (4.6)	CaPbF ₆	20463	6.8 (6.8)
Ba ₃ P ₄	14289	1.2 (1.2)	Ba ₃ In ₂ O ₆	20352	2.6 (3.1)	BPS ₄	27724	4.2 (4.6)	NaI	23268	6.8 (6.8)
Na ₄ FeO ₄	19022	1.2 (1.2)	Ca(AuO ₂) ₂	2898	2.7 (2.7)	Y ₂ NCl ₃	28580	4.2 (4.7)	KLi ₆ TaO ₆	9059	6.8 (6.9)
InP	20351	1.2 (1.2)	NaMgAs	5962	2.7 (2.7)	CaSe	1415	4.2 (5.1)	CaZn ₂ (PO ₄) ₂	18308	6.8 (6.9)
Tl ₅ Se ₂ Br	28921	1.2 (1.2)	Al ₂ ZnTe ₄	7908	2.7 (2.7)	SrZnO ₂	5637	4.3 (4.3)	KHSeO ₃	24433	6.8 (6.9)
Ca(MgBi) ₂	29208	1.2 (1.2)	Cs ₂ ZrSe ₃	9856	2.7 (2.7)	NaGeSbO ₅	6526	4.3 (4.3)	K ₂ BeO ₂	27915	6.8 (6.9)
BaLa ₄	30111	1.2 (1.2)	KBaPSe ₄	18156	2.7 (2.7)	ZnWO ₄	18918	4.3 (4.3)	Na ₃ BO ₃	510256	6.8 (6.9)
Sr ₃ GeO	30950	1.2 (1.2)	HfPbS ₃	22147	2.7 (2.7)	TlCl	23167	4.3 (4.3)	CaI ₂	30031	6.8 (7.2)
LaRhO ₃	5163	1.2 (1.2)	In ₂ O ₃	22323	2.7 (2.7)	K ₄ I ₂ O ₉	27764	4.3 (4.3)	NaCdF ₃	4360	6.9 (6.9)
Ga ₂ HgTe ₄	16337	1.2 (1.2)	Bi ₂ S ₃	22856	2.7 (2.7)	K ₃ IO	28171	4.3 (4.3)	K ₂ SeO ₄	5226	6.9 (6.9)
LiBiO ₃	29077	1.2 (1.3)	AgHgSI	23140	2.7 (2.7)	Na ₃ AuO ₂	28365	4.3 (4.3)	KLao ₂	7958	6.9 (6.9)
RuSe ₂	1922	1.2 (1.4)	Br	23154	2.7 (2.7)	KGaI ₄	29402	4.3 (4.3)	K ₃ AlO ₃	9157	6.9 (6.9)
CoAsS	4627	1.2 (1.4)	KAuCl ₄	27181	2.7 (2.7)	ClF	29504	4.3 (4.3)	Ba ₁₀ P ₆ SO ₂₄	16990	6.9 (6.9)

Ba ₂ GeF ₂	8194	1.2 (1.4)	Cs ₂ PtBr ₆	30062	2.7 (2.7)	K ₃ BrO	504857	4.3 (4.3)	K ₃ Na(SeO ₄) ₂	17839	6.9 (6.9)
Rb ₂ Ni ₃ Se ₄	18691	1.2 (1.4)	Na ₃ MoN ₃	541291	2.7 (2.7)	CsPbI ₃	540839	4.3 (4.3)	NaSi ₂ N ₃	8973	6.9 (6.9)
ZrSe ₃	1683	1.2 (1.4)	Al ₂ CdTe ₄	7909	2.7 (2.7)	CdWO ₄	19387	4.3 (4.4)	ZnCl ₂	22909	6.9 (6.9)
As ₂ Os	2455	1.2 (1.4)	K ₂ AgSb	7643	2.7 (2.8)	Ca ₃ AsBr ₃	504488	4.3 (4.4)	SrO	2472	6.9 (7.0)
Li ₃ Bi	23222	1.2 (1.8)	K ₂ NbCuSe ₄	9003	2.7 (2.8)	Na ₄ ReN ₃	10419	4.3 (4.4)	Sr ₃ GaO ₄ F	6509	6.9 (7.0)
LiNbS ₂	7936	1.2 (1.9)	Rbln ₅ S ₈	20938	2.7 (2.8)	ScCuO ₂	3642	4.3 (4.7)	Rb ₂ Li ₂ GeO ₄	8450	6.9 (7.0)
PdS ₂	13682	1.2 (1.9)	ImSbS ₃	21365	2.7 (2.8)	BaHgO ₂	3915	4.3 (4.9)	K ₄ CdCl ₆	23392	6.9 (7.0)
TlSnPt	30847	1.2 (1.9)	IBr	27639	2.7 (2.8)	Na ₈ Sr ₄ (BN ₂) ₃	10811	4.3 (5.0)	As ₂ SO ₆	27230	6.9 (7.0)
AgF	7592	1.2 (2.6)	RhCl ₃	27770	2.7 (2.8)	NaYS ₂	10226	4.3 (5.1)	ZnF ₂	1873	6.9 (7.0)
Sr ₂ Si	1106	1.3 (1.3)	BiTeCl	28944	2.7 (2.8)	MgTe	1039	4.4 (4.4)	K ₂ WO ₄	18780	6.9 (7.0)
CdGeP ₂	3668	1.3 (1.3)	PdCl ₂	29487	2.7 (2.8)	Li ₅ ReN ₄	3838	4.4 (4.4)	BaSi ₃ SnO ₉	18502	6.9 (7.1)
SrCaSi	7084	1.3 (1.3)	CsCuF ₄	540921	2.7 (2.8)	LiSbO ₃	4995	4.4 (4.4)	SbF ₃	1880	6.9 (7.2)
SrCaGe	12418	1.3 (1.3)	VHgO ₃	541588	2.7 (2.8)	Li ₃ AuS ₂	15999	4.4 (4.4)	Rb ₂ Si ₃ SnO ₉	17382	6.9 (7.2)
Tl ₂ Pt ₂ O ₇	13801	1.3 (1.3)	P ₂ Pd ₃ S ₈	3006	2.7 (2.8)	KVO ₃	18815	4.4 (4.4)	HfO ₂	352	7.0 (7.0)
Ba ₂ Tl ₂ O ₅	18327	1.3 (1.3)	Na ₂ B ₂ Se ₇	5004	2.7 (2.8)	CsBrF	22935	4.4 (4.4)	RbN ₃	743	7.0 (7.0)
CsAuI ₃	28453	1.3 (1.3)	Pd(SeCl ₃) ₂	28175	2.7 (2.8)	CsPbCl ₃	23037	4.4 (4.4)	Cs ₂ Li ₂ GeO ₄	8313	7.0 (7.0)
Ba(MgBi) ₂	29209	1.3 (1.3)	Rb ₄ Zr ₃ Se ₁₄	542013	2.7 (2.8)	VInO ₄	25113	4.4 (4.4)	Tl ₂ SnF ₆	10401	7.0 (7.0)
HfBr ₃	30302	1.3 (1.3)	NaSi	2402	2.7 (2.9)	KTiCl ₄	27385	4.4 (4.4)	Cs ₆ Si ₂ O ₇	18315	7.0 (7.0)
NbSe ₃	541817	1.3 (1.3)	Na ₂ ZrSe ₃	7219	2.7 (2.9)	RbInI ₄	28198	4.4 (4.4)	Na ₃ Ca ₂ TaO ₆	18480	7.0 (7.0)
CdSe	2691	1.3 (1.3)	NaBeAs	9573	2.7 (2.9)	TlCdBr ₃	28219	4.4 (4.4)	LiI	22899	7.0 (7.0)
NaZnP	4824	1.3 (1.3)	Rb ₂ NbCuSe ₄	32542	2.7 (3.0)	K ₄ Br ₂ O	28627	4.4 (4.4)	Rb ₄ CdCl ₆	22930	7.0 (7.0)
HfTiCuSe ₃	9397	1.3 (1.3)	Hg ₂ WO ₄	9564	2.7 (3.0)	Na ₄ SnS ₄	29628	4.4 (4.4)	BaLa ₂ BeO ₅	18414	7.0 (7.0)
Ba(ScTe ₂) ₂	17501	1.3 (1.3)	Ca(MgAs) ₂	2172	2.7 (3.2)	Na ₃ AsS ₃	5830	4.4 (4.4)	LaGeBO ₅	19957	7.0 (7.0)
Te ₂ I	27655	1.3 (1.3)	AlAs	2172	2.7 (3.2)	Cs ₂ PF ₆	9262	4.4 (4.4)	PNCl ₂	23375	7.0 (7.0)
Sb(IF ₃) ₂	504965	1.3 (1.3)	LiMgAs	12558	2.7 (3.2)	Na ₃ GaSe ₃	17148	4.4 (4.4)	NaYGeO ₄	17543	7.0 (7.1)
MgP ₄	384	1.3 (1.4)	KYTe ₂	16763	2.7 (3.6)	K ₃ TaS ₄	18148	4.4 (4.4)	Ba(BrO ₃) ₂	505008	7.0 (7.1)
Rb ₂ As ₃	8279	1.3 (1.4)	La ₄ Se ₃ O ₄	4412	2.8 (2.8)	KCuS	28270	4.4 (4.4)	PbSO ₄	22298	7.0 (7.2)
GeAs ₂	15556	1.3 (1.4)	Tl ₃ BO ₃	4584	2.8 (2.8)	Na ₅ InS ₄	505414	4.4 (4.4)	NaScO ₂	7914	7.0 (7.7)
GeAs ₂	17524	1.3 (1.4)	KTa(CuSe ₂) ₂	6013	2.8 (2.8)	ZrNCl	542791	4.4 (4.4)	LaAlO ₃	2920	7.1 (7.1)
Ta ₃ I ₇	23238	1.3 (1.4)	K ₂ Sn ₂ O ₃	8624	2.8 (2.8)	CsNO ₂	3288	4.4 (4.5)	CaMgAsO ₄ F	7035	7.1 (7.1)
P ₁₀ AurI	27370	1.3 (1.4)	CsNbN ₂	8978	2.8 (2.8)	K ₂ B ₂ S ₇	4351	4.4 (4.5)	LiInP ₂ O ₇	8491	7.1 (7.1)
NbTeBr ₃	28038	1.3 (1.4)	BaHFN ₂	10322	2.8 (2.8)	Sr ₂ Ta ₂ N ₃	17518	4.4 (4.5)	CsNa ₂ BO ₃	8871	7.1 (7.1)
K ₂ SnTe ₅	28080	1.3 (1.4)	CsLaCdTe ₃	12491	2.8 (2.8)	Na ₅ AsO ₅	17816	4.4 (4.5)	RbAlO ₂	14070	7.1 (7.1)
VS ₄	541155	1.3 (1.4)	ZnPdF ₆	13983	2.8 (2.8)	Ge ₂ S ₃ Br ₂	540792	4.4 (4.5)	Na ₄ Hf ₂ (GeO ₄) ₃	14526	7.1 (7.1)
SnSe	691	1.3 (1.4)	Cs ₃ Na ₂ SnP ₃	17707	2.8 (2.8)	Zn(GaO ₂) ₂	5794	4.4 (4.5)	K ₂ ZrGe ₂ O ₇	16871	7.1 (7.1)
Zn ₂ Cu(AsO ₄) ₂	6278	1.3 (1.4)	K ₃ InP ₂	20256	2.8 (2.8)	Y ₆ WO ₁₂	19005	4.4 (4.5)	Zr ₃ Tl ₂ O _F ₁₂	17315	7.1 (7.1)
NaSb	7944	1.3 (1.4)	Sr(InSe) ₂	21733	2.8 (2.8)	Cs ₂ SeCl ₆	27830	4.4 (4.5)	CdS ₂ O ₇	17586	7.1 (7.1)
Tl ₃ GeTe ₃	17217	1.3 (1.5)	TlSbS ₂	28230	2.8 (2.8)	InGaBr ₄	541283	4.4 (4.5)	RbZnPO ₄	18463	7.1 (7.1)
Tl ₂ Te ₃	29711	1.3 (1.5)	Ca ₂ TeSe ₂	28423	2.8 (2.8)	NaInO ₂	5175	4.4 (4.6)	Rb ₃ PbCl ₅	29883	7.1 (7.1)

Appendix A. Calculated Bandgaps of the Materials Project Entries

In ₂ HgS ₄	22356	1.3 (1.5)	Na ₂ PdCl ₄	29359	2.8 (2.8)	HgCl	22897	4.4 (4.6)	Y ₂ C(NO) ₂	546864	7.1 (7.1)
KNbS ₂	7938	1.3 (1.6)	Cl ₂ O	505466	2.8 (2.8)	BiF ₅	27743	4.4 (4.6)	CsSO ₂ F	6368	7.1 (7.2)
LiCuO ₂	9158	1.3 (1.6)	Ga ₂ HgS ₄	4809	2.8 (2.8)	ZnSO	3519	4.4 (5.0)	Li ₂ CN ₂	9610	7.1 (7.2)
Cu ₂ Te ₂ Cl	30971	1.3 (1.7)	Sr ₃ (AlP ₂) ₂	9843	2.8 (2.8)	CaHgO ₂	7041	4.4 (5.0)	Rb ₂ LiAsO ₄	14363	7.1 (7.2)
NaNbS ₂	7937	1.3 (1.9)	K ₃ Ag ₃ As ₂	14206	2.8 (2.8)	Sr ₄ Li(BN ₂) ₃	9723	4.4 (5.1)	KScO ₂	8188	7.1 (7.5)
NbFeSb	9437	1.3 (2.0)	NaBiO ₂	22984	2.8 (2.8)	Li ₂ Te	2530	4.4 (5.2)	Li ₄ GeO ₄	4558	7.2 (7.2)
Ag ₂ CO ₃	4691	1.3 (2.1)	TlAuCl ₄	28368	2.8 (2.8)	BeSe	1541	4.4 (5.9)	LiScO ₂	5840	7.2 (7.2)
ScN	2857	1.3 (2.2)	Cs ₂ Au ₂ Se ₃	29194	2.8 (2.8)	NO ₂	2789	4.5 (4.5)	Cs ₂ NaAsO ₄	8314	7.2 (7.2)
RbSb	7444	1.4 (1.4)	NaAgO	6983	2.8 (2.9)	Rb ₂ HgO ₂	5072	4.5 (4.5)	Cs ₂ ZrO ₃	8759	7.2 (7.2)
LiZnN	7575	1.4 (1.4)	Tl ₂ PAuS ₄	9510	2.8 (2.9)	KBaPS ₄	17088	4.5 (4.5)	Ba ₃ (AsO ₄) ₂	9783	7.2 (7.2)
Sr(ZnP) ₂	8276	1.4 (1.4)	RbTa ₃ (CuSe ₂) ₂	11925	2.8 (2.9)	NaVCuO ₄	19449	4.5 (4.5)	ZnSnF ₆	13903	7.2 (7.2)
Ba(AgTe) ₂	18501	1.4 (1.4)	AgAsS ₂	13740	2.8 (2.9)	I ₂ O ₅	23261	4.5 (4.5)	CsZnPO ₄	18673	7.2 (7.2)
InAgS ₂	19833	1.4 (1.4)	K ₇ TaAs ₄	18073	2.8 (2.9)	HgBr ₂	23292	4.5 (4.5)	IF ₅	23257	7.2 (7.2)
RbPb	21525	1.4 (1.4)	InI	23202	2.8 (2.9)	TiBr ₄	27634	4.5 (4.5)	Ca ₂ Hf ₇ O ₁₆	27221	7.2 (7.2)
KPb	21526	1.4 (1.4)	Ca ₃ C ₃ Cl ₂	28160	2.8 (2.9)	Ti(SeO ₃) ₂	29260	4.5 (4.5)	TaAgF ₆	29993	7.2 (7.2)
Cs ₂ PtI ₆	23060	1.4 (1.4)	HgI	22859	2.8 (2.9)	GaCuCl ₄	505410	4.5 (4.5)	Si ₂ CN ₄	30161	7.2 (7.2)
Bi ₂ Pt ₂ O ₇	23341	1.4 (1.4)	K ₄ CdP ₂	28302	2.8 (2.9)	CsSbO ₂	510273	4.5 (4.5)	Sr ₁₀ P ₆ SO ₂₄	17447	7.2 (7.2)
TlAgSe	29238	1.4 (1.4)	Cs(SbS ₂) ₂	8890	2.8 (3.0)	MgGeN ₂	7798	4.5 (4.5)	NaBrO ₃	23339	7.2 (7.2)
BaNaBi	31235	1.4 (1.4)	Tl ₃ BS ₃	505399	2.8 (3.0)	KNaTe	8755	4.5 (4.5)	La ₂ MgGeO ₆	11585	7.2 (7.3)
Nb ₁₃ O	546285	1.4 (1.4)	Cs ₂ Ti(CuSe ₂) ₂	10489	2.8 (3.0)	LaVO ₄	19162	4.5 (4.5)	Cs ₁ Na ₃ Li ₁₂ (GeO ₄) ₄	17125	7.2 (7.3)
Te ₂ Mo	602	1.4 (1.4)	Rb ₂ TeI ₆	28070	2.8 (3.0)	Rb ₄ In ₂ S ₅	27670	4.5 (4.5)	Na ₄ SiO ₄	7500	7.2 (7.3)
ZnCu ₂ GeS ₄	6408	1.4 (1.4)	SnS ₂	1170	2.8 (3.1)	Rb ₂ SnO ₂	27931	4.5 (4.5)	Cs ₂ Li ₂ TiO ₄	8294	7.2 (7.3)
PbSe	20667	1.4 (1.4)	LiCuO	5127	2.8 (3.1)	K ₂ HgS ₂	28859	4.5 (4.5)	Si ₃ N ₄	988	7.2 (7.4)
In ₂ HgSe ₄	20731	1.4 (1.4)	Cs ₂ NbCuSe ₄	15223	2.8 (3.1)	CsBiO ₂	29506	4.5 (4.5)	TlTeF ₅	29903	7.2 (7.4)
K(MoS) ₃	8116	1.4 (1.5)	RbBiS ₂	505761	2.8 (3.2)	Sr ₂ SnS ₄	30294	4.5 (4.5)	BasO ₄	3277	7.2 (7.6)
Rb(MoS) ₃	8117	1.4 (1.5)	LaBi ₂ IO ₄	546672	2.8 (3.2)	Ge ₂ N ₂ O	4187	4.5 (4.6)	SrGa ₂ (SiO ₄) ₂	14235	7.3 (7.3)
Ba ₂ Cu(PO ₄) ₂	9372	1.4 (1.5)	NbCu ₃ S ₄	5621	2.8 (3.2)	Sn ₂ OF ₂	27480	4.5 (4.6)	Na ₄ TiO ₄	14726	7.3 (7.3)
Ag ₂ GeS ₃	9900	1.4 (1.5)	LaSO	28626	2.8 (3.4)	P ₂ S ₅	541788	4.5 (4.6)	KLi ₃ GeO ₄	18002	7.3 (7.3)
K ₂ Pd ₃ Se ₄	14339	1.4 (1.5)	RbYTe ₂	16764	2.8 (3.6)	PbF ₄	341	4.5 (4.7)	KI	22898	7.3 (7.3)
Ca ₃ (GeAs ₂) ₂	18504	1.4 (1.5)	B ₆ O	1346	2.9 (2.9)	InClO	27702	4.5 (4.7)	RbI	22903	7.3 (7.3)
BeP ₂	27148	1.4 (1.5)	ZnGeN ₂	2979	2.9 (2.9)	Li ₄ TaN ₃	505795	4.5 (4.7)	Li ₂ CaGeO ₄	7611	7.3 (7.3)
Te ₂ Br	27648	1.4 (1.5)	Hg ₂ NO ₄	5824	2.9 (2.9)	Ca ₃ AsCl ₃	28069	4.5 (4.7)	SrZn ₂ (PO ₄) ₂	8810	7.3 (7.3)
Na ₂ SbAu	7774	1.4 (1.5)	Sr ₄ As ₂ O	8299	2.9 (2.9)	SnF ₃	8289	4.5 (4.8)	LiGa ₅ SiO ₄	18147	7.3 (7.3)
TlInTe ₂	22791	1.4 (1.5)	Rb ₂ PtC ₂	10919	2.9 (2.9)	BaNb ₂ O ₆	28150	4.5 (4.8)	BaIF	22951	7.3 (7.3)
Cs ₂ PdI ₆	505635	1.4 (1.5)	BaPdF ₄	12623	2.9 (2.9)	La ₂ SeO ₂	7233	4.5 (4.9)	K ₄ Be ₃ O ₅	28158	7.3 (7.3)
Cs ₂ Ni ₃ Se ₄	14336	1.4 (1.6)	K ₂ CuAs	15684	2.9 (2.9)	SrSe	2758	4.5 (5.0)	NaLi ₂ AsO ₄	9066	7.3 (7.4)
Sr ₃ As ₄	15339	1.4 (1.6)	BaAgTeF	16742	2.9 (2.9)	LiCa ₄ (BN ₂) ₃	6799	4.5 (5.1)	CaO	2605	7.3 (7.6)
P ₂ Os	2319	1.4 (1.7)	K ₄ Ta ₂ S ₁₁	18664	2.9 (2.9)	Rb ₂ HgF ₄	8962	4.5 (5.6)	CdSnF ₆	13907	7.4 (7.4)
CoAgO ₂	19178	1.4 (1.7)	LiInSe ₂	20187	2.9 (2.9)	Na ₂ Te	2784	4.6 (4.6)	KZnPO ₄	18591	7.4 (7.4)

Cd ₂ As ₃ I	27577	1.4 (1.7)	K ₄ BeAs ₂	29584	2.9 (2.9)	Cs ₃ NaTe	5339	4.6 (4.6)	NbF ₅	18687	7.4 (7.4)
SnSe ₂	665	1.4 (1.8)	MgB ₉ N	30091	2.9 (2.9)	CaGeN ₂	7801	4.6 (4.6)	LaBrO	23023	7.4 (7.4)
P ₂ Pt	730	1.4 (1.9)	Ga ₂ PdBr ₈	30945	2.9 (2.9)	NaLiTe	8754	4.6 (4.6)	K ₂ ZrO ₃	18449	7.4 (7.4)
Li ₄ NCl	29149	1.4 (2.0)	K ₂ CuP	8446	2.9 (2.9)	NaAlSe ₂	17060	4.6 (4.6)	SrIF	23046	7.4 (7.4)
ZrCoBi	31451	1.4 (2.1)	K ₂ AgP	9778	2.9 (2.9)	TlSnF ₇	17649	4.6 (4.6)	Ba ₃ Nb ₂ O ₈	542201	7.4 (7.4)
TiCoSb	5967	1.4 (2.2)	Cs ₂ Pt ₃ S ₄	13992	2.9 (2.9)	NaVO ₃	19083	4.6 (4.6)	AlTiF ₄	3751	7.4 (7.5)
CdHgO ₂	9146	1.5 (1.5)	SrCuSeF	21228	2.9 (2.9)	KNaV ₂ O ₆	19432	4.6 (4.6)	Li ₃ AsO ₄	9197	7.4 (7.5)
BaCu ₂ SnSe ₄	12364	1.5 (1.5)	K ₂ NaInP ₂	21511	2.9 (2.9)	CsCu ₂ Cl ₃	23065	4.6 (4.6)	Zr ₂ P ₂ O ₉	27132	7.4 (7.5)
Zn(InTe ₂) ₂	20832	1.5 (1.5)	ReNClF ₅	23098	2.9 (2.9)	KIO ₃	23487	4.6 (4.6)	PbF ₂	315	7.4 (7.5)
PbS	21276	1.5 (1.5)	Ba(AlTe ₂) ₂	28505	2.9 (2.9)	K ₂ SnCl ₆	23499	4.6 (4.6)	NaZnF ₃	3795	7.5 (7.5)
ClO ₂	23207	1.5 (1.5)	InTeI	505356	2.9 (2.9)	LiGaBr ₃	28327	4.6 (4.6)	Li ₂ TiF ₆	7603	7.5 (7.5)
Ba ₃ (Si ₂ P ₃) ₂	27887	1.5 (1.5)	AuF ₃	942	2.9 (3.0)	Cs ₂ AgI ₃	540881	4.6 (4.6)	InBF ₄	8586	7.5 (7.5)
Sr ₃ (InP ₂) ₂	28324	1.5 (1.5)	CdO ₂	2310	2.9 (3.0)	BaTeO ₃	5431	4.6 (4.6)	AlBr ₃	23288	7.5 (7.5)
Y ₄ OsBr ₄	28744	1.5 (1.5)	Rb ₂ S ₃	7446	2.9 (3.0)	K ₂ HgO ₂	5860	4.6 (4.6)	BaTiF ₆	8291	7.5 (7.5)
Te ₄ MoBr	29190	1.5 (1.5)	NbNO	7596	2.9 (3.0)	TaTi ₃ S ₄	7562	4.6 (4.6)	Rb ₂ LiGaF ₆	14638	7.5 (7.5)
Na ₁₀ CaSn ₁₂	30252	1.5 (1.5)	K ₄ HgP ₂	8753	2.9 (3.0)	BaTi(BO ₃) ₂	11659	4.6 (4.6)	CsMgBr ₃	29750	7.5 (7.5)
SrLiBi	510112	1.5 (1.5)	K ₂ NaAlAs ₂	9069	2.9 (3.0)	KL ₂ Si ₄	12924	4.6 (4.6)	RbGaCl ₄	30231	7.5 (7.5)
Nb ₂ Se ₉	541106	1.5 (1.5)	BaSnS ₂	12181	2.9 (3.0)	Rb ₃ Ta ₅	17220	4.6 (4.6)	BiF ₃	23237	7.5 (7.6)
K ₂ NiAs ₂	9673	1.5 (1.5)	SrLiP	13276	2.9 (3.0)	LiInGeO ₄	17854	4.6 (4.6)	LiYO ₂	7020	7.6 (7.6)
CdCu ₂ GeS ₄	13982	1.5 (1.5)	SbSI	23041	2.9 (3.0)	Na ₂ Si ₂ Se ₅	18562	4.6 (4.7)	AsPO ₄	8140	7.6 (7.6)
LiAg ₃ O ₂	27227	1.5 (1.5)	Na ₃ BiO ₄	27345	2.9 (3.0)	Sr ₂ ZnWO ₆	19282	4.6 (4.7)	ScBO ₃	8697	7.6 (7.6)
NaAg ₃ O ₂	27303	1.5 (1.5)	K ₃ SnSe ₃	541875	2.9 (3.0)	Tl ₂ SnCl ₆	27832	4.6 (4.7)	NaAlO ₂	9212	7.6 (7.6)
CuP ₂	927	1.5 (1.6)	NaAlTe ₂	10163	2.9 (3.0)	SB ₂ O	28407	4.6 (4.7)	LaCl ₃	22896	7.6 (7.6)
CuSbSe ₂	20331	1.5 (1.6)	TlI ₃	28329	2.9 (3.0)	BaS	1500	4.6 (4.7)	CsAsF ₄	5707	7.6 (7.6)
Rb ₂ (NbCl ₃) ₃	22976	1.5 (1.6)	Ag ₂ SO ₄	5625	2.9 (3.1)	Na ₃ AgS ₂	9634	4.6 (4.8)	CsK ₂ Sc(PO ₄) ₂	8564	7.6 (7.7)
CuBiSeO	23116	1.5 (1.6)	BaYAgSe ₃	6647	2.9 (3.1)	CsAgCl ₂	542772	4.6 (4.9)	LiGeBO ₄	8873	7.6 (7.8)
ZrCl ₂	23162	1.5 (1.6)	Ca ₄ As ₂ O	8789	2.9 (3.1)	Na ₂ O ₂	2340	4.6 (4.9)	K ₂ Pb(SO ₄) ₂	21099	7.6 (7.8)
Rb ₃ Bi	23304	1.5 (1.6)	K ₂ Tel ₆	27688	2.9 (3.1)	BiClO	22939	4.6 (5.2)	BN	984	7.6 (7.9)
RbAuBr ₃	27300	1.5 (1.6)	Sr ₂ PbO ₄	20944	2.9 (3.1)	Cs ₂ HgF ₄	8963	4.6 (5.6)	CsLiBr ₂	23057	7.6 (7.9)
CuBiS ₂	22982	1.5 (1.7)	Na ₂ PtO ₂	22313	2.9 (3.2)	BaZnO ₂	4236	4.7 (4.7)	Na ₂ MgSiO ₄	6406	7.7 (7.7)
Hg ₂ As ₃ Br	28899	1.5 (1.7)	K ₂ SiP ₂	8235	2.9 (3.3)	Sr(BS ₂) ₂	8947	4.7 (4.7)	InF ₃	6949	7.7 (7.7)
VCu ₃ Se ₄	7670	1.5 (1.7)	Cs ₂ SiP ₂	8932	2.9 (3.4)	KAg(NO ₃) ₂	18429	4.7 (4.7)	K ₆ Si ₂ O ₇	30990	7.7 (7.7)
Ca(BC) ₂	21855	1.5 (1.8)	HgF	706	2.9 (3.7)	Sr ₂ CaWO ₆	18742	4.7 (4.7)	ScOF	4661	7.7 (7.7)
LaS ₂	1508	1.5 (2.0)	RbAu	30373	2.9 (4.0)	Sr ₂ MgWO ₆	19420	4.7 (4.7)	AlAsO ₄	7849	7.7 (7.7)
TlInS ₂	20042	1.5 (2.0)	AIP	1550	2.9 (4.6)	TlIO ₃	22981	4.7 (4.7)	Ba ₂ Zn ₇ F ₁₈	541827	7.7 (7.7)
NaSnP	29529	1.5 (2.0)	GaN	805	3.0 (3.0)	GaBr ₂	28384	4.7 (4.7)	GaPO ₄	3518	7.8 (7.8)
SrP	7931	1.5 (2.1)	LaSF	5394	3.0 (3.0)	HfNCl	29302	4.7 (4.7)	Zn(PO ₃) ₂	8230	7.8 (7.8)
K ₂ Te ₂ Pt	8623	1.5 (2.1)	Tl ₃ VS ₄	5513	3.0 (3.0)	NaNbO ₃	541911	4.7 (4.7)	Cs ₂ NbF ₆	8995	7.8 (7.8)
							4514	4.7 (4.7)	NaPN ₂	10572	7.8 (7.8)

Appendix A. Calculated Bandgaps of the Materials Project Entries

Bi ₂ SeO ₂	552098	1.5 (2.3)	NaNb(CuS ₂) ₂	6181	3.0 (3.0)	CsO	7896	4.7 (4.8)	Na ₃ TaF ₈	17245	7.8 (7.8)
CaAgO ₂	11020	1.5 (2.5)	YSF	10086	3.0 (3.0)	Ba ₂ CaWO ₆	19182	4.7 (4.8)	BaBr ₂	27456	7.8 (7.8)
TaSbRu	31454	1.5 (2.5)	NaSrP	13275	3.0 (3.0)	Cl ₂	22848	4.7 (4.8)	Na ₄ B ₂ O ₅	27564	7.8 (7.8)
ZnSiAs ₂	3595	1.6 (1.6)	NaBiO ₃	23054	3.0 (3.0)	RbGeO ₆	549697	4.7 (4.8)	SrBe ₃ O ₄	27791	7.8 (7.8)
KCuTe	7436	1.6 (1.6)	Tl ₂ PtCl ₆	504695	3.0 (3.0)	Ba ₃ Nb ₂ ZnO ₉	7249	4.7 (4.9)	Rb ₂ NbF ₆	8994	7.8 (7.8)
MgAs ₄	7623	1.6 (1.6)	AuBr	505366	3.0 (3.0)	KLAs ₂	15781	4.7 (4.9)	K ₃ Sc(PO ₄) ₂	17035	7.8 (7.8)
BaP ₃	7808	1.6 (1.6)	Hg ₃ (TeBr) ₂	27853	3.0 (3.0)	Bi ₃	23189	4.7 (4.9)	BaZnCl ₄	23373	7.8 (7.8)
RbAs	10802	1.6 (1.6)	Al ₂ PdCl ₈	504547	3.0 (3.1)	BaTiO ₃	5020	4.7 (5.0)	Sr ₂ Si ₂ O ₇	5594	7.8 (7.9)
NaSe	15668	1.6 (1.6)	Sr ₄ P ₂ O	8298	3.0 (3.1)	RbLaS ₂	9361	4.7 (5.0)	LiBiF ₄	505032	7.8 (8.1)
PdI ₂	23484	1.6 (1.6)	K ₃ Cu ₃ As ₂	14205	3.0 (3.1)	LiZnPS ₄	11175	4.7 (5.0)	SrCO ₃	3822	7.9 (7.9)
Na ₁₀ SrSn ₁₂	27747	1.6 (1.6)	BaLa ₂ ZnS ₅	16452	3.0 (3.1)	KLiTe	4495	4.8 (4.8)	Si ₂ N ₂ O	4497	7.9 (7.9)
Ca ₃ BiN	30253	1.6 (1.6)	PPbSe ₃	20316	3.0 (3.1)	Al ₂ CdS ₄	5928	4.8 (4.8)	CsAlO ₂	14069	7.9 (7.9)
Sb ₂ Se ₃	31149	1.6 (1.6)	As(BrF ₂) ₃	28159	3.0 (3.1)	Cd ₂ B ₂ O ₅	7210	4.8 (4.8)	Se ₂ (SO ₄) ₃	16800	7.9 (7.9)
Sr ₃ SbN	2160	1.6 (1.6)	Pd(SCl ₃) ₂	28174	3.0 (3.1)	Sr ₂ Ta ₂ O ₇	12286	4.8 (4.8)	MgBr ₂	30034	7.9 (7.9)
Ca(ZnP) ₂	7752	1.6 (1.6)	CsBiS ₂	541378	3.0 (3.1)	KBS ₂	15012	4.8 (4.8)	LiInF ₄	8892	7.9 (7.9)
Rb ₂ Te ₃	9569	1.6 (1.6)	K ₂ P ₂ Se ₇	542637	3.0 (3.1)	MgSe ₂ O ₅	16771	4.8 (4.8)	LaClO	17208	7.9 (7.9)
NaAuSe ₂	2095	1.6 (1.7)	Na ₃ AgO ₂	3527	3.0 (3.1)	Ba ₃ Te ₂ O ₉	17009	4.8 (4.8)	LaClO	23025	7.9 (7.9)
TeAuI	29139	1.6 (1.7)	Cs ₂ NbAgSe ₄	14637	3.0 (3.1)	Tl ₂ MoO ₄	18938	4.8 (4.8)	Na ₂ SiO ₃	4533	7.9 (8.1)
Rb ₂ Pd ₃ Se ₄	504668	1.6 (1.7)	CsCu ₃ O ₂	553303	3.0 (3.1)	Rb ₂ SnCl ₆	23059	4.8 (4.8)	ZrSiO ₄	4820	7.9 (8.1)
Rb ₃ Sn ₄ Au	14340	1.6 (1.7)	Ca ₄ P ₂ O	5380	3.0 (3.2)	KTiF ₄	27209	4.8 (4.8)	Ca ₄ LaB ₃ O ₁₀	6076	8.0 (8.0)
TeRhCl	17401	1.6 (1.7)	Zr(PS ₃) ₂	8203	3.0 (3.2)	Sr(BiO ₂) ₂	29048	4.8 (4.8)	KNbF ₆	7571	8.0 (8.0)
Y ₂ Cl ₃	22945	1.6 (1.7)	Ca ₂ PbO ₄	21137	3.0 (3.2)	AlBiBr ₆	31268	4.8 (4.8)	NaBr	22916	8.0 (8.0)
SnS	27678	1.6 (1.7)	BiIO	22987	3.0 (3.3)	TiSO ₅	505270	4.8 (4.8)	Li ₆ MgBr ₈	29008	8.0 (8.0)
K ₂ Ni ₃ S ₄	2231	1.6 (1.8)	Sn ₂ OF ₅	29590	3.0 (3.6)	TaCl ₄ F	27854	4.8 (4.8)	NaBO ₂	3889	8.0 (8.0)
LaI ₂	17228	1.6 (1.8)	Mg ₃ P ₂	2514	3.1 (3.1)	K ₃ Ta ₃ (BO ₆) ₂	9870	4.8 (4.9)	CsNbF ₆	11980	8.0 (8.1)
CuTe ₂ Br	23194	1.6 (1.9)	Rb ₂ GeSe ₃	9794	3.1 (3.1)	MgWO ₄	18875	4.8 (4.9)	BCl ₃	23184	8.0 (8.1)
NaTaN ₂	31036	1.6 (1.9)	K ₄ ZnP ₂	11719	3.1 (3.1)	Sr ₂ CdWO ₆	19014	4.8 (4.9)	ScPO ₄	4200	8.0 (8.2)
BaAg ₂ GeS ₄	5475	1.6 (2.0)	CdPdF ₆	13984	3.1 (3.1)	NbBiO ₄	23413	4.8 (4.9)	CaBr ₂	22888	8.1 (8.1)
KAg ₂ AsO ₄	7394	1.6 (2.4)	Y ₂ MgSe ₄	15803	3.1 (3.1)	Li ₅ Br ₂ N	29025	4.8 (4.9)	CsBr	22906	8.1 (8.1)
GeSe	12015	1.6 (2.5)	K ₂ PdCl ₄	22956	3.1 (3.1)	TeSeO ₄	29299	4.8 (4.9)	RbLiBr ₂	28237	8.1 (8.1)
Ga ₂ Te ₅	700	1.7 (1.7)	PtCl ₂	23290	3.1 (3.1)	Tl ₂ ZnI ₄	30532	4.8 (4.9)	NaTeF ₅	29355	8.1 (8.1)
SrLiSb	2371	1.7 (1.7)	K ₃ Al ₂ As ₃	28347	3.1 (3.1)	RbCdBr ₃	504529	4.8 (4.9)	CsCaBr ₃	30056	8.1 (8.2)
KZrCuS ₃	7756	1.7 (1.7)	Sr ₂ GeSe ₄	30293	3.1 (3.1)	Ca ₃ V ₂ O ₈	542076	4.8 (4.9)	Sr ₃ Sc(BO ₃) ₃	17562	8.1 (8.2)
Ca(CdP) ₂	9317	1.7 (1.7)	KAgF ₄	7387	3.1 (3.2)	Ba(BS ₂) ₂	30126	4.8 (4.9)	SrLiBO ₃	10814	8.1 (8.3)
YAgTe ₂	9570	1.7 (1.7)	K ₃ Cu ₃ P ₂	7439	3.1 (3.2)	InPO ₄	7566	4.8 (5.0)	LiAlO ₂	3427	8.2 (8.2)
RbPt ₂ Se ₃	12903	1.7 (1.7)	PBr ₅	22874	3.1 (3.2)	CsAu ₃ S ₂	9384	4.8 (5.0)	Ba ₂ Mg(BO ₃) ₂	9259	8.2 (8.2)
Zn(GaTe ₂) ₂	14797	1.7 (1.7)	SbSBr	22971	3.1 (3.2)	Ba ₂ SnO ₄	3359	4.8 (5.1)	ZnP ₄ O ₁₁	15438	8.2 (8.2)
	15777	1.7 (1.7)	HgPS ₃	27178	3.1 (3.2)	SO ₂	27726	4.8 (5.2)	Sr ₂ SiO ₄	18510	8.2 (8.2)

Sr ₃ (GeAs ₂) ₂	17504	1.7 (1.7)	SmI ₂	27194	3.1 (3.2)	CaS	1672	4.8 (5.5)	Na ₂ CO ₃	22381	8.2 (8.2)
PtBr ₃	23165	1.7 (1.7)	IrCl ₃	27666	3.1 (3.2)	HfSO	7787	4.8 (5.5)	Sr(ClO ₃) ₂	504991	8.2 (8.3)
TiNCl	27850	1.7 (1.7)	ZrP ₂ S ₇	31014	3.1 (3.2)	Na ₂ Se	1266	4.9 (4.9)	LaOF	7100	8.2 (8.4)
ReSe ₂	541582	1.7 (1.7)	K ₂ NaGaP ₂	9666	3.1 (3.2)	LiGaS ₂	3647	4.9 (4.9)	BeSiN ₂	7913	8.2 (8.4)
CdAg ₄ Ge ₂ S ₇	542200	1.7 (1.7)	SeBr	540943	3.1 (3.2)	KGeNO	6955	4.9 (4.9)	ZrPbF ₆	7310	8.3 (8.3)
Tl ₂ O	551470	1.7 (1.7)	Rb ₂ Tl(CuS ₂) ₂	7129	3.1 (3.3)	MgSe	13031	4.9 (4.9)	Mg ₂ BO ₃ F	7995	8.3 (8.3)
KTe	2072	1.7 (1.7)	V ₂ O ₅	510583	3.1 (3.3)	ZnSe ₂ O ₅	18373	4.9 (4.9)	Na ₃ Sc ₂ (PO ₄) ₃	16956	8.3 (8.3)
Ga ₂ HgSe ₄	4730	1.7 (1.7)	Tl ₂ SiSe ₃	14241	3.1 (3.3)	CaMoO ₄	19330	4.9 (4.9)	LiBr	23259	8.3 (8.3)
LiCaSb	16264	1.7 (1.7)	YBi ₂ BrO ₄	553243	3.1 (3.4)	PbBrF	23008	4.9 (4.9)	Ge(SF ₆) ₂	28291	8.3 (8.3)
Ca(RhO ₂) ₂	17998	1.7 (1.7)	KTlO	27716	3.1 (3.5)	KNaSe	28595	4.9 (4.9)	NaCNO	546500	8.3 (8.5)
TePb	19717	1.7 (1.7)	YBi ₂ IO ₄	551816	3.1 (3.5)	OsO ₄	540783	4.9 (4.9)	AsF ₅	8723	8.4 (8.4)
TiBrN	27849	1.7 (1.7)	BaS ₂	684	3.2 (3.2)	Ba ₃ SbClO ₂	545500	4.9 (4.9)	Ba ₂ SiO ₄	17612	8.4 (8.4)
Na ₂ AsAu	7773	1.7 (1.8)	TaTl(CuS ₂) ₂	9815	3.2 (3.2)	BaO	1342	4.9 (4.9)	RbBr	22867	8.4 (8.4)
RbCu ₃ S ₂	10985	1.7 (1.8)	Ba(BeN) ₂	12927	3.2 (3.2)	K ₂ ZnO ₂	8187	4.9 (4.9)	YClO	504786	8.4 (8.4)
KNa ₄ GeAs ₃	16921	1.7 (1.8)	CuBS ₂	12954	3.2 (3.2)	RhIO ₃	27193	4.9 (4.9)	KBr	23251	8.4 (8.4)
Si ₂ O _s	17123	1.7 (1.8)	K ₃ GeSe ₃	14435	3.2 (3.2)	MgTi ₂ O ₅	28232	4.9 (4.9)	BaSiO ₃	7339	8.4 (8.5)
TaI ₂ O	29027	1.7 (1.8)	Rb ₂ WS ₄	17048	3.2 (3.2)	CsNaSe	8658	4.9 (5.0)	AsF ₃	28027	8.4 (8.5)
TeAuBr ₈	541134	1.7 (1.8)	RbPSe ₆	17945	3.2 (3.2)	Ca(BeN) ₂	11918	4.9 (5.0)	BaHf(PO ₄) ₂	545548	8.4 (8.5)
Cs ₂ Pd(IBr ₂) ₂	543024	1.7 (1.8)	Na ₃ GeSe ₃	18411	3.2 (3.2)	LaCuO ₂	20072	4.9 (5.0)	MgCO ₃	5349	8.4 (8.9)
Na ₂ GeAs ₃	16861	1.7 (1.8)	KPS ₆	18625	3.2 (3.2)	Na ₃ BS ₃	29976	4.9 (5.0)	YOF	3637	8.5 (8.5)
K ₂ VCuSe ₄	15220	1.7 (1.9)	PbF ₃	20652	3.2 (3.2)	Tl ₃ AsO ₄	15573	4.9 (5.1)	BaZnF ₄	3881	8.5 (8.5)
AuClO	27265	1.7 (1.9)	Rb ₂ PbO ₃	21489	3.2 (3.2)	KAs ₄ BrO ₆	23083	4.9 (5.1)	Tl ₂ SIF ₆	5033	8.5 (8.5)
Bi ₄ O ₇	30303	1.7 (1.9)	Na ₄ SnSe ₄	28768	3.2 (3.2)	InBO ₃	7027	4.9 (5.3)	KAsF ₆	7569	8.5 (8.5)
Ba(PdS ₂) ₂	505230	1.7 (1.9)	AsCl ₅	30106	3.2 (3.2)	Rb ₂ O	1394	4.9 (5.3)	KAlSiO ₄	9480	8.5 (8.5)
YN	2114	1.7 (2.0)	Hg ₃ (TeCl) ₂	504706	3.2 (3.2)	P ₃ N ₅	1954	4.9 (5.6)	CaCO ₃	3953	8.5 (8.5)
NaCuO ₂	4541	1.7 (2.0)	Ba ₂ PdF ₆	505621	3.2 (3.2)	CdCO ₃	4385	4.9 (5.7)	CsMgPO ₄	18329	8.5 (8.5)
K ₂ Sn ₂ Se ₅	8966	1.7 (2.0)	Cs ₂ AgSbS ₄	510710	3.2 (3.2)	RbLiSe	9250	5.0 (5.0)	BaBeSiO ₄	550751	8.5 (8.6)
NaInTe ₂	22483	1.7 (2.0)	AsS	542810	3.2 (3.2)	RbBS ₂	15013	5.0 (5.0)	K ₂ ZnF ₄	9583	8.5 (9.4)
FeS ₂	1522	1.7 (2.1)	LaCuSeO	552488	3.2 (3.2)	Sr ₂ InI ₅	23504	5.0 (5.0)	GaF ₃	588	8.6 (8.6)
RuS ₂	2030	1.7 (2.1)	MgPdF ₆	7921	3.2 (3.2)	KSn ₂ Cl ₅	23539	5.0 (5.0)	RbNa ₃ Li ₁₂ (SiO ₄) ₄	17240	8.6 (8.6)
Li ₃ Sb	2074	1.7 (3.3)	HgF ₂	8177	3.2 (3.2)	CsSnCl ₃	27394	5.0 (5.0)	SrBrF	23024	8.6 (8.6)
ZnTe	2176	1.8 (1.8)	Ba ₂ SnSe ₃ F ₂	17805	3.2 (3.2)	Na ₃ SbO ₄	7404	5.0 (5.0)	YCl ₃	27455	8.6 (8.6)
Cd ₂ SnO ₄	5966	1.8 (1.8)	InOF	27175	3.2 (3.2)	SrGa ₄ O ₇	18253	5.0 (5.0)	Ba ₃ In ₂ F ₁₂	28274	8.6 (8.6)
KYO ₂	8409	1.8 (1.8)	Ca(AuF ₆) ₂	28153	3.2 (3.2)	Ba ₂ Ga ₂ S ₅	18421	5.0 (5.0)	CsKNa ₂ Li ₁₂ (SiO ₄) ₄	17718	8.6 (8.7)
TlP ₂ S ₃	9272	1.8 (1.8)	Cd(AuF ₄) ₂	29169	3.2 (3.2)	CsIO ₃	28295	5.0 (5.0)	CaMg(CO ₃) ₂	6459	8.6 (8.8)
LaCuSe ₂	11790	1.8 (1.8)	Cs ₂ PtC ₂	505825	3.2 (3.2)	NaLiSe	28603	5.0 (5.0)	Li ₄ SiO ₄	11737	8.6 (8.8)
BaCuTeF	13287	1.8 (1.8)	V ₂ CdO ₆	550436	3.2 (3.2)	Cs ₂ Zn ₃ S ₄	505633	5.0 (5.0)	KCaCO ₃ F	6867	8.7 (8.7)
Cd(GaTe ₂) ₂	13949	1.8 (1.8)	K ₂ TaCuSe ₄	8972	3.2 (3.3)	Li ₂ WO ₄	19260	5.0 (5.1)	Y ₂ Si ₂ O ₇	5652	8.7 (8.7)
Ca ₃ AlAs ₃	17186	1.8 (1.8)	NaCuO	14580	3.2 (3.3)	Tl ₃ PO ₄	5709	5.0 (5.2)	TlClO ₄	30530	8.7 (8.7)

Appendix A. Calculated Bandgaps of the Materials Project Entries

Cs ₇ Te ₁₀	18388	1.8 (1.8)	Rb ₂ B ₂ Se ₇	16184	3.2 (3.3)	CdSe ₂ O ₅	9178	5.0 (5.2)	HfSiO ₄	4609	8.7 (8.8)
NaGe	29657	1.8 (1.8)	Zn(AuF ₄) ₂	17512	3.2 (3.3)	Rb ₂ Se	11327	5.0 (5.2)	Cs ₂ NaYCl ₆	23120	8.8 (8.8)
WBr ₆	504993	1.8 (1.8)	RbI ₃	28328	3.2 (3.3)	SrS	1087	5.0 (5.4)	RbMgCl ₃	504459	8.8 (8.8)
Ba ₃ GaP ₃	541715	1.8 (1.8)	P ₂ PdO ₆	29274	3.2 (3.3)	Cd ₄ P ₆ SN ₁₂	8921	5.1 (5.1)	BaBrF ₃	23070	8.8 (8.8)
BaLiAs	10616	1.8 (1.8)	Cs ₇ Au ₅ O ₂	510075	3.2 (3.3)	Str ₂ BN ₂ F	10234	5.1 (5.1)	Li ₂ O	553090	8.8 (8.8)
RbCuPdSe ₅	11115	1.8 (1.8)	KSb(PSe ₃) ₂	7123	3.2 (3.3)	TiCdO ₃	13641	5.1 (5.1)	La ₂ SO ₆	4078	8.8 (9.0)
KAgSe	16236	1.8 (1.8)	AsSe ₃ (ClF ₂) ₃	23575	3.2 (3.3)	PbSeO ₃	20716	5.1 (5.1)	Li ₂ SiO ₃	5012	8.8 (9.0)
NaSbS ₂	5414	1.8 (1.9)	KBi(WO ₄) ₂	510667	3.2 (3.3)	Rb ₃ InS ₃	22303	5.1 (5.1)	Rb ₂ SrP ₂ O ₇	14354	8.9 (8.9)
KV(CuS ₂) ₂	6376	1.8 (1.9)	Rb ₂ TaCuSe ₄	11924	3.2 (3.4)	Rb ₂ ZnI ₄	505748	5.1 (5.1)	MgF ₄ O ₁₁	15437	8.9 (8.9)
BaLiSb	10485	1.8 (1.9)	InGaO ₃	22606	3.2 (3.4)	CsCdBr ₃	541899	5.1 (5.1)	Li ₂ AlSiO ₄	18220	8.9 (9.0)
Tl ₂ Sn ₂ S ₃	28011	1.8 (1.9)	YBi ₂ ClO ₄	552604	3.2 (3.4)	K ₃ Ta ₃ Si ₂ O ₁₃	16855	5.1 (5.1)	Mg ₃ (BO ₃) ₂	5005	8.9 (9.2)
CuTe ₂ I	31037	1.8 (1.9)	PtPbF ₆	20458	3.2 (3.5)	Sn ₃ BrF ₅	23452	5.1 (5.1)	Li ₂ CaSiO ₄	7610	8.9 (9.3)
Cs ₂ Pd ₃ Se ₄	504855	1.8 (1.9)	K ₂ SeBr ₆	23036	3.2 (3.5)	CdBr ₂	27934	5.1 (5.1)	RbSbF ₆	9821	9.0 (9.0)
K ₂ LiInAs ₂	505431	1.8 (1.9)	Hg ₂ P ₂ S ₇	27171	3.2 (3.5)	BiBO ₃	31250	5.1 (5.1)	Cs ₂ SrP ₂ O ₇	14355	9.0 (9.0)
AuCl ₂	541656	1.8 (1.9)	NaV(OF) ₂	18953	3.2 (3.6)	Ba ₃ Zn ₆ Si ₄ TeO ₂₀	543034	5.1 (5.1)	Na ₂ BeB ₂ O ₅	16737	9.0 (9.0)
LiP	9588	1.8 (2.0)	Ba ₂ BiSbO ₆	23127	3.2 (4.0)	MgGeO ₃	4819	5.1 (5.2)	P ₂ O ₅	2452	9.0 (9.0)
Rb ₂ VAgSe ₄	14635	1.8 (2.0)	CaTe	1519	3.2 (4.2)	TlNO ₃	5915	5.1 (5.2)	BaSnF ₆	8290	9.0 (9.0)
Sr(InTe) ₂	20397	1.8 (2.0)	BeTe	252	3.2 (4.9)	K ₃ BS ₃	29975	5.1 (5.2)	BaCl ₂	23199	9.0 (9.0)
Ba(InTe) ₂	21183	1.8 (2.0)	Ga ₂ S ₃	539	3.3 (3.3)	Cs ₂ Sn(GeO ₃) ₃	540707	5.1 (5.2)	Mg ₂ B ₂ O ₅	18256	9.0 (9.1)
KAuSe ₂	29138	1.8 (2.0)	K ₂ PAuS ₄	9509	3.3 (3.3)	Sr ₃ V ₂ O ₈	19386	5.1 (5.2)	BeBr ₂	30139	9.0 (9.2)
VCu ₃ S ₄	3762	1.8 (2.1)	K ₂ SnSe ₃	9693	3.3 (3.3)	NbInO ₄	9595	5.1 (5.3)	CsSbF ₆	9636	9.1 (9.1)
RbTe	9064	1.8 (2.2)	Sr(CuO) ₂	13900	3.3 (3.3)	Ta ₂ O ₅	10390	5.1 (5.3)	SrAl ₂ B ₂ O ₇	15939	9.1 (9.1)
Zr ₂ SN ₂	11583	1.8 (2.8)	Mg(InS ₂) ₂	20493	3.3 (3.3)	Pb ₂ OF ₂	27355	5.1 (5.3)	RbBaPO ₄	17832	9.1 (9.1)
MoSe ₂	1634	1.9 (1.9)	Li ₄ PbO ₄	22170	3.3 (3.3)	BaBiO ₂	551243	5.1 (5.3)	KSrPO ₄	17975	9.1 (9.1)
Cs ₂ Se ₃	7449	1.9 (1.9)	ICl ₃	27229	3.3 (3.3)	AsBr ₃	23317	5.1 (5.3)	KHCO ₃	23724	9.1 (9.1)
Al ₂ HgTe ₄	7910	1.9 (1.9)	GaCuL ₄	29403	3.3 (3.3)	BeS	422	5.1 (7.5)	Rb ₂ Zr ₃ OF ₁₂	17085	9.1 (9.2)
Ba ₄ Sb ₂ O	9774	1.9 (1.9)	Au ₂ S	947	3.3 (3.3)	LiAlSe ₂	7117	5.2 (5.2)	Na ₂ S ₂ O ₇	31269	9.1 (9.2)
PdF ₄	13868	1.9 (1.9)	YCuS ₂	10533	3.3 (3.3)	Ba ₂ YNbO ₆	7251	5.2 (5.2)	CsLiCl ₂	23364	9.1 (9.3)
ZrSnS ₃	17324	1.9 (1.9)	Sr ₂ LiReO ₆	12525	3.3 (3.3)	CaPS ₃	9789	5.2 (5.2)	LiBO ₂	3635	9.2 (9.2)
K ₂ Se ₅	18609	1.9 (1.9)	CsI ₃	22876	3.3 (3.3)	CaTiGeO ₅	17784	5.2 (5.2)	Mg ₃ (PO ₄) ₂	14396	9.2 (9.2)
InSe	22691	1.9 (1.9)	KLi ₆ BiO ₆	23582	3.3 (3.3)	K ₃ PS ₄	17989	5.2 (5.2)	Rb ₂ B ₄ O ₇	16980	9.2 (9.2)
Tel	23273	1.9 (1.9)	Hg ₃ (SeCl) ₂	27851	3.3 (3.3)	LiAl(MoO ₄) ₂	19209	5.2 (5.2)	Ca ₄ Cl ₆ O	23326	9.2 (9.2)
CuSe ₂ Br	29567	1.9 (1.9)	Cs ₂ PdCl ₄	30314	3.3 (3.3)	NaCaVO ₄	19302	5.2 (5.2)	AlH ₁₂ (ClO ₂) ₃	23743	9.2 (9.2)
YZnAsO	546011	1.9 (1.9)	LiCaN	31468	3.3 (3.3)	Na ₄ WO ₅	19334	5.2 (5.2)	Na ₂ Ca(PO ₃) ₄	541522	9.2 (9.2)
LaTa ₂ N ₂ O	550514	1.9 (1.9)	CsCuO	541037	3.3 (3.3)	RbLa(WO ₄) ₂	19680	5.2 (5.2)	NaAlP ₂ O ₇	16777	9.2 (9.2)
Na ₃ Sb	7956	1.9 (1.9)	Cd ₂ SiO ₄	4530	3.3 (3.4)	KInBr ₄	22932	5.2 (5.2)	K ₂ Be ₂ PbF ₈	7385	9.2 (9.3)
K ₂ P ₃	8262	1.9 (1.9)	Ba(GaSe) ₂	7841	3.3 (3.4)	K ₂ Te	1747	5.2 (5.2)	K ₂ MgCl ₄	27207	9.2 (9.4)
HfTiCuS ₃	9396	1.9 (1.9)	K ₂ GeSe ₃	9692	3.3 (3.4)	Al ₂ S ₃	2654	5.2 (5.2)	SrCl ₂	23209	9.2 (9.5)
Cd(InSe) ₂	22304	1.9 (1.9)	Ag ₂ SeO ₃	16913	3.3 (3.4)	Ta ₂ ZnO ₆	17765	5.2 (5.2)	Al ₂ O ₃	1143	9.3 (9.3)

Zn(InSe ₂) ₂	22607	1.9 (1.9)	MgCrO ₄	19120	3.3 (3.4)	HgCl ₂	22855	5.2 (5.2)	CsBePO ₄	15395	9.3 (9.3)
Ca ₃ BN ₃	30315	1.9 (1.9)	TaTeBr ₉	29716	3.3 (3.4)	RbO	7895	5.2 (5.3)	KNa ₂ (PO ₃) ₃	17889	9.3 (9.3)
NbCl ₄	31040	1.9 (1.9)	Rb ₂ Cd(PSec ₃) ₂	541897	3.3 (3.4)	KLiSe	8756	5.2 (5.3)	Na ₂ B ₄ O ₇	17941	9.3 (9.3)
BaSe ₂	7547	1.9 (2.0)	Ca ₂ PI	23040	3.3 (3.6)	MgMoO ₄	19047	5.2 (5.3)	AlClO	27863	9.3 (9.3)
K ₂ As ₂ Pd	8147	1.9 (2.0)	GeI ₂	504756	3.3 (3.6)	Sr ₃ Te ₄ O ₁₁	30026	5.2 (5.3)	Al ₂ O ₃	552558	9.3 (9.3)
K ₅ As ₂ Au	8683	1.9 (2.0)	CdPS ₃	5328	3.3 (3.7)	RbPb ₂ Br ₅	23043	5.2 (5.4)	NaAlPO ₄ F	8678	9.3 (9.3)
Sr ₃ P ₄	14288	1.9 (2.0)	TaCu ₃ S ₄	10748	3.3 (3.7)	CaInBr ₃	505024	5.2 (5.4)	K ₂ Zr ₃ O ₇ F ₂	17888	9.3 (9.3)
I	23153	1.9 (2.0)	PbO	20442	3.3 (3.7)	Cd ₂ P ₂ O ₇	27686	5.2 (5.5)	CsCl	22865	9.3 (9.3)
Bi(TeBr ₂) ₂	29127	1.9 (2.0)	Li ₂ ZrN ₂	3216	3.3 (4.0)	BaPS ₃	11006	5.3 (5.3)	CsMgCl ₃	23004	9.3 (9.3)
Cu ₂ Se ₂ Cl	31038	1.9 (2.0)	KPS ₃	8267	3.4 (3.4)	Rb ₃ PS ₄	16863	5.3 (5.3)	Ba ₃ (PO ₄) ₂	3857	9.3 (9.4)
Rb ₅ SiAs ₃	17490	1.9 (2.0)	Rb ₂ SnSe ₃	9145	3.4 (3.4)	SrTi(MoO ₄) ₂	19450	5.3 (5.3)	SrZnF ₄	5078	9.4 (9.4)
TiI ₄	541013	1.9 (2.0)	CsAuO	10548	3.4 (3.4)	Na ₃ BiO ₃	27914	5.3 (5.3)	BaMgP ₂ O ₇	18343	9.4 (9.4)
Cu ₅ Sb ₂	4468	1.9 (2.1)	Sr ₂ LiReN ₄	10556	3.4 (3.4)	TlCdCl ₃	28218	5.3 (5.3)	SrMgP ₂ O ₇	18469	9.4 (9.4)
TlPd ₃ O ₄	5478	1.9 (2.1)	K ₂ Mg(PSec ₃) ₂	11643	3.4 (3.4)	P ₄ N ₃ Cl ₁₁	28792	5.3 (5.3)	RbPO ₃	4135	9.4 (9.4)
Na ₂ AgSb	7392	1.9 (2.1)	Ge ₃ N ₄	13852	3.4 (3.4)	La ₃ TaO ₇	510513	5.3 (5.3)	RbLiCl ₂	504888	9.4 (9.4)
Cs ₂ As ₂ Pd	8857	1.9 (2.1)	Li ₂ PdF ₆	13985	3.4 (3.4)	Na ₃ SbO ₃	8076	5.3 (5.3)	YAl ₃ (BO ₃) ₄	6062	9.4 (9.5)
AlTiSe ₂	9579	1.9 (2.1)	Mg(ScS ₂) ₂	14307	3.4 (3.4)	SrPS ₃	9788	5.3 (5.3)	Mg(PO ₃) ₂	18620	9.4 (9.5)
ScTiSe ₂	13313	1.9 (2.1)	CaCrO ₄	19215	3.4 (3.4)	Zn(IO ₃) ₂	23360	5.3 (5.3)	Sr ₃ (PO ₄) ₂	4632	9.4 (9.5)
Au ₂ O ₃	27253	1.9 (2.1)	SbPbClO ₂	23138	3.4 (3.4)	Na ₄ Br ₂ O	28599	5.3 (5.3)	BaBe ₂ Si ₂ O ₇	12797	9.4 (9.6)
P ₄ Ru	504443	1.9 (2.1)	Rb ₂ PtCl ₆	23350	3.4 (3.4)	Ba ₃ V ₂ O ₈	19365	5.3 (5.4)	MgSO ₄	7572	9.5 (9.5)
BaYAgTe ₃	10337	1.9 (2.1)	Tl ₆ Si ₂ O ₇	27228	3.4 (3.4)	PbBr ₂	28077	5.3 (5.4)	Na ₂ SnF ₆	8811	9.5 (9.5)
Rb ₃ Ce ₄ Au	17830	1.9 (2.1)	GaTeCl	27449	3.4 (3.4)	LiBeN	29463	5.3 (5.4)	NaAlCl ₄	23363	9.5 (9.5)
Nb ₂ Hg ₂ O ₇	13803	1.9 (2.3)	Be ₄ TeO ₇	27608	3.4 (3.4)	Ga ₁₀ GePb ₃ O ₂₀	504827	5.3 (5.4)	Na ₆ S ₂ ClO ₈ F	23657	9.5 (9.5)
Na ₂ PtSe ₂	14588	1.9 (2.3)	Cs ₂ HgI ₄	28421	3.4 (3.4)	KSbO ₃	547792	5.3 (5.4)	SiCl ₄	28391	9.5 (9.5)
VAg ₃ O ₄	18889	1.9 (2.3)	Ca ₄ GeN ₄	29808	3.4 (3.4)	LiNO ₃	8180	5.3 (5.6)	Ba(AlCl ₄) ₂	505755	9.5 (9.5)
B	160	1.9 (2.4)	CsI ₂ Br	504641	3.4 (3.4)	Ca(SbO ₃) ₂	9125	5.3 (5.6)	Na ₂ SO ₄	4770	9.6 (9.6)
Hg ₂ P ₃ Cl	28875	1.9 (2.4)	Cd(GaO ₂) ₂	3443	3.4 (3.4)	SnF ₂	7457	5.3 (6.0)	Cs ₂ SnF ₆	7297	9.6 (9.6)
ScAgSe ₂	12908	1.9 (2.4)	RbCuO	8665	3.4 (3.4)	AgClO ₄	22993	5.3 (6.1)	KAl(SO ₄) ₂	7645	9.6 (9.6)
Ca(MgSb) ₂	9565	1.9 (2.5)	Cs ₂ WS ₄	17361	3.4 (3.4)	Ca ₂ SnO ₄	4747	5.4 (5.4)	NaCl	22862	9.6 (9.6)
Ba(MgSb) ₂	9567	1.9 (2.6)	RbSnI ₃	29405	3.4 (3.4)	Na ₄ SnO ₄	9655	5.4 (5.4)	BaGeF ₆	14006	9.6 (9.6)
Li ₃ As	757	1.9 (2.9)	RuS ₃ Cl ₈	29568	3.4 (3.4)	Na ₃ PS ₃ O	11738	5.4 (5.4)	RbCl	23295	9.6 (9.6)
AgBr	23231	1.9 (3.2)	GaS	2507	3.4 (3.5)	SrTa ₂ O ₆	17715	5.4 (5.4)	LiClO ₄	30301	9.6 (9.7)
BP	1479	1.9 (4.1)	Na ₃ AlP ₂	5122	3.4 (3.5)	Ba ₂ ZnO ₃	17911	5.4 (5.4)	SiO ₂	6945	9.7 (9.7)
CaCuS ₂	5238	2.0 (2.0)	Ba ₃ BA ₃ O ₃	9793	3.4 (3.5)	AlTi(MoO ₄) ₂	18733	5.4 (5.4)	Li ₂ GeF ₆	7791	9.7 (9.7)
Ca ₂ Pt ₃ O ₈	8710	2.0 (2.0)	RbCaAs	9845	3.4 (3.5)	SrMoO ₄	18834	5.4 (5.4)	LiAlCl ₄	22983	9.7 (9.7)
Ca ₃ VN ₃	9029	2.0 (2.0)	PI ₂	29443	3.4 (3.5)	K ₃ VO ₄	19052	5.4 (5.4)	CsAlCl ₄	27260	9.7 (9.7)
Ba ₂ ZnN ₂	9307	2.0 (2.0)	CsSnI ₃	27381	3.4 (3.5)	PBr ₂ N	23457	5.4 (5.4)	CaCl ₂	22904	9.7 (9.7)
Cd(RhO ₂) ₂	14100	2.0 (2.0)	K ₃ SiTe ₃	7657	3.4 (3.6)	LiBF ₆	27419	5.4 (5.4)	Li ₂ BeSiO ₄	8070	9.7 (9.9)
K ₂ WSe ₄	18138	2.0 (2.0)	Ba ₃ BPO ₃	9712	3.4 (3.6)	TiBO ₂	28244	5.4 (5.4)	NaClO ₄	22968	9.7 (9.9)

Appendix A. Calculated Bandgaps of the Materials Project Entries

K ₃ Na ₂ SnAs ₃	18447	2.0 (2.0)	HgMoO ₄	19363	3.4 (3.6)	CsAl(MoO ₄) ₂	542116	5.4 (5.4)	Al ₄ (B ₂ O ₅) ₃	510509	9.8 (10.0)
Ge ₁ 9(PI) ₄	23420	2.0 (2.0)	Rb ₂ TeBr ₆	23383	3.4 (3.6)	LiNbO ₃	3731	5.4 (5.4)	YPO ₄	5132	9.8 (9.8)
K ₂ SnTe ₃	29835	2.0 (2.0)	BaTe	1000	3.4 (3.7)	Li ₃ BS ₃	5614	5.4 (5.4)	KCl	23193	9.8 (9.8)
WS ₂	1821	2.0 (2.0)	KS	1287	3.4 (3.7)	KAl(MoO ₄) ₂	19352	5.4 (5.4)	KClO ₄	23526	9.8 (9.8)
Rb ₂ As ₂ Pt	13445	2.0 (2.0)	Li ₁₀ BrN ₃	28989	3.4 (3.7)	K ₂ Se	8426	5.4 (5.5)	RbClO ₄	28433	9.8 (9.8)
Ba(YTe ₂) ₂	17872	2.0 (2.0)	K ₂ W ₂ O ₇	19037	3.4 (3.9)	Ba(SbO ₃) ₂	9127	5.4 (5.5)	K ₃ Na(SO ₄) ₂	22457	9.8 (9.9)
Ta(ICI) ₂	28683	2.0 (2.0)	SiC	7631	3.4 (4.5)	Cd(IO ₃) ₂	27640	5.4 (5.5)	BaCIF	23432	9.8 (9.9)
Rb ₂ P ₃	2079	2.0 (2.1)	Al ₂ CdSe ₄	3159	3.5 (3.5)	NaNO ₃	4531	5.4 (5.5)	HfF ₄	31033	9.8 (9.9)
ZnGeP ₂	4524	2.0 (2.1)	Ba(CuO) ₂	7374	3.5 (3.5)	SbOF	7609	5.4 (5.6)	K ₂ ZrF ₆	5450	9.9 (9.9)
Fe(SiP) ₄	9198	2.0 (2.1)	ZnPtF ₆	8256	3.5 (3.5)	Sr ₂ BN ₂ Cl	23131	5.4 (5.6)	MgCl ₂	23210	9.9 (9.9)
Cs ₃ Ge ₄ Au	510341	2.0 (2.1)	RbAgO	8603	3.5 (3.5)	CdSO ₄	8459	5.4 (5.7)	CaSnF ₆	8224	9.9 (9.9)
GaTe	542812	2.0 (2.1)	Na ₃ AsSe ₃	8686	3.5 (3.5)	Li ₂ Se	2286	5.4 (5.8)	Li ₃ PO ₄	13725	9.9 (9.9)
TlInSe ₂	22232	2.0 (2.1)	K ₄ BeF ₂	9872	3.5 (3.5)	TaBO ₄	4624	5.5 (5.5)	Li ₃ P ₇ O ₁₂	16828	10.0 (10.0)
K ₂ Te ₂ As	29380	2.0 (2.1)	RbAuO	10547	3.5 (3.5)	KNO ₃	5158	5.5 (5.5)	Rb ₂ Hf ₃ OF ₁₂	17256	10.0 (10.0)
KTiO ₂	8175	2.0 (2.2)	Al ₂ Se ₃	11674	3.5 (3.5)	Sr ₂ YNbO ₆	6019	5.5 (5.5)	KLiSO ₄	6800	10.0 (10.0)
PdPbF ₄	20805	2.0 (2.2)	SrCuSF	12444	3.5 (3.5)	Na ₄ L ₂ O	22937	5.5 (5.5)	BaZr ₂ F ₁₀	505400	10.0 (10.0)
K ₂ AgBi	27549	2.0 (2.2)	NaTi ₂ RhF ₆	14037	3.5 (3.5)	AsCl ₂ F ₃	23444	5.5 (5.5)	SrSO ₄	5285	10.0 (10.1)
Cs ₂ P ₃	14652	2.0 (2.2)	CsAgO	14579	3.5 (3.5)	Na ₃ ClO	28602	5.5 (5.5)	Li ₅ Li	15141	10.0 (10.1)
Rb(SbSe ₂) ₂	9798	2.0 (2.3)	RbSbS ₂	15366	3.5 (3.5)	Te ₂ O ₃ F ₂	29185	5.5 (5.5)	GeF ₄	9816	10.0 (10.2)
Sc ₂ CCl ₂	28479	2.0 (2.3)	Sr ₃ (GaN ₂) ₂	16945	3.5 (3.5)	Cs ₂ LiVO ₄	541190	5.5 (5.5)	SiO ₂	547211	10.1 (10.1)
Na ₂ PdS ₂	10223	2.0 (2.4)	K ₂ S ₅	17146	3.5 (3.5)	BaBiClO ₂	552806	5.5 (5.5)	SF ₆	8560	10.1 (10.1)
InAgO ₂	22660	2.0 (2.5)	Tl ₃ B ₃ S ₁₀	17823	3.5 (3.5)	Rb ₂ LiVO ₄	19123	5.5 (5.5)	CaSO ₄	4406	10.1 (10.5)
Ba ₄ LiCu(CO ₅) ₂	15472	2.0 (2.5)	K ₂ Pb ₂ O ₃	20694	3.5 (3.5)	PBr ₃	27257	5.5 (5.5)	AlPO ₄	7848	10.2 (10.2)
K ₂ PtSe ₂	8621	2.0 (2.5)	SbI ₃	23281	3.5 (3.5)	K ₃ BiO ₃	29524	5.5 (5.5)	K ₂ GeF ₆	14168	10.3 (10.3)
Tl ₂ PdCl ₄	29889	2.0 (2.5)	BiS ₂	23318	3.5 (3.5)	SrSiN ₂	4549	5.5 (5.6)	LiCl	22905	10.3 (10.3)
ScTiS ₂	13312	2.0 (3.0)	KTiBr ₄	28048	3.5 (3.5)	LiTa ₃ O ₈	7638	5.5 (5.6)	LiSiBO ₄	8874	10.4 (10.8)
Li ₃ P	736	2.0 (3.3)	La ₃ AgSnS ₇	542888	3.5 (3.5)	Cs ₂ NaVO ₄	19447	5.5 (5.6)	Rb ₂ GeF ₆	8812	10.5 (10.5)
GeS	2242	2.1 (2.1)	NaAuF ₄	7388	3.5 (3.5)	RbLa(MoO ₄) ₂	19687	5.5 (5.6)	CsF	1784	10.5 (10.8)
NaNbO ₂	3744	2.1 (2.1)	LiAuF ₄	12263	3.5 (3.5)	PbSeO ₄	22342	5.5 (5.6)	Cs ₂ GeF ₆	8217	10.6 (10.6)
KZnP	7437	2.1 (2.1)	ScPS ₄	6999	3.5 (3.6)	CsBiF ₆	27422	5.5 (5.6)	CsBe ₂ BO ₃ F ₂	553342	10.7 (10.7)
HfSnS ₃	8725	2.1 (2.1)	Hg ₃ (SF) ₂	7580	3.5 (3.6)	Cs ₃ As ₅ O ₉	30300	5.5 (5.6)	RbH ₂ OF	23700	10.7 (10.7)
K ₂ GeAs ₂	8930	2.1 (2.1)	TlBS ₂	8946	3.5 (3.6)	TaBiO ₄	30900	5.5 (5.6)	Cs ₂ NaAlF ₆	6528	10.8 (10.8)
SrTiN ₂	9517	2.1 (2.1)	Rb ₃ BAS ₂	9718	3.5 (3.6)	NOF	505726	5.5 (5.6)	B ₂ O ₃	306	10.8 (10.9)
Sr ₃ (SiAs ₂) ₂	11677	2.1 (2.1)	RbCaSb	9846	3.5 (3.6)	BaSn(GeO ₃) ₃	540635	5.5 (5.6)	K ₂ HfF ₆	14128	10.8 (10.9)
AlAgTe ₂	14092	2.1 (2.1)	K ₂ NbAgS ₄	15214	3.5 (3.6)	Tl ₂ CO ₃	543045	5.5 (5.6)	BeCl ₂	23267	10.9 (11.0)
Ti(SnO ₂) ₂	18288	2.1 (2.1)	AuI	27725	3.5 (3.6)	SrBiBrO ₂	552234	5.5 (5.6)	KBr ₂ BO ₃ F ₂	6870	11.0 (11.0)
Sr ₃ (GeP ₂) ₂	18351	2.1 (2.1)	RbAuSe	9731	3.5 (3.6)	BaSiN ₂	3777	5.5 (5.6)	KRb ₂ GaF ₆	13190	11.0 (11.0)
K ₂ NaInAs ₂	21510	2.1 (2.1)	KCuO	14296	3.5 (3.6)	Mg ₃ TeO ₆	3118	5.5 (5.7)	Li ₂ ZrF ₆	4002	11.0 (11.1)
Na ₄ Ge ₂ Te ₅	28107	2.1 (2.1)	AsI ₃	23218	3.5 (3.6)	SrO ₂	2697	5.5 (5.7)	ScF ₃	10694	11.0 (11.4)

Co(ClO ₄) ₂	31621	2.1 (2.1)	Tl ₂ TeBr ₆	31076	3.5 (3.6)	SbBr ₃	27399	5.5 (5.7)	SiH ₄	23739	11.1 (11.1)
Pb ₃ O ₄	542494	2.1 (2.1)	NaInS ₂	20289	3.5 (3.7)	SiS ₂	1602	5.5 (5.8)	BeO	2542	11.1 (11.1)
ZnSe	1190	2.1 (2.1)	Cs ₂ TeBr ₆	23405	3.5 (3.7)	Rb ₂ S	8041	5.5 (5.8)	LiCaCaF ₆	12829	11.1 (11.2)
NaP	7440	2.1 (2.1)	Sr ₂ Sb ₂ O ₇	4103	3.5 (3.8)	SeO ₂	726	5.5 (5.9)	KBe ₃ ZnF ₉	18509	11.2 (11.2)
In ₂ S ₃	22216	2.1 (2.1)	PbCN ₂	19727	3.5 (3.8)	K ₂ O	971	5.5 (5.9)	RbF	11718	11.3 (11.4)
CuBr	22913	2.1 (2.1)	SrTe	1958	3.5 (4.2)	Rb ₂ CdCl ₄	505668	5.5 (5.9)	CsCOF ₃	14734	11.4 (11.4)
BiAuBr ₆	541774	2.1 (2.1)	TlF ₃	2632	3.6 (3.6)	La ₂ SO ₂	4511	5.5 (6.0)	Li ₂ CaHF ₈	16577	11.4 (11.4)
Tl ₂ Sn(AsS ₃) ₂	6023	2.1 (2.2)	LaSeF	7738	3.6 (3.6)	MgS	1315	5.5 (6.3)	BeSO ₄	505568	11.4 (11.5)
K ₂ Pd ₃ S ₄	9910	2.1 (2.2)	Al ₂ HgS ₄	7906	3.6 (3.6)	CaN ₆	676	5.6 (5.6)	SrB ₄ O ₇	5540	11.4 (11.7)
O ₂	12957	2.1 (2.2)	KAgO	8660	3.6 (3.6)	BaO ₂	1105	5.6 (5.6)	CO ₂	20066	11.5 (11.5)
Ag ₂ PdCl ₄	28557	2.1 (2.2)	Ba ₂ LiReN ₄	10555	3.6 (3.6)	Li ₃ SbO ₄	5769	5.6 (5.6)	BPO ₄	3589	11.6 (11.6)
Cs ₂ CuF ₆	28692	2.1 (2.2)	ZnS	10695	3.6 (3.6)	KSeO ₂ F	9205	5.6 (5.6)	Cs ₂ CaF ₄	15157	11.7 (11.8)
Ba(TeP ₂) ₂	31275	2.1 (2.2)	NaS ₂	12180	3.6 (3.6)	In ₂ P ₂ O ₇	17100	5.6 (5.6)	Rb ₂ MgF ₄	8861	12.1 (12.2)
PtI ₂	28319	2.1 (2.2)	KAuF ₆	12442	3.6 (3.6)	BiOF	23074	5.6 (5.6)	KF	463	12.2 (12.2)
Be ₂ Te ₇ Cl ₆	505788	2.1 (2.2)	Na ₃ SiTe ₃	17291	3.6 (3.6)	BrF ₅	27987	5.6 (5.6)	Cs ₂ HF ₆	13948	12.2 (12.2)
Tl ₂ GeSe ₃	14242	2.1 (2.3)	Mg(AuF ₄) ₂	17555	3.6 (3.6)	Na ₂ O	2352	5.6 (5.6)	RbCaF ₃	3654	12.3 (12.4)
Na ₂ CuAs	15685	2.1 (2.3)	K ₄ SnSe ₄	18132	3.6 (3.6)	CsGaS ₂	5038	5.6 (5.7)	NaF	682	12.4 (12.4)
NaO ₃	22464	2.1 (2.3)	BiSBr	23324	3.6 (3.6)	Y ₂ O ₂	12894	5.6 (5.7)	KPF ₆	4608	12.4 (12.4)
Ca ₄ Bi ₂ O	551873	2.1 (2.3)	Ga ₂ TeS ₂	27255	3.6 (3.6)	LiGaCl ₃	29344	5.6 (5.7)	MgF ₂	1810	12.5 (12.5)
AgHgAsS ₃	6215	2.1 (2.3)	Rb ₂ Zn ₃ O ₄	505501	3.6 (3.6)	Na ₂ ZnGeO ₄	6402	5.6 (5.7)	CsCaF ₃	7104	12.5 (12.5)
LiBeAs	9562	2.1 (2.3)	ZrI ₄	541112	3.6 (3.6)	RbNaS	8799	5.6 (5.7)	BaF ₂	1029	12.5 (12.6)
KInTe ₂	19851	2.1 (2.3)	Rb ₂ S ₅	16911	3.6 (3.6)	Sr ₂ CuBrO ₂	552537	5.6 (5.7)	K ₂ MgF ₄	31212	12.5 (12.6)
RbCuO ₂	7467	2.1 (2.4)	K ₂ PtCl ₄	22934	3.6 (3.6)	BaAl ₂ Sb ₂ O ₇	12885	5.6 (5.8)	PF ₅	8511	12.6 (12.6)
Na ₂ CuP	7639	2.1 (2.4)	LiGaI ₃	29345	3.6 (3.6)	YNbO ₄	5387	5.6 (5.8)	SrF ₂	981	12.7 (12.7)
Al ₂ Te ₅	9254	2.1 (2.4)	MgPSe ₃	30943	3.6 (3.6)	NaReO ₄	5558	5.7 (5.7)	Cs ₂ NaAl ₃ F ₁₂	12309	12.7 (12.7)
TaCu ₃ Te ₄	9295	2.1 (2.4)	KAuSe	9881	3.6 (3.7)	Mg ₂ As ₂ O ₇	5618	5.7 (5.7)	Rb ₃ NaBe ₂ F ₈	13630	12.7 (12.8)
K ₂ VCuS ₄	15147	2.1 (2.4)	CaPSe ₃	11007	3.6 (3.7)	CsNaS	6973	5.7 (5.7)	KMgF ₃	3448	12.7 (12.9)
Rb ₂ VCuS ₄	15219	2.1 (2.4)	K ₂ ZnTe ₂	12535	3.6 (3.7)	BaTiOF ₄	16915	5.7 (5.7)	K ₂ NaAlF ₆	6586	12.8 (12.8)
PdSeO ₃	545482	2.1 (2.4)	Ba ₃ (AlN ₂) ₂	17133	3.6 (3.7)	CaNb ₂ O ₆	17101	5.7 (5.7)	KAlF ₄	2910	12.8 (12.8)
AlSb	2624	2.1 (2.4)	Ba ₂ CaMoO ₆	19403	3.6 (3.7)	LiZnAsO ₄	18048	5.7 (5.7)	LiPF ₆	9143	12.8 (12.8)
Cs(SbSe ₂) ₂	3312	2.1 (2.4)	CsBr ₂ F	28650	3.6 (3.7)	Rb ₄ CdBr ₆	28315	5.7 (5.7)	CaF ₂	2741	12.8 (13.0)
Bi ₂ SO ₂	27891	2.1 (2.4)	K ₂ PdF ₄	504853	3.6 (3.7)	LiCaBr ₄	28326	5.7 (5.7)	BaSiF ₆	5588	12.9 (12.9)
LiBC	9244	2.1 (2.5)	NClO	505727	3.6 (3.7)	SnClF	504519	5.7 (5.7)	K ₂ AlF ₅	9486	12.9 (12.9)
Ag ₃ SbS ₃	4515	2.1 (2.6)	SrSnO ₃	2879	3.6 (3.7)	SrBiClO ₂	547244	5.7 (5.7)	NaPF ₆	10474	12.9 (12.9)
Be ₂ C	1569	2.1 (5.5)	RbAu ₃ Se ₂	9385	3.6 (3.8)	Be ₃ N ₂	18337	5.7 (5.7)	CaAlF ₅	8836	13.0 (13.0)
Na ₃ P	1598	2.2 (2.2)	V ₂ Cd ₂ O ₇	18740	3.6 (3.8)	SbClF ₈	27314	5.7 (5.7)	SrAlF ₅	16557	13.0 (13.0)
GaAgS ₂	5343	2.2 (2.2)	Tl ₄ Si ₄	8479	3.6 (3.8)	CaWO ₄	510563	5.7 (5.7)	YF ₃	2416	13.1 (13.1)
La ₂ S ₃	7475	2.2 (2.2)	La ₂ TeO ₂	4547	3.6 (3.9)	BaAl ₄ S ₇	8258	5.7 (5.8)	NaCaAlF ₆	17944	13.2 (13.2)
CsTe	8361	2.2 (2.2)	HgBr	23177	3.6 (3.9)	MgSeO ₄	12630	5.7 (5.8)	AlF ₃	468	13.3 (13.3)

Na ₂ AgAs	8411	2.2 (2.2)	ScAgO ₂	11022	3.6 (4.0)	Na ₃ Mo(OF) ₃	18753	5.7 (5.8)	Rb ₂ SiF ₆	10492	13.3 (13.3)
Ba(AgS) ₂	8579	2.2 (2.2)	As ₂ PbO ₆	20015	3.6 (4.0)	Ga ₂ PbO ₄	20496	5.7 (5.8)	K ₂ SiF ₆	3042	13.4 (13.4)
Ba ₂ HfS ₄	9321	2.2 (2.2)	CsAu	2667	3.6 (4.1)	Ge ₃ (BiO ₃) ₄	23560	5.7 (5.8)	LiYF ₄	3700	13.4 (13.4)
HfS ₃	9922	2.2 (2.2)	LiInO ₂	5488	3.6 (4.2)	SbAsO ₃	28109	5.7 (5.8)	Na ₂ LiBe ₂ F ₇	12240	13.5 (13.6)
Ag ₃ PS ₄	12459	2.2 (2.2)	CdPtF ₆	5858	3.7 (3.7)	AlCuCl ₄	28020	5.7 (5.8)	LiCaAlF ₆	6134	13.6 (13.6)
Hg ₂ GeO ₄	13995	2.2 (2.2)	Al ₂ ZnSe ₄	7907	3.7 (3.7)	CsTa ₃ (BO ₃) ₂	9309	5.7 (5.9)	SiF ₄	1818	14.0 (14.4)
Ba ₂ SiTe ₄	14448	2.2 (2.2)	Na ₃ SbS ₄	10167	3.7 (3.7)	BiCl ₃	22908	5.7 (5.9)	LiF	1138	14.6 (14.6)
AgAuF ₄	16060	2.2 (2.2)	SrMg ₂ N ₂	10550	3.7 (3.7)	Bi ₃ B ₅ O ₁₂	23549	5.7 (5.9)	BeF ₂	15951	14.6 (14.8)
Rb ₅ GeF ₃	17978	2.2 (2.2)	Rb ₂ NaRhF ₆	14038	3.7 (3.7)	Na ₂ S	648	5.8 (5.8)	CF ₄	1167	16.0 (16.1)

Table A.1: List of the indirect (direct) bandgaps sorted for increasing gap, in eV, of the calculated Materials Project structures. The formula and the Materials Project's Id are also included.

Appendix B

Theoretical Efficiencies of the Thin Film Solar Cells

This Appendix contains the theoretical efficiencies and calculated bandgaps of the materials that might be used in a thin film solar cell, described in Chapter 9. The additional information available in the table are the chemical formula, and the id of the structure from the Materials Project database.¹⁶

Id	Formula	Materials	Bandgap	Efficiency	Efficiency
		Project Id		1-layer	2-layer
1	K_2TiS_3	28766	2.3	17.1%	25.7%
2	BP	1479	4.1	0.0%	0.0%
3	$NaNbS_2$	7937	1.9	15.2%	31.3%
4	$Sr(ZnP)_2$	8276	1.4	26.3%	21.9%
5	ZrS_2	1186	3.0	2.1%	2.6%
6	O_2	12957	2.2	10.7%	13.0%
7	Mg_2Si	1367	2.5	2.6%	9.2%
8	Na_3P	1598	2.2	18.0%	27.2%
9	FeS_2	1522	2.1	16.6%	28.9%
10	$ZnSiP_2$	4763	2.3	12.2%	17.3%
11	ZnO	2133	2.4	14.0%	20.3%
12	B	160	2.4	6.8%	10.3%
13	$NaNbO_2$	3744	2.1	19.9%	30.5%
14	P	157	0.6	14.6%	0.0%
15	$NaCuO_2$	4541	2.0	8.7%	15.3%
16	PbS	21276	1.5	0.4%	0.5%
17	$ZrCl_2$	23162	1.6	27.6%	39.9%
18	Zr_2Sn_2	11583	2.8	3.3%	5.4%
19	MnP_4	487	1.1	29.8%	0.0%
20	WBr_6	504993	1.8	26.6%	45.7%
21	CuCl	22914	2.5	12.8%	18.4%
22	TiBrN	27849	1.7	28.9%	45.7%
23	MgP_4	384	1.4	29.2%	18.6%
25	$Sr(ZnAs)_2$	7770	0.5	13.5%	0.0%
26	Cu_2O	361	1.0	31.5%	0.0%
27	$Fe(SiP)_4$	9198	2.1	17.7%	28.2%
28	Na_2CuP	7639	2.4	12.9%	19.9%

Appendix B. Theoretical Efficiencies of the Thin Film Solar Cells

29	ZrS ₃	9921	2.3	8.5%	11.2%
30	NaSnP	29529	2.0	4.3%	6.3%
31	Si ₃ NiP ₄	8311	0.9	22.9%	0.0%
32	I	23153	2.0	20.9%	34.9%
34	KZnP	7437	2.1	21.4%	33.6%
35	K ₂ P ₃	8262	1.9	24.5%	39.1%
36	Ba ₂ ZnN ₂	9307	2.0	17.6%	23.9%
37	SrP	7931	2.1	12.6%	23.8%
38	Sr ₃ SbN	7752	1.6	28.3%	40.1%
39	CuP ₂	927	1.6	27.3%	34.5%
40	VNCl ₄	27868	2.2	14.0%	19.3%
41	MgB ₄	365	1.0	10.6%	0.0%
42	NaO ₃	22464	2.3	7.6%	11.6%
42	WS ₂	224	2.3	7.6%	22.1%
43	Si	149	3.1	1.2%	2.7%
44	ZnSiAs ₂	3595	1.6	28.5%	40.0%
45	NbI ₃ O	546285	1.4	23.0%	19.7%
46	K(MoS) ₃	8116	1.5	28.7%	27.3%
47	Ba ₂ Cu(PO ₄) ₂	9372	1.5	29.5%	25.3%
48	NaSbS ₂	5414	1.9	15.4%	38.0%
48	Sb ₂ WO ₆	541435	1.1	15.4%	0.0%
49	Sr ₂ ZnN ₂	9306	2.2	12.0%	16.9%
50	Ba ₄ NaCu(CO ₅) ₂	6841	2.7	6.9%	9.2%
51	MgSiP ₂	2961	2.5	9.1%	12.2%
52	SrTiN ₂	9517	2.1	20.2%	31.3%
53	KZrCuS ₃	9317	1.7	28.3%	47.5%
54	BaP ₃	7808	1.6	26.3%	39.2%
55	NaP	7440	2.1	20.5%	32.2%
56	Cu ₃ PS ₄	3934	2.4	13.9%	20.4%
57	BaSnO ₃	3163	2.6	8.3%	12.2%
58	TiNb ₃ O ₆	29699	1.3	27.8%	13.0%
59	LaZnPO	7060	1.2	17.1%	10.0%
60	TiCoSb	5967	2.2	10.9%	21.8%
61	KSnSb	3486	0.8	24.0%	0.0%
62	NaAsS ₂	5942	2.4	13.1%	18.5%
63	VCu ₃ S ₄	3762	2.1	17.0%	28.2%
64	KSb ₂	29055	1.1	21.5%	0.0%
65	Nb ₂ SnO ₆	3324	2.5	11.7%	16.8%
66	SnS	2231	1.8	23.3%	42.5%
67	Sr ₃ P ₄	14288	2.0	20.9%	34.7%
68	K ₂ NiAs ₂	9673	1.5	30.2%	32.7%
69	TiNCl	27850	1.7	28.3%	47.5%

Table B.1: List of the calculated materials for thin film solar cell applications, with the corresponding Id from Chapter 9 and from the Materials Project database, the bandgap, in eV, and the theoretical efficiency for the single- and double-layer device.

Appendix **C**

Papers

Paper I

Computational Screening of Perovskite Metal Oxides for Optimal Solar Light Capture

Ivano E. Castelli, Thomas Olsen, Soumendu Datta, David D. Landis, Søren Dahl, Kristian S. Thygesen, and Karsten W. Jacobsen

Energy Environ. Sci. **5**, 5814-5819, 2012.

Computational screening of perovskite metal oxides for optimal solar light capture†

Ivano E. Castelli,^a Thomas Olsen,^a Soumendu Datta,^a David D. Landis,^a Søren Dahl,^b Kristian S. Thygesen^a and Karsten W. Jacobsen^{*a}

Received 20th September 2011, Accepted 17th November 2011

DOI: 10.1039/c1ee02717d

One of the possible solutions to the world's rapidly increasing energy demand is the development of new photoelectrochemical cells with improved light absorption. This requires development of semiconductor materials which have appropriate bandgaps to absorb a large part of the solar spectrum at the same time as being stable in aqueous environments. Here we demonstrate an efficient, computational screening of relevant oxide and oxynitride materials based on electronic structure calculations resulting in the reduction of a vast space of 5400 different materials to only 15 promising candidates. The screening is based on an efficient and reliable way of calculating semiconductor band gaps. The outcome of the screening includes all already known successful materials of the types investigated plus some new ones which warrant further experimental investigation.

Introduction

The high living standard created in the world during the last century is to a large extent due to easy access to cheap fossil fuels. These resources are limited, and the ever increasing energy demands, together with the CO₂ related climate problems, make the development of sustainable energy technology one of the most important problems of today.¹ Direct harvesting and conversion of solar light to electrical energy in photovoltaic (PV) cells or to chemical energy by photoelectrochemical (PEC)

reactions are the most obvious technologies to address this problem. Conventionally, both technologies rely on light collection in semiconductor (SC) materials with appropriate bandgaps that match the solar spectrum in order to obtain high energy conversion efficiency.^{2–4} Here, we demonstrate an efficient, computational screening of relevant oxide and oxynitride materials based on electronic structure calculations showing that less than 1 out of 350 materials are realistic candidates for light-induced splitting of water.

The tremendous increase of computational power over the last couple of decades, in combination with methodological improvements, has made it possible to guide the development of new materials using first principles quantum mechanical calculations. Examples include the development of battery cathodes,⁵ the construction of semiconductor superlattices,⁶ searching for high stability alloys,⁷ and, very recently, screening for high-performance piezoelectrics,⁸ for organic photovoltaics^{9,10} and for inorganic scintillator materials.¹¹ Here, we show that a newly

^aCenter for Atomic-scale Materials Design, Department of Physics, Technical University of Denmark, DK - 2800 Kongens Lyngby, Denmark. E-mail: kwj@fysik.dtu.dk

^bCenter for Individual Nanoparticle Functionality, Department of Physics, Technical University of Denmark, DK - 2800 Kongens Lyngby, Denmark

† Electronic supplementary information (ESI) available: Methods, Cubic Perovskite Oxides and Cubic Perovskite Oxynitrides sections; Table 1, 2, 3; Fig. 1, 2. See DOI: 10.1039/c1ee02717d

Broader context

For almost 40 years, researchers have tried to identify semiconductors suitable for photoelectrochemical water splitting under solar light. Investigations have focused on oxides and, more recently, on oxynitrides, due to their good properties with respect to stability. Inspired by this, we have performed a comprehensive computational screening of more than 5400 oxide/oxynitride compounds in the cubic perovskite structure covering 52 metals. The screening is based on criteria for stability and for the size and position of the bandgap. The material should allow for collecting a significant part of the solar photons and be able to drive the uphill water splitting reaction. The calculations of the bandgaps go beyond standard (semi-)local DFT and take into account explicitly the derivative discontinuity providing realistic estimates of the gaps. We end up with 10 oxides and 5 oxynitrides as candidates for light harvesting materials including AgNbO₃, BaSnO₃, BaTaO₂N, CaTaO₂N, SrTaO₂N, and LaTiO₂N, which are well known in the water splitting community. We suggest 9 new combinations for further experimental investigation.

implemented density functional method allows for completely new possibilities of screening material properties involving their band gaps.

The properties determining the usefulness of a SC material as light harvester in a PEC cell include^{12,13} (i) a band gap allowing the utilization of a significant fraction of the solar spectrum; (ii) well positioned band edges relative to the water redox levels; (iii) high mobilities, allowing electrons and holes to reach the surface and reduce/oxidize the targets before recombining, and (iv) chemical/structural stability under irradiation. In addition, low cost and non-toxicity are necessary properties. Numerous efforts have been made to find an efficient material for splitting water into H₂ and O₂ under visible light irradiation going more than 40 years back to Honda and Fujishima's report on electrochemical photolysis using TiO₂,¹⁴ but so far the ideal material has not been found.³

Here, we focus mainly on aspects (i), (ii) and (iv) mentioned above, namely the search for stable materials with optimal, well positioned, bandgaps. We consider metal oxides and oxynitrides, due to their high stability, and we concentrate on the cubic perovskite structure with general formula ABO₃ (space group *Pm3m*), due to the large variety of properties and applications of materials in this structure.¹⁵ We first consider the binary oxides where much experimental information is already available. The screening method is then applied to binary oxynitrides which generally have better positioning of the bandgap for water splitting compared to the oxides, but where much less experimental information is available, making theoretical screening necessary. Our study points to six new oxides and one oxynitride candidate for water splitting which should warrant experimental investigation.

Results and discussion

The first step is to find and validate an appropriate method for calculation of oxide and oxynitride stabilities and bandgaps. With respect to the stability, we use a standard DFT-GGA in the form of the RPBE-functional.¹⁶ (Details of the methods used in this paper can be found in the Methods section in the ESI †).

Reliable calculations of the bandgaps require a density functional beyond GGA. We use the so-called GLLB-SC functional^{17,18} which is demonstrated in Fig. 1 to predict the magnitudes of the bandgaps of a selection of non-magnetic metal oxides with different equilibrium structures¹⁹ within an absolute deviation of 0.5 eV—an accuracy sufficient for the present screening study. The computational cost of DFT-GLLB-SC is significantly lower than for many-body perturbation techniques such as the GW approximation and is crucial for the success of the screening. We use the GPAW code^{20,21} for all calculations presented in the following.

A cubic perovskite (see structure in Fig. 2C) consists of large 12-coordinated cations at the so-called A sites and small 6-coordinated cations at the B sites. Compounds with different combinations of cation charges in the A and B sites, e.g. 1 + 5, 2 + 4, and 3 + 3, have been found in nature. We consider all the possible combinations of perovskites obtained starting from the non-radioactive metals of the periodic table.

We define the formation energy, ΔE , of the perovskite metal oxides as the energy difference in the following reaction:

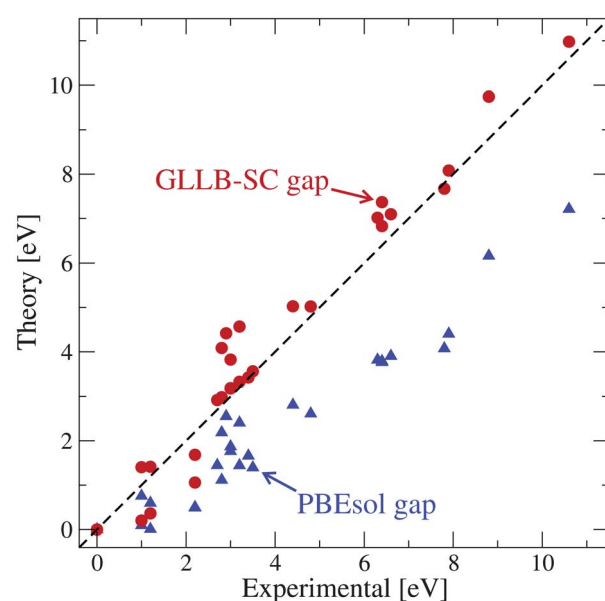


Fig. 1 DFT calculated bandgaps of selected oxides. Comparison between the theoretical and experimental bandgap of non-magnetic metal oxides in their most stable structure. The gaps are calculated using both the standard PBEsol (blue triangles) and the GLLB-SC functional (red circles). The dashed line represents the perfect matching between experiments and theory. (Details of the calculations with a list of the calculated oxides can be found in Table 1 of the ESI†).



We use water and H₂ as reference for O₂ instead of molecular oxygen, because the material we are looking for has to work in an aqueous environment. This choice is conservative with respect to O₂ because water is more stable than molecular oxygen and hydrogen by 2.46 eV per water molecule. The reaction energy is calculated directly from the DFT total energies of the participating molecules and solids. We estimate the Gibbs free energy of the reaction with water in the liquid phase following Nørskov *et al.*²² to be within 0.1 eV of the calculated DFT total energy difference. We therefore simply use ΔE for the perovskite oxide to estimate the stability relative to the two metals in their most stable structures.

Fig. 2A summarizes the results for the formation energies per atom and bandgaps for the 2704 investigated oxides in the perovskite structure. In the figure, the square corresponding to a given oxide containing two metals is split into two parts with the lower, left triangle indicating the stability (from red to blue with decreasing stability) and the upper, right triangle the bandgap (Fig. 2B). The data are available in the database *Computational Materials Repository*,²³ developed at CAMD, at the web address <http://cmr.fysik.dtu.dk/>.

The stability of a compound can be seen to be the result of three factors: (i) the sum of the possible oxidation numbers of the two metals has to be equal to 6 since the three oxygen atoms in the unit cell require 2 electrons each in order to form a compound without free charge; (ii) the radii of the A and B ions have to be in reasonable proportions and (iii) elements with low electronegativity are preferable for forming bonds with oxygen. The last

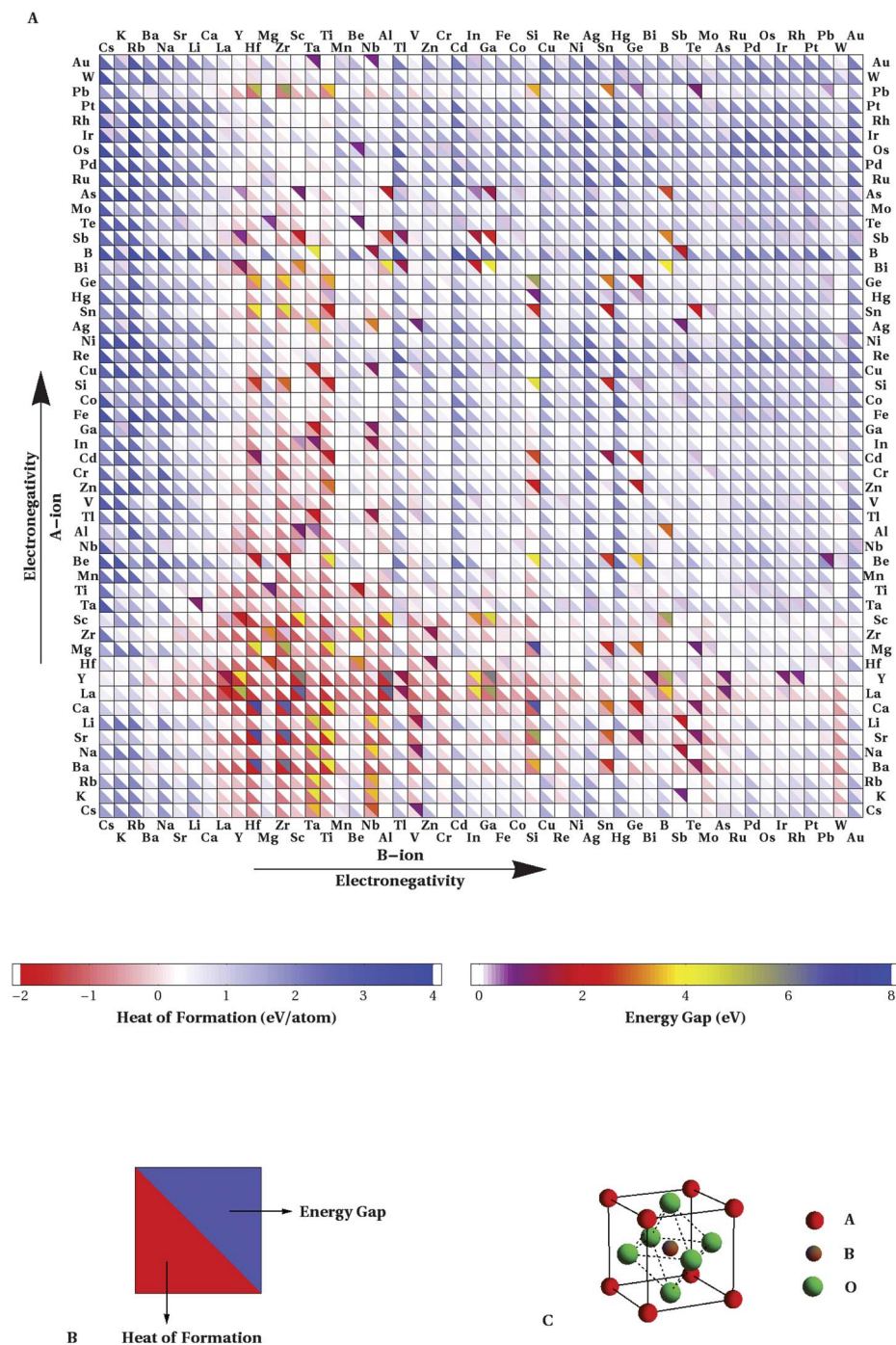


Fig. 2 (A) DFT calculated heat of formations per atom and bandgaps of perovskite binary metal oxides. (B) Each square represents an oxide with the lower, left triangle showing the formation energy with red indicating stability (and blue instability) while the upper, right triangle showing the bandgap with red indicating an advantageous bandgap in the range 1.5–3.0 eV. White indicates zero bandgap, purple indicates too small a gap, while yellow or blue indicates bandgaps larger than 3 eV. The pure chemical elements are sorted for increasing electronegativity. (C) reports the unit cell of the cubic perovskite structure. Data available at the web address: <http://cmr.fysik.dtu.dk/>.

factor is more relevant for the atoms in the A site due to the nonequivalence of the A and B ion positions.

The second design criterion we focus on is the size of the bandgap which we require to be in the range 1.5 eV to 3 eV. The lower limit comes about as the water-splitting threshold of 1.23 eV plus ~ 0.25 eV to account for the electrochemical

overpotentials.³ A more realistic limit may be even higher since the splitting of the quasi-Fermi level is smaller than the gap when the SC is under illumination.²⁴ However, for tandem cells the lower bandgap limit is relevant.³ Beyond the higher limit of 3.0 eV too little of the solar spectrum is left to be of interest. Depending on construction of the solar cell device, the light

capture in a cell may be thin or thick and we therefore perform the search for either the direct or the indirect gap. The color scale applied for the bandgap in Fig. 2 is chosen so that red indicates a gap in the design window. Compounds with good stabilities and gaps can thus be spotted as red squares.

We note that in accordance with Aguiar *et al.*,²⁵ the bandgap is seen to decrease when increasing the electronegativity of the B ion or when increasing the crystallographic symmetry by adjusting the size of the A ion.

The stabilities and the bandgaps are somewhat correlated as can be seen in Fig. 3, where the pale orange area indicates the region we are interested in. It is a challenge to combine a small gap with a high stability. However, quite a few of the compounds with very small or zero bandgap also exhibit high stability. To this group belong all the perovskites with an odd number of electrons for which the bands at the Fermi level are not completely filled or empty even if considering the possibility of a spin up and spin down occupation.

At this stage the screening identifies 43 binary oxides which fulfill the two design criteria: $\Delta E < 0.2$ eV/atom and $1.5 < \text{bandgap} < 3.0$ eV where we allow for a small positive energy of 0.2 eV/atom to allow for mildly metastable compounds. Many of the resulting candidates are in fact unstable towards a combination of restructuring and decomposition and we therefore expand our pool of reference systems used to assess stability to include not only the bulk metals but also the most stable single- and bi-metal oxides in their equilibrium structures as listed in the ICSD¹⁹ and the Materials Genome^{26,27} databases.

An additional criteria to stability and bandgap is the position of the band edges: for evolving both hydrogen and oxygen, the calculated gap should straddle both the hydrogen and oxygen evolution potentials (horizontal lines in Fig. 4). To estimate the band edges, we use an empirical method suggested and investigated by Butler and Ginley²⁸ and validated by Xu and Schoonen.²⁹ The scheme proceeds by positioning the middle of the gap at $E_0 + (\chi_A \chi_B \chi_O^3)^{1/5}$, where E_0 is the difference between the normal hydrogen electrode level and vacuum ($E_0 = -4.5$ eV) and χ_M denotes the electronegativity of the neutral atom M in the Mulliken scale, and the two edges are obtained by adding or subtracting half of the gap.

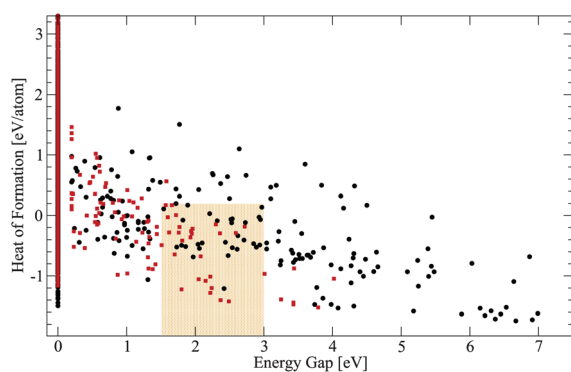


Fig. 3 Correlation between the heat of formation per atom and the bandgap for the oxide (black circles) and oxynitride (red squares) compounds. The region for candidates for solar light harvesting corresponds to the orange area.

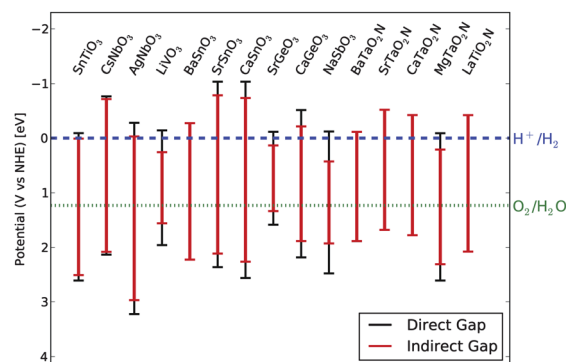


Fig. 4 The identified oxides and oxynitrides in the cubic perovskite structure with potential for splitting water in visible light. The figure shows the calculated band edges for both the direct (red) and indirect (black) gaps. The levels for hydrogen and oxygen evolution are also indicated.

After considering the more stringent stability criterion and the positions of the band edges the procedure results in only 10 binary oxides as candidate materials as indicated in the left part of Fig. 4. (A more detailed list is found in Table 2 and Fig. 1 of the ESI†). Some of these compounds are actually known to exist in other periodic structures, but including those in the pool of references does not change the list of candidates. However, two of the materials (SrSnO_3 and CaSnO_3) undergo lattice distortions and thereby obtain larger gaps beyond the visible light absorption limit. Two compounds are already known in the cubic perovskite structure: AgNbO_3 and BaSnO_3 . Of these, AgNbO_3 is well-known to split water in visible light in the presence of sacrificial reagents,³⁰ while BaSnO_3 performs less well because of defect-assisted recombination.³¹ It can be noted that if we relax the criterion on the bandgap we find oxides which can split water in UV light. 10 materials, like AgTaO_3 and SrTiO_3 , which are well known to split water in UV light,¹² have a gap in a range between 3 and 4 eV. To our knowledge no other cubic perovskites that can split water in visible light have been identified, and we therefore conclude that the screening procedure performs well and we turn our attention to the more unexplored territory of oxynitrides.

The oxynitrides are especially interesting from the point of view of the gap position relative to the energy levels for hydrogen and oxygen evolution. This is because the valence band (VB) edge is usually dominated by N p-orbitals which are higher in energy than the O p-orbitals, that mainly compose the VB of the oxides.

Using the same approach as for the oxides, we screen the possible combinations of two metals in the oxynitride cubic perovskite structure (ABO_2N) using the same three design criteria as for the oxides, where we now also include the most stable single- and bi-metal nitrides (M_xN_y and $\text{M}_x^1\text{M}_y^2\text{N}_z$) and the single-metal oxynitrides ($\text{M}_x\text{N}_y\text{O}_z$) in the pool of reference systems. The chemical potential of a nitrogen atom is taken from the nitrogen molecule.

Fig. 5 reports the results for the formation energies per atom and bandgaps for the 2704 oxynitrides with the cubic perovskite structure. As also shown in Fig. 3, the oxygen substitution is followed by a general reduction in the size of the bandgap. The

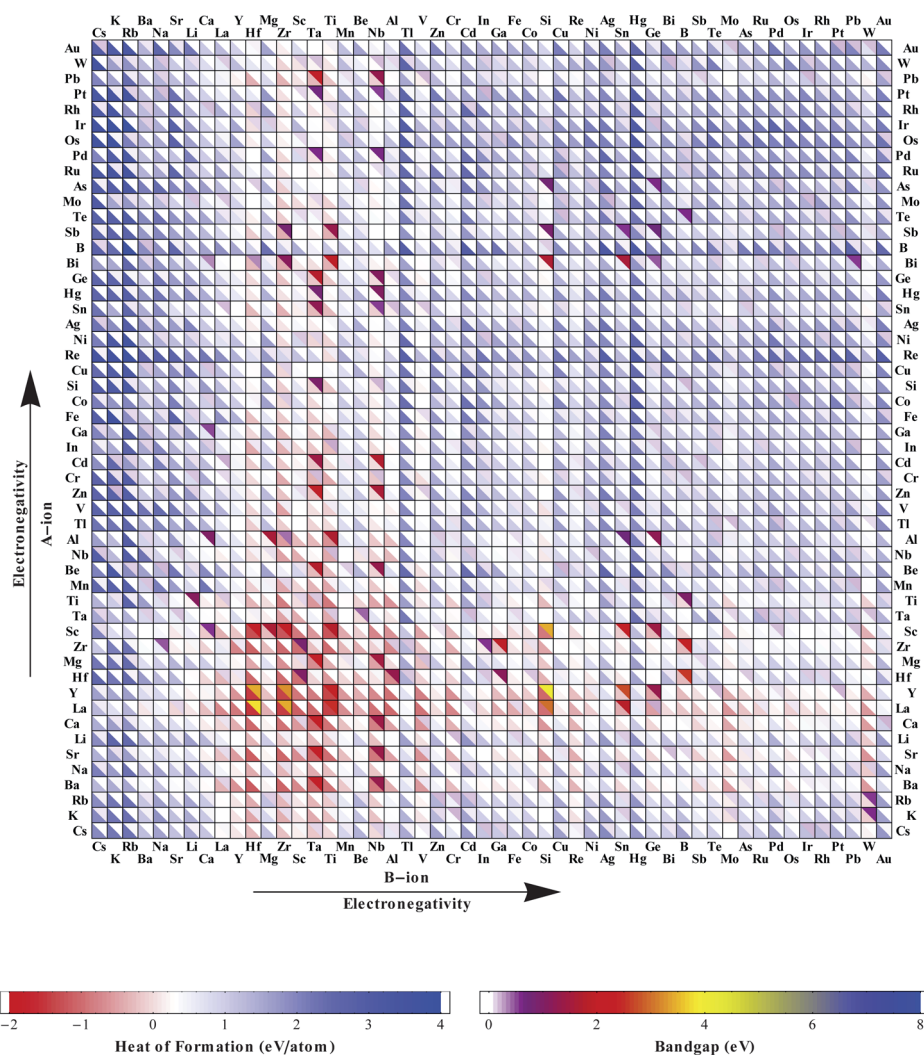


Fig. 5 DFT calculated heat of formations per atom and bandgaps of perovskite binary metal oxynitrides. The color bars are the same as used in Fig. 2.

effect of more general anion substitution especially in relation to the size and the position of the bandgap is relevant for the design of new materials able to split water. An investigation of those effects will be performed in the future.

The resulting five best candidates are shown in Fig. 4 and in more detail in Table 3 and Fig. 2 of the ESI.† Four of these combinations are already known (BaTaO₂N, SrTaO₂N, CaTaO₂N and LaTiO₂N) and perform well for hydrogen evolution.³² In fact, these compounds are, to our knowledge, the only cubic perovskite oxynitrides which have been shown experimentally to split water. We take this as a strong validation of our approach. The last compound, MgTaO₂N, has not yet been investigated experimentally.

Conclusions

In summary we have demonstrated that fast computational screening with respect to stability and bandgap is an efficient way to discover new light harvesting materials for water splitting. The method is based on a special exchange-correlation functional that produces sufficiently reliable bandgaps at low

computational cost. The method is verified by screening 2704 oxides with the cubic perovskite structure in order to find the best candidate for photoelectrolytic hydrogen production by water splitting. Ten materials, of which two are already known, fulfilled the requirements set up in the screening. This remarkable result shows the strength of the screening approach. We have continued with screening of oxynitrides in the same structure and found five possible candidates of which four are already known. To the best of our knowledge, the set of 15 candidates coming out from our screening includes all the compounds in the cubic perovskite structure that are known to be suitable for water splitting. It seems natural to move forward with the method for other materials that are relevant for photocatalytic water splitting or other related technologies, like thin film solar cells.

Acknowledgements

The authors acknowledge support from the Danish Center for Scientific Computing through grant HDW-1103-06, from the Catalysis for Sustainable Energy initiative funded by the Danish Ministry of Science, Technology and Innovation, and from the

Danish Council for Strategic Research's Programme Commission on Strategic Growth-Technologies (NABIIT). The Center for Atomic-scale Materials Design is sponsored by the Lundbeck Foundation.

References

- 1 N. Lewis and D. Nocera, *Proc. Natl. Acad. Sci. U. S. A.*, 2006, **103**, 15729–15735.
- 2 W. Shockley and H. J. Queisser, *J. Appl. Phys.*, 1961, **32**, 510–519.
- 3 M. G. Walter, E. L. Warren, J. R. McKone, S. W. Boettcher, Q. Mi, E. A. Santori and N. S. Lewis, *Chem. Rev.*, 2010, **110**, 6446–6473.
- 4 M. Gratzel, *Nature*, 2001, **414**, 338–344.
- 5 G. Ceder, Y.-M. Chiang, D. R. Sadoway, M. K. Aydinol, Y.-I. Jang and B. Huang, *Nature*, 1998, **392**, 694.
- 6 A. Franceschetti and A. Zunger, *Nature*, 1999, **402**, 60.
- 7 G. H. Johansson, T. Bligaard, A. V. Ruban, H. L. Skriver, K. W. Jacobsen and J. K. Nørskov, *Phys. Rev. Lett.*, 2002, **88**, 255506.
- 8 R. Armiento, B. Kozinsky, M. Fornari and G. Ceder, *Phys. Rev. B: Condens. Matter Mater. Phys.*, 2011, **84**, 014103.
- 9 J. Hachmann, R. Olivares-Amaya, S. Atahan-Evrenk, C. Amador-Bedolla, R. S. Sanchez-Carrera, A. Gold-Parker, L. Vogt, A. M. Brockway and A. Aspuru-Guzik, *J. Phys. Chem. Lett.*, 2011, **2**, 2241–2251.
- 10 N. M. O'Boyle, C. M. Campbell and G. R. Hutchison, *J. Phys. Chem. C*, 2011, **115**, 16200–16210.
- 11 W. Setyawan, R. M. Gaume, S. Lam, R. S. Feigelson and S. Curtarolo, *ACS Comb. Sci.*, 2011, **13**, 382–390.
- 12 A. Kudo and Y. Miseki, *Chem. Soc. Rev.*, 2009, **38**, 253–278.
- 13 X. Chen, S. Shen, L. Guo and S. S. Mao, *Chem. Rev.*, 2010, **110**, 6503–6570.
- 14 A. Fujishima and K. Honda, *Nature*, 1972, **238**, 37–38.
- 15 T. Ishihara, *Perovskite Oxide for Solid Oxide Fuel Cells*, Springer Verlag, 2009.
- 16 B. Hammer, L. B. Hansen and J. K. Nørskov, *Phys. Rev. B: Condens. Matter*, 1999, **59**, 7413–7421.
- 17 O. Gritsenko, R. van Leeuwen, E. van Lenthe and E. J. Baerends, *Phys. Rev. A: At., Mol., Opt. Phys.*, 1995, **51**, 1944.
- 18 M. Kuisma, J. Ojanen, J. Enkovaara and T. T. Rantala, *Phys. Rev. B: Condens. Matter Mater. Phys.*, 2010, **82**, 115106.
- 19 *ICSDWeb*, http://www.fiz-karlsruhe.de/icsd_web.html.
- 20 J. J. Mortensen, L. B. Hansen and K. W. Jacobsen, *Phys. Rev. B: Condens. Matter Mater. Phys.*, 2005, **71**, 35109.
- 21 J. Enkovaara, C. Rostgaard, J. J. Mortensen, J. Chen, M. Dulak, L. Ferrighi, J. Gavnholt, C. Glinsvad, V. Haikola, H. A. Hansen, H. H. Kristoffersen, M. Kuisma, A. H. Larsen, L. Lehtovaara, M. Ljungberg, O. Lopez-Acevedo, P. G. Moses, J. Ojanen, T. Olsen, V. Petzold, N. A. Romero, J. Stausholm-Møller, M. Strange, G. A. Tritsarlis, M. Vanin, M. Walter, B. Hammer, H. Hakkinen, G. K. H. Madsen, R. M. Nieminen, J. K. Nørskov, M. Puska, T. T. Rantala, J. Schiøtz, K. S. Thygesen and K. W. Jacobsen, *J. Phys.: Condens. Matter*, 2010, **22**, 253202.
- 22 J. Nørskov, J. Rossmeisl, A. Logadottir, L. Lindqvist, J. Kitchin, T. Bligaard and H. Jonsson, *J. Phys. Chem. B*, 2004, **108**, 17886–17892.
- 23 *Computational Materials Repository*, <https://wiki.fysik.dtu.dk/cmr/> (software), and <https://cmr.fysik.dtu.dk/> (database).
- 24 M. F. Weber and M. J. Dignam, *Int. J. Hydrogen Energy*, 1986, **11**, 225–232.
- 25 R. Aguiar, D. Logvinovich, A. Weidenkaff, A. Rachel, A. Reller and S. G. Ebbinghaus, *Dyes Pigm.*, 2008, **76**, 70–75.
- 26 *Materials Genome*, <http://www.materialsgenome.org/>.
- 27 A. Jain, G. Hautier, C. J. Moore, S. P. Ong, C. C. Fischer, T. Mueller, K. A. Persson and G. Ceder, *Comput. Mater. Sci.*, 2011, **50**, 2295–2310.
- 28 M. A. Butler and D. S. Ginley, *J. Electrochem. Soc.*, 1978, **125**, 228–232.
- 29 Y. Xu and M. A. Schoonen, *American Mineralogist*, 2000, **85**, 543–556.
- 30 H. Kato, H. Kobayashi and A. Kudo, *J. Phys. Chem. B*, 2002, **106**, 12441–12447.
- 31 W. Zhang, J. Tang and J. Ye, *J. Mater. Res.*, 2007, **22**, 1859–1871.
- 32 D. Yamasita, T. Takata, M. Hara, J. Kondo and K. Domen, *Solid State Ionics*, 2004, **172**, 591–595.

Computational Screening of Perovskite Metal Oxides for Optimal Solar Light Capture[†] - Electronic Supplementary Information

Ivano E. Castelli,^a Thomas Olsen,^a Soumendu Datta,^a David D. Landis,^a Søren Dahl,^b Kristian S. Thygesen,^a and Karsten W. Jacobsen,^{*a}

Received 20th September 2011, Accepted 17th November 2011

First published on the web Xth XXXXXXXXXXXX 200X

DOI: 10.1039/C1EE02717D

Methods

All calculations are performed for the primitive unit cell containing 5 atoms: 3 oxygen and 2 metals. Each simulation is composed of two parts: the optimization of the structure and the calculation of the bandgap.

With respect to the stability, Calle-Vallejo *et al.*¹ have recently shown that the trends in the heat of formation for oxides in the perovskite structure are well reproduced with Density Functional Theory (DFT)² using the generalized-gradient-approximation (GGA) in form of the RPBE-functional³ for the exchange-correlation energy. Even the absolute values of the heats of formation can be determined within a few tenths of an electronvolt per metal atom.¹ We have therefore adopted this scheme for the calculation of stabilities.

For each combination, we scan for the optimal lattice parameter, relax positions of the atoms inside the cell, until the residual forces are less than 0.05 eV Å⁻¹ and scan again for the lattice parameter with a mesh of 64 k-points in the Brillouin zone and a grid spacing equal to 0.17. For the total energy calculation, we use a mesh of 216 k-points in the Brillouin zone and a grid spacing equal to 0.15. The calculations performed are converged with respect to these parameters.

The GLLB-SC functional works by adding the derivative discontinuity to the Kohn-Sham gap to obtain the quasiparticle gap. For light harvesting one is really interested in the photo-absorption gap which may differ from the quasiparticle gap because of excitonic effects. However, for the class of materials that we study here we expect these effects to be only moderate. Using this functional, we need a mesh of about 400 k-points. We calculate the GLLB-SC gap only for the combinations with a RPBE direct gap larger than 0.2 eV. This does not affect the screening since we are looking for a material with a visible-light bandgap.

All the calculations are performed on our linux cluster Nifheim with 5640 CPU cores.

A linear programming algorithm (LP) was adopted to determine the stability relative to a pool of reference systems. For the oxides, we include the single-metal bulk and the most

stable single-metal oxides and compare them with the DFT energy of the combination in the perovskite structure. We consider a compound non-stable when the ABO₃ energy is 0.2 eV/atom greater than the best outcome from the LP:

$$\begin{aligned} \Delta E &= \text{ABO}_3(\text{s}) + \\ &- \min_{c_i} (c_1\text{A}(\text{s}) + c_2\text{B}(\text{s}) + \\ &+ c_3\text{A}_x\text{O}_y(\text{s}) + c_4\text{B}_x\text{O}_y(\text{s}) + c_5\text{O}), \end{aligned} \quad (1)$$

where A and B are the bulk metals, A_xO_y and B_xO_y are the single metal oxides included in the references and O is simply obtained from H₂O – H₂. The problem is solved with the constraints:

$$c_1 + c_3 = 1, \quad c_2 + c_4 = 1, \quad c_3 + c_4 + c_5 = 3, \quad (2)$$

for the A, B metals and oxygen, respectively, to obtain the perovskite stoichiometry. A similar analysis has been performed for the oxynitrides with the most stable single- and bi-metal nitrides and single-metal oxynitrides in the pool of reference system and with the constraints that the sum of the oxygen and nitrogen atoms must be equal to 2 and 1, respectively.

Bandgaps of Single-Metal Oxides

In † Table 1 we report the comparison between the theoretical gaps evaluated using the GLLB-SC functional^{26,27} with the experimental values in the most stable single-metal oxide structure obtained from the ICSD database.²⁸ Those values have been used for Fig. 1 in the manuscript. For each structure, we use the same procedure used for the screening: i.e. starting from the experimental data, we find the lattice parameters and we completely relax the internal degrees of freedom using an RPBE functional³ and afterward we evaluate the gaps using the GLLB-SC functional.

Cubic Perovskite Oxides

† Table 2 reports the combinations that fulfill the conditions for stability and for the gap. We specify the heat of formation and the indirect (direct) bandgap. The heat of formation

Oxide	GLLB-SC Gap [eV]	Expt. Gap [eV]	Method	Oxide	GLLB-SC Gap [eV]	Expt. Gap [eV]	Method
BeO	10.9	10.6	Optical ⁴	Rh ₂ O ₃	1.4	1.2	⁵
MgO	8.1	7.9	Thermal ⁶	PdO	0.2	1.0	⁷
CaO	7.7	7.8	Thermal ⁸	PtO ₂	1.4	1.8	⁹
SrO	7.4	6.4	Thermal ⁸	Cu ₂ O	1.1	2.2	¹⁰
BaO	5.0	4.4	Thermal ⁸	Ag ₂ O	0.4	1.2	¹¹
Sc ₂ O ₃	7.0	6.3	¹²	ZnO	3.3	3.3	Optical ¹³
TiO ₂ (r)	3.8	3.0	¹⁴	CdO	1.7	2.2	Optical ¹⁵
TiO ₂ (a)	4.6	3.2	¹⁶	Al ₂ O ₃	9.7	8.8	Optical ¹⁷
ZrO ₂ (r)	7.1	6.6	¹⁸	Ga ₂ O ₃	5.0	4.8	¹⁹
ZrO ₂ (m)	6.8	5.3	²⁰	In ₂ O ₃	3.0	2.6	²¹
Nb ₂ O ₅	3.4	3.4	⁷	SnO ₂	3.6	3.6	Photoemission ²²
MoO ₃	3.2	3.0	⁷	PbO	4.1	2.8	Indirect ²³
WO ₃	2.9	2.7	Optical ²⁴	Bi ₂ O ₃	4.4	2.9	Optical ²⁵

Table 1 bandgaps: theoretical and experimental bandgap evaluated for the metal oxides included in Fig. 1 of the manuscript. The type of the experimental gap is reported, when available, in the method column.

	ΔE [eV/atom]	Gap [eV]	Band Edges
TlTaO ₃	0.10	2.0 (2.0)	
GaTaO ₃	-0.03	2.1 (2.2)	
SnTiO ₃	0.10	2.5 (2.7)	✓
CsNbO ₃	0.18	2.8 (2.9)	✓
AgNbO ₃ ^a	0.20	2.9 (3.5)	✓
NaVO ₃	0.10	1.0 (1.7)	
LiVO ₃	0.17	1.3 (2.0)	✓
BaSnO ₃ ^a	-0.08	2.5	✓
SrSnO ₃ ^b	0.01	2.9 (3.4)	✓
CaSnO ₃ ^b	0.16	3.0 (3.6)	✓
SrGeO ₃	0.16	1.2 (1.7)	✓
CaGeO ₃	0.16	2.1 (2.7)	✓
NaSbO ₃	0.20	1.5 (2.6)	✓

Table 2 Cubic Perovskite Oxides: Formation energies (ΔE) per atom and indirect (direct) bandgap for the candidates for a new solar light capture material. It is also indicated (✓) if the band edges match with the water redox potential. ^a The experimental bandgaps for the two known cubic perovskite materials, AgNbO₃ and BaSnO₃, are equal to 2.8 eV²⁹ and 3.1 eV³⁰, respectively. ^b SrSnO₃ and CaSnO₃ suffer from a lattice distortion and they show an orthorhombic perovskite with a DFT (experimental) bandgaps equal to 4.2 (4.1) eV³⁰ and 3.8 (4.4) eV³⁰, respectively.

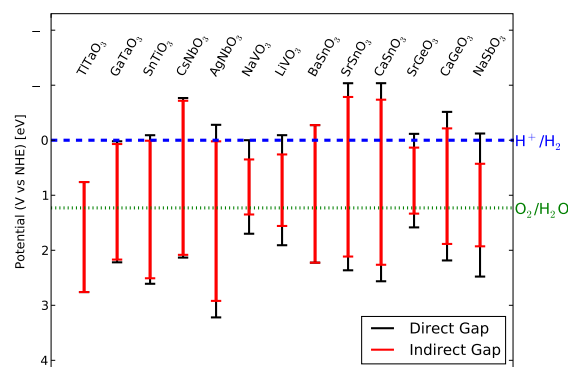


Fig. 1 Band edge position evaluated for the combinations of † Table 2. In the figure, we indicate the band edge position for the indirect (in red) and direct (in black) gap.

is obtained using the linear programming approach with the single-metal bulks, the single- and bi-metal oxides as pool of references. We report also if the band edges match with the water redox potential and the experimental bandgap for the combinations showing a perovskite or a perovskite-like experimental structure.

† Fig 1 reports the band edge positions, evaluated using the empirical rule provided by Butler and Ginley³¹ and using the DFT gaps calculated here, for all the combinations of † Table 2. Three combinations do not match with the H⁺/H₂ po-

	ΔE [eV/atom]	DFT Gap [eV]	Band Edges	Experimental Gap [eV]
BaTaO ₂ N	-0.01	2.0	✓	2.0 ³²
SrTaO ₂ N	0.00	2.1	✓	2.1 ³²
CaTaO ₂ N	0.09	2.2	✓	2.5 ³²
MgTaO ₂ N	0.19	2.1 (2.8)	✓	
PbTaO ₂ N	0.19	1.9 (2.1)		
LaTiO ₂ N	0.05	2.5	✓	2.1 ³³

Table 3 Cubic perovskite oxynitrides: Formation energies (ΔE) per atom and indirect (direct) bandgap for the candidates for a new solar light capture material. It is also indicated (✓) if the position of the band edges matches with the water redox potential and the experimental bandgap for the cubic perovskites known structures.

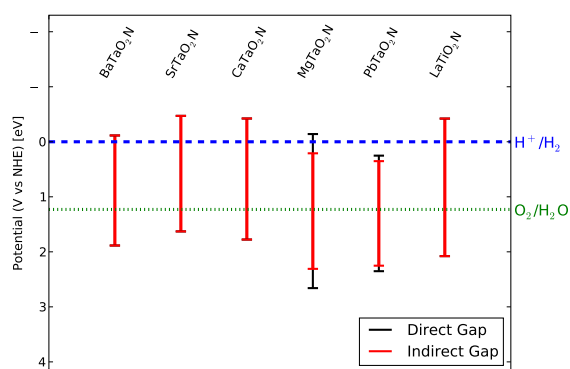


Fig. 2 Band edge position evaluated for the oxynitride combinations of † Table 3.

tential. All the combinations are suitable for oxygen evolution: this is a feature of the oxides.

Including the criteria on the band edge positions in addition to the rules on the heat of formation and on the gaps, we reduce the list of candidates from 13 to the 10 of Fig. 4 in the paper.

Cubic Perovskite Oxynitrides

As in † Table 2 for the oxides, in † Table 3 we list the combinations that comes out after the screening on the stability and on the bandgap. In addition we report if the position of band edges matches with the water redox potential. The experimental values for the gaps are in a good agreement with the DFT values.

† Fig 2 shows the bands position of all the combinations of † Table 3.

References

- 1 F. Calle-Vallejo, J. I. Martínez, J. M. García-Lastra, M. Mogensen and J. Rossmeisl, *Angewandte Chemie (International ed in English)*, 2010, **49**, 7699–7701.
- 2 P. Hohenberg and W. Kohn, *Physical Review*, 1964, **136**, 864.
- 3 B. Hammer, L. B. Hansen and J. K. Nørskov, *Physical Review B (Condensed Matter and Materials Physics)*, 1999, **59**, 7413–7421.
- 4 I. N. Ogorodnikov, V. I. Kirpa and A. V. Kruzhalov, *Technical Physics*, 1993, **38**, 404–408.
- 5 J. Ghose and A. Roy, Proceedings of the conference of the American Physical Society topical group on shock compression of condensed matter. AIP Conference Proceedings, 1996, pp. 901–904.
- 6 S. Mochizuki and T. Sakurai, *Physica Status Solidi a-Applied Research*, 1977, **41**, 411–415.
- 7 M. S. Seehra and H. Wijn, *Magnetic Properties - Magnetic Properties of Non-Metallic Inorganic Compounds Based on Transition Elements - Various Other Oxides - 6.1.5 Oxides of 4d and 5d Transition Elements.*, Springer Materials - The Landolt-Börnstein Database, 1992, vol. 27G.
- 8 N. N. Kovalev, Y. A. Logachev, A. V. Petrov and O. V. Sorokin, *Sov Phys Solid State*, 1975, **16**, 2367–2368.
- 9 J. Zhensheng, X. Chanjuan, Z. Qingmei, Y. Feng, Z. Jiazheng and X. Jinzhen, *Journal of Molecular Catalysis - A - Chemical*, 2003, **191**, 61–66.
- 10 S. Nikitine, *Journal of Physics and Chemistry of Solids*, 1961, **17**, 292–300.
- 11 L. Tjeng, M. Meinders, van Elp J, J. Ghijsen, G. Sawatzky and R. Johnson, *Physical Review B*, 1990, **41**, 3190–3199.
- 12 A. M. Herrero, B. P. Gila, C. R. Abernathy, S. J. Pearton, V. Craciun, K. Siebein and F. Ren, *Applied Physics Letters*, 2006, **89**, 2117.
- 13 J. M. Calleja and M. Cardona, *Physical Review B (Solid State)*, 1977, **16**, 3753–3761.
- 14 J. Pascual, J. Camassel and H. Mathieu, *Physical Review B (Condensed Matter)*, 1978, **18**, 5606–5614.
- 15 I. D. Makuta, S. K. Poznyak and A. I. Kulak, *Solid State Communications*, 1990, **76**, 65–68.
- 16 G. J. B., *Advances in Chemistry CY -*, American Chemical Society, 2011, pp. 113–137.
- 17 L. Y. L. Shen, G. A. Pasteur and D. E. Aspnes, *Physical Review B (Solid State)*, 1977, **16**, 3742–3745.
- 18 R. French, S. Glass, F. Ohuchi, Y. Xu and W. Ching, *Physical Review B*, 1994, **49**, 5133–5142.
- 19 L. Binet, D. Gourier and C. Minot, *Journal of Solid State Chemistry*, 1994, **113**, 420–433.
- 20 D.-Y. Kim, C.-H. Lee and S. J. Park, *Journal of Materials Research*, 1996, **11**, 2583–2587.
- 21 R. L. Weiher and R. P. Ley, *Journal of Applied Physics*, 1966, **37**, 299–302.
- 22 J. M. Themlin, R. Sporcken, J. Darville, R. Caudano, J. M. Gilles and R. L. Johnson, *Physical Review B (Condensed Matter)*, 1990, **42**, 71956–71925.
- 23 V. A. Izvozhikov, *Soviet Physics-Solid State*, 1963, **4**, 2014–2017.
- 24 E. Salje, *Journal of Applied Crystallography*, 1974, **7**, 615–617.
- 25 V. Dolocan, *Applied Physics*, 1978, **16**, 405–407.
- 26 O. Gritsenko, R. van Leeuwen, E. van Lenthe and E. J. Baerends, *Physical Review A (Atomic)*, 1995, **51**, 1944.
- 27 M. Kuisma, J. Ojanen, J. Enkovaara and T. T. Rantala, *Physical Review B*, 2010, **82**, 115106.
- 28 *ICSD Web*, http://www.fiz-karlsruhe.de/icسد_web.html.
- 29 H. Kato, H. Kobayashi and A. Kudo, *The Journal of Physical Chemistry B*, 2002, **106**, 12441–12447.

30 H. Mizoguchi, H. W. Eng and P. M. Woodward, *Inorg. Chem*, 2004, **43**, 1667–1680.

31 M. A. Butler and D. S. Ginley, *Journal of The Electrochemical Society*, 1978, **125**, 228–232.

32 D. Yamasita, T. Takata, M. Hara, J. Kondo and K. Domen, *Solid State Ionics*, 2004, **172**, 591–595.

33 H. Zhang, Y. Li, Q. Zhang and H. Wang, *Materials Letters*, 2008, **62**, 2729–2732.

Paper II

New Cubic Perovskites for One- and Two-photon Water Splitting Using the Computational Materials Repository

Ivano E. Castelli, David D. Landis, Kristian S. Thygesen, Søren Dahl, Ib Chorkendorff, Thomas F. Jaramillo, and Karsten W. Jacobsen.

Energy Environ. Sci. **5**, 9034-9043, 2012.

New cubic perovskites for one- and two-photon water splitting using the computational materials repository

Ivano E. Castelli,^a David D. Landis,^a Kristian S. Thygesen,^a Søren Dahl,^b Ib Chorkendorff,^b Thomas F. Jaramillo^c and Karsten W. Jacobsen^{*a}

Received 25th May 2012, Accepted 20th July 2012

DOI: 10.1039/c2ee22341d

A new efficient photoelectrochemical cell (PEC) is one of the possible solutions to the energy and climate problems of our time. Such a device requires development of new semiconducting materials with tailored properties with respect to stability and light absorption. Here we perform computational screening of around 19 000 oxides, oxynitrides, oxysulfides, oxyfluorides, and oxyfluoronitrides in the cubic perovskite structure with PEC applications in mind. We address three main applications: light absorbers for one- and two-photon water splitting and high-stability transparent shields to protect against corrosion. We end up with 20, 12, and 15 different combinations of oxides, oxynitrides and oxyfluorides, respectively, inviting further experimental investigation.

Introduction

The conversion of solar light into energy by photoelectrochemical reactions is one of the possible ways to address the world's pressing energy supply and storage problem.¹ This technology is based on the direct harvest of photons by semiconductor materials (SCs) and using the energy from the created electron–hole pairs to run certain chemical reactions. One example is the water-splitting reaction which turns water into hydrogen and oxygen which may then be used later as fuels in for example fuel cells. The number of photons collected to run the reactions, the number of

different materials involved and the size of their bandgaps can be combined and optimized in order to obtain the highest possible efficiency.^{2–5} The simplest way to construct such a device is to use a single material with a bandgap in the visible range, well positioned with respect to the redox potential of water. This method has been known since 1972 for water splitting under UV-light using TiO₂ (ref. 6) albeit with very low efficiency and high additional electrical and chemical bias. A more complicated but also a potentially more efficient way is to use two photons and combine two SC materials to split water in a tandem cell.^{4,7}

The search for new materials using *ab initio* quantum mechanical calculations has been possible because of the methodological improvements and the increase of computational powers. Examples include the construction of semiconductor superlattices,⁸ the development of battery cathodes,⁹ searching for high stability alloys,¹⁰ screening for inorganic scintillator materials,¹¹ for high-performance piezoelectrics,¹² for organic photovoltaics using molecules,^{13–15} and bandgap engineering.^{16,17}

^aCenter for Atomic-scale Materials Design, Department of Physics, Technical University of Denmark, DK-2800 Kongens Lyngby, Denmark. E-mail: kwj@fysik.dtu.dk

^bCenter for Individual Nanoparticle Functionality, Department of Physics, Technical University of Denmark, DK-2800 Kongens Lyngby, Denmark

^cDepartment of Chemical Engineering, Stanford University, Stanford, CA 94305, USA

Broader context

The development of semiconductors suitable for photo-electrochemical water splitting under solar light is currently under intense investigation. In particular the focus has been on oxides and oxynitrides where a few materials have shown good activity for light-induced splitting of water. We have performed a computational screening of about 19 000 cubic perovskites obtained by combining 52 different metals with oxygen, nitrogen, sulfur and fluorine as anions. We have focused on three applications: one- and two-photon water splitting and transparent shielding against corrosion. We have also implemented a database and presentation system, the Computational Materials Repository, for easy access and analysis of the data. Since a successful material should collect a significant part of the solar spectrum, we have performed our screening based on criteria of size and position of the bandgap as well as on stability. We find 20, 12, and 15 materials with potential interest for one- and two-photon water splitting, and shielding purposes, respectively. Among them, 7, 4, and 6 are already known in the cubic perovskite structure and/or in the water splitting community. 13, 8, and 9 new materials invite further experimental investigation.

Here, we search for materials to be used in such water-splitting devices. We focus mainly on perovskite oxides with one or more replacements for oxygen neighbors in the periodic table. The space of investigation is composed of around 19 000 compounds collected and analyzed in the Computational Materials Repository (CMR).^{18,19}

The present work expands on previous studies of perovskite materials²⁰ both by considering a broader range of compositions with new elements and by studying not only one-photon water splitting but also two-photon (Z-scheme) water splitting and transparent shielding of photocatalysts.

Our study suggests five and twelve new materials for the one- and two-photon processes, respectively, and fifteen for the transparent shield. These materials therefore lend themselves to further experimental investigation. In addition, we have analyzed the correlation between the bandgap and the heat of formation for the different datasets in order to obtain a more general picture of the material requirements.

Methods

Our screening is performed using the Density Functional Theory (DFT) real space code GPAW^{23,24} with a standard DFT-GGA exchange–correlation functional in the form of the RPBE-approximation²⁵ for the evaluation of the stabilities and a more sophisticated semi-local functional called GLLB-SC^{26,27} for the calculation of the bandgaps. The latter functional is computationally cheaper than many-body methods like GW and its precision is of the order of 0.5 eV. The details about the method have been described and validated in a previous paper²⁰ where we proposed 15 oxides and oxynitrides (ABO₃ and ABO₂N) for the one-step water splitting.

A linear programming (LP) algorithm has been adopted to determine whether a compound is stable or not with respect to the pool of reference systems listed in Table 1. This method has been used in the past for example for obtaining effective cluster interactions,²⁸ and more recently for prediction of thermodynamically reversible hydrogen storage reactions²⁹ and for the design of new semiconductors for water splitting.²⁰ We choose the chemical potential for oxygen to refer to water in the gas phase because the materials have to work in an aqueous environment. Indeed, it has been recently shown that the presence of a water film is a necessary condition to run the water splitting reaction since it increases the mobility of H⁺.³⁰ The Gibbs free energy of the reaction with water in the liquid phase following Nørskov *et al.*³¹ is estimated to be within 0.1 eV of the calculated DFT total energy difference. The oxygen reference has been calculated as the energy difference between water and hydrogen (H₂O–H₂) in the gas phase. Otherwise the chemical potentials for

nitrogen, sulfur and fluorine have been taken from the standard references in the gas phase, *i.e.* N₂, S₈, and F₂. An ABON₂ compound is considered stable when its DFT energy relative to the best outcome from the LP, ΔE , is no more than 0.2 eV per atom. The small positive value allows for some metastability and inaccuracy in the calculations. The energy difference, ΔE , can thus be written as

$$\begin{aligned} \Delta E = & \text{ABON}_2(\text{s}) - \min_{c_i} (c_1\text{A}(\text{s}) + c_2\text{B}(\text{s}) + c_3\text{A}_{a_3}\text{O}_{o_3}(\text{s}) \\ & + c_4\text{B}_{b_4}\text{O}_{o_4}(\text{s}) + c_5\text{A}_{a_5}\text{N}_{n_5}\text{O}_{o_5}(\text{s}) + c_6\text{B}_{b_6}\text{N}_{n_6}\text{O}_{o_6}(\text{s}) \\ & + c_7\text{A}_{a_7}\text{N}_{n_7}(\text{s}) + c_8\text{B}_{b_8}\text{N}_{n_8}(\text{s}) + c_9\text{A}_{a_9}\text{B}_{b_9}\text{O}_{o_9}(\text{s}) \\ & + c_{10}\text{A}_{a_{10}}\text{B}_{b_{10}}\text{N}_{n_{11}}(\text{s}) + c_{11}\text{O} + c_{12}\text{N}_2), \end{aligned} \quad (1)$$

where all the chemical formulae are reported in Table 1. The LP problem is solved with the constraints

$$\begin{aligned} \sum_i a_i c_i = 1, \quad \sum_i b_i c_i = 1, \\ \sum_i o_i c_i = 1, \quad \sum_i n_i c_i = 2, \end{aligned} \quad (2)$$

which ensure the correct stoichiometry of ABON₂ and with

$$c_i \geq 0, \quad (3)$$

which guarantees that only the references containing A, B, N, or O are taken into account. A similar investigation has been performed for the other compounds considered in this work.

To evolve hydrogen and oxygen, a matching between the positions of the band edges of the compound and the redox potential of water is required. It is complicated and computationally expensive to calculate the band edges using DFT because it requires the investigation of one or more material surfaces, and the outcoming results are complicated further by the role of water present on the surface and of the pH of the environment. For these and other issues, we use an empirical formula based on the electronegativity and on the size of the bandgap^{32,33} to estimate the positions of the edges. According to this formula the positions of the valence and conduction band edges, $E_{\text{VB,CB}}$, are given by

$$E_{\text{VB,CB}} = E_0 + (\chi_{\text{A}}\chi_{\text{B}}\chi_{\text{O}}\chi_{\text{N}}^2)^{1/5} \pm E_{\text{gap}}/2, \quad (4)$$

where E_0 is the difference between the normal hydrogen electrode (NHE) and the vacuum ($E_0 = -4.5$ eV) and χ_{M} is the electronegativity of the neutral atom M in the Mulliken scale. Eqn (4) refers to the ABON₂ perovskite; for the other combinations, we need to change the $\chi_{\text{O}}\chi_{\text{N}}^2$ in the geometric mean to, for example, $\chi_{\text{O}}^2\chi_{\text{F}}$ for the ABO₂F perovskites. The evaluation of the position of the band edges given by this equation is of sufficient quality to be used during the screening process.³³

Table 1 Pool of systems chosen as references in the linear programming algorithm as available from the ICSD database²¹ and from the Materials Project.²² M indicates the metallic element in the composition

Chemical formula	Description
M _x	Most stable, single-metal bulk
M _x O _y , M _x N _y , M _x S _y , M _x F _y	Most stable, single-metal oxide, nitride, sulfide, fluoride
M _x N _y O _z , M _x S _y O _z , M _x F _y O _z	Most stable, single-metal oxynitride, oxysulfide, oxyfluoride
M _x ¹ M _y ² O _z , M _x ¹ M _y ² N _z , M _x ¹ M _y ² S _z , M _x ¹ M _y ² F _z	Most stable, bi-metal oxide, nitride, sulfide, fluoride
M _x ¹ M _y ² N _z O _k , M _x ¹ M _y ² F _z O _k	Most stable, bi-metal oxynitride, oxyfluoride

Results and discussion

The crystal structure selected for the screening is the cubic perovskite (space group $Pm\bar{3}m$) because of its simplicity, and its wide applicability in general.³⁴ We select 52 metals from the periodic table to occupy the A- and B-ion positions in the structure. We have previously investigated the results of a nitrogen substitution in an ABO_3 cell²⁰ and the beneficial effects that a lower-electronegativity element, like nitrogen, has for the design of new water splitting materials based on a one-photon process. Driven by this, we here screen for other anion combinations than O_3 and O_2N . In particular, we are interested in unit cells with a larger concentration of nitrogen ($ABON_2$ and ABN_3) and in replacing oxygen with its neighbors in the periodic table (ABO_2S and ABO_2F). A combination of oxygen, nitrogen, and fluorine ($ABOFN$) has been studied as well.

A material needs at least three main properties to be used in a water splitting device: (i) it needs to be stable, (ii) it needs to have a bandgap in an appropriate range and (iii) its band edges need to match the redox potential of water. As described above (i) is considered based on a comparison between the DFT energy of the perovskite compound and the DFT energies of a pool of references into which each compound can split (LP). In this comparison, we take the chemical potential of oxygen from water (instead of the oxygen molecule) in order to get a more realistic heat of formation for a compound in contact with water. We note that this stability measure does not take into account any influence from the illumination. (ii) is treated by calculating the bandgap using the GLLB-SC functional. (iii) uses the bandgap obtained in (ii) and eqn (4).

The database – general trends

Oxides are well known for their high stabilities and for their large bandgaps, even though metallic oxides have been synthesized. Efficiency for light harvesting requires a material with a bandgap below 3 eV, well positioned around the hydrogen and oxygen evolution potentials. This matching is difficult to accomplish in the oxide class.

The most natural element to be used as a replacement for oxygen is nitrogen because of its similar atomic radius. Oxy-nitrides are less stable than oxides and the loss in stability is correlated to the increase of the nitrogen/oxygen ratio in the unit cell. Nitrogen is slightly less electronegative than oxygen. This has two effects: a general reduction in the width of the bandgaps and a shifting up in the valence band positions. These effects are very interesting for the design of the next generation of light harvesters.

Fig. 1 shows the correlation between the bandgaps and heats of formation for all the classes of materials considered in this work. Results are shown relative to both the standard states of the elements, except for oxygen which is taken from water vapor (upper panel), and the larger pool of reference systems used here (lower panel) where we thus include the possibility of phase separation into single compounds like single-metal oxides or other systems in the pool of references (Table 1). A wider bandgap is seen to correspond to a higher stability for both sets of reference systems even if stable zero-gap compounds are also found. The correlation is most clear for the standard reference

systems. A large bandgap in a two-metal compound is a sign of stability, even when the heat of formation is calculated relative to a broad set of reference systems that may already exhibit a bandgap. The resulting stability of the two-metal oxides is therefore smaller than when the comparison is made with metals in their standard states. The most stable compounds are oxides, and an oxygen replacement with another non-metal brings about a reduction of both the stability and the size of the gap.

Sulfur is close to nitrogen in electronegativity, with the same charge as oxygen but a larger radius. On the one hand, the bandgaps are of the same order of magnitude as for the oxynitrides and with well positioned band edges; on the other hand, the distortion introduced into the cells due to a too large radius reduces the stabilities of the compounds and the heats of formation are generally above 0.2 eV which we set as the threshold. No stable combination has been found in the ABO_2S perovskite and other structures have to be considered.

Fluorine is the most electronegative element. The oxyfluorides show a wide range of gaps like the oxides. The radius of fluorine is slightly smaller than that of oxygen, with the consequence of a reduction in the stability of the compounds due to a reduction of the symmetry in the unit cells.

A co-doping of N and F in TiO_2 to $TiO_xN_yF_z$ has been shown to be effective for water oxidation.³⁵ The sizes of the gap for the $ABONF$ compounds are comparable with the oxynitrides, but the highly distorted cells result in low stabilities and heats of formation above 0.2 eV.

Handling the data using the computational materials repository

The Computational Materials Repository (CMR)^{20,36} is a set of computational tools and a database for handling large amounts of computational electronic-structure data. The CMR software³⁶ supported the present screening by storing the calculated results (Fig. 1) and making the analysis possible through its python and web interfaces. In order to make the process of finding the results efficient, the individual calculations and combinations thereof (so-called computational “groups”) were annotated with keywords like “perovskite” and fields (name/value pairs) such as “gllb_sc_dir_gap = 0.3” or “A = Bi”, “B = Si” and “anion = N₃” for $BiSiN_3$. After choosing a combination such as ABN_3 or ABO_2S and the set of reference energies in the web interface, the necessary data to determine the heat of formation are automatically fed into the linear programming algorithm. The results can then be further restricted by other fields as for example the position of the band edges.

Fig. 2 shows an example of a search in the CMR database. We are here interested in $ABON_2$ combinations that are stable, *i.e.* with a heat of formation smaller than 0.2 eV, a bandgap in the visible range, *i.e.* between 1.5 and 3 eV, and band edges matching the redox potential of water. The results are shown in Fig. 3. As we will discuss later on, these properties are required for materials to be used in the one-photon (overall) water splitting device shown in Fig. 4(a). Two materials for overall water splitting have been found in the $ABON_2$ combination: $LaTaON_2$ and $YTaN_2$. The figure reports the crystal structure (using Jmol³⁷) and some interesting properties like heat of formation, size and

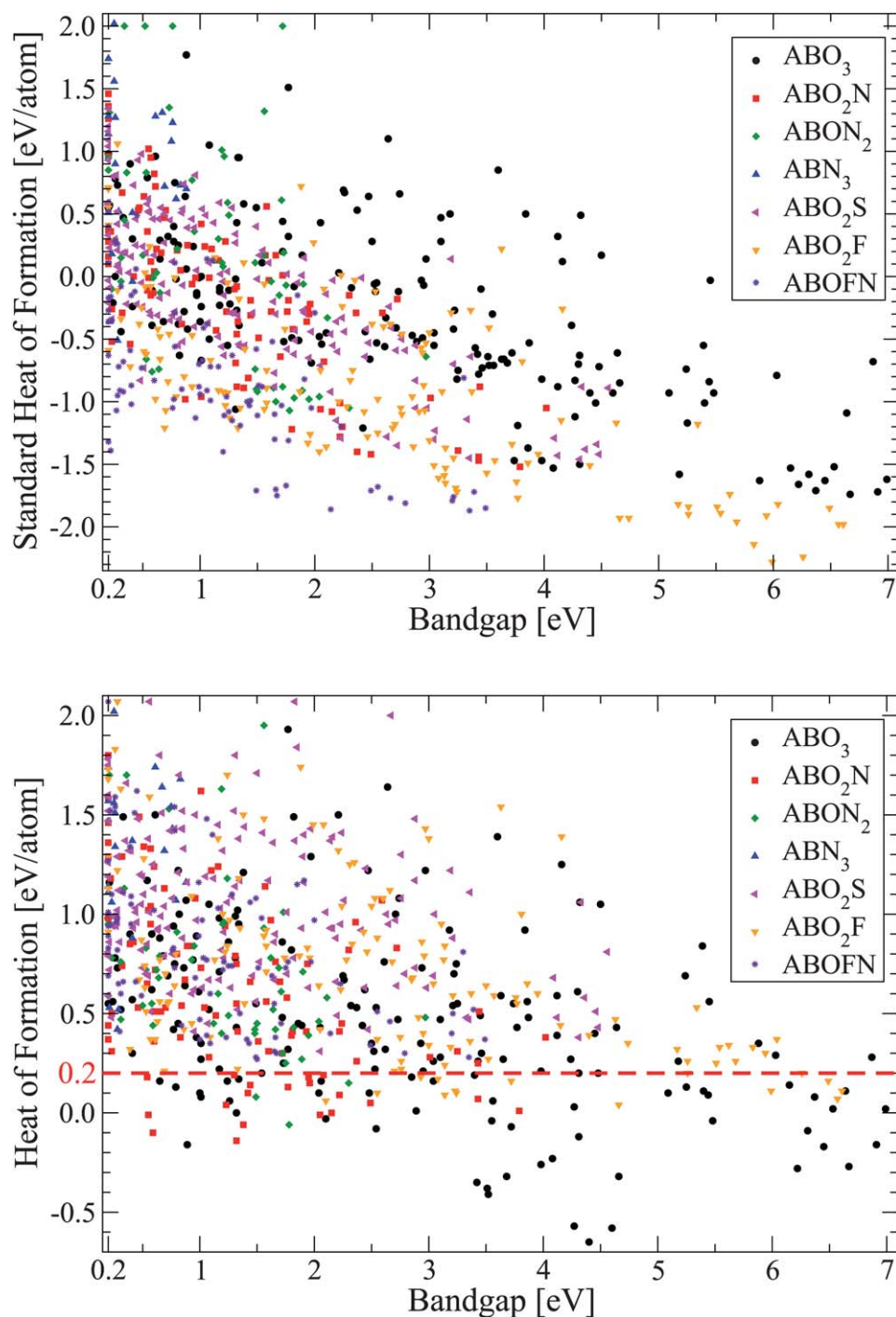


Fig. 1 Correlation between bandgap and heat of formation for the datasets under investigation. The figure includes only the compounds showing a gap (>0.2 eV). The upper figure shows the calculated standard heat of formation relative to the elements in their standard states except the oxygen chemical potential which is taken from water vapor because our material has to be stable in a water environment. The lower figure shows the heat of formation relative to the larger pool of reference systems as explained in the text. The heat of formation threshold of 0.2 eV is also displayed.

position of the bandgap, paper where the computation for this structure appears for the first time, *etc.* It is also possible to download the atomic positions as an *xyz*-file; all details of the calculations are for further use.

The same approach proposed here has been used for all the different applications we are going to describe in the next sections. All involved calculations and the analysis tools are available at <https://cmr.fysik.dtu.dk>.

One-photon water splitting

In 1972 Honda and Fujishima reported their results on electrochemical photolysis using TiO_2 .⁶ For 40 years, numerous efforts have been made to find an efficient material for simultaneous production of both H_2 and O_2 (one-photon or overall water splitting) under visible light irradiation, but so far the ideal material has not been found.³ The overall water splitting process

Computational Materials Repository

Fig. 2 Example of a search in CMR for materials with particular properties, like bandgap in the visible range and matching the redox potential of water. A stability criterion is also required. Other properties can be easily investigated.

is schematized in Fig. 4(a): an electron–hole pair is created by a single photon, the electron and the hole, after reaching two different regions of the surface in order to avoid recombination, evolve hydrogen and oxidize water, respectively.

The criteria for a candidate to be used for solar light capture that we shall use here are: (i) chemical and structural stability, (ii) bandgap in the visible light range, *i.e.* between 1.5 and 3 eV, (iii) band edges straddling with the oxygen and hydrogen evolution potentials, and (iv) high mobility to avoid recombination. Properties (i), (ii), and (iii) are taken into account during this screening. The requirements are schematized in Table 2.

Fig. 4(b) reports the 20 candidates resulting from the screening. On the left of the figure, there are the ABO₃ and ABO₂N combinations published in a previous paper²⁰ and included here for completeness. Out of the remaining 5 compounds, one, LaTaON₂, is already known and performing relatively well for hydrogen evolution when a noble metal is deposited on it, but no O₂ evolution was detected.³⁸ No experimental photoelectrochemical studies have been reported for the last four materials. There is no evidence of other competing crystal structures with the same chemical composition and thus they can be suggested for experimental investigation. Considering all datasets, we have found in total 20 materials suitable for collecting visible light and for the evolution of both hydrogen and oxygen.

Once the electron–hole pair is formed, the electron and the hole need to reach two different points at the surface to evolve hydrogen and oxygen. This mechanism depends on the mobility of the charges and thus the effective masses. It is presently not well understood what the optimal values for the mobility or the free electron mass are so we cannot use this as a criterion for the screening. However, we can perform an *a posteriori* investigation of the effective masses for the materials resulting from the screening.

The effective mass m^* is defined as

$$m^* = \hbar^2 \left(\frac{\partial^2 \varepsilon}{\partial k_i \partial k_j} \right)^{-1}, \quad (5)$$

i.e., as the second derivative of the energy band with respect to two orientations, i and j , in reciprocal space evaluated at the LUMO (HOMO) for the electron (hole). The parabolical approximation of the band is true only in a small interval of the LUMO (HOMO), thus we need to run calculations with finer sampling of k -points. While the effective mass is a 3×3 matrix with eigenvalues depending on the coordinate system, the trace of the mass matrix, defined as

$$\frac{1}{M^*} = \frac{1}{3} \left(\frac{1}{m_x^*} + \frac{1}{m_y^*} + \frac{1}{m_z^*} \right), \quad (6)$$

is a unique number independent of the orientation.

For all the candidates in Fig. 4(b), the LUMO is at the Gamma-point, $\Gamma = (0,0,0)$. The role of the different metals and anions is more crucial for determining the HOMO: the oxides show the HOMO mostly at $R = (\frac{1}{2}, \frac{1}{2}, \frac{1}{2})$ and at $M_{xz} = (\frac{1}{2}, 0, \frac{1}{2})$ or $M_{xy} = (\frac{1}{2}, \frac{1}{2}, 0)$, the oxynitrides and oxyfluorides at Γ and R .

The upper panel of Fig. 5 shows the electron and hole masses (calculated using eqn (6)) for the 20 candidates. The masses span over one order of magnitude. In general, the oxides show very light electron masses and hole masses above $1 m_e$, one order of magnitude higher than the electron masses. In addition to the hole masses shown in the figure, NaSbO₃, SrGeO₃, CaGeO₃, BaSnO₃, and SrSnO₃ have also heavier hole masses, not included in the figure, of more than $10 m_e$ due to a degeneracy of the HOMO (at R -point). The gap between the electron and hole masses close to the oxynitrides and the masses have values between 0.5 and $1 m_e$ with lighter hole masses compared to the oxides. For the oxyfluorides, the hole masses are heavier than the ones of the oxynitrides while the electron masses are of the same order of magnitude. The green region highlights the materials known to evolve hydrogen/oxygen in the presence of a sacrificial agent and the orange region indicates the material known for failing as a

Jmol	Id_ref	A	B	anion	heat_of_formation	glbbsc_dir-gap	glbbsc_ind-gap	CB_dir	CB_ind	VB_dir	VB_ind	atoms	db_keywords	doi	Ingredients	db_description	downloads
	840810	Y	Ta	ON2	0.14	2.50	2.30	-0.21	-0.11	2.29	2.19	N O Ta	ABON2 moxn N	10.1039/C2EE223410	0.02 O48Y32	Screening cubic perovskite structures, metal oxynitrides	
	842064	La	Ta	ON2	-0.02	2.10	1.80	-0.07	0.08	2.03	1.88	La N O Ta	ABON2 La Ta LaTaNO2 moxn (1La, N O ON2, perovskite Ta tandem Y TaTaNO2	10.1039/C2EE223410	0.26 N3Ta3 + 0.28 N2 + 0.06 La6N12Ta4 + 0.33 La2O3	Screening cubic perovskite structures, metal oxynitrides	

Fig. 3 Result for the search table of Fig. 2. Two candidates for one-photon water splitting have been found in the ABON₂ combination.

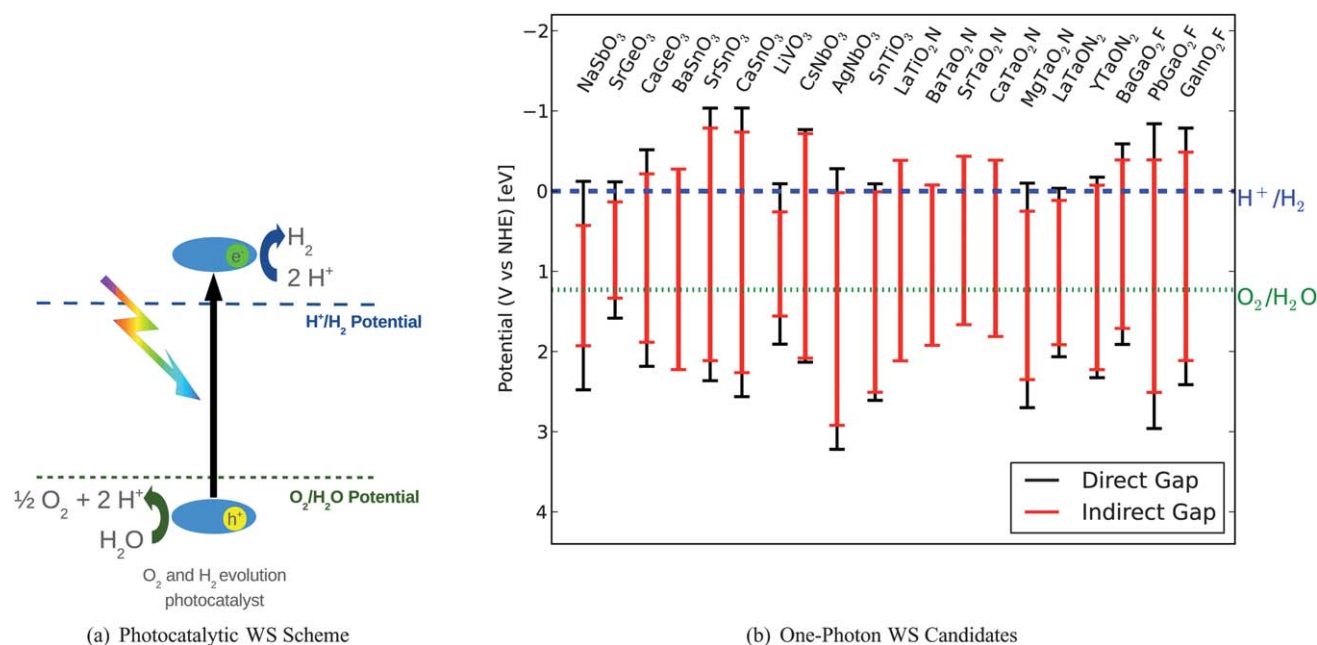


Fig. 4 (a) Overall water splitting scheme. One photon creates an electron–hole pair that evolves simultaneously oxygen and hydrogen from water. (b) The identified candidates in the cubic perovskite structure with potential for a photocatalytic water splitting device. The figure shows the calculated band edges for both the direct (red) and indirect (black) gaps. The levels for hydrogen and oxygen evolution are also indicated.

photocatalyst possibly due to defect assisted recombination.³⁹ It seems that a light electron mass and a heavy hole mass are not a good combination because it is difficult to maintain the neutral charge of the compound and to avoid fast recombination. It would be possible to analyze further the role of the effective masses if some of the other compounds proposed here would be synthesized.

The lower panel of Fig. 5 shows the ratio between the highest and lowest values of the electron and hole masses for each combination. The oxides with the HOMO at the *R*-point are isotropic in the three directions both for the electron and hole masses. For the others, the LUMO (HOMO) shows a flatband in at least one direction leading to an anisotropy in the mass. Both the oxynitrides and the oxyfluorides show anisotropy for the electron and hole masses due to a flatband in one direction generated by the oxygen substitution. An additional investigation on the relationship between the effective masses, the different orientations and the photocatalytic activity will be performed in the future since such properties could be potentially used for designing water splitting devices. An ideal device could be highly anisotropic, for example a pillared structure, with a long direction for efficient harvesting of the light and short directions to allow the electrons and holes to reach the surfaces.

Table 2 Screening parameters used for the applications considered

Screening parameters	One-photon WS	Two-photon WS	Transparent shield (TS)
Chemical/structural stability (ΔE)	$\Delta E \leq 0.2$ eV	$\Delta E \leq 0.2$ eV	$\Delta E \leq 0.2$ eV
Bandgap (E_{gap})	$1.5 \leq E_{\text{gap}} \leq 3$ eV	$1.3 \leq E_{\text{gap}} \leq 3$ eV	$E_{\text{gap}}^{\text{dir}} > 3$ eV
Band edges	$\text{VB}_{\text{edge}} > 1.23$ eV	$\text{VB}_{\text{edge}}^{\text{anode}} > 1.23$ eV	Photoanode TS
($\text{VB}_{\text{edge}}, \text{CB}_{\text{edge}}$)	$\text{CB}_{\text{edge}} < 0$ eV	$\text{CB}_{\text{edge}}^{\text{cathode}} < 0$ eV	$1.7 < \text{VB}_{\text{edge}} < 2.5$ eV
		$\text{VB}_{\text{edge}}^{\text{cathode}} > \text{CB}_{\text{edge}}^{\text{anode}}$	Photocathode TS $-0.7 < \text{CB}_{\text{edge}} < 0$ eV

Two-photon water splitting

A rough calculation of the efficiency of the overall scheme of Fig. 4(a), considering the losses, results in a conversion efficiency limit of around only 7%.⁴⁰

A different approach to achieve the water splitting under visible light is to divide the process into a two-step mechanism,^{4,41} called Z-scheme or tandem cell (Fig. 8(a)), where two photons are required and two different semiconductors are responsible for the H₂ and O₂ evolution.

The requirements for the two-step water splitting process are: (i) structural/chemical stability, (ii) visible light bandgaps with the appropriate sizes for a good efficiency, and (iii) an optimal matching between the band edges of the semiconductors and the redox potential of water. (iv) in addition to the usual requirements for the position of the band edges for the overall water splitting, the electron transfer in the tandem cell also requires that the electron generated in the anode that oxidizes water to oxygen is higher in energy than the hole generated by the cathode reducing 2H⁺ to H₂.

Fig. 6 shows the ideal efficiency of such a device without any losses considering the spectral distribution of the solar photon flux at AM1.5 and calculating the different ratios of absorbed photons from the layered semiconductors. The maximum

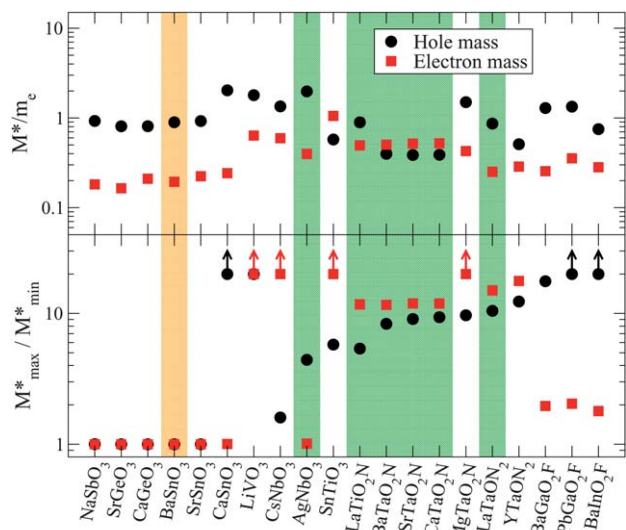


Fig. 5 Average effective masses calculated using eqn (6) (upper panel) and ratio between the highest and lowest effective masses for the candidates in Fig. 4(b). The upper-arrow indicates a very high anisotropy between the masses in different directions. In the green area, the materials that are able to split water in the presence of a sacrificial agent are shown. In the orange area the material known to not work as a photocatalyst because of defect assisted recombination is shown.

efficiency is obtained when the two materials absorb the same number of photons. For working in a photocatalytic tandem cell, the sum of the bandgaps of the two semiconductors needs to be at around 2.8 eV (black line in Fig. 6). This value is obtained based on the estimates shown in Fig. 7. The bare energy required to split

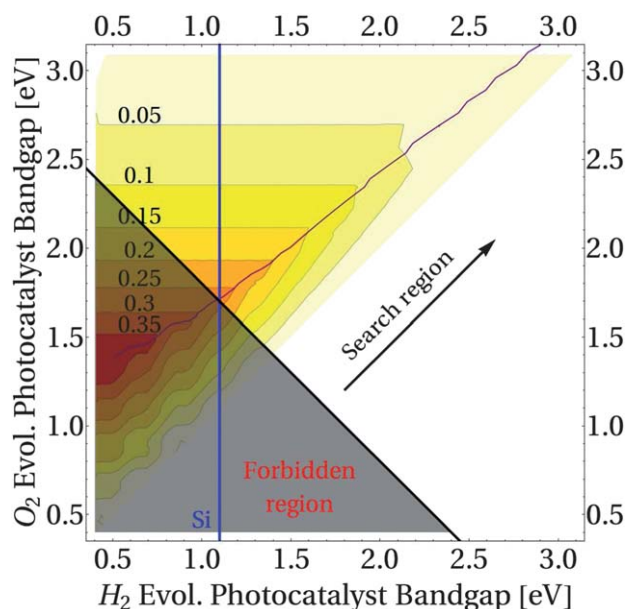


Fig. 6 Theoretical efficiency of the two-photon water splitting. The blue line corresponds to the experimental bandgap of silicon and the black line is the minimum combination of gap for running the reaction. The purple line corresponds to the highest efficiency achievable once the H_2 photocatalyst is chosen. The numbers in the contour plot correspond to the ideal efficiency.

water is 1.23 eV. However, additional energy is required to overcome the overpotential for the oxygen and hydrogen evolution processes and to compensate for the positions of the quasi Fermi levels within the bandgaps. We take as a rough estimate the sum of the two overpotentials to 0.5 eV, 0.1 eV for the cathode and 0.4 eV for the anode.⁴² When the system is running, the electrons and holes are in a non-equilibrium distribution described by quasi Fermi levels. Those levels correspond to the work that the electrons and holes can do and they reduce the effect of the bandgap by around 0.5 eV per semiconductor. Allowing for an additional 0.1 eV related to the electron transfer between the semiconductors we reach the limiting sum of the two bandgaps to be 2.8 eV. The problem of band banding required for e^-h^+ separation is not considered as it can be solved by appropriate doping of the SC and by the pn-junction.³

Returning to the calculated efficiencies in Fig. 6 we see that the optimum values of the bandgaps are 1.7 eV and 1.1 eV. A perfect candidate for the hydrogen evolution semiconductor is therefore silicon with a bandgap of 1.1 eV as indicated by the vertical blue line in the figure. In fact, the DFT GLLB-SC calculation of bulk silicon in the diamond structure gives a 1.2 eV indirect bandgap with a perfect match of the conduction band edge with the hydrogen potential. In addition, it is a well-known material with an advanced fabrication technology at hand and it has recently been shown to work well with non-noble hydrogen evolution catalysts.⁴³ A theoretical efficiency of more than 25% is seen to be obtained by combining silicon with a ~ 1.7 eV bandgap-semiconductor.

In order to find interesting candidates for the anode, we shall in the following screen for semiconductors with bandgaps in the range between 1.3 and 3.0 eV (Table 2). The losses described above give a lower limit of 1.7 eV for a semiconductor to be combined with silicon. However, we widen the search window a bit in order to take the inaccuracy of the GLLB-SC bandgap calculations of about 0.5 eV into account.

All the compositions shown in Fig. 4(b) are possible materials to be used in a Z-scheme cell for hydrogen or oxygen evolution. In particular, the oxynitrides, that are able to reduce water in the presence of a sacrificial agent,⁴⁴ might also be used for the same

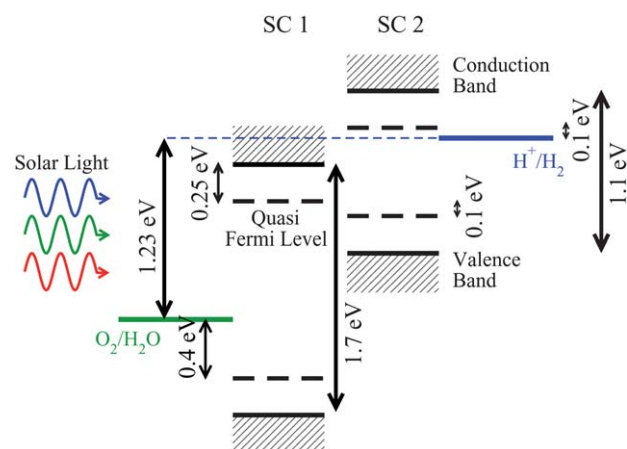


Fig. 7 Sketch of the electronic levels in the tandem device. The positions of the quasi Fermi levels and the required overpotentials result in a minimal requirement for the sum of the two bandgaps of 2.8 eV.

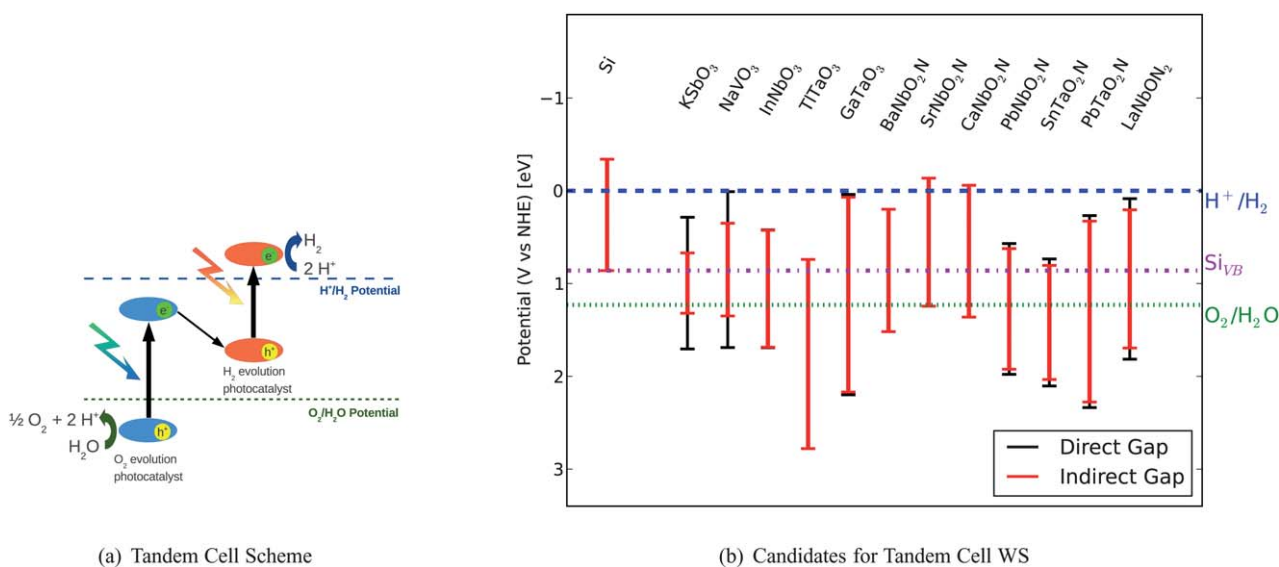


Fig. 8 (a) Tandem cell scheme in which two photons and two semiconductors are required for the evolution of oxygen and hydrogen. (b) The identified candidates in the cubic perovskite structure with potential for a tandem cell device. The figure shows the calculated band edges for both the direct (red) and indirect (black) gaps. The valence band for silicon (calculated using eqn (4) and the GLLB-SC bandgap) and the levels for hydrogen and oxygen evolution are also indicated.

purpose in a tandem cell instead of silicon. This class of materials is characterized by a bandgap of ~ 1 eV larger than the theoretical optimum for the hydrogen evolution photocatalyst. The best solution in terms of efficiency is obtained by swapping the two layers with respect to Fig. 8(a) so the part of the solar spectrum at higher energy is absorbed by the hydrogen evolution photocatalyst (now with a larger bandgap than silicon) and the remainder goes through and is absorbed by the oxygen photocatalyst, *i.e.* the large bandgap does not necessarily need to be the anode side.

Fig. 8(b) shows the candidates for oxygen evolution not yet presented in Fig. 4(b). None of the oxides are experimentally known and all of them are possible solutions to the oxygen evolution problem. Some of the niobates oxynitride (CaNb_2N , SrNbO_2N , BaNbO_2N , and LaNbON_2) have been recently synthesized.⁴⁵ The GLLB-SC bandgaps for those materials are slightly smaller than the experimental values because of a small distortion in the crystal cells that contributes to opening up the gaps. CaNbO_2N shows activity both in water oxidation and reduction with sacrificial agents, and SrNbO_2N has a low rate of O_2 evolution. No activity has been found for both BaNbO_2N and LaNbON_2 probably because of too small gaps that are insufficient to overcome the overpotentials required for starting the reaction or due to a recombination enhanced by defects. The other oxynitrides have not been investigated.

If we relax the criterion that the conduction band edge of the semiconductor has to be above the valence band edge of silicon we find only one more material, TlNbO_3 . This material could potentially be used for oxygen evolution in combination with a hydrogen evolution photocatalyst with a lower valence band than silicon (like the tantalate or niobate oxynitrides). TlNbO_3 has a gap of 1.3 eV, small enough for achieving a good efficiency, and the VB position is well positioned in energy compared with the oxynitrides for allowing the electron transfer between the materials to take place.

No candidates for only H_2 evolution have been found because the stability requirement seems to automatically lead to bandgaps which are positioned fairly low relative to the water redox potentials.

Transparent shield

One problem related to the use of materials for oxygen production is photocorrosion. A possible solution is to develop a highly stable and at the same time transparent thin film to cover the oxygen evolution photocatalyst as a protective shield, as shown in Fig. 9(a). The transparency can be obtained with a semiconductor with a large bandgap of, say, more than 3 eV, and as we have seen a large bandgap generally nicely correlates with high stability (Fig. 1), especially when we consider the standard references (upper panel).

The device illustrated in Fig. 9(a) is the photoanode protecting shield for a tandem cell but the principle can also be used for the one-photon scheme. The electron with higher energy evolves hydrogen, while the hole at lower energy moves through the transparent film and evolves oxygen. The size of the gap and the position of the edges are crucial for such a material: it needs a direct bandgap in the UV range in order to avoid absorbing a part of the visible light spectrum, and the valence band level needs to be placed between the edges of the photocatalyst and the potential of oxygen evolution so that the hole can reach the reaction region with a small energy loss (< 0.5 eV). Here we do not consider the possibility of tunneling charge transport through the protective layer⁴⁶ as the dominant mechanism. The screening criteria can be summarized as

$$E_{\text{gap}}^{\text{dir}} > 3.0 \text{ eV}, 1.7 \text{ eV} < \text{VB}_{\text{edge}} < 2.5 \text{ eV}. \quad (7)$$

VB_{edge} is chosen to take into consideration the errors in the bandgap and in the positions of the band edges and the

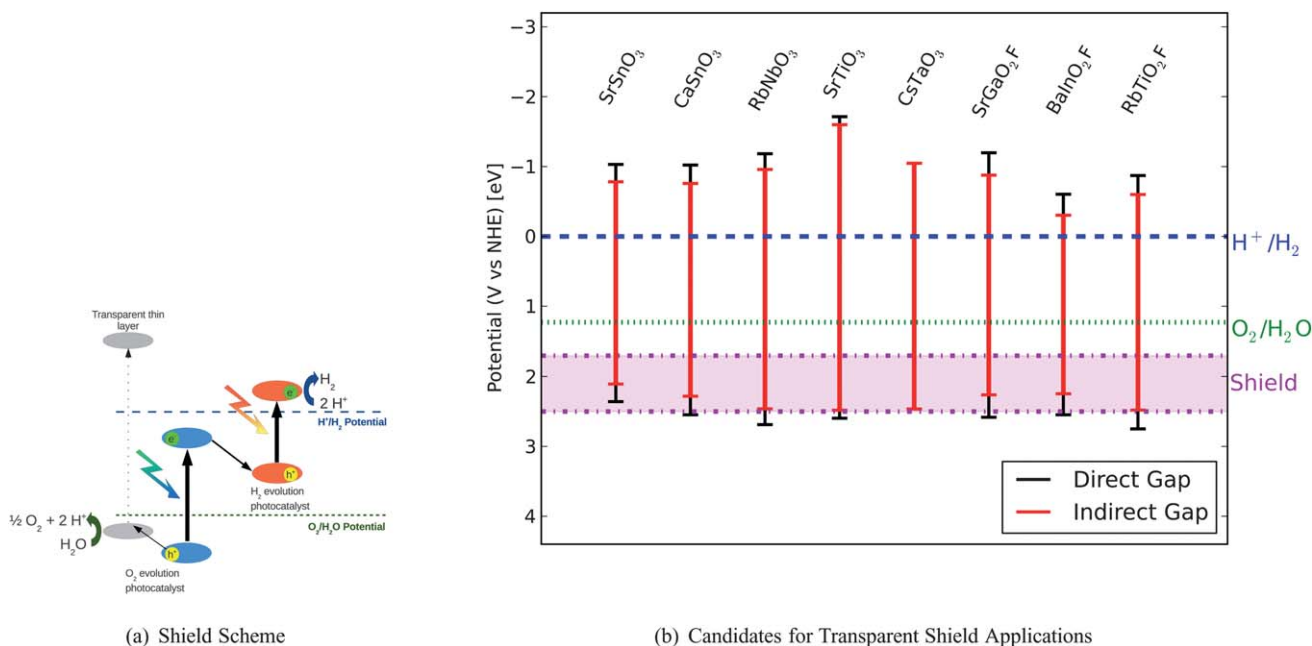


Fig. 9 (a) Scheme of a tandem cell with a transparent protecting shield on the oxygen evolution photocatalyst for avoiding photocorrosion. (b) The identified candidates in the cubic perovskite structure to be used as a transparent shield for a photoanode material. The figure shows the calculated band edges for both the direct (red) and indirect (black) gaps.

overpotential of oxygen. As before we furthermore apply a stability threshold of 0.2 eV per atom (Table 2).

Eight compounds fulfill the selected criteria (Fig. 9(b)). Because of the large bandgap required, the only perovskite classes of interest are the oxides and the oxyfluorides. SrSnO₃, CaSnO₃, and SrTiO₃ are stable in the perovskite structure (SrSnO₃ and CaSnO₃ are experimentally known in the distorted perovskite structure with even larger bandgaps than the ones predicted here). In particular, SrTiO₃ is a well-known material for water splitting under UV light, it has all the requirements for being used also as a transparent shield in a visible-light device. The other 5 candidate compounds have not been synthesized yet.

The same idea can be used to develop a protecting shield for the photocathode.⁴⁷ In this device, the electron with higher energy is transported from the photocathode conduction band to the one of

the protecting shield where it evolves hydrogen. As shown in Table 2, the only change in the screening parameters is the position of the conduction band edge that has to be between -0.7 and 0 eV. This range allows the candidates to work with silicon and various other photocathodes.

Fig. 10 shows the nine candidates as protecting materials for the cathode. AgNbO₃ is known as a good photocatalyst and it can also be used as a protecting shield because of its direct bandgap in the UV range (the indirect bandgap is in the visible part of the solar spectrum). AgTaO₃ and KTiO₂F are experimentally known to exist in the perovskite structure, while the other six compounds are currently unknown. Only two combinations, RbTiO₂F and BaInO₂F, can be used as a transparent shield in combination with both a cathode and an anode.

Conclusions

In this work, we have combined the screening approach and a database to investigate several properties related to the problem of light harvesting and water splitting. The method proposed here has been applied to about 19 000 different compounds and we identify some 20 candidates for the overall water splitting, 12(+20) for the development of a tandem cell device, and 8 and 9 to be used as transparent protecting shields for the oxygen and the hydrogen evolution reactions, respectively. Some of these materials are already known in the water splitting community, but several are also completely new suggestions. The same method described here could also be applied to search for other applications like the design of new highly-stable conductors to be used as electrodes.

The most important limitation of the study is the focus on only a single crystal structure, the cubic perovskite, but the extensive stability analysis involving many different combinations and also different crystal structures for the reference systems lend credibility

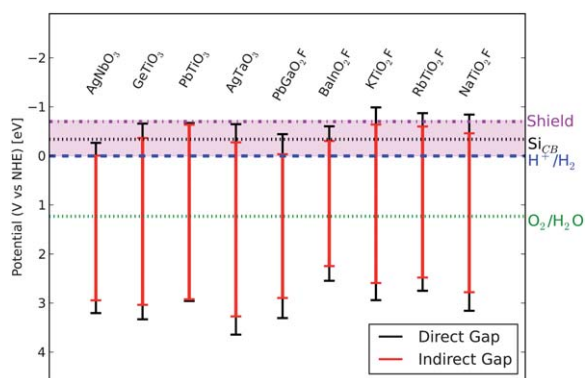


Fig. 10 The identified candidates in the cubic perovskite structure to be used as a transparent shield for a photocathode material. The figure shows the calculated band edges for both the direct (red) and indirect (black) gaps. The conduction band of silicon is also indicated.

to the identified candidates. However, in future work it would be natural to combine our approach with structure prediction tools to widen the scope of the materials search even further.

We finally note that the issues addressed here of efficient absorption of solar light and appropriate electron–hole mobilities only constitute one part of the challenges behind the function of an optimal photoelectrochemical device. Another key issue is to find appropriate (co-)catalysts to minimize the overpotentials which lead to energy loss in the chemical reactions.^{3,48}

Acknowledgements

The authors acknowledge support from the Danish Center for Scientific Computing through grant HDW-1103-06 and from the Catalysis for Sustainable Energy (CASE) initiative funded by the Danish Ministry of Science, Technology and Innovation. The Center for Atomic-scale Materials Design (CAMD) is sponsored by the Lundbeck Foundation. The Center for Individual Nanoparticle Functionality (CINF) is funded by the Danish National Research Foundation. T.F.J. and K.W.J. are supported by the Center on Nanostructuring for the Efficient Energy Conversion (CNEEC) at Stanford University, an Energy Frontier Research Center founded by the U.S. Department of Energy, Office of Science, Office of Basic Energy Sciences under award number DE-SC0001060.

References

- 1 N. Lewis and D. Nocera, *Proc. Natl. Acad. Sci. U. S. A.*, 2006, **15729**–15735.
- 2 W. Shockley and H. J. Queisser, *J. Appl. Phys.*, 1961, **32**, 510–519.
- 3 M. G. Walter, E. L. Warren, J. R. McKone, S. W. Boettcher, Q. Mi, E. A. Santori and N. S. Lewis, *Chem. Rev.*, 2010, **110**, 6446–6473.
- 4 M. Gratzel, *Nature*, 2001, **414**, 338–344.
- 5 A. B. Laursen, S. Kegnaes, S. Dahl and I. Chorkendorff, *Energy Environ. Sci.*, 2012, **5**, 5577–5591.
- 6 A. Fujishima and K. Honda, *Nature*, 1972, **238**, 37–38.
- 7 S. Dahl and I. Chorkendorff, *Nat. Mater.*, 2012, **11**, 100–101.
- 8 A. Franceschetti and A. Zunger, *Nature*, 1999, **402**, 60.
- 9 G. Ceder, Y.-M. Chiang, D. R. Sadoway, M. K. Aydinol, Y.-I. Jang and B. Huang, *Nature*, 1998, **392**, 694.
- 10 G. H. Johannesson, T. Bligaard, A. V. Ruban, H. L. Skriver, K. W. Jacobsen and J. K. Nørskov, *Phys. Rev. Lett.*, 2002, **88**, 255506.
- 11 W. Setyawan, R. M. Gaume, S. Lam, R. S. Feigelson and S. Curtarolo, *ACS Comb. Sci.*, 2011, **13**, 382–390.
- 12 R. Armiento, B. Kozinsky, M. Fornari and G. Ceder, *Phys. Rev. B: Condens. Matter Mater. Phys.*, 2011, **84**, 14103.
- 13 J. Hachmann, R. Olivares-Amaya, S. Atahan-Evrenk, C. Amador-Bedolla, R. S. Sanchez-Carrera, A. Gold-Parker, L. Vogt, A. M. Brockway and A. Aspuru-Guzik, *J. Phys. Chem. Lett.*, 2011, **2**, 2241–2251.
- 14 R. Olivares-Amaya, C. Amador-Bedolla, J. Hachmann, S. Atahan-Evrenk, R. S. Sanchez-Carrera, L. Vogt and A. Aspuru-Guzik, *Energy Environ. Sci.*, 2011, **4**, 4849–4861.
- 15 N. M. O'Boyle, C. M. Campbell and G. R. Hutchison, *J. Phys. Chem. C*, 2011, **115**, 16200–16210.
- 16 W.-J. Yin, H. Tang, S.-H. Wei, M. M. Al-Jassim, J. Turner and Y. Yan, *Phys. Rev. B: Condens. Matter Mater. Phys.*, 2010, **82**, 045106.
- 17 M. d'Avezac, J.-W. Luo, T. Chanier and A. Zunger, *Phys. Rev. Lett.*, 2012, **108**, 027401.
- 18 Center for Atomic-scale Materials Design, <http://www.camd.dtu.dk/>.
- 19 *Computational Materials Repository*, [https://wiki.fysik.dtu.dk/cmrf/\(Documentation\)andhttps://cmr.fysik.dtu.dk/\(Database\)](https://wiki.fysik.dtu.dk/cmrf/(Documentation)andhttps://cmr.fysik.dtu.dk/(Database)).
- 20 I. E. Castelli, T. Olsen, S. Datta, D. D. Landis, S. Dahl, K. S. Thygesen and K. W. Jacobsen, *Energy Environ. Sci.*, 2012, **5**, 5814.
- 21 *ICSDWeb*, http://www.fiz-karlsruhe.de/icsd_web.html.
- 22 *Materials Project – A Materials Genome Approach*, <http://materialsproject.org/>.
- 23 J. J. Mortensen, L. B. Hansen and K. W. Jacobsen, *Phys. Rev. B: Condens. Matter Mater. Phys.*, 2005, **71**, 35109.
- 24 J. Enkovaara, C. Rostgaard, J. J. Mortensen, J. Chen, M. Dulak, L. Ferrighi, J. Gavnholt, C. Glinsvad, V. Haikola, H. A. Hansen, H. H. Kristoffersen, M. Kuisma, A. H. Larsen, L. Lehtovaara, M. Ljungberg, O. Lopez-Acevedo, P. G. Moses, J. Ojanen, T. Romero, V. Petzold, N. A. Romero, J. Stausholm-Møller, M. Strange, G. A. Tritsarlis, M. Vanin, M. Walter, B. Hammer, H. Hakkinen, G. K. H. Madsen, R. M. Nieminen, J. K. Nørskov, M. Puska, T. T. Rantala, J. Schiøtz, K. S. Thygesen and K. W. Jacobsen, *J. Phys.: Condens. Matter*, 2010, **22**, 253202.
- 25 B. Hammer, L. B. Hansen and J. K. Nørskov, *Phys. Rev. B: Condens. Matter*, 1999, **59**, 7413–7421.
- 26 O. Gritsenko, R. van Leeuwen, E. van Lenthe and E. J. Baerends, *Phys. Rev. A: At., Mol., Opt. Phys.*, 1995, **51**, 1944.
- 27 M. Kuisma, J. Ojanen, J. Enkovaara and T. T. Rantala, *Phys. Rev. B: Condens. Matter Mater. Phys.*, 2010, **82**, 115106.
- 28 G. D. Garbulsky and G. Ceder, *Phys. Rev. B: Condens. Matter*, 1995, **51**, 67–72.
- 29 V. Ozolins, E. H. Majzoub and C. Wolverton, *J. Am. Chem. Soc.*, 2009, **131**, 230–237.
- 30 F. Dionigi, P. C. K. Vesborg, T. Pedersen, O. Hansen, S. Dahl, A. Xiong, K. Maeda, K. Domen and I. Chorkendorff, *Energy Environ. Sci.*, 2011, **4**, 2937–2942.
- 31 J. Nørskov, J. Rossmeisl, A. Logadottir, L. Lindqvist, J. Kitchin, T. Bligaard and H. Jonsson, *J. Phys. Chem. B*, 2004, **108**, 17886–17892.
- 32 M. A. Butler and D. S. Ginley, *J. Electrochem. Soc.*, 1978, **125**, 228–232.
- 33 Y. Xu and M. A. Schoonen, *Am. Mineral.*, 2000, **85**, 543–556.
- 34 T. Ishihara, *Perovskite Oxide for Solid Oxide Fuel Cells*, Springer Verlag, 2009.
- 35 K. Nukumizu, J. Nunoshige, T. Takata, J. N. Kondo, M. Hara, H. Kobayashi and K. Domen, *Chem. Lett.*, 2003, 196.
- 36 D. D. Landis, J. S. Hummelshøj, S. Nestorov, J. Greeley, M. Dulak, T. Bligaard, J. K. Nørskov and K. Jacobsen, *Comput. Sci. Eng.*, 2012, in press.
- 37 *Jmol: an open-source Java viewer for chemical structures in 3D*, <http://jmol.sourceforge.net/>.
- 38 M. Liu, W. You, Z. Lei, T. Takata, K. Domen and C. Li, *Chin. J. Catal.*, 2006, **27**, 556–558.
- 39 W. Zhang, J. Tang and J. Ye, *J. Mater. Res.*, 2007, **22**, 1859–1871.
- 40 M. R. Weber and M. J. Dignam, *Int. J. Hydrogen Energy*, 1986, **11**, 225–232.
- 41 M. Grätzel, *Chem. Lett.*, 2005, 8–13.
- 42 S. Trasatti, *Croat. Chem. Acta*, 1990, **63**, 313–329.
- 43 Y. Hou, B. Abrams, P. Vesborg, M. Björketun, K. Herbst, L. Bech, A. Setti, C. Damsgaard, T. Pedersen, O. Hansen, J. Rossmeisl, S. Dahl, J. Nørskov and I. Chorkendorff, *Nat. Mater.*, 2011, **10**, 434–438.
- 44 D. Yamasita, T. Takata, M. Hara, J. Kondo and K. Domen, *Solid State Ionics*, 2004, **172**, 591–595.
- 45 B. Siritanaratkul, K. Maeda, T. Hisatomi and K. Domen, *ChemSusChem*, 2011, **4**, 74–78.
- 46 Y. Chen, J. Prange, S. Dhnen, Y. Park, M. Gunji, C. Chidsey and P. McIntyre, *Nat. Mater.*, 2011, **10**, 539–544.
- 47 B. Seger, A. B. Laursen, P. C. Vesborg, T. Pedersen, O. Hansen, S. Dahl and I. Chorkendorff, *Angew. Chem., Int. Ed.*, 2012, **51**, DOI: 10.1002/anie.201203585.
- 48 L. Duan, L. Tong, Y. Xu and L. Sun, *Energy Environ. Sci.*, 2011, **4**, 3296–3313.

Paper III

Bandgap Engineering of Double Perovskites for One- and Two-photon Water Splitting

Ivano E. Castelli, Kristian S. Thygesen, and Karsten W. Jacobsen.

MRS Online Proceedings Library **1523**, 2013.

Bandgap Engineering of Double Perovskites for One- and Two-photon Water Splitting

Ivano E. Castelli¹ and Kristian S. Thygesen¹ and Karsten W. Jacobsen¹

¹Center for Atomic-scale Materials Design, Department of Physics, Technical University of Denmark, Kongens Lyngby, DK-2800, Denmark.

ABSTRACT

Computational screening is becoming increasingly useful in the search for new materials. We are interested in the design of new semiconductors to be used for light harvesting in a photoelectrochemical cell. In the present paper, we study the double perovskite structures obtained by combining 46 stable cubic perovskites which was found to have a finite bandgap in a previous screening-study.¹ The four-metal double perovskite space is too large to be investigated completely. For this reason we propose a method for combining different metals to obtain a desired bandgap. We derive some bandgap design rules on how to combine two cubic perovskites to generate a new combination with a larger or smaller bandgap compared with the constituent structures. Those rules are based on the type of orbitals involved in the conduction bands and on the size of the two cubic bandgaps. We also see that a change in the volume has an effect on the size of the bandgap. In addition, we suggest some new candidate materials that can be used as photocatalysts in one- and two-photon water splitting devices.

INTRODUCTION

Density Functional Theory (DFT) is a powerful method to investigate structural and electronic properties of materials. The enormous increase of computational power in combination with theory developments, like the implementation of new, more reliable exchange-correlation functionals, have made it possible to search for new materials using *ab-initio* quantum mechanical calculations involving several thousands of simulations. Many efforts we have been recently made to design new materials using computational tools, for example screening for organic photovoltaics,²⁻³ inorganic scintillators⁴ and bandgap engineering.^{1,5-7} In previous works,^{1,6} we addressed one of the most pressing problems of our time, i.e. the development of sustainable energy technology, focusing on the photoelectrochemical conversion of water into hydrogen and oxygen using visible solar light considering both the one- and two-photon water splitting processes. Out of 19000 materials in the cubic perovskite structure, obtained by combining 52 interesting metals with oxygen, nitrogen, sulfur and fluorine, we suggested 20 combinations for one-photon water splitting and 12 additional ones for the two-photon process.

In this work, we consider the double perovskite structure for finding new rules to combine metals to obtain the desired bandgap size and to predict new candidates for water splitting. In the previous study we identified 46 stable ABO_3 perovskites with a non-vanishing bandgap and here we look at combinations of those in the so-called double perovskite structure shown in Figure 1A. The chemical formula is $A_1A_2B_1B_2O_6$; A_1 and A_2 have an oxygen coordination of 12 and are in general of larger radius than the B_1 and B_2 ions where the coordination is only 6. The unit cell is composed of 20 atoms. Double perovskites have been first synthesized in 1998⁸ and they have been investigated theoretically because of their various properties, like ferroelectricity and high magnetic Curie temperature⁹ or small bandgap.¹⁰

THEORY

A material should at least fulfill three main requirements to be a good photocatalyst for water splitting: (i) structural and chemical stability against oxidation, (ii) optimal bandgap to absorb the visible part of the solar spectrum, and (iii) well positioned band edges with respect to the oxygen and hydrogen evolution potentials. In addition, the electrons and the holes should show a good mobility to reach the surface before recombining, and to be an eco-friendly material, the combination should not contain expensive or toxic chemical elements. We screen only for (i), (ii), and (iii), i.e. we search for a stable semiconductor with well positioned band edges with respect to the water redox potential. The screening is performed using the DFT-code GPAW.¹¹⁻¹² All the structures under investigation are fully relaxed using a standard DFT-GGA exchange-correlation functional (RPBE-approximation¹³) and the formation energies are calculated with respect to a pool of reference systems in which the material can be decomposed using a linear programming method. The pool contains the single- and bi-metal oxides as well as single metal bulks in their most stable structure as present in the experimental ICSD and in the Materials Project databases.¹⁴⁻¹⁵ The chemical potential for oxygen is taken relative to water because the material will be working in an aqueous environment. The bandgaps are obtained using the GLLB-SC exchange-correlation potential,¹⁶ that includes the calculation of the derivative discontinuity and gives reliable results compared to experiments.¹ The evaluation of the positions of the band edges in principle requires the construction of a surface and a reliable modeling of the water layer on it. We do not use this approach because it is computationally expensive. More recently, Wu *et al.*¹⁷ have proposed a method for evaluating the positions of the band edges in three steps that involve two bulk calculations (the material and water) and an interfacial slab. This method has also been used to propose new oxynitrides to be used as photocatalyst in a water splitting device.⁷ Instead, here we use an empirical equation that gives the position of the center of the bandgap as the geometrical average of the electronegativities in the Mulliken's scale of the chemical constituents. The position of the edges is thus obtained adding and subtracting half of the bandgap.¹⁸ This approach has been validated and extensively used in our previous papers.^{1,6}

RESULTS

Using the method described above, we calculate the heats of formation and the bandgaps for the double perovskites under investigation. Almost all the double perovskites are stable (within a threshold we use of 0.2 eV per atom) when compared to the existing structures into which the material can be split apart. The double perovskite maintains the structural characteristic of the two ABO_3 perovskites and the major improvement in the stability is given by a possible octahedral tilting of the oxygen atoms that cannot appear in the small 5 atoms unit cell used for the cubic perovskite.

Figure 1B reports the bandgaps for all the combinations investigated. The bandgaps are seen to span over a region from 0 to more than 7 eV. The cubic perovskites along the two axes of the plot are sorted using a cluster analysis, which brings two compounds close to each other if they behave similarly with respect to bandgap formation.¹⁹ Most of the combinations investigated are seen to be insulators with a bandgap larger than 4 eV and rather few have bandgaps in the visible range.

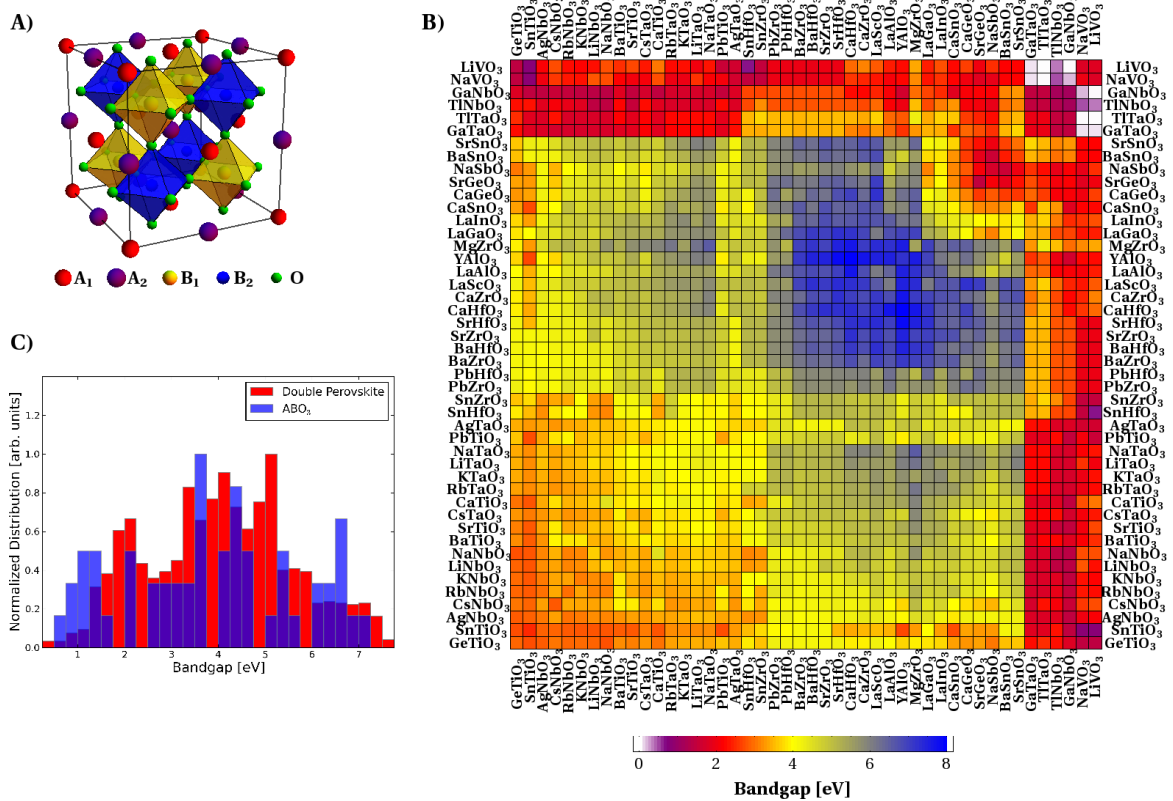


Figure 1: A) Double perovskite crystal structure. B) Calculated bandgaps for all the possible combinations. The ideal bandgap for one-photon water splitting is the red region. C) Normalized distribution of the calculated bandgaps for the ABO₃ (in blue) and double perovskite (in red) structures.

The normalized distributions of the bandgaps for the cubic and double perovskites are shown in Figure 1C. The distribution of the double perovskite bandgaps is less fluctuating than the one for the cubic perovskites simply because of the larger space under investigation. In fact, we are considering around 1100 double perovskite and only 46 cubic ones. In general, there is not much difference between the two distributions: both structures have a high tendency for forming large bandgap insulators and do not exhibit many compounds with a bandgap in the visible range. In the region between 0.5 eV and 1.5 eV there seems to be relatively few double perovskite while there seems to be a bit more in the region between 1.5 eV and 2.5 eV. This might be caused by the octahedral distortion that leads by itself to an increase of the bandgap. The 5 atoms unit cell used to model the cubic perovskite does not allow the system to show the octahedral tilting.

In Figure 2A we show the calculated difference between the bandgaps obtained for the double perovskites and the average of the two bandgaps of the constituents ABO₃ (calculated for the 20 atoms unit cell). Most of the double perovskites have a bandgap close to the average gap of the constituent structures (in white). ABO₃ materials with small bandgaps (below 1.5 eV) show a general reduction of the bandgap (in blue). However, there are also combinations for which there is a significant increase of the bandgap (up to 3 eV, in red). This happens when we

combine a d-metal with a p-metal in the two B-ion positions. In contrast with this, the elements in the A-ion positions do not affect the size of the resulting bandgap very much.

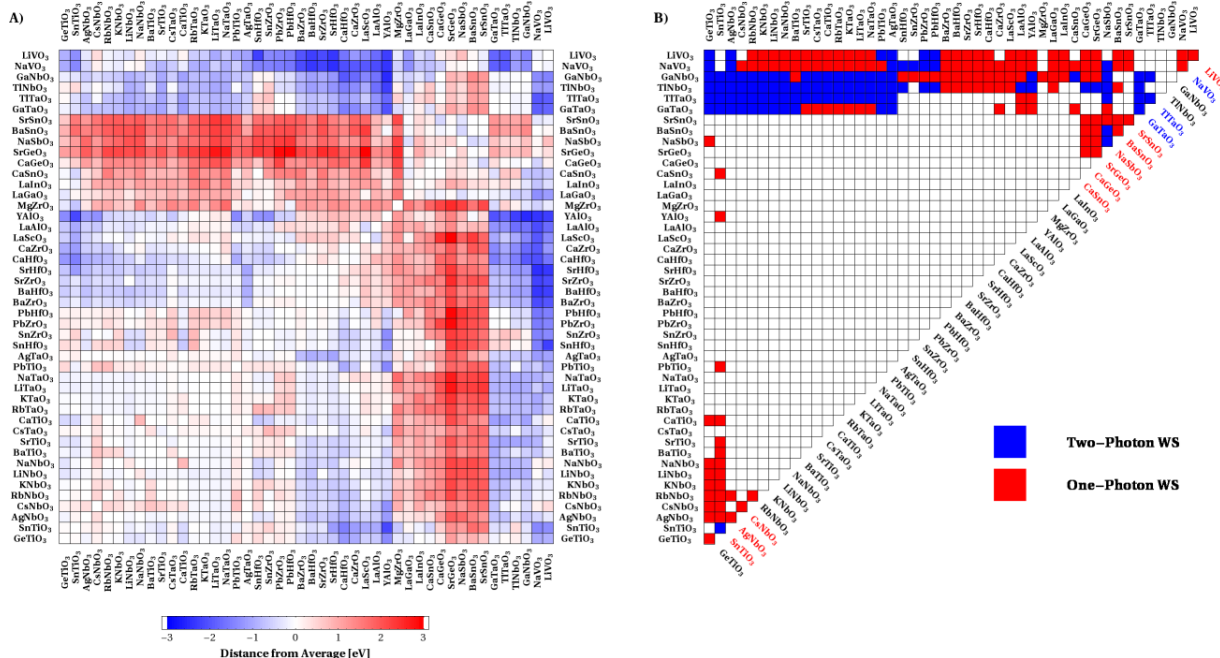


Figure 2: A) Difference between the double perovskite bandgap and the average gaps of the constituent perovskites. B) Candidates for one- and two-photon water splitting. The colored font for the name of the structure indicates that that cubic perovskite was already found as a candidate for one- or two-photon water splitting.

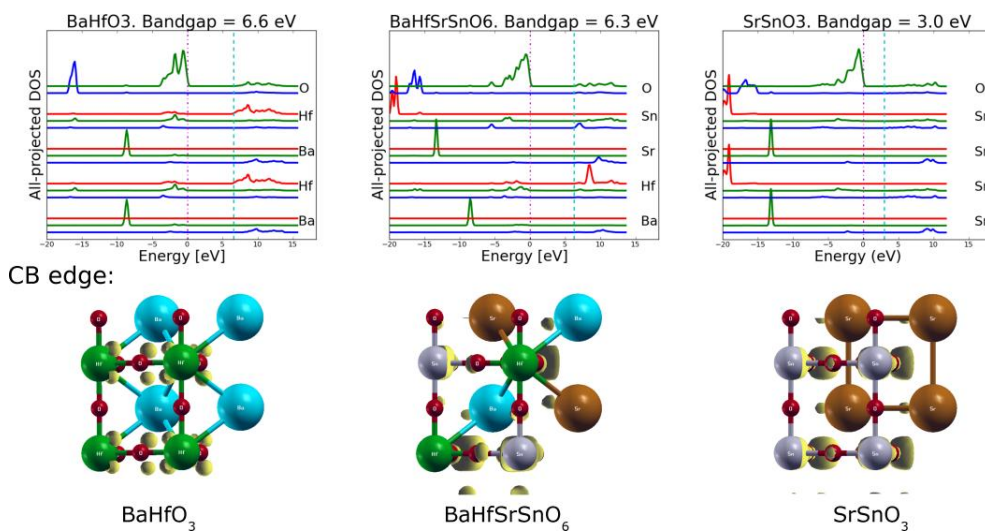


Figure 3: Projected density of states for BaHfO_3 , BaHfSrSnO_6 , and SrSnO_3 . The s, p, and d orbitals are drawn in blue, green, and red, respectively. The size of the bandgap, the conduction band edges (HOMO, in magenta) and the valence band edges (LUMO, in cyan) are also indicated. The zero energy is set to correspond to the HOMO level. The increase in the bandgap for the combined perovskite is due to a strong hybridization between the p- and d-metals in the B-ion positions. The wavefunctions of the conduction band (CB) edge states of the three combinations are also plotted.

The reason for the opening of the bandgap compared to the average value is a strong hybridization between the p- and d-metals in the B-ion positions as shown in Figure 3 where we plot the projected density of states (DOS) for three systems: BaHfO₃, SrSnO₃, and their combination BaHfSrSnO₆. The projected DOS for the Hf-d and Sn-s/p orbitals change when considering the two separated structures compared to the double perovskite and they show peaks, in particular Hf and Sn, in the double perovskite that are not present in the cubic ones. The conduction band wavefunctions for the systems follow the densities: the d-like wavefunction present around Hf in the BaHfO₃ disappears in favor of a more intense s-like wavefunction around Sn in the BaHfSrSnO₆. The highest occupied molecular orbital (HOMO) is in general formed by oxygen 2p states and the lowest unoccupied molecular orbital (LUMO) by states of the B-ions. These features are typical of the perovskite oxides.

Candidates for One- and Two-photon Water Splitting

On top of analyzing the bandgap formation, we screen for two applications: one- and two-photon water splitting. In the one-photon water splitting, a photon is absorbed by a single semiconductor and creates an electron-hole pair. The electron and hole reach two different points of the surface and evolve hydrogen and oxygen, respectively. In the two-photon water splitting, two materials and two photons are needed for the evolution of H₂ and O₂. Even if two photons are required, the efficiency of a tandem device can be higher than the one obtained for the one-photon device because of different bandgap windows under consideration. In fact, to run the one-photon reaction a bandgap between 1.5 and 3 eV is required, while for the two-photon water splitting, the optimal bandgap combination is 1.1 and 1.7 eV. In our screening, we consider silicon as the 1.1 eV bandgap semiconductor for the evolution of hydrogen, in combination with a material with a bandgap in the range 1.3 - 3 eV responsible for the oxygen evolution. In the one-photon water splitting the band edges should straddle the redox potentials of water. For the two-photon device, the valence band of the cathode should be above the conduction band of the anode to let the electron move from the semiconductor to silicon and combine with the hole in order to keep the charge neutrality. More detailed explanations can be found in Ref. 7.

The outcome of the screening is shown in Figure 2B. We find around 150 and 100 combinations for one- (in red) and two-photon (in blue) water splitting, respectively. 6 cubic perovskites are particularly good to generate candidates independently of the other structure. As described before, the unit cell is composed of 20 atoms. The resulting candidates for the screening of the cubic perovskite oxides are shown with colored fonts in the diagonal of Figure 2B. Comparing the results obtained for the 5 and the 20 atoms unit cell, some combinations now fall in or out of the interesting window for the one- or two-photon water splitting because of distortions of the structure. This is the case, for example, of CaGeO₃ or CaSnO₃, for which the most common structure is the orthorhombic perovskite with a significant octahedral tilting followed by an increase of the bandgap that is now outside the visible range window, i.e. larger than 3 eV. For some combinations the bandgap changes compared with the one calculated with the 5 atoms unit cell because of a different lattice parameters. In general, the size of the bandgap can be tuned applying a strain to the cell. This happens for GeTiO₃ and RbNbO₃, for example, where the bandgaps narrow and lie in the visible range so that they might be used as light harvesting materials.

CONCLUSIONS

In this work, we have applied a screening approach to investigate the electronic properties of semiconductors in the double perovskite structure. We have focused on the problem of light harvesting and of solar light conversion into hydrogen and oxygen. We have found a general rule for combining elements to obtain a desired bandgap: two combinations with only p- or d-metals in the B-ion positions show bandgaps close to the average gaps of the constituents, while the combination of a p- and a d-metal results in an increase of the double perovskite bandgap. The hybridization of the orbitals of the two A-ions is very small, so it has only little influence on the change of the bandgap. A change in the volume is also influencing the size of the bandgap. We have also proposed some combinations that potentially can be used as light harvesting materials and that requires for a more thorough theoretical and experimental investigation.

ACKNOWLEDGMENTS

The authors acknowledge support from the Danish Center for Scientific Computing through grant HDW-1103-06, from the Catalysis for Sustainable Energy (CASE) initiative funded by the Danish Ministry of Science, Technology and Innovation, and from the Center on Nanostructuring for the Efficient Energy Conversion (CNEEC) at Stanford University.

REFERENCES

1. I.E. Castelli, T. Olsen, S. Datta, D.D. Landis, S. Dahl, K.S. Thygesen and K.W. Jacobsen, *Energy Environ. Sci.*, 2012, 5, 5814.
2. R. Olivares-Amaya, C. Amador-Bedolla, J. Hachmann, S. Atahan-Evrenk, R.S. Sanchez-Carrera, L. Vogt and A. Aspuru-Guzik, *Energy Environ. Sci.*, 2011, 4, 4849.
3. N.M. O'Boyle, C.M. Campbell and G.R. Hutchison, *J. Phys. Chem. C*, 2011, 115, 16200.
4. R. Armiento, B. Kozinsky, M. Fornari and G. Ceder, *Phys. Rev. B*, 2011, 84, 14103.
5. M. d'Avezac, J.-W. Luo, T. Chanier and A. Zunger, *Phys. Rev. Lett.*, 2012, 108, 027401.
6. I.E. Castelli, D.D. Landis, K.S. Thygesen, S. Dahl, I. Chorkendorff, T.F. Jaramillo, and K.W. Jacobsen, *Energy Environ. Sci.*, 2012, 5, 9034.
7. Y. Wu, P. Lazic, G. Hautier, K. Persson and G. Ceder, DOI: 10.1039/C2EE23482C.
8. K.-I. Kobayashi, T. Kimura, H. Sawada, K. Terakura and Y. Tokura, *Nature*, 1998, 395, 677.
9. Z.W. Song, and B.G. Liu, arXiv:1210.5981
10. R.F. Berger and J.B. Neaton, arXiv:1209.2187
11. J.J. Mortensen, L.B. Hansen and K.W. Jacobsen, *Phys. Rev. B*, 2005, 71, 35109.
12. J. Enkovaara, *et al.*, *J. Phys.: Condens. Matter*, 2010, 22, 253202.
13. B. Hammer, L.B. Hansen and J.K. Nørskov, *Phys. Rev. B*, 1999, 59, 7413.
14. ICSD database, http://www.fiz-karlsruhe.de/icsd_web.htm
15. Materials Project - A Materials Genome Approach, <http://materialsproject.org/>
16. O. Gritsenko, R. van Leeuwen, E. van Lenthe and E.J. Baerends, *Phys. Rev. A*, 1995, 51, 1944.
17. Y. Wu, M.K.Y. Chan, and G. Ceder, *Phys. Rev. B*, 2011, 83, 235301 .
18. M.A. Butler and D.S. Ginley, *Journal of The Electrochemical Society*, 1978, 125, 228.
19. I.E. Castelli, K.S. Thygesen and K.W. Jacobsen, in preparation.

Paper IV

Performance of Genetic Algorithms in Search for Water Splitting Perovskites

Anubhav Jain, [Ivano E. Castelli](#), Geoffroy Hautier, David H. Bailey, and Karsten W. Jacobsen.

J. Mat. Science **Published Online**, DOI: 10.1007/s10853-013-7448-9, 2013.

Performance of genetic algorithms in search for water splitting perovskites

Anubhav Jain · Ivano E. Castelli · Geoffroy Hautier ·
David H. Bailey · Karsten W. Jacobsen

Received: 13 March 2013 / Accepted: 14 May 2013
© Springer Science+Business Media New York 2013

Abstract We examine the performance of genetic algorithms (GAs) in uncovering solar water light splitters over a space of almost 19,000 perovskite materials. The entire search space was previously calculated using density functional theory to determine solutions that fulfill constraints on stability, band gap, and band edge position. Here, we test over 2500 unique GA implementations in finding these solutions to determine whether GA can avoid the need for brute force search, and thereby enable larger chemical spaces to be screened within a given computational budget. We find that the best GAs tested offer almost a 6 times efficiency gain over random search, and are comparable to the performance of a search based on informed chemical rules. In addition, the GA is almost 10 times as efficient as random search in finding half the solutions within the search space. By employing chemical rules, the performance of the GA can be further improved to approximately 12–17 better than random search. We discuss the effect of population size, selection function, crossover function, mutation rate, fitness function, and

elitism on the final result, finding that selection function and elitism are especially important to GA performance. In addition, we determine that parameters that perform well in finding solar water splitters can also be applied to discovering transparent photocorrosion shields. Our results indicate that coupling GAs to high-throughput density functional calculations presents a promising method to rapidly search large chemical spaces for technological materials.

Introduction

The discovery of improved materials benefits science, technology, and society. While there exist many methods to uncover new materials, one promising and fairly recent approach to materials discovery uses density functional theory (DFT) calculations [1, 2] to predict properties of known and hypothetical materials across a large chemical space. This approach can be quicker and cheaper than direct experimental study, and has led to new experimental findings in fields as disparate as Li ion batteries, hydrogen storage, magnetic materials, multiferroics, and catalysts [3, 4].

One pressing societal problem is meeting world energy demand in an environmentally responsible manner. A possible contribution is to convert solar energy into hydrogen and oxygen by means of a photoelectrocatalytic solar cell. In this device, one or more photons split water into H₂ and O₂ gases. These gases are stored and later recombined to produce energy. An interesting class of materials for solar water splitters is the perovskite family, which consists of materials with general formula ABX₃.

Recently, Castelli et al. [5, 6] used DFT to screen approximately 19,000 perovskite materials as potential

A. Jain (✉) · D. H. Bailey
Computational Research Division, Lawrence Berkeley National
Laboratory, 1 Cyclotron Rd, Berkeley, CA 94720, USA
e-mail: ajain@lbl.gov

I. E. Castelli · K. W. Jacobsen
Center for Atomic-scale Materials Design,
Department of Physics, Technical University of Denmark,
2800 Kongens Lyngby, Denmark

G. Hautier
ETSF, Institute of Condensed Matter and Nanosciences,
Université Catholique de Louvain, 1348 Louvain-la-Neuve,
Belgium

solar water splitters, and 20 interesting compounds were identified for experimental followup. However, the result highlights a fundamental challenge in materials discovery: the number of *interesting* compounds comprises a small fraction of the total number of *possible* compounds. Therefore, a large number of calculations are needed to find a relatively small number of interesting materials.

While exhaustive search is sometimes achievable, search spaces for new materials might encompass on the order of millions or tens of millions of hypothetical compounds. For example, the 5-atom perovskites screened by Castelli et al. make up only a small portion of potentially promising materials for this application. Unfortunately, the number of DFT calculations that can reasonably be performed on today's computers is limited to the order of tens of thousands. For example, the Materials Project required over 10 million CPU hours to generate structural and energetic data for about 30,000 materials [7, 8]. It is therefore essential to improve the efficiency of computational search, so that enumeration of all members of a search space is not needed to confidently uncover all good candidates.

In this study, we investigate the use of evolutionary algorithms [9] (which we subsequently refer to as “genetic algorithms”) as an optimization model to reduce the number of DFT computations needed to discover new materials. We re-examine the dataset produced by Castelli et al. [5, 6] to determine whether the same promising candidates could be discovered with fewer computations by employing a genetic algorithm (GA). Our goal is to demonstrate that optimization algorithms coupled to DFT calculations present a path forward to searching very large chemical spaces for interesting technological materials.

Several other researchers have investigated tiered or algorithmic screening processes coupled to calculation [10–13], and sometimes by employing GAs [14–20]. The goal of this study is not to find new materials, but rather to assess the robustness of the GA as an inverse solver for the perovskite photocatalysis problem. We compare the efficiency of GA search to competing methods of screening materials, such as random search and a chemical rule-based search. In addition, we distinguish between different forms of GA by testing the performance of over 2592 parameter sets in over 50,000 GA trials. We report the most crucial parameters for achieving efficient GAs within the perovskite photocatalysis problem. Finally, we investigate transferability of optimized GA parameters by applying them to a second problem of searching for transparent photocorrosion shields.

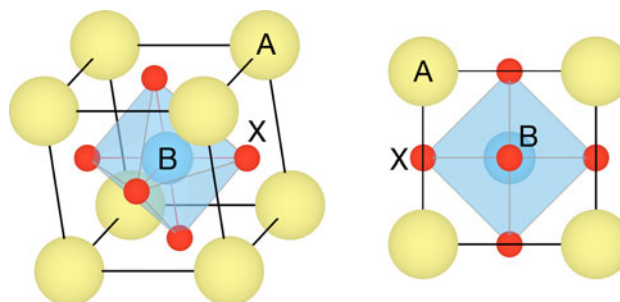


Fig. 1 Two views of the cubic perovskite crystal structure for ABX_3 compounds. Atoms of type A (in yellow) are positioned at the cube corners, B atoms (in blue) at the cube center, and X atoms (in red) at cube faces. The B atoms are octahedrally coordinated by X, whereas the A atoms are 12-fold coordinated by X (Color figure online)

Calculation methods

Search space and criteria for solar water splitting

Our search space consists of ABX_3 cubic perovskites with 5-atom unit cells. Perovskites are an interesting search space because they display a diverse set of properties, and many are technologically useful [21, 22]. The cubic perovskite crystal structure is illustrated in Fig. 1. For the cations A and B, a set of 52 potential elements were selected as described by Castelli et al. [5, 6]. For the anion group X_3 , the search included seven mixtures of oxygen, nitrogen, sulfur, and fluorine: O_3 , O_2N , ON_2 , N_3 , O_2F , O_2S , and OFN . In total, the search space consists of 18,928 compounds. The complete data set has been reported previously [5, 6] and is freely available at the Computational Materials Repository (CMR) web site [5, 23, 24].

Potential water splitting materials were identified based on band gap, enthalpy of formation, and band edge positions [5, 6]. A material is considered a *solution* if:

- The band gap (either direct or indirect) falls in the range 1.5–3 eV.
- The heat of formation is less than 0.2 eV/atom. The heat of formation is calculated using a linear programming approach that considers a reference set of approximately 400 elements, bulk single, and bi-metal oxides, fluorides, sulfides, nitrides, oxyfluorides, oxy-sulfides, and oxynitrides.
- The band edges (either direct or indirect) straddle the H^+/H_2 and O_2/H_2O band level positions.

The total number of solutions within the search space, including both known and yet examined compounds, is 20 [5, 6]. These compounds are listed in Table 1.

Table 1 Solutions to the solar water splitting problem, and their calculated properties

Formula	ΔH_f	$E_{\text{gap}}^{\text{dir}}$	$E_{\text{cb}}^{\text{dir}}$	$E_{\text{vb}}^{\text{dir}}$	$E_{\text{gap}}^{\text{ind}}$	$E_{\text{cb}}^{\text{ind}}$	$E_{\text{vb}}^{\text{ind}}$
LiVO ₃	0.18	2.05	-0.12	1.93	1.34	0.24	1.58
NaSbO ₃	0.20	2.55	-0.10	2.45	1.54	0.41	1.95
MgTaO ₂ N	0.18	2.73	-0.11	2.62	2.08	0.22	2.30
CaGeO ₃	0.16	2.74	-0.54	2.20	2.06	-0.20	1.86
CaSnO ₃	0.16	3.57	-1.02	2.55	3.04	-0.76	2.28
CaTaO ₂ N	0.08	2.22	-0.43	1.79	2.22	-0.43	1.79
SrGeO ₃	0.16	1.70	-0.12	1.58	1.24	0.11	1.35
SrSnO ₃	0.00	3.39	-1.03	2.36	2.89	-0.78	2.11
SrTaO ₂ N	0.00	2.15	-0.50	1.65	2.15	-0.50	1.65
YTaN ₂	0.14	2.50	-0.21	2.29	2.30	-0.11	2.19
AgNbO ₃	0.20	3.47	-0.27	3.20	2.95	-0.01	2.94
SnTiO ₃	0.10	2.71	-0.10	2.61	2.48	0.02	2.50
CsNbO ₃	0.18	2.87	-0.75	2.12	2.85	-0.74	2.11
BaGaO ₂ F	0.10	2.50	-0.24	2.26	2.10	-0.04	2.06
BaInO ₂ F	0.10	3.20	-0.63	2.57	2.60	-0.33	2.27
BaSnO ₃	-0.08	2.54	-0.29	2.25	2.54	-0.29	2.25
BaTaO ₂ N	-0.02	2.05	-0.14	1.91	2.05	-0.14	1.91
LaTiO ₂ N	0.06	2.49	-0.42	2.07	2.49	-0.42	2.07
LaTaON ₂	-0.02	2.10	-0.07	2.03	1.80	0.08	1.88
PbGaO ₂ F	0.18	3.80	-0.47	3.33	2.90	-0.02	2.88

These materials were originally reported by Castelli et al. [5], and the full data set can be downloaded at the Computational Materials Repository [5, 23, 24]. All units are in eV; the designations “dir” and “ind” correspond to direct and indirect, respectively. The zero reference for band levels corresponds to the H₂/H⁺ energy

Calculation details

The DFT calculations were performed using the GPAW code [25, 26]. Total energies and structural relaxations were calculated under the RPBE approximation [27]; band gaps were calculated using the GLLB-SC semilocal functional [28, 29] that was previously demonstrated to improve the reliability of predicted gaps [6]. The band edge positions were determined by an empirical method [30, 31] that positions the center of the gap (E_F) at:

$$E_F = E_0 + (\chi_A \chi_B \chi_X^3)^{1/5}$$

where E_0 is the difference between the hydrogen electrode level and vacuum ($E_0 = -4.5$ eV) and χ_i denotes the Mulliken electronegativity of the element on site i . For multiple elements composing the anion X₃, the geometric mean of electronegativities was used. The band edge positions were obtained by adding and subtracting half the calculated band gap from E_F .

All magnetic ions were initialized ferromagnetically. To break cubic symmetry, atomic positions were displaced by 0.01 Å prior to structural relaxation. However, we note that several perovskite chemistries possess large driving forces for more complex distortions [32], and any effect of these

distortions on the band structure were not modeled in the data.

Genetic algorithm method

For a general introduction to GAs, we refer to several previous works [20, 33–35]. We performed the GA in Python using the open-source code Pyevolve, version 0.6rc1 [36, 37]. We modified some of the Pyevolve code such that the GA engine operates as described in the following sections. Because the entire search space has been precomputed with DFT, we fetch the result of all fitness evaluations from an internal database rather than performing a DFT calculation on-demand within the GA framework. The same material might appear in multiple generations of the GA; we only count unique materials when reporting performance.

To account for variability in GA results, we repeat the GA optimization routine 20 times (using different initializations) and report the average and standard deviation of the trials for each parameter set. In total, 2592 unique parameter set combinations were attempted, leading to $2592 \times 20 = 51,840$ independent GA runs. The same

procedure was repeated for optimizing transparent photo-corrosion shields (51,840 additional GA runs). The parameters we tested are described in more detail in the following subsections.

Candidate encoding

Each potential materials candidate in the ABX_3 chemical space was encoded as a three-element composition vector $C = [A, X_3, B]$. The first and third positions represent the A and B cations in the ABX_3 composition, and contain one of 52 values, each of which corresponds to an element. The middle position for X_3 has one of seven values, each representing a potential anion group. As an example, the vector [3, 1, 4] corresponds to the perovskite candidate “LiBeO₃” (the Z values of Li and Be are 3 and 4, respectively, and $X_3 = 1$ represents O₃ in our convention). We structured the candidate vector in the order [A, X_3 , B].

We note that our choice of encoding means that our technique is more appropriately described as an evolutionary algorithm rather than a GA (in the latter, binary strings are used for encodings). We examine this choice in greater detail in the “Discussion”.

Population size and initialization

We tested three population sizes: 100, 500, and 1000. The lower range of this set corresponds to approximately 0.5 % of the total search space, whereas the upper range corresponds to over 5 % of the search space. We found that reducing the population size significantly below 100 led to stagnation from insufficient diversity within the population, making it difficult to obtain converged results.

The initial population was generated using random values for each component of the composition vector. For each GA input parameter set, the same set of 20 random initial populations was repeated.

Fitness function

We note that when optimizing multiple, independent objectives (e.g., stability, gap, and band edge position), there is no “correct” way to rank materials. We tested three different strategies for assigning a numerical fitness function to individuals in the multivariate case, although other strategies such as the Pareto optimality ranking [35, 38] also exist.

The first fitness function, which we call “Discontinuous”, sums the values of a stability score, a band gap score, and two band edge position scores. These component scores are plotted in Fig. 2. The principle of the “Discontinuous” fitness function is to withhold awarding any points unless a target property is fully met.

We label the second fitness function tested as “Smooth”. This function also sums a stability score, a band gap score, and two band edge position scores. However, in contrast to the “Discontinuous” function, the “Smooth” function continuously increases the fitness score as an individual becomes closer to meeting a target property. The component scores for the “Smooth” fitness function are also plotted in Fig. 2.

The third fitness function, which we denote as “Smooth Product”, employs the same component fitness functions as the “Smooth” fitness function (Fig. 2). However, rather than summing the component fitnesses, we take a product of the stability fitness with the sum of the band gap and band edge position fitness. The principle of the “Smooth Product” function is to assign higher fitness to compounds that balance stability and desired electronic structure.

In each case, we normalize the maximum score to 30 potential points. For the band gap and band edges, we use the higher score based on independent assessments of the direct gap and indirect gap data.

Selection function and scaling factor

We tested three algorithms for selecting individuals as parents for mating:

- Uniform selection—random individuals in the population are selected to be parents without regard to fitness score
- Roulette Wheel selection—the probability of an individual to be selected as a parent is proportional to its fitness function
- Tournament Wheel selection—a set of *tournaments* are performed. In each tournament, a sample of the population is randomly selected. The selected individual is the one with the highest fitness within the tournament sample.

Whereas uniform selection involves no additional parameters, both roulette wheel and tournament selection are tunable through parameters that affect *selection pressure*. A high selection pressure biases selection towards the stronger individuals at the expense of population diversity.

For roulette wheel selection, we tune the selection pressure through a linear scaling of the raw fitness scores. The linear scaling approach prevents early dominance of a single individual and helps distinguish individuals in later generations (when raw fitness values might all be close to optimal). Linear scaling modifies the raw fitness values in each generation such that:

$$f' = af + b$$

where f' is the scaled fitness, f is the raw fitness and a and b are constants that change upon each generation. The

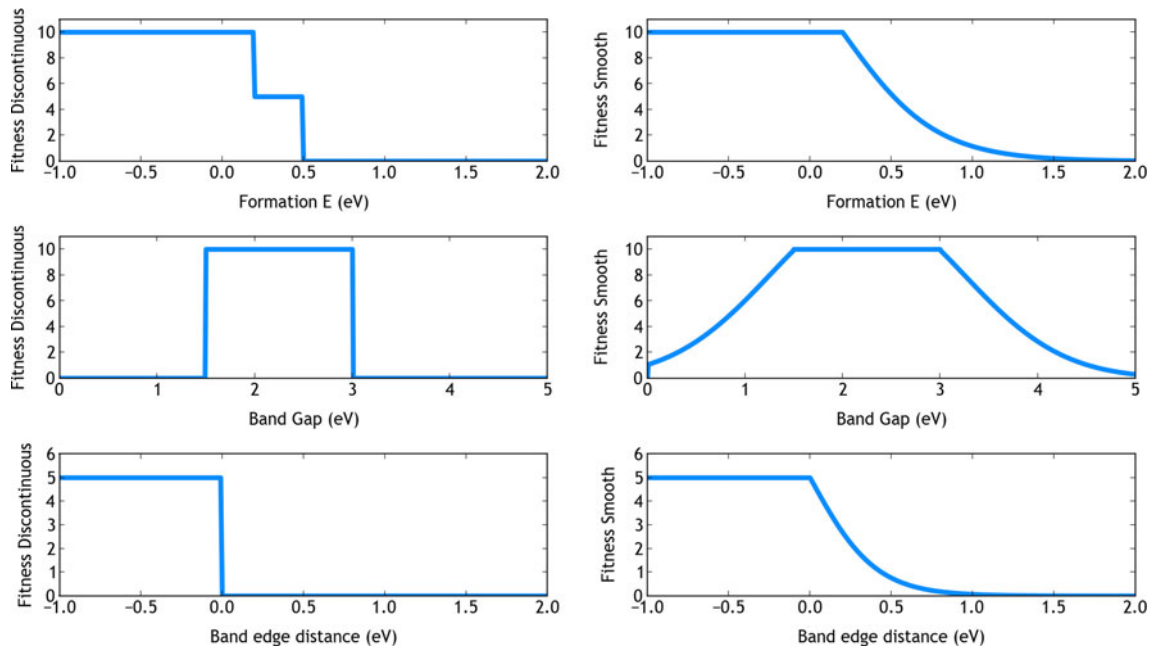


Fig. 2 The component fitness functions for solar water splitting. The functions corresponding to the “Discontinuous” strategy are depicted in the *left column*, whereas the component functions for the “Smooth” strategy are plotted on the *right side*. We note that for

the “Smooth” band gap function, we added a discontinuity for metals (gap of zero), awarding such compounds zero points. The overall fitness function involves either sums or products of the component fitness functions, as described in the text

constants are selected such that (i) the average fitness within the generation is maintained ($f_{avg} = f'_{avg}$) and (ii) the maximum fitness is equal to a constant C multiplied by the average fitness ($f'_{max} = Cf'_{avg}$). The constant C is a free parameter that represents the desired selection pressure. We tested several values of C ranging from 1.25 to 10 in our study, but automatically adjust it when necessary to prevent negative scaled fitness scores.

In tournament selection, the scaling parameter does not affect the results because the selected member depends only on the fitness rank rather than its absolute value. We instead tune the selection pressure through the tournament size, with larger tournaments creating greater selection pressure. We test a commonly used tournament size of two individuals, as well as tournament sizes that are 5 and 10 % of the overall population size.

Crossover function and rate

The crossover function determines how children are generated given two parents. We tested three crossover functions:

- Single-point crossover—The parents swap either the A or B cation (but not both) to produce two children.
- Two-point crossover—The parents swap the anion X_3 to produce two children.
- Uniform crossover—A, B, and X_3 are randomly swapped between two parents. We explicitly prevent

the children from being identical to the parents unless parents are identical.

A pictorial representation of the crossover operations is presented in Fig. 3.

The *crossover rate* determines what percent of the parents mate to produce children; this parameter was set to 90 %, such that most parents selected for mating produce children. The remaining 10 % are passed to the next generation without modification. This choice of crossover rate is consistent with suggestions from previous studies [39, 40].

Elitism

In many optimization problems, the performance of the GA can be improved by intentionally carrying over some of the fittest individuals of the current generation to the next generation. In our implementation, such “elite” individuals replace the least fit individuals of the new population. We tested our GA with elitism turned off, and with 10, 50, and 75 % of the fittest individuals carried over to the next generation.

Mutation function and rate

Our mutation function modifies an element of the composition vector to a random value. We tested mutation rates of 1, 5, and 10 %. We note that other potential mutation

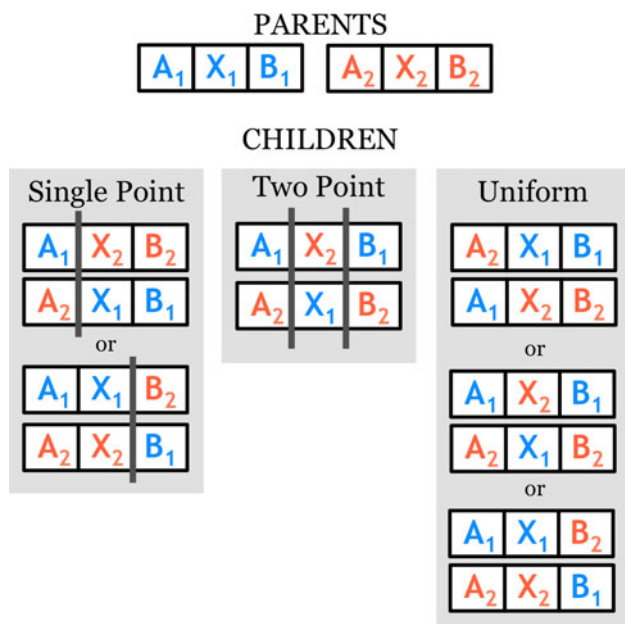


Fig. 3 Representation of crossover operations. A pair of parents produces a set of two children. For single-point and uniform crossover, multiple sets of children are possible and one is selected at random

operators are also possible, such as switching the identities of the A and B cation.

Convergence and additional mutation operators

When a single solution is targeted, typical convergence criteria for GA are stagnation of population diversity or failure of the fittest individual to improve with generation number. However, our GA problem is *multimodal*, i.e., there exist several individuals that maximize our fitness function. Our goal is to find all possible materials that meet our design criteria, and we aim to prevent population convergence to a single optimum rather than promote it.

To encourage multimodal optimization, we introduce two additional mutation operators. The first, which we call *local mutation*, mutates a single gene of any duplicated individuals within a generation. This operator can be thought of as performing a local search around a duplicated solution. In addition to local mutation, we detect when all members of the population were previously explored in a previous generation. In these instances, we introduce a *global mutation* that mutates a single gene of the entire population and increases the crossover rate to 100 % for a single generation. This “resets” the search space when the GA becomes stuck on solutions already explored in the past. We found that absent these operators, our GA could stagnate for several thousand generations, recycling the same individuals without producing new solutions.

Other methods to tackle multimodal problems have been developed; for example, a well-studied class of techniques to handle multimodal problems, termed *niching*, attempts to find specialized solutions within several regions of a problem space. However, there exist many methods of implementing niching, and additional parameters must be optimized within each niching implementation [20, 35, 38, 41–44]. Therefore, we leave a comprehensive exploration of niching to a future study.

Evaluating performance

To evaluate the performance of the GA, we tested it against other methods and also on a different (but related) application of transparent photocorrosion shields.

Chemical rule-based search method

In addition to the GA, we independently tested a rule-based method of selecting compounds. This “chemical rule-based search” provides a sense of how to prioritize a search space using empirical knowledge and scientific principles. In particular, we apply the following rules:

1. “Valence balance rule”—the formal oxidation states of all the elements in a realistic ionic material must sum to zero, such that the overall material is valence-neutral. In situations where elements are known to display multiple oxidation states (for example, the transition metals), the condition must be met for at least one of the oxidation state combinations. Materials that cannot be valence-balanced, such as LiCaO_3 , are completely excluded from the search.
2. “Even–odd electrons rule”—materials containing an odd number of electrons are excluded because they will contain a partially occupied eigenstate at the Fermi level. These materials will necessarily be metallic with zero band gap and therefore unsuitable for solar water splitting.
3. “Goldschmidt tolerance factor ranking”—materials fulfilling the first two rules are ranked using their Goldschmidt tolerance factor [45]. The Goldschmidt tolerance factor t is based on the geometry of the perovskite cell and assesses the likelihood of a material to form the perovskite crystal structure. It is defined as:

$$t = \frac{(r_A + r_X)}{\sqrt{2}(r_B + r_X)}$$

where r_i corresponds to ionic radii of the $i = A, B,$ and X_3 sites. In an ideal perovskite, t is equal to unity ($t_{\text{ideal}} = 1$). We ranked perovskites by the absolute deviation from this ideal value, that is by $|t - t_{\text{ideal}}|$, such that compositions

that more closely meet the ideal perovskite structure are tested first. For metals with multiple known ionic radii, we used an unweighted average of known radii as the radius. When the anion site X_3 contains multiple elements, we used a weighted average of the individual ionic radii.

These rules might approximate the intuition of a researcher in prioritizing perovskite compounds for computation.

Transparent photocorrosion shield screening

In addition to solar water splitters, the perovskite dataset can also be used to screen potential transparent shields to protect against photocorrosion, as recently reported by Castelli et al. [5]. The need for a transparent protecting shield lies in the difficulty of finding stable, medium-gap perovskites needed for water splitting; usually, stable perovskites tend to also have wide gaps [5, 6]. A wide-gap shield might therefore be placed in front of a medium-gap photo-absorber to enhance protection against (photo)corrosion without affecting light capture properties.

From the point of view of the GA, the only component that requires modification to address this new problem is the fitness function. In particular, we are now screening for direct gap semiconductors with gaps greater than 3 eV in order to obtain transparency. In addition, the band edge position criteria now stipulates that the valence band of the shield must lie between the valence band position of the water splitter and the oxygen evolution potential. This corresponds to a valence band position lying between 1.7 and 2.5 eV with respect to the H^+/H_2 level [5]. There is no restriction on the position of the conduction band, other than that implied by the band gap and valence band criteria.

The modified component fitness functions are plotted in Fig. 4. The overall fitness functions, “Discontinuous”, “Smooth”, and “Smooth Product” are taken as sums and products of the component functions similarly to solar water splitting. There exist 8 solutions in our search space to the transparent shield screening problem (Table 2).

We re-tested all 2592 GA parameter sets that were examined for water splitting for the transparent shield problem, with 20 trials for each parameter set, resulting in 51,840 additional GA runs.

Efficiency metric

We evaluate the robustness of both GAs and chemical rules against a standard benchmark of random guesses within the search space. The metric used for comparing algorithms is the expected number of computations needed to produce a given number of solutions to the problem. In particular, we focus on the average number of computations needed to

uncover all solutions as well as the average number of computations to produce any half of solutions. We define the *efficiency* (or *robustness*) of an optimization strategy as the ratio of the average number of calculations needed for random search to the average number of calculations needed by the GA to produce a given number of solutions:

$$e^n = \frac{c_{\text{rand}}^n}{c_{\text{opt}}^n}$$

where e^n represents our definition of efficiency in finding n solutions, c_{opt}^n is the average number of calculations needed by the optimization strategy to find n solutions, and c_{rand}^n is the average number of calculations needed for a random search strategy to find n solutions. For random search, the average number of computations c to produce n solutions is given mathematically by [46]:

$$c_{\text{rand}}^n = \frac{n(x+1)}{(s+1)}$$

where x is the size of the search space (18,928) and s is the total number of solutions (20 for water splitting and 8 for photocorrosion shields). The number of computations c_{rand}^n needed to obtain $n = 10$ and $n = 20$ solutions for water splitting is 9014 and 18,028, respectively, when randomly choosing candidates. An efficiency of 2 therefore indicates that 4507 and 9014 computations were needed to find $n = 10$ and $n = 20$ solutions, respectively.

ANOVA

To compare the contributions of each parameter choice to the GA's efficiency, we used the analysis of variance (ANOVA) method [47–49]. ANOVA allows one to assess what factors are statistically relevant to influencing a result, the relative degree of importance of each factor, and potential interactions between parameters. We performed the ANOVA using Matlab's multi-way *anovan()* method. Statistical tests were performed with a 95 % confidence level, and the multiple comparison test was performed using “Tukey's honestly significant difference” criterion.

Results

Now that we have introduced our GA parameter choices and efficiency measure, we compare a GA-guided search to random and chemical rule-based search. In Fig. 5, we plot the average number of fitness evaluations (DFT computations) needed to achieve a given number of solutions. Random search, depicted by a black line, requires on average over 18,000 fitness evaluations in order to find all solutions in the search space. The best-performing GA is

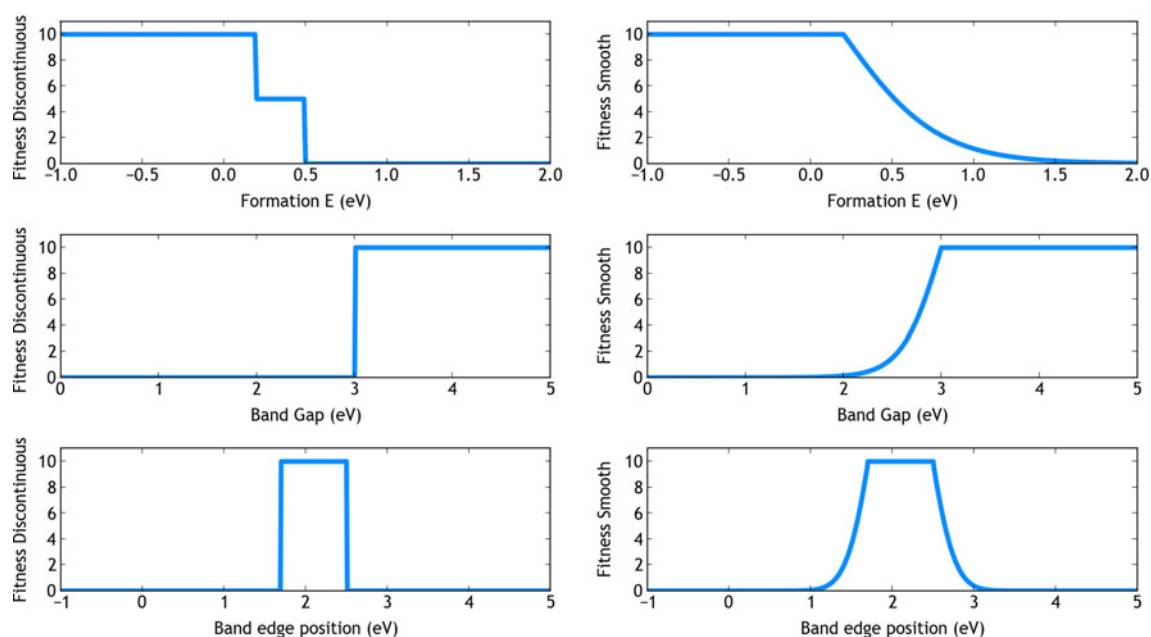


Fig. 4 The component fitness functions for photocorrosion transparent shields. Similar to the water splitting case, the overall fitness function involves either sums or products of the component fitness

functions, as described in the text. The band edge position corresponds to the valence band, with the zero value taken to be at the H^+/H_2 level

Table 2 Potential photoanode shields investigated in this work, and their calculated properties

Formula	ΔH_f	$E_{\text{gap}}^{\text{dir}}$	$E_{\text{cb}}^{\text{dir}}$	$E_{\text{vb}}^{\text{dir}}$	$E_{\text{gap}}^{\text{ind}}$	$E_{\text{cb}}^{\text{ind}}$	$E_{\text{vb}}^{\text{ind}}$
CaSnO ₃	0.16	3.57	-1.02	2.55	3.04	-0.76	2.28
RbTiO ₂ F	0.16	3.60	-0.86	2.74	3.10	-0.61	2.49
RbNbO ₃	-0.36	3.87	-1.18	2.69	3.42	-0.96	2.46
SrTiO ₃	-0.24	4.31	-1.71	2.60	4.08	-1.60	2.48
SrGaO ₂ F	0.18	3.80	-1.21	2.59	3.10	-0.86	2.24
SrSnO ₃	0.00	3.39	-1.03	2.36	2.89	-0.78	2.11
CsTaO ₃	-0.38	3.51	-1.05	2.46	3.51	-1.05	2.46
BaInO ₂ F	0.10	3.20	-0.63	2.57	2.60	-0.33	2.27

These materials were originally reported by Castelli et al. [5], and the data can be downloaded at the Computational Materials Repository [5, 23, 24]. All units are in eV, the designations “dir” and “ind” correspond to direct and indirect, respectively. The zero reference for band levels corresponds to the H_2/H^+ energy

reported in Table 3 and represented in blue in Fig. 5. On average, this GA requires fewer than 3100 calculations to find all 20 solutions in a space of almost 19,000 possibilities, making it 5.8 times as efficient at searching the perovskite chemical space compared with random search (Table 4). The variation in performance over 20 trials is small compared to the total number of evaluations (Fig. 5), with the standard deviation ranging from 81 evaluations in finding a single solution to 712 evaluations in finding all 20 solutions. Therefore, by employing a GA, one could have confidently searched the entire chemical space of ABX₃ peroxides using only about one-sixth as many calculations compared with computing the entire space. Stated another way, our result suggests that given a fixed computational

budget, the use of the GA allows one to search chemical spaces that are much larger than the number of available calculations.

In Fig. 6, we compare the performance of our best GA versus the chemical rule-based strategy described in “Chemical rule-based search method”. We note that our chemical rules are a difficult benchmark to surpass; rules (1) and (2) of our rule-based search eliminate 11,587 compounds, or 60 % of the search space, from the search. In addition, rule (3) informs which of the remaining individuals are likely to be stable based on specific knowledge of the perovskite structure. In contrast, the GA must learn these types of rules dynamically over the course of optimization without *any* prior knowledge. The GA has no

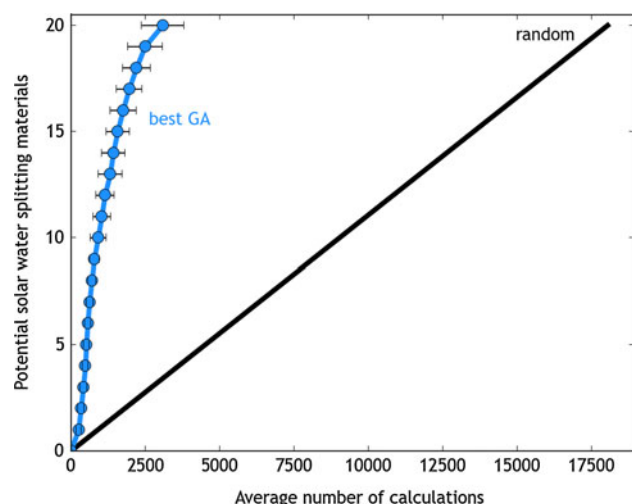


Fig. 5 The average number of calculations needed to produce a given number of solutions to the solar water splitting problem for genetic algorithms versus a random strategy. The best-performing GA (*blue*) requires significantly fewer calculations than a random strategy (*black*) to find potential solar water splitters. The *error bars* represent one standard deviation from the average performance over 20 independent runs of the genetic algorithm (Color figure online)

Table 3 Parameters for the best GA in finding both 10 and 20 solutions, as described in the text

Parameter	Value
Population size	100
Fitness function	Smooth product
Selection function	Binary tournament
Crossover function	Single point
Elitism	50 %
Mutation rate	5 %

The performance data for this parameter set is listed in Table 4

knowledge of what the genome or the fitness function represents; its only information comes from matching genome vectors to the numerical results of fitness evaluations. Despite these limitations, the best GA is comparable to search with basic chemical rules designed to tackle a specific materials problem (Fig. 6). This suggests that GAs might provide a path forward in problems where chemical rules are not available to the researcher in advance.

We also investigated whether the GA can benefit from knowledge of chemical rules. We re-ran the best GA but simulated a situation in which the 11,587 compounds that can be excluded based on chemical rules (1) and (2) are not calculated. The GA proceeds as before, but we return a fitness function of zero for any excluded compound and do not count it as as being ‘searched’. This method crudely approximates a “knowledge-directed” GA in which outside information is employed to guide the search. The

Table 4 Efficiency of chemical rules and GA in finding 10 and 20 solutions to the one-photon water splitting problem

Parameter set	10 solutions	All 20 solutions
Chemical rules	9.2	4.5
Best GA	9.8	5.8
Best GA + chemical rules	16.9	11.7

Random search is defined to have an efficiency of 1

results for this method are indicated in green in Fig. 6 and demonstrate that a knowledge-directed GA outperforms both chemical rules and uninformed GA by themselves. The knowledge-directed algorithm represents factors of 11.7, 2.6, and 2.0 improvements in finding all solutions compared with random search, chemical rules alone, and GA alone, respectively. The performance data for all methods is summarized in Table 4.

Next, we examine how the six GA parameters (crossover type, population size, selection method, mutation rate, elitism, and fitness) influence robustness of the GA in finding all 20 solutions. We first analyze the data using ANOVA without considering interactions between parameters. We find that all parameters except the mutation rate statistically influence the GA efficiency using a 5 % confidence test (the mutation rate has a *p* value of 18 %). It may be the case that the local and global mutation operators introduced in “Convergence and additional mutation operators” generate sufficient population diversity such that additional mutations are not needed to improve GA performance.

After removing mutation from the analysis, we assessed the contribution of each remaining parameter to the GA’s robustness through the η^2 parameter. A large η^2 indicates a large effect of the parameter on GA efficiency while a small η^2 suggests that the parameter (while statistically significant) produces only a small effect. The portion of the result that cannot be prescribed to a single parameter is lumped into an “error” term. This term encompasses both interactions between parameters and also randomness of the GA (e.g., due to different initial populations). Table 5 lists the η^2 measure for all parameters and the error term. The two major parameters affecting the results are elitism and selection method (Table 5). The population size, crossover type, and fitness function have statistically significant but marginal effects on the results.

We also studied an ANOVA model with pair interactions included (Table 6). Almost all interactions are very small. However, there exists one very significant interaction between elitism and the selection function. This strong interaction can be attributed to an unfavorable combination of zero elitism paired with either uniform selection or “weak” roulette selection (scaling factor of 1.25). In the

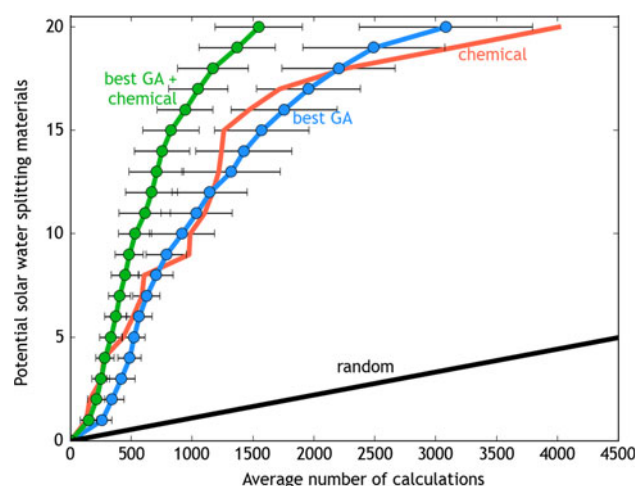


Fig. 6 The average number of calculations needed to produce a given number of solutions to the solar water splitting capture problem for genetic algorithms versus chemical search. The best GA without any chemical guidance (*blue*) performs comparably to chemical rules (*orange*). The “knowledge-directed” GA for which the search space is reduced through chemical constraints (*green*) significantly improves upon chemical rule-based search and uninformed GA. The *error bars* represent one standard deviation from the average performance over 20 independent runs of the genetic algorithm (Color figure online)

case of uniform selection, the fitness function is used nowhere in the GA when elitism is absent; we are essentially performing a random search. We suspect that weak roulette selection behaves similarly, with the fitness function too weakly distinguishing good and bad individuals without the added selection pressure of elitism.

Now that we have determined which factors and interactions are most important to the GA robustness, we examine exact parameter values that yield good or bad efficiency using a multiple comparison test. This test produces the marginal mean number of calculations required to find 20 solutions to solar water splitting along with a confidence interval. It allows us to determine which parameter values are distinct from one another, and how they affect robustness. In Fig. 7, we plot the results of the multiple comparison test for selection method, crossover, population size, elitism, and fitness function. Parameters with the same color and symbol in Fig. 7 do not differ much in their effect and can be considered equivalent.

In terms of selection, there exist two groups of parameters (Fig. 7). The uniform and “weak” roulette ($C = 1.25$) methods both perform poorly compared to other selection methods. As discussed previously, these selection methods either partially or completely fail to take into account the fitness function. The best results are found for “strong” roulette (i.e., roulette with a scaling factor equal or higher than 2.5), although similar results can also be obtained with tournament selection. While robustness slightly increases as roulette selection becomes stronger, it

Table 5 Percentage of variance (η^2) prescribed to various GA parameters from ANOVA (run without interactions) for the problem of finding all 20 solar water splitters

Parameter	Percentage of variance (η^2)
Elitism	33.9
Selection function	19.4
Population size	3.0
Crossover function	2.8
Fitness function	2.0
Error	39

The effect of the mutation rate is not statistically significant

slightly decreases as tournament selection becomes stronger.

Figure 7 highlights that the absence of elitism is extremely undesirable. However, the positive effect of adding elitism appears to saturate somewhere around 50 %; we do not see any difference between the elitism rate set at 50 and 75 %.

When examining the crossover function, both single-point and uniform crossover significantly outperform two-point crossover (Fig. 7). Two-point crossover operator swaps X_3 between parents to produce children, but our problem contains only seven potential values of X_3 . Many parents will share the same X_3 , and children will be identical to parents. The two-point crossover is therefore not appropriate for our problem as it is unlikely to generate sufficient population diversity. In general, it should be noted that our results regarding crossover operations are for a 3-element genome and may not apply to the more common situation of having larger genomes. Therefore, our results on crossover should be viewed as specific to this application.

Regarding the fitness function, Fig. 7 demonstrates that the “Smooth Product” function performs the best, followed by the “Smooth” function and finally the “Discontinuous” function. These results suggest two guidelines in designing the fitness function. First, awarding partial points for partial solutions is helpful for the GA. Second, when designing multi-objective functions it appears to be beneficial to take products of individual fitness functions rather than sums.

Finally, Fig. 7 suggests that the population size should not be too large. For a given number of total calculations, large population sizes involve fewer generations and therefore fewer GA operations per individual. The poorer performance of large populations reported in our study may largely be due to this discrepancy.

A visual summary of the effects of various parameter choices is presented in Fig. 8. The diagonal elements in Fig. 8 represent the average efficiency when holding a single GA parameter constant while averaging over all

Table 6 Percentage of variance (η^2) prescribed to various GA parameters and two-parameter interactions from ANOVA for the problem of finding all 20 solar water splitters

Parameter	Percentage of variance (η^2)
Elitism	33.9
Selection function	19.4
Elitism and selection function	21.7
Population size	3.0
Crossover function	2.8
Fitness function	2.0
Population size and elitism	0.6
Population size and selection function	0.4
Crossover function and selection function	0.4
Selection function and fitness function	0.3
Elitism and fitness function	0.3
Crossover function and elitism	0.1
Population size and fitness function	0.1
Crossover and fitness function	0.1
Error	14.8

Insignificant parameters and interactions are not listed

potential values of the remaining parameters. Off-diagonal elements in Fig. 8 represent the average efficiency when holding two parameters constant and averaging over the remaining parameter values. By examining Fig. 8, we see visually many of the conclusions determined through ANOVA. For example, the dark row and column in the matrix where elitism is zero illustrates the strong negative effect of this parameter choice. It is also easy to pinpoint the unfavorable interaction between lack of elitism and uniform selection or weak roulette selection (dark red). However, it is difficult to assess the statistical significance of differences. Therefore, Fig. 8 should be considered a rough overview map of parameter space.

In summary, our study suggests several guidelines when designing GA for perovskite oxide solar water splitters. First, elitism should be set high, for example to half the population. A “strong” roulette or tournament selection method should be used. While of less importance than selection and elitism, we can also recommend a population size small enough to enable several GA operations per individual (100, or 0.5 % of the search space, was optimal in our tests) and a Smooth fitness function that is the product of several individual functions.

While these recommendations pertain to finding all 20 solutions to the perovskite solar water splitting problem, it is interesting to test how they generalize to other problems. As a first example, we consider the problem of finding only half the number of solutions in the search space and re-examine our suggestions for parameter choices. The metric

of evaluations needed to find any 10 solutions might be important in computational screening if our desire is to quickly pinpoint a few compounds for laboratory followup. Table 7 lists the η^2 values for single-factor ANOVA but for the problem of finding 10 solutions to the solar water splitting problem.

The main difference between the ANOVA results for the 10 versus 20 solutions is with respect to the population size. While the population size explained only 3 % of the variance for 20 candidates, it is much important (13.2 %) for 10 candidates. In both problems, smaller population sizes (100) are more favorable than larger ones. However, the benefits of a small population size are much more pronounced when targeting 10 candidates. This might be because small population sizes carry less diversity than large populations, presenting a natural disadvantage in searching globally for multiple optima. Large populations are slow to find initial solutions because of fewer GA operations for a given number of calculations, as discussed earlier. However, once these rules are discovered the greater diversity in large populations could become advantageous in searching globally for solutions.

Using a multiple comparison test (Fig. 9), we find that another major difference in finding 10 versus 20 solutions is the choice of selection method. Whereas obtaining 20 solutions favored strong roulette selection, obtaining 10 solutions favors a strong tournament selection rule (tournament size of 5 or 10 %). In both cases, binary tournament selection performs similarly to strong roulette selection. It might be the case that tournament selection overall creates more selection pressure than roulette selection. Similar to small population sizes, the very high selection pressure of strong tournament selection might be advantageous for finding solutions within a small region of chemical space but be suboptimal in finding solutions globally.

Figure 10 plots the efficiencies of finding ten and all solutions for each of the 2592 parameter sets. The two properties are correlated, suggesting that the same parameters might be used for both problems. In particular, we label the “best” GA overall, and note that it performed optimally in finding both 10 and 20 solutions. As discussed previously, Fig. 10 indicates that large population sizes (green diamonds) are less efficient than small population sizes (blue circles and orange squares), and even more so when attempting to find only ten solutions.

As a second test to the transferability of our recommended GA parameters, we attempt to identify transparent photocorrosion shields as described in “[Transparent photocorrosion shield screening](#)”. In Fig. 11, we compare the efficiency of each set of GA parameters in optimizing the solar water splitter problem to the efficiency in optimizing the transparent shield problem. We note that the

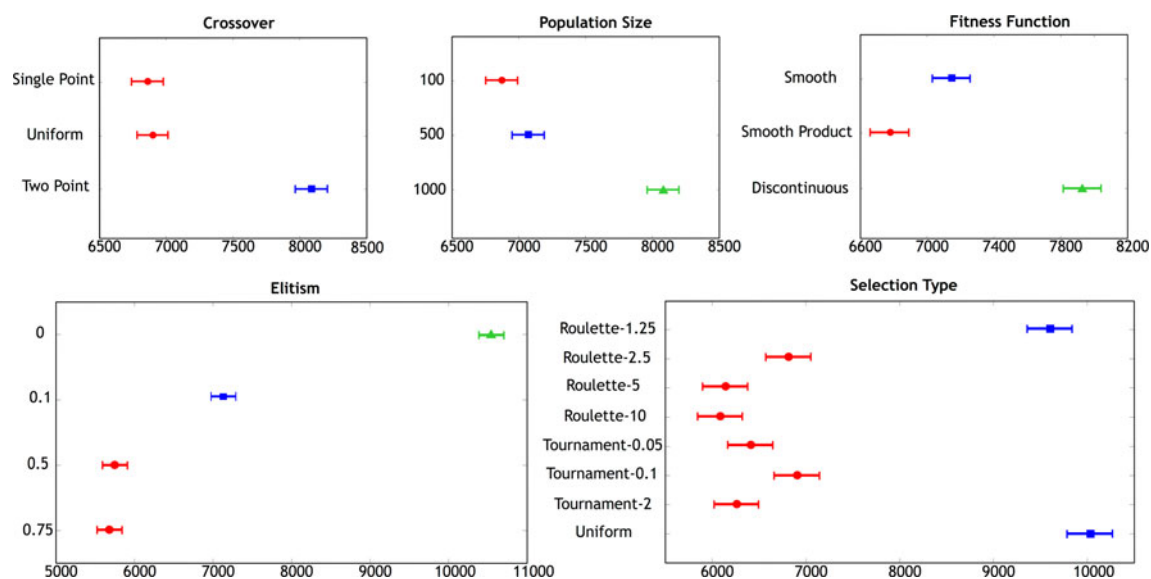
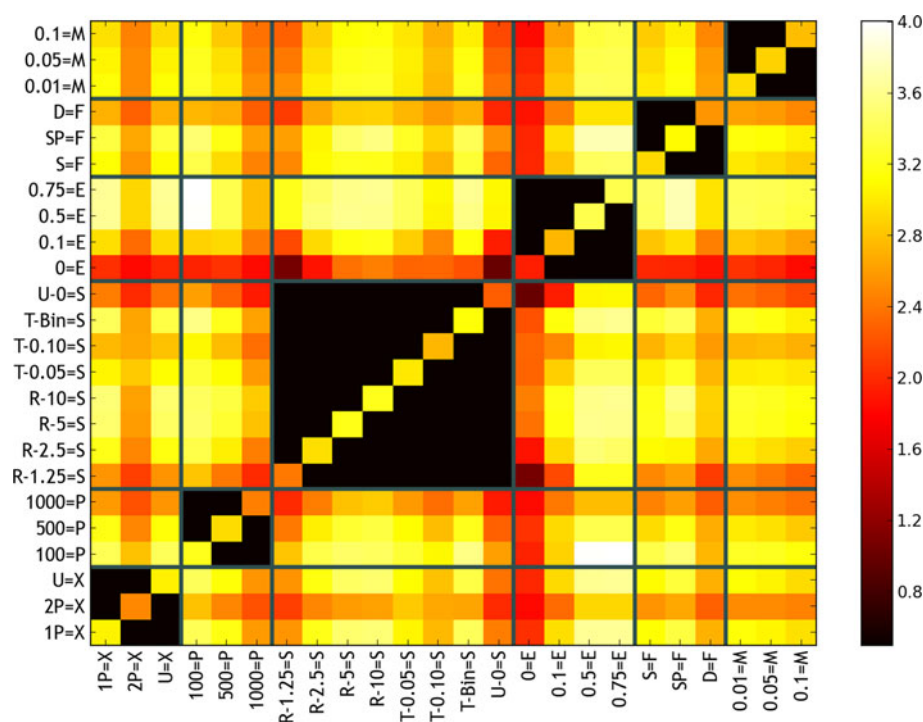


Fig. 7 Multiple comparison test demonstrating the effect of various parameter choices. Parameters that are statistically different from one another are represented by different colors and symbols. For example, single-point and uniform crossover are statistically different from

two-point crossover, but not from each other. The value on the x-axis represents average number of computations needed to reach 20 solutions to the solar water splitting problem; lower values represent better performance (Color figure online)

Fig. 8 Average efficiency in finding 20 solutions when constraining one or two parameters while averaging over other parameter values. The values along the diagonal constrain a single parameter; off-diagonal elements constrain two parameters. The designations M, F, E, S, P, and X refer to mutation rate, fitness function, elitism, selection function, population size, and crossover function, respectively. The designations D, SP, S, T, R, U, 2P, and 1P refer to discontinuous, smooth product, smooth, tournament selection, roulette selection, uniform, two-point, and single-point, respectively



best performance for the transparent shield problem is approximately 8 times more efficient than random search (Fig. 11), demonstrating the GA is also applicable to a second problem.

In general, there exists a correlation between the two problems: a GA parameter set that performs well in identifying solar water splitters is also more likely to identify transparent shields efficiently (Fig. 11). However, there is

considerable scatter in the relation, which suggests that unfortunately even similar problems over the same chemical space require slightly different GA parameters for optimal performance.

It should be noted that chemical search outperforms the GA in finding transparent shields, with 13.4 times improvement over random search to find all 8 solutions. Chemical rules might perform better in finding fewer

Table 7 Percentage of variance (η^2) prescribed to various GA parameters from ANOVA (run without interactions) for the problem of finding 10 solar water splitters (half of all potential solutions)

Parameter	Percentage of variance (η^2)
Selection function	25.6
Elitism	20.4
Population size	13.2
Crossover function	1.2
Fitness function	1.0
Error	38.6

The effect of the mutation rate is not statistically significant

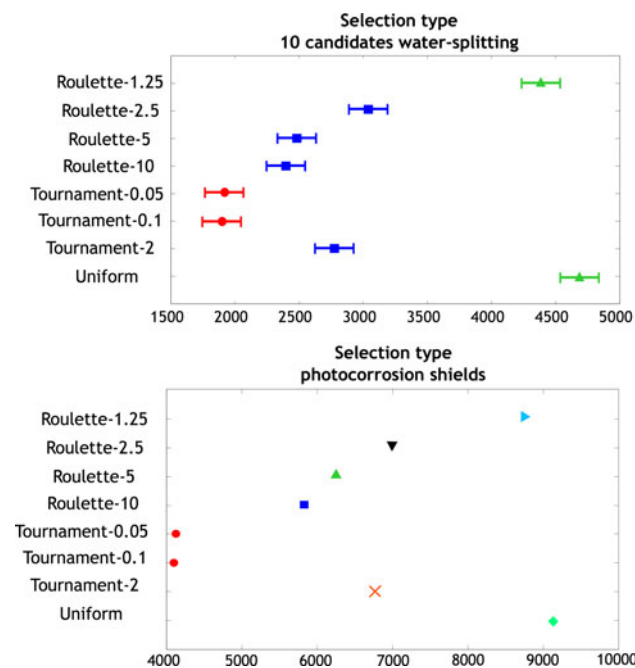


Fig. 9 Multiple comparison tests illustrating the effect of selection function in determining the number of calculations needed to find 10 solutions for water splitting (*top*) and all 8 solutions for photocorrosion shields (*bottom*). The uncertainty values for photocorrosion shields are similar in magnitude to the marker size, and are omitted. Parameters that are statistically different from one another are represented by different colors and symbols. In both problems, tournament selection with a high tournament rate outperforms roulette selection

solutions (as in the transparent shields problem), whereas GA might be able to outperform chemical rules when finding a greater number of solutions (as in water splitting). In Fig. 6, for example, we see a sharp dropoff in the performance of chemical rules after about 15 solutions found.

We perform a single-factor ANOVA on the photocorrosion shield data set to assess any difference in important parameters compared to solar water splitting. The results, presented in Table 8, are mostly similar to the water splitting case. However, elitism is an even greater factor in the transparent shields problem. In addition, a multiple

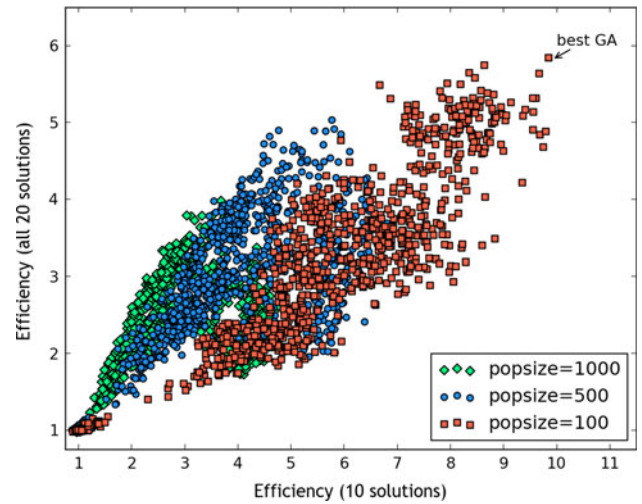


Fig. 10 Efficiency of the GA in finding all 20 solutions (y-axis) versus efficiency in finding 10 solutions (x-axis) to the solar water splitting problem. Each point represents one of the 2592 parameter sets tested. The data is labeled by population size. The parameter set we consider to be the “best” exhibits optimal efficiency in finding both 10 and 20 solutions

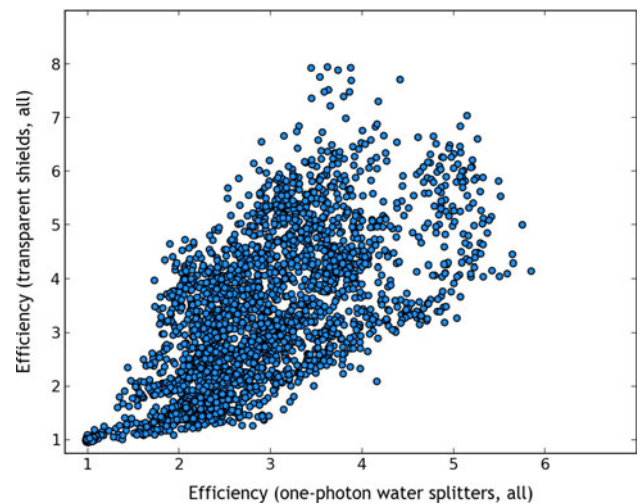


Fig. 11 Efficiency of the GA in finding all 8 photoanode transparent shields (y-axis) versus efficiency in finding all 20 one-photon water splitters (x-axis). Each point represents one set of GA parameters

comparison test (Fig. 9) demonstrates that strong tournament selection is optimal for finding all transparent shields, whereas strong roulette selection was optimal for finding all solar water splitters (Fig. 7). In this respect, finding all transparent shields is similar to finding only 10 solutions for water splitting. This similarity might originate because there exist only 8 solutions for the transparent shield in the search space, suggesting that we should use parameters that rapidly find a small number of solutions.

In conclusion, the parameters with the largest effects on the results are elitism, selection method, and population size.

Table 8 Percentage of variance (η^2) prescribed to various GA parameters from ANOVA (run without interactions) for the problem of finding all 8 transparent photocorrosion shields

Parameter	Percentage of variance (η^2)
Elitism	43.1
Selection function	20.0
Population size	5.0
Fitness function	0.8
Crossover function	0.4
Error	30.6

The effect of the mutation rate is not statistically significant

In particular, zero elitism is particularly detrimental to GA performance, especially when employing weak selection methods. The exact tuning of the parameters, and in particular the choice of strong roulette versus strong tournament selection, appears to depend on the problem. For example, our results suggest that higher selection pressures should be used when targeting fewer solutions. However, there exists overall a strong correlation between parameters that perform well on one problem versus other similar problems.

Discussion

While we have so far mainly discussed the GA as a “black box” optimizer, we now consider its operation in more detail. To help understand how a GA might improve performance in our problem, we refer to a previous study by Calle-Vallejo et al. [50] on trends in perovskite stability in pure oxides. Using DFT computations similar to those employed in this work, Calle-Vallejo et al. [50] observed that the enthalpy of formation was mostly constant for a given B ion (B^{3+} and B^{4+} behave differently). This result might help explain the efficiency of the GA: we would expect that ‘fit’ parents with favorable ‘B’ genes will produce children that inherit this B-site ‘gene’ that confers good formation enthalpy. In addition, there is also evidence from Calle-Vallejo et al.’s results that perturbations to the formation enthalpy due to the A site should follow the same rank and general direction independently of the B site (although the magnitude might vary depending on B) [50]. Thus there also exist ‘desirable’ values of the A gene that could be passed between generations. We speculate that similar trends may hold true for the band gap and band position criteria. For example, there exists a weak relation between formation enthalpy and band gap that suggests that the factors that control formation enthalpy might also tune the band gap [5, 6].

We note that our choice of encoding of a material into a genome string might affect GA robustness. Our encoding

employed a short genome of length 3 with a high cardinality alphabet that contained up to 52 values. The advantage of this encoding was that it was trivial to encode and decode between a perovskite material and its genomic representation. However, this might not be an optimal encoding in terms of robustness, because it treats each element in the periodic table as an independent entity. In particular, it neglects chemical relationships between elements in the periodic table. For example, our encoding prevents a crossover operation from mixing an early transition metal with a late transition metal to produce an intermediate transition metal. Such an operation might be achieved by representing each element in a binary or Gray coding that represents electronegativity or Mendeleev number. This representation would allow a child to inherit an element that is intermediate in chemical behavior to its parents. In GA terms, this would create a long genome with a low cardinality alphabet. Such representations present more opportunities to find and mix building blocks that confer fitness, thereby enhancing efficiency [9, 35, 51].

Our target problem was difficult in some respects: it is a multimodal problem with several solutions and in which the relationship between formation enthalpy, band gap, and band edge position is complex and unknown. However, our search problem was also simpler than many realistic materials design scenarios because our search space only involved a single generalized composition (ABX_3) and a single crystal structure (perovskites). Many important materials design studies must search over several different composition templates and structure prototypes. For example, a recent computational investigation by Berger and Neaton [52] suggested that a Cr–V mixture in a double perovskite structure might be interesting for water splitting, and a separate computational study by Wu et al. [53], found many potentially interesting water splitters by canvassing chemical substitutions into the ICSD database. Extension of our scheme to double-perovskites should be straightforward by increasing the length of the feature vector, but significant changes to materials encoding and crossover operations would be needed to test all the diverse structures found in the ICSD. However, we believe that this issue does not pose a major barrier to employing GA in more sophisticated searches. In particular, there exists a rich and successful history of employing GA coupled with computation to predict new crystal structures [33], and appropriate operators for crossover, selection, etc., have already been developed for searching over both crystal structures and compositions with a GA [54, 55].

We note that integrating GAs, or any optimization algorithm, into high-throughput computational searches still requires further effort. In particular, the GA implementation tested herein relies on completing one generation of computations before beginning the next generation.

The typical way to parallelize this type of GA is to assign a “controller” node to coordinate the GA engine and assign the remaining nodes as “workers” that perform fitness evaluations (DFT computations). There are at least two major limitations with this setup. The first limitation is that the number of worker nodes must always balance the number of fitness evaluations needed in each generation in order to keep the workers occupied with computing tasks. Therefore, the number of worker nodes and the parallelizability of the fitness evaluations will restrict the choice of GA parameters. More worker nodes will stipulate higher population sizes, lower elitism, or improved parallelizability in evaluating the fitness function. A second limitation is that the controller node must wait for all fitness evaluations within a generation to complete before proceeding with selection, crossover, and mutation operations. A single DFT computation that is slow-to-converge might thus impede the progress of the entire GA. This is a real problem with DFT computations because time to completion can vary by days and is difficult to predict in advance.

Fortunately, alternate GA models have been designed that overcome such limitations in parallelization [35, 56, 57]. For example, in an asynchronous GA, the GA operators are immediately applied after each fitness evaluation using the population available at the time. Another technique is to perform independent GAs on different processors, but to communicate fittest individuals observed between GA instances. These methods, as well as others that have been devised [35], solve both issues presented earlier by ensuring that compute nodes are never kept idle. We note while other optimization techniques such as simulated annealing are also available [13], a major advantage of the GA is its potential for attaining high parallel performance [58] and integration into high-throughput computation. However, a necessary step forward to the automated inverse design of materials is the integration of the optimizer into one of several existing high-throughput DFT frameworks [7, 23, 59, 60].

We hypothesize that a more advanced GA might further improve performance beyond the values reported in this work. For example, niching, the use of a Pareto optimal rank fitness function, and a more flexible encoding were already mentioned as potential enhancements [35]. In addition, previous work by Balamurugan et al. [61], suggests that a “hybrid” approach, whereby a GA is coupled to local search using alchemical derivatives [62, 63], might be a promising avenue for further performance improvements.

Conclusion

We demonstrated that use of a GA improves the efficiency of searching a chemical space of almost 19,000 perovskites for

solar water splitters. The GA was especially useful at rapidly finding half of the solutions (almost 10 times efficiency gain over random search), and provided up to a 5.8 greater efficiency in finding all solutions. The performance of the best GA tested was comparable to a set of chemical rules we designed to filter and rank perovskite materials for this problem. A GA might therefore be applied in situations where chemical rules are not known in advance. Combining the GA with chemical rules further improved performance, leading to 16.9 and 11.7 times less fitness evaluations needed than random search to find 10 and all 20 solutions, respectively. We further found that in an alternate problem aimed at uncovering transparent photocorrosion shields, the GA performed 8 times more efficiently than random search.

Using ANOVA, we determined that the most important parameters for good performance were elitism and selection function. The GA performed best when the elitism was set to at least 50 %. The appropriate selection function appears to depend on the number of solutions in the search space. For finding all 20 solutions to the solar water splitting problem, strong roulette selection performs best. For finding 10 solutions to the water splitting problem or 8 solutions to the photocorrosion problem, a strong tournament selection performs better. In all cases, we found small population sizes to be beneficial, although the advantage diminished with the desired number of solutions.

We speculate that further gains in GA performance might be obtained through niching, longer genome encodings, or a Pareto optimal fitness function. While significant work still remains to couple a GA “control loop” to an automated and rapid DFT computation framework, our results suggest that such a technique presents a viable method to rapidly screen large chemical spaces for technological materials.

Acknowledgements We thank Dr. Shahar Keinan, Dr. Yosuke Kanai, Dr. Jeffrey Tilson, and Dr. Robert Fowler for their thoughts and assistance in designing this study. We thank Dr. Byron Schmuland for providing an elegant derivation of the random choosing probability problem via Math Exchange. Geoffroy Hautier acknowledges the F.R.S.-FNRS Belgium for financial support under a “Chargé de Recherche” grant. Anubhav Jain acknowledges funding through the U.S. Government under Contract DE-AC02-05CH11231 and the Luis W. Alvarez Fellowship in Computational Science. Ivano E. Castelli and Karsten W. Jacobsen acknowledge support from the Danish Center for Scientific Computing through grant HDW-1103-06, from the Catalysis for Sustainable Energy (CASE) initiative funded by the Danish Ministry of Science, Technology and Innovation and from the Center for Atomic-scale Materials Design (CAMD) sponsored by the Lundbeck Foundation. This research is supported by the Office of Science of the U.S. Department of Energy under contract DE-AC02-05CH11231.

References

1. Hohenberg P, Kohn W (1964) *Phys Rev* 136:B864
2. Kohn W, Sham LJ (1965) *Phys Rev* 140:1133

3. Hautier G, Jain A, Ong SP (2012) *J Mater Sci* 47:7317. doi: [10.1007/s10853-012-6424-0](https://doi.org/10.1007/s10853-012-6424-0)
4. Hafner J, Wolverton C, Ceder G (2006) *MRS Bull* 31:659
5. Castelli IE, Landis DD, Thygesen KS, Dahl S, Chorkendorff I, Jaramillo TF et al (2012) *Energy Environ Sci* 5:9034
6. Castelli IE, Olsen T, Datta S, Landis DD, Dahl S, Thygesen KS et al (2012) *Energy Environ Sci* 5:5814
7. Jain A, Hautier G, Moore CJ, Ong SP, Fischer CC, Mueller T et al (2011) *Comput Mater Sci* 50:2295
8. Materials Project (2011) <http://www.materialsproject.org>
9. Holland JH (1975) *Adaptation in natural and artificial systems*. University of Michigan Press, Ann Arbor
10. Hautier G, Fischer C, Ehlacher V, Jain A, Ceder G (2011) *Inorg Chem* 50:656
11. Hautier G, Fischer CC, Jain A, Mueller T, Ceder G (2010) *Chem Mater* 22:3762
12. Balachandran PV, Broderick SR, Rajan K (2011) *Proc R Soc A* 467:2271
13. Franceschetti A, Zunger A (1999) *Nature* 402:60
14. Kim K, Graf PA, Jones WB (2005) *J Comput Phys* 208:735
15. Dudiy S, Zunger A (2006) *Phys Rev Lett* 97:1
16. d'Avezac M, Luo J-W, Chanier T, Zunger A (2012) *Phys Rev Lett* 108:1
17. Johannesson G, Bligaard T, Ruban A, Skriver H, Norskov JK (2002) *Phys Rev Lett* 1:255506
18. Graf PA, Kim K, Jones WB, Hart GLW (2005) *Appl Phys Lett* 87:243111
19. Piquini P, Graf P, Zunger A (2008) *Phys Rev Lett* 100:1
20. Chakraborti N (2004) *Genetic algorithms in materials design and processing*. *Int Mater Rev* 49:246
21. Bhalla A, Guo R, Roy R (2000) *Mater Res Innov* 4:3
22. Peña MA, Fierro JL (2001) *Chem Rev* 101:1981
23. Landis DD, Hummelshøj JS, Nestorov S, Greeley J, Dulak M, Bligaard T et al (2012) *Comput Sci Eng* 14:51
24. Computational Materials Repository (2013) <https://cmr.fysik.dtu.dk/cmr/index.php>
25. Enkovaara J, Rostgaard C, Mortensen JJ, Chen J, Duřak M, Ferrighi L et al (2010) *J Phys Condens Matter* 22:253202
26. Mortensen J, Hansen L, Jacobsen K (2005) *Phys Rev B* 71:1
27. Hammer B, Hansen L, Nørskov J (1999) *Phys Rev B* 59:7413
28. Kuisma M, Ojanen J, Enkovaara J, Rantala T (2010) *Phys Rev B* 82:1
29. Gritsenko O, van Leeuwen R, van Lenthe E, Baerends E (1995) *Phys Rev A* 51:1944
30. Xu Y, Schoonen M (2000) *Am Mineral* 85:543
31. Butler MA, Ginley DS (1978) *J Electrochem Soc* 125:228
32. Armiento R, Kozinsky B, Fornari M, Ceder G (2011) *Phys Rev B* 84:04103
33. Oganov A, Lyakhov A, Valle M (2011) *Acc Chem Res* 44:227
34. Sastry K, Goldberg D, Kendall G (2005) In: Burke EK, Kendall G (eds) *Search methodologies*. Springer, New York, p 97
35. Goldberg D (1989) *Genetic algorithms in search, optimization, and machine learning*. Addison Wesley, Reading
36. Perone C (2012) Pyevolve software <https://github.com/perone/Pyevolve>
37. Perone CS (2009) *ACM SIGEVOlution* 4:12
38. Konak A, Coit DW, Smith AE (2006) *Reliab Eng Syst Saf* 91:992
39. Mercer RE (1977) *Adaptive search using a reproductive meta-plan*. University of Alberta, Edmonton
40. Grefenstette JJ (1986) *IEEE Trans Syst Man Cybern* 16:122
41. Sastry K, Abbass H, Goldberg D, Johnson DD (2005) In: *Proceedings of the 2005 conference on genetic and evolutionary computation*, p 671
42. Perry ZA (1984) *Experimental study of speciation in ecological niche theory using genetic algorithms*. Doctoral Thesis, University of Michigan
43. Mauldin M (1984) In: *Proceedings of the national conference on artificial intelligence*, Austin, TX, p 247
44. Goldberg DE, Richardson J (1987) In: *Proceedings of the second international conference on genetic algorithms*, p 41
45. Goldschmidt VM (1926) *Naturwissenschaften* 14:477
46. Schmuland B (2012) *Math Exchange Forum*. <http://math.stackexchange.com/questions/206798/pul>
47. Fisher RA (1925) *Math Proc Camb Philos Soc* 22:700
48. Rojas I, González J, Pomares H, Merelo JJ, Castillo PA, Romero G (2002) *IEEE Trans Syst Man Cybern Part C* 32:31
49. Sahai H, Ageel MI (2000) *The analysis of variance: fixed, random and mixed models*. Birkhäuser, Boston
50. Calle-Vallejo F, Martínez JI, García-Lastra JM, Mogensen M, Rossmeisl J (2010) *Angew Chem Int Ed* 49:7699
51. Holland J (1968) *Hierarchical descriptions of universal spaces and adaptive systems*. Technical Report, University of Michigan, Department of Computer and Communication Sciences
52. Berger R, Neaton J (2012) *Phys Rev B* 86:1
53. Wu Y, Lazic P, Hautier G, Persson K, Ceder G (2013) *Energy Environ Sci* 6:157
54. Oganov AR, Glass CW (2006) *J Chem Phys* 124:244704
55. Woodley S (2004) *Appl Evol Comput Chem* 110:95
56. Bethke AD (1976) *Comparison of genetic algorithms and gradient-based optimizers on parallel processors: efficiency of use of processing capacity*. Technical Report, University of Michigan, Logic of Computers Group
57. Cantu-Paz E (2000) *Efficient and accurate parallel genetic algorithms*. Springer, New York
58. Bandow B, Hartke B (2006) *J Phys Chem A* 23:5809
59. Munter TR, Landis DD, Abild-Pedersen F, Jones G, Wang S, Bligaard T (2009) *Comput Sci Discov* 2:015006
60. Ortiz C, Eriksson O, Klintonberg M (2009) *Comput Mater Sci* 44:1042
61. Balamurugan D, Yang W, Beratan DN (2008) *J Chem Phys* 129:174105
62. von Lilienfeld OA (2009) *J Chem Phys* 131:164102
63. Wang M, Hu X, Beratan DN, Yang W (2006) *J Am Chem Soc* 128:3228

Paper V

Calculated Pourbaix Diagrams of Cubic Perovskites for Water Splitting: Corrosion Against Stability

Ivano E. Castelli, Kristian S. Thygesen, and Karsten W. Jacobsen.

Accepted, 2013.

Calculated Pourbaix Diagrams of Cubic Perovskites for Water Splitting: Corrosion Against Stability

Ivano E. Castelli · Kristian S. Thygesen · Karsten W. Jacobsen

Received: date / Accepted: date

Abstract We use density functional theory (DFT) calculations to investigate the stability of cubic perovskites for photo-electrochemical water splitting taking both solids in their bulk crystal structure and dissolved phases into account. The method is validated through a detailed comparison of the calculated and experimental Pourbaix diagrams for TiO_2 and ZnO . For a class of 23 oxides, oxynitrides, and oxyfluorides, which were recently proposed as candidates for one-photon water splitting, our calculations predict most of the materials to be stable at potentials around the water redox level. The oxides become less stable at lower potentials, while the oxynitrides become unstable at higher potentials. We discuss the implications of these findings for the problem of photo-corrosion of water splitting electrodes.

The authors acknowledge support from the Catalysis for Sustainable Energy (CASE) initiative funded by the Danish Ministry of Science, Technology and Innovation, and from the Center on Nanostructuring for the Efficient Energy Conversion (CNEEC) at Stanford University.

Ivano E. Castelli
Center for Atomic-scale Materials Design, Department of Physics, Technical University of Denmark, Kongens Lyngby, DK-2800, Denmark.
E-mail: ivca@fysik.dtu.dk

Kristian S. Thygesen
Center for Atomic-scale Materials Design, Department of Physics, Technical University of Denmark, Kongens Lyngby, DK-2800, Denmark.

Karsten W. Jacobsen
Center for Atomic-scale Materials Design, Department of Physics, Technical University of Denmark, Kongens Lyngby, DK-2800, Denmark.

Keywords Water splitting · Density Functional Theory · Pourbaix diagrams · Corrosion · Photo-corrosion

PACS 82.20.Wt · 82.45.Bb · 82.60.Lf

1 Introduction

Over the past decade, the interest in using *ab-initio* computational methods for accelerated materials discovery has increased dramatically. This trend has been fueled by the continuous increase in computer power and improvements in the methodology, but has also relied on the development of a better understanding of how the ultimate properties of a material for a given application can be inferred from simpler microscopic quantities (descriptors) that can be obtained efficiently from first principles calculations [1,2]. As a few examples where quantum mechanical calculations have been used to search for new, cheaper and more efficient materials we mention computational screening for highly stable metal alloys [3], semiconductor superlattices with tailored band gaps [4], battery cathode [5] and inorganic scintillator materials [6], molecules for organic photo-voltaics [7–9], and high-performance piezoelectrics [10].

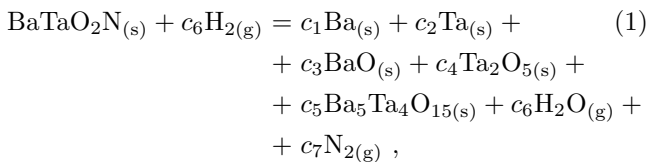
The single, most important criterion for a material to be used in any type of application is stability. The precise requirements on the material stability of course depend on the application and may be more or less restrictive depending on the conditions under which the material should function. Here we consider a case where stability is of key importance, namely the search for new electrode materials for photo-catalytic water splitting. The present work is a continuation of our earlier works [11,12] where we proposed 20 candidate materials based on an extensive computational screening of

cubic perovskites in which the stability and position of the conduction and valence band edges were evaluated against a set of design criteria [11,12]. Here we extend the stability analysis to include the possibility of corrosion of the perovskites under different electron potential and pH conditions using the so-called Pourbaix diagrams.

The one-photon water splitting device splits water by a direct use of the energy from the Sun: a photon with suitable energy is collected by a nanoparticle immersed in water and an electron-hole pair is created. The electron and hole reach two different points of the surface of the materials and, if their band edges are well positioned with respect to the red-ox potentials of water, the electron evolves hydrogen and the hole oxidizes water. A number of materials have been studied in depth in connection with the water splitting problem, mainly because of their high stability and/or good optical properties. A few examples are TiO_2 [13] (that works in UV light) and, more recently under visible light, the solid solution GaN:ZnO [14] as well as few oxynitrides in the perovskite structure [15]. However, due to the harsh oxidizing conditions and the light irradiation, most materials with optimal band edge positions are either oxidized or corrodes away, making the search for stable and efficient photo-electrodes a highly challenging task.

2 Method

In our previous work [11,12,16], we evaluated the stability of a compound by a direct comparison with a linear combination of the most stable, solid, experimental structures with the same chemical elements as present in the ICSD or in the Materials Project databases [17, 18]. We calculated all the energies using the electronic structure code GPAW [19,20] with a standard generalized gradient approximation (GGA) exchange-correlation functional in the form of the RPBE-approximation [21]. As an example, we consider the possible phase separation of the BaTaO_2N cubic perovskite:



where (s) and (g) indicate that the reference is in the solid and gas phase, respectively. Because the energy of the oxygen molecule is not well described by standard DFT we obtained the energy of oxygen as the energy difference between water and a hydrogen molecule (i.e., $\text{O} = \text{H}_2\text{O} - \text{H}_2$). With this definition, each oxygen atom

is taken at the chemical potential of water. Hydrogen is at its standard reference, H_2 in the gas phase. The formation energy, ΔE , is thus defined as:

$$\begin{aligned} \Delta E = & \text{BaTaO}_2\text{N} + \\ & - \min_{c_i} (c_1\text{Ba} + c_2\text{Ta} + c_3\text{BaO} \\ & + c_4\text{Ta}_2\text{O}_5 + c_5\text{Ba}_5\text{Ta}_4\text{O}_{15} + c_6\text{O} + c_7\text{N}_2) , \end{aligned} \quad (2)$$

with the constraints:

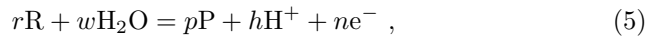
$$\begin{aligned} \sum_i c_i\text{Ba} = 1 , \quad \sum_i c_i\text{Ta} = 1 , \\ \sum_i c_i\text{O} = 2 , \quad \sum_i c_i\text{N} = 1 , \end{aligned} \quad (3)$$

which ensures the correct and with

$$c_i \geq 0 , \quad (4)$$

which ensures that only the references containing Ba, Ta, O, and N are considered. A material is defined stable if $\Delta E \leq 0.2$ eV/atom allowing for some metastability and inaccuracy in the calculations.

The scheme proposed so far did not cover the following two scenarios: (i) chemical reactions of the material with the water, and (ii) corrosion of the materials, i.e. its dissolution into charged ions in aqueous solution. The general reaction describing both of these effects is:



where R and P stand for reactants and products, and H^+ , and e^- indicates a dissolved proton and an electron at the Fermi level of the material, respectively. The equilibrium between reactants and products in (5) can be calculated using the Nernst equation. For a given concentration of the involved species (a_i), the electrochemical potential, U , (which sets the energy of the electrons) under which the reaction (5) is in equilibrium, is given by

$$nU = \Delta G + 0.0591 \log \frac{(a_{\text{P}})^p (a_{\text{H}^+})^h}{(a_{\text{R}})^r (a_{\text{H}_2\text{O}})^w} , \quad (6)$$

where ΔG is the standard free energy of the reaction in eV, the number 0.0591 equals $RT \ln(10)$ at room temperature ($T = 25^\circ\text{C}$). Taking $a_{\text{H}_2\text{O}} = 1$ and $\text{pH} = -\log a_{\text{H}^+}$, we can rewrite Eq. 6:

$$nU = \Delta G + 0.0591 \log \frac{(a_{\text{P}})^p}{(a_{\text{R}})^r} - 0.0591h \text{ pH} . \quad (7)$$

One of the main limitations of the Nernst equation is that it does not include the reaction kinetics, but only the thermodynamics. Other problems are that at high concentrations the true activity of the ions must be used instead of their concentrations, and it applies only when there is no current flow between the electrode that might change the activity of the ions. The Nernst equation 7 is used to draw the stability diagram of a

material as a function of the concentration of ions H^+ (pH) and of the potential U . The concentrations of the other involved ions are usually taken as the low value of 10^{-6} M. The phase diagram plotted as function of U along the y -axis and pH along the x -axis, is called a Pourbaix diagram after its inventor. The Pourbaix diagram consists of regions defined by straight lines which represent different equilibrium reactions and can be of three types [22]:

- Vertical lines: the reaction involves solid and dissolved substances with hydrogen ions but without free electrons so that the equilibrium is independent of the potential.
- Horizontal lines: the reaction involves solid and dissolved substances with free electrons but without hydrogen ions so that the equilibrium is independent of the pH.
- Straight lines with a slope equal to $0.0591h/n$: the reaction involves solid and dissolved substances with free electrons and hydrogen ions as in the reaction 5.

We now include in the pool of references all the dissolution energies available in Ref. [23] (and updates) and Ref. [24], while we calculate the energies of the solid references using DFT. The same procedure has been recently used by Persson *et al.* [25] to calculate the Pourbaix diagrams of several oxides and nitrides. In their work, the total energies of the pure chemical elements were corrected by a comparison with the experimental energies. Here, we do not apply any correction. Around 3000 bulk solids are included in the pool of references. Even if a surface might be more stable than the corresponding material in the bulk phase, the pool of references does not include any surface. To include also the surfaces, it will be necessary to find the most stable surface for each material depending on the pH and potential, and to study its possible passivations.

In our previous papers, we used the chemical potential of water for the oxygen molecule. This choice was supported by the fact that at least a thin layer of water has to be present to run the reaction [26]. In the present work, we define the chemical potential of oxygen from its standard state, i.e. the oxygen molecule in the gas phase for two reasons: (i) conventionally, the Pourbaix diagrams are drawn with all the chemical elements in their standard states, and (ii) the oxygen generated by the separation of the semiconductor into its constituents will be at the chemical potential of water only if hydrogen is present at high enough pressure that it can combine with the oxygen to form water. This will not occur if the water splitting device is efficient enough to collect the generated hydrogen so that the backreaction $H_2 + 1/2 O_2 \rightarrow H_2O$ is suppressed. This can be

accomplished by the use of a co-catalyst [27]. The effect of using the standard state of oxygen rather than taking it from water is a higher stability of the solid perovskites. Specifically, in addition to the 20 candidates identified in Ref. [12], the structures $MgSnO_3$, $LiSbO_3$, and $SrInO_2F$ are now also predicted to be stable (and with band gaps and band edge alignments fulfilling the design criteria) with respect to a phase separation in solid substances.

3 Pourbaix Diagrams

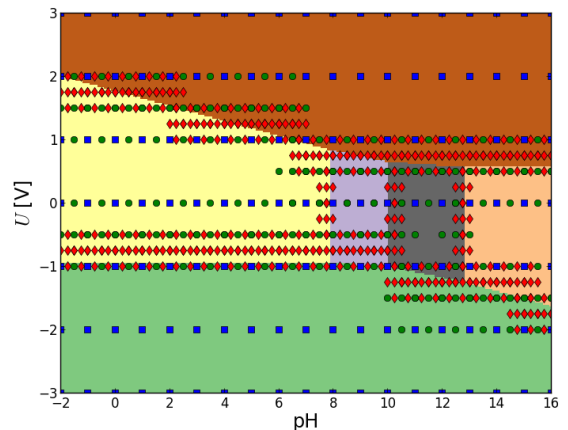


Fig. 1 Example of the bisection method used to construct the Pourbaix diagrams in this work [28]. The most stable phase of the material is calculated for a rough sampling of the region (blue squares). If the most stable phase at a given point is not the same at all its neighboring points, the sampling is refined (green circles) and the procedure repeats (red diamonds). The Pourbaix diagram shown here is for ZnO.

In this section, we first validate our method by calculating the Pourbaix diagrams for TiO_2 and ZnO and comparing with the experimental diagrams. We then construct the diagrams for nine perovskites that are known to exist in nature. The diagrams, are constructed for a region of pH between -2 and 16 and of potential between -3 and 3 eV (relative to the Standard Hydrogen Electrode). An efficient way to construct the Pourbaix diagram is to use a bisection method, as shown in Fig. 1: we start by calculating the most stable phase of the material for a fairly rough sampling, indicated by blue squares, of the relevant region. If the most stable phase at a given point is the same at all its neighboring points, we consider this phase to be stable within the region defined by the corners. If this is not the case, we refine the grid within the small region (the refined sampling are indicated as green circles) and repeat the

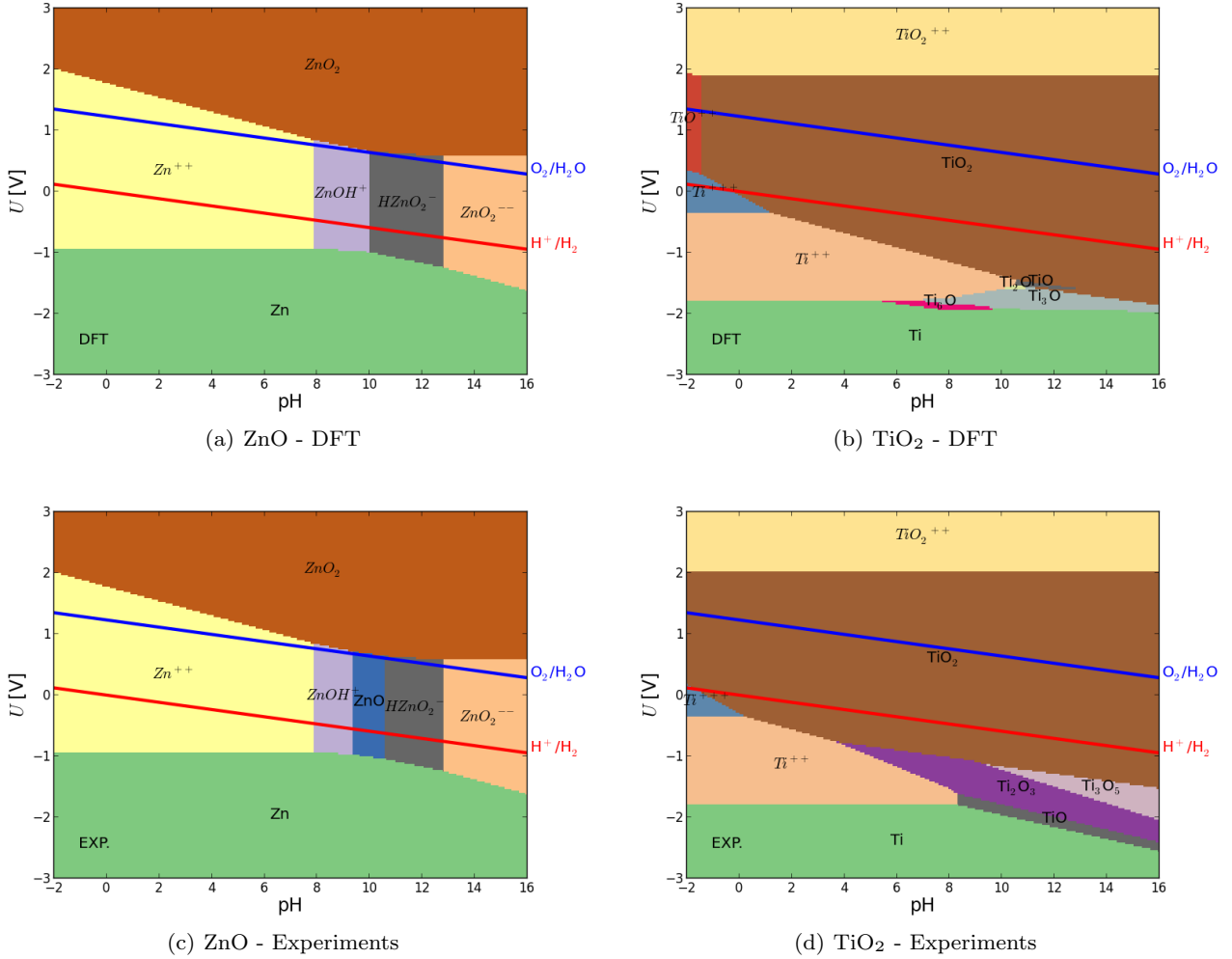


Fig. 2 Calculated and experimental Pourbaix diagrams for ZnO and TiO₂ (ZnO: (a) and (c); TiO₂: (b) and (d)). The diagrams are drawn for a concentration of 10^{-6} M at 25°C. The chemical formula in *italic* indicates an aqueous compound. The positions of the red-ox potentials of water is also indicated.

procedure (red diamonds) until a sufficiently accurate resolution has been obtained.

Figs. 2(a) and 2(c) show the Pourbaix diagrams for ZnO when the free energies are calculated with DFT or obtained from experiments, respectively. Overall, the two diagrams are very similar. A small difference occurs for potentials around 0 and pH around 10, where ZnO should be stable while DFT predicts that it is dissolved into HZnO_2^- . The energy difference between the two phases is, however, rather small (≈ 0.15 eV/atom), and if we consider an energy threshold of 0.2 eV/atom, to account for possible inaccuracy in the DFT energies, the calculated diagram ZnO turns out to be stable in the same region as in the experiments.

Figs. 2(b) and 2(d) show the calculated and experimental Pourbaix diagrams for TiO₂. Again, the two diagrams are very similar, except for the region of pH

above 7 and potentials between -1 and -2 V. The reason for this difference is related to the lack of experimental data for some of the phases present in the calculated diagram and possibly inaccuracies in the calculated energies. There is a broad region where TiO₂ is stable against oxidation, in particular around the red-ox potential of water, for all the values of pH. This is an important reason why TiO₂ has received so much attention in connection with water splitting. However, as is well known the band gap of TiO₂ lies in the UV range making it highly inefficient for light absorption and conversion into electron-hole pairs.

We now move on to investigate the stability of ternary compounds. To this end we selected nine oxides in the cubic perovskite structure that are all known to exist in nature and to be stable. Fig. 3 shows the formation energy of the nine cubic perovskites with respect to

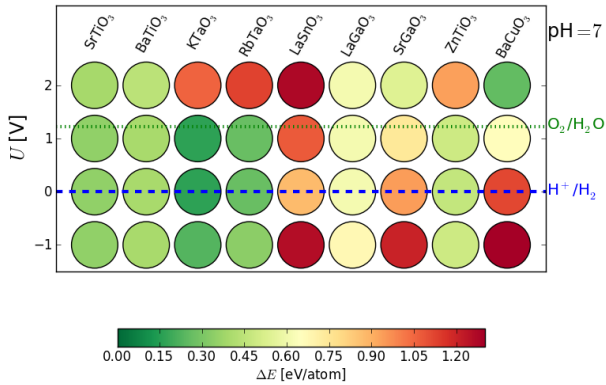


Fig. 3 Energy differences, ΔE [eV/atom] between the cubic perovskite phase and the most stable experimental known phases in which each material can separate calculated at $\text{pH} = 7$ and at a potential equal to $-1, 0, 1,$ and 2 V. The perovskites under consideration are stable in nature.

the most stable linear combinations of known solid and aqueous phases at $\text{pH} = 7$ and for four values of the potential ($-1, 0, 1,$ and 2 V). From the Nernst equation it is clear that the stability is more sensitive to variations in the potential compared to the pH . In fact, in the calculation of the free energy, the pH is scaled by the small number 0.0591 eV/ pH .

Out of the nine perovskites shown in Fig. 3, only KTaO_3 is predicted to be stable at zero potential (using an energy threshold of 0.2 eV/atom). This is in contrast to the experimental fact that most of these materials have been used for water splitting in the UV and were not found to corrode in contact with water. This indicates that the threshold of $\Delta E \leq 0.2$ eV/atom might be too strict when the effect of corrosion is taken into account. We should, however, remember that the Pourbaix diagram only assesses the thermodynamic stability while the kinetic of the reactions is not included. Thus a possible explanation for the apparent disagreement between theory and experiment could be that the materials are in fact meta stable with large barriers separating the solid and dissolved phases. It might also be that the passivation of the surface layer plays a key role in their stability in water. A few of the compounds considered become stable when the threshold is increased to 0.5 eV/atom. There is a trend of reduced stability with an increase of the potential. An increased potential stabilizes the free electrons in the material thus favoring the dissolution of the metal into free electrons at the Fermi level of the electrode and dissolved ions.

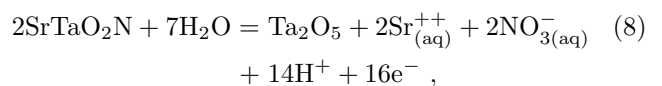
Figs. 4(a) and 4(b) show the calculated Pourbaix diagrams for SrTiO_3 and KTaO_3 . The diagrams for these

ternary compounds conserve some of the features of the diagrams of the constituent chemical elements [24]. The energy difference, ΔE , as a function of the pH and potential between the cubic perovskite and the most stable phase into which the perovskite can separate is shown in Figs. 4(c) and 4(d) for SrTiO_3 and KTaO_3 , respectively. Both the perovskites become less stable at higher and lower potentials as well as under more acidic conditions. In fact, an increase in the potential leads to the dissolution of the solid into positive ions. The amount of oxygen in the solid substance is increasing moving towards higher pH . The energy difference is thus a convex surface, called convex hull, and the region where the cubic perovskite is more favorable takes place around the red-ox potential of water. The Pourbaix diagram and the energy difference are combined in Fig. 4(e) for SrTiO_3 and in Fig. 4(f) for KTaO_3 : the colored regions represent the different phases and the energy difference is plotted along the z -axis for a range of pH and potential corresponding to that of Figs. 4(a) and 4(b).

4 Candidates for One-Photon Water Splitting

In this section, we calculate the Pourbaix diagrams for all the cubic perovskites that we have previously identified as candidates for one-photon water splitting [12]. We are mainly interested in materials that are stable at $\text{pH} \approx 7$ and potentials in the range from -1 V to 2 V covering roughly the red-ox potentials of water (the evolution of oxygen and hydrogen requires 1.23 and 0 V, respectively) and the energy barriers and overpotentials.

Fig. 5 shows the energy difference between the cubic perovskites and the most stable phases. For all the candidates there exist potentials where $\Delta E \leq 0.5$ eV/atom. As discussed earlier, when we include the dissolved phases, it might be necessary to increase the energy threshold to 0.5 eV/atom to account for metastability, kinetic of the reactions, and energy barriers between the structures. Usually, at zero potential the cubic perovskites have the highest stability. The oxides and oxyfluorides are in general stable also at higher potentials. In contrast, the oxynitrides, become unstable at higher potentials. This is due to the large number of free electrons present in the reaction and they become more stable with an increase of the potential. For example, the reaction for SrTaO_2N at $\text{pH} = 7$ and $U = 2$ V, is



with 16 electrons involved in the reaction.

Figs. 6(a) and 6(b) show the Pourbaix diagrams of AgNbO_3 and BaTaO_2N in a region of pH between 4 and 10 and potential between -3 and 3 V. As shown before in Figs. 4(a) and 4(b), the ternary diagrams largely conserve the features of the diagrams of the constituent chemical elements.

The energy differences between the perovskite and the most stable phases are shown in Figs. 6(c) and 6(d). Both have a poor stability for lower potentials. At higher potentials, the corrosion reaction for BaTaO_2N involves several electrons, similar to reaction 8, and consequently the perovskite becomes less stable. The stability of both AgNbO_3 and BaTaO_2N is almost insensitive to a change in pH in the region of investigation.

Photocorrosion

So far, we have investigated the stability against corrosion. Another related issue is the stability against photocorrosion. In fact, under high light intensity, the photo-excited electrons in the conduction band and the holes left behind in the valence band might be able to induce unwanted chemical reactions instead of merely splitting water. To simulate this non-equilibrium electron/hole distribution, we consider the stability of the materials at pH=7 and potentials -1 V (roughly corresponding to the conduction band energy) and 2 V (roughly corresponding to the valence band energy).

We find that all the candidates are less stable at potentials -1 and 2 V. In particular, the oxides become less stable at the lower potential, while, with a few exceptions, they remain stable at a potential of 2 V. The situation is the opposite for the oxynitrides which become less stable at high potential. This is due to the large number of electrons involved in the relevant reactions which makes the dissolution of the material more favourable at higher potentials. For the oxyfluorides, the change in stability due to a change in the potential is rather weak.

5 Conclusions

In the present work, we have combined density functional theory (DFT) calculations with experimental dissolution energies to construct Pourbaix diagrams for general materials in contact with water. The procedure was validated by comparing the calculated Pourbaix diagram of ZnO and TiO_2 with the experimental diagrams. Very good agreement between theory and experiment was found with only small differences arising from free energy differences between different phases on the order of less than 0.2 eV/atom.

The scheme was used to analyze the stability of a set of 23 cubic perovskites which were recently suggested as candidate materials for photo-catalytic water splitting. We have found that those perovskites are in general stable at pH = 7 and $U = 0$ V when an uncertainty of 0.5 eV/atoms on the calculated energies is taken into account. This threshold energy accounts for metastability, inaccuracy in the calculations, and for an approximate kinetic of the dissolution reaction.

To investigate the stability against photocorrosion, we have considered potentials of -1 and 2 V corresponding roughly to the conduction and valence band edges, respectively. At these potentials, all the materials were found to be less stable indicating that photocorrosion is a serious challenge for the development of efficient water splitting materials with long term stability.

Acknowledgements The authors would like to thank Prof. Jan Rossmeisl for useful discussions.

References

1. J. Greeley, T.F. Jaramillo, J. Bonde, I. Chorkendorff, J.K. Nørskov, *Nature Materials* **5**(11), 909 (2006). DOI 10.1038/nmat1752
2. S. Curtarolo, G.L.W. Hart, M.B. Nardelli, N. Mingo, S. Sanvito, O. Levy, *Nature Materials* **12**(3), 191 (2013). DOI 10.1038/nmat3568
3. G.H. Johannesson, T. Bligaard, A.V. Ruban, H.L. Skriver, K.W. Jacobsen, J.K. Nørskov, *Physical Review Letters* **88**(25), 255506 (2002)
4. A. Franceschetti, A. Zunger, *Nature* **402**, 60 (1999)
5. G. Ceder, Y.M. Chiang, D.R. Sadoway, M.K. Aydinol, Y.I. Jang, B. Huang, *Nature* **392**, 694 (1998)
6. W. Setyawan, R.M. Gaume, S. Lam, R.S. Feigelson, S. Curtarolo, *ACS Combinatorial Science* **13**(4), 382 (2011). DOI 10.1021/co200012w
7. J. Hachmann, R. Olivares-Amaya, S. Atahan-Evrenk, C. Amador-Bedolla, R.S. Sanchez-Carrera, A. Gold-Parker, L. Vogt, A.M. Brockway, A. Aspuru-Guzik, *The Journal of Physical Chemistry Letters* **2**(17), 2241 (2011). DOI 10.1021/jz200866s
8. R. Olivares-Amaya, C. Amador-Bedolla, J. Hachmann, S. Atahan-Evrenk, R.S. Sanchez-Carrera, L. Vogt, A. Aspuru-Guzik, *Energy Environ. Sci.* **4**, 4849 (2011). DOI 10.1039/C1EE02056K. URL <http://dx.doi.org/10.1039/C1EE02056K>
9. N.M. O'Boyle, C.M. Campbell, G.R. Hutchison, *Journal of Physical Chemistry C* **115**(32), 16200 (2011). DOI 10.1021/jp202765c
10. R. Armiento, B. Kozinsky, M. Fornari, G. Ceder, *Physical Review B (Condensed Matter and Materials Physics)* **84**(1) (2011)
11. I.E. Castelli, T. Olsen, S. Datta, D.D. Landis, S. Dahl, K.S. Thygesen, K.W. Jacobsen, *Energy Environ. Sci.* **5**, 5814 (2012). DOI 10.1039/C1EE02717D. URL <http://dx.doi.org/10.1039/C1EE02717D>
12. I.E. Castelli, D.D. Landis, K.S. Thygesen, S. Dahl, I. Chorkendorff, T.F. Jaramillo, K.W. Jacobsen, *Energy*

- Environ. Sci. **5**, 9034 (2012). DOI 10.1039/C2EE22341D. URL <http://dx.doi.org/10.1039/C2EE22341D>
13. A. Fujishima, K. Honda, Nature **238**(5358), 37 (1972)
 14. K. Maeda, K. Teramura, D. Lu, T. Takata, N. Saito, Y. Inoue, K. Domen, Nature **440**(7082), 295 (2006)
 15. D. Yamasita, T. Takata, M. Hara, J. Kondo, K. Domen, Solid State Ionics **172**, 591 (2004)
 16. I.E. Castelli, K.S. Thygesen, K.W. Jacobsen, MRS Online Proceedings Library **1523** (2013). DOI 10.1557/opl.2013.450. URL http://journals.cambridge.org/article_S1946427413004508
 17. ICSDWeb. http://www.fiz-karlsruhe.de/icsd_web.html
 18. Materials Project - A Materials Genome Approach. <http://materialsproject.org/>
 19. J.J. Mortensen, L.B. Hansen, K.W. Jacobsen, Physical Review B **71**(3), 35109 (2005)
 20. J. Enkovaara, C. Rostgaard, J.J. Mortensen, J. Chen, M. Dulak, L. Ferrighi, J. Gavnholt, C. Glinsvad, V. Haikola, H.A. Hansen, H.H. Kristoffersen, M. Kuisma, A.H. Larsen, L. Lehtovaara, M. Ljungberg, O. Lopez-Acevedo, P.G. Moses, J. Ojanen, T. Olsen, V. Petzold, N.A. Romero, J. Stausholm-Møller, M. Strange, G.A. Tritsarlis, M. Vanin, M. Walter, B. Hammer, H. Hakkinen, G.K.H. Madsen, R.M. Nieminen, J.K. Nørskov, M. Puska, T.T. Rantala, J. Schiøtz, K.S. Thygesen, K.W. Jacobsen, Journal of Physics Condensed Matter **22**(25), 253202 (2010). DOI doi:10.1088/0953-8984/22/25/253202
 21. B. Hammer, L.B. Hansen, J.K. Nørskov, Physical Review B (Condensed Matter and Materials Physics) **59**(1), 7413 (1999)
 22. E.D. Verink, *Simplified Procedure for Constructing Pourbaix Diagrams* (John Wiley & Sons, Inc., 2011), pp. 93–101. DOI 10.1002/9780470872864.ch7. URL <http://dx.doi.org/10.1002/9780470872864.ch7>
 23. J.W. Johnson, E.H. Oelkers, H.C. Helgeson, Computers & Geosciences **18**(7), 899 (1992). DOI 10.1016/0098-3004(92)90029-Q. URL <http://www.sciencedirect.com/science/article/pii/009830049290029Q>
 24. M. Pourbaix, *Atlas of electrochemical equilibria in aqueous solutions*. No. v. 1 in Atlas of Electrochemical Equilibria in Aqueous Solutions (Pergamon Press, 1966)
 25. K.A. Persson, B. Waldwick, P. Lazic, G. Ceder, Phys. Rev. B **85**, 235438 (2012). DOI 10.1103/PhysRevB.85.235438. URL <http://link.aps.org/doi/10.1103/PhysRevB.85.235438>
 26. F. Dionigi, P.C.K. Vesborg, T. Pedersen, O. Hansen, S. Dahl, A. Xiong, K. Maeda, K. Domen, I. Chorkendorff, Energy Environ. Sci. **4**, 2937 (2011). DOI 10.1039/C1EE01242H. URL <http://dx.doi.org/10.1039/C1EE01242H>
 27. F. Dionigi, P.C. Vesborg, T. Pedersen, O. Hansen, S. Dahl, A. Xiong, K. Maeda, K. Domen, I. Chorkendorff, Journal of Catalysis **292**(0), 26 (2012). DOI 10.1016/j.jcat.2012.03.021. URL <http://www.sciencedirect.com/science/article/pii/S0021951712000930>
 28. J. Connolly, Earth and Planetary Science Letters **236**(12), 524 (2005). DOI 10.1016/j.epsl.2005.04.033. URL <http://www.sciencedirect.com/science/article/pii/S0012821X05002839>

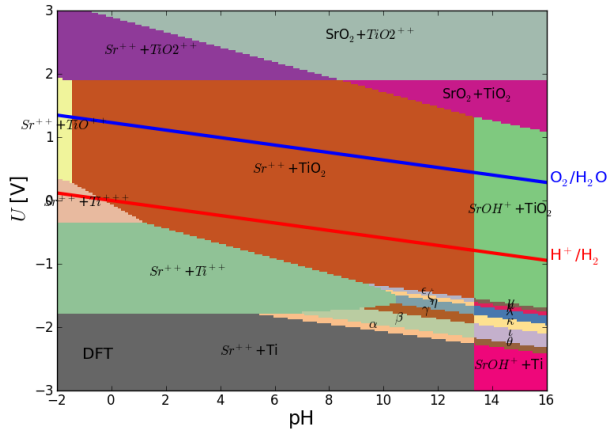
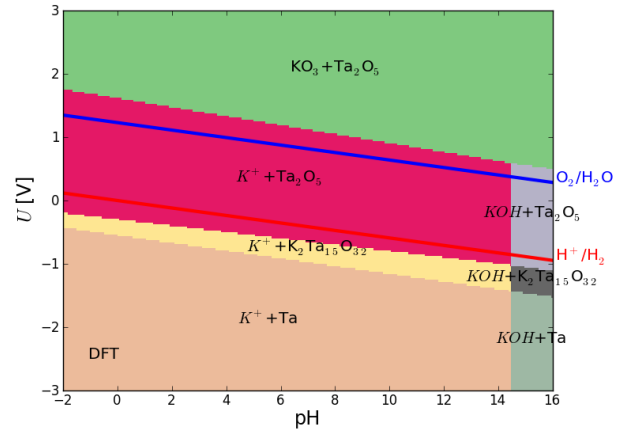
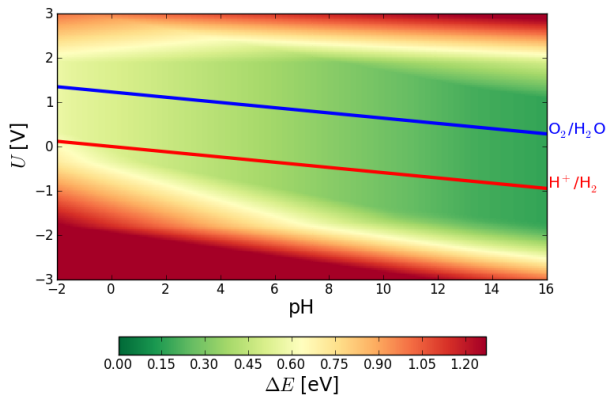
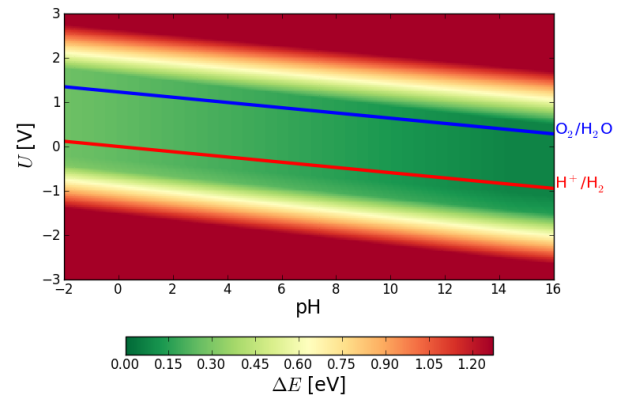
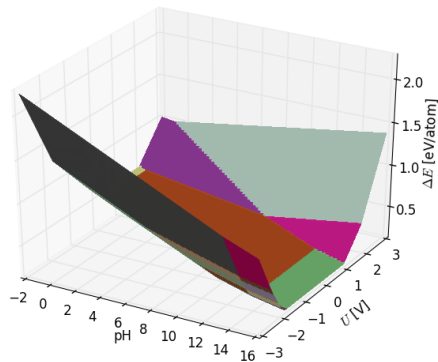
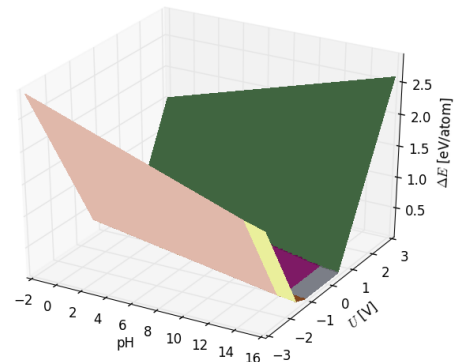
(a) SrTiO₃ - DFT(b) KTaO₃ - DFT(c) SrTiO₃ - Energy difference(d) KTaO₃ - Energy difference(e) SrTiO₃ - 3D convex hull(f) KTaO₃ - 3D convex hull

Fig. 4 Calculated Pourbaix diagrams for SrTiO₃ (a) and KTaO₃ (b). The diagrams are drawn for a concentration of 10⁻⁶ M at 25°C. The chemical formula in *italic* indicates an aqueous compound. The Greek letters in (a) indicate the phases in which SrTiO₃ splits (α : Sr⁺⁺+Ti₆O; β : Sr⁺⁺+Ti₃O; γ : Sr⁺⁺+Ti₂O; ϵ : Sr⁺⁺+Ti₃O₅; ζ : Sr⁺⁺+Ti₂O₃; η : Sr⁺⁺+TiO; θ : SrOH⁺+Ti₆O; ν : SrOH⁺+Ti₃O; κ : SrOH⁺+Ti₂O; λ : SrOH⁺+TiO; μ : SrOH⁺+Ti₂O₃; ν : SrOH⁺+Ti₃O₅). (c) and (d) show the energy differences between the cubic perovskite phases and the most stable phases for SrTiO₃ and KTaO₃, respectively. (e) and (f) combine the Pourbaix plots and the energy differences between the cubic perovskite and the most stable phase into the so-called convex hull. The colors of the different phases correspond to the ones shown in (a) and (b).

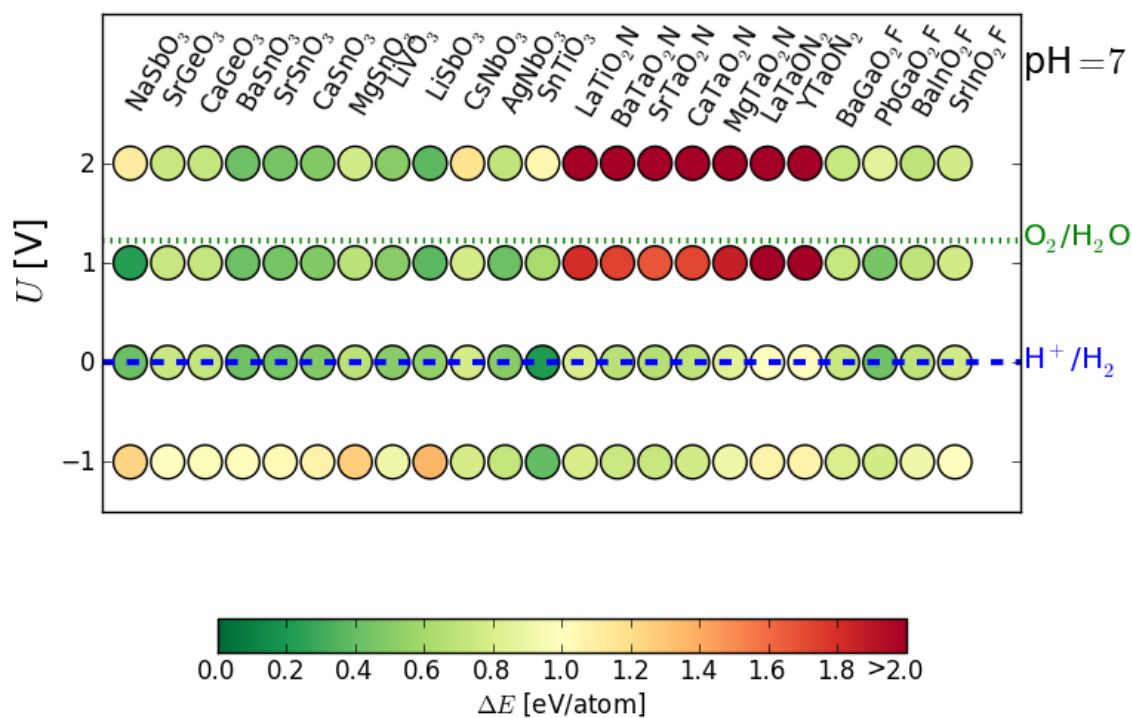


Fig. 5 Energy differences, ΔE [eV/atom] between the candidates for one-photon water splitting in cubic perovskite phases and the most stable experimental known phases in which each material can separate calculated at pH = 7 and at a potential equal to -1, 0, 1, and 2 V.

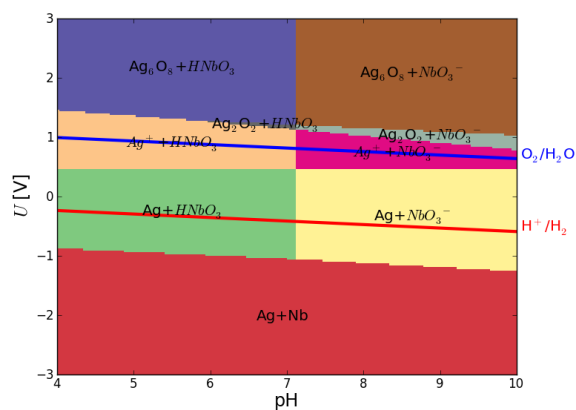
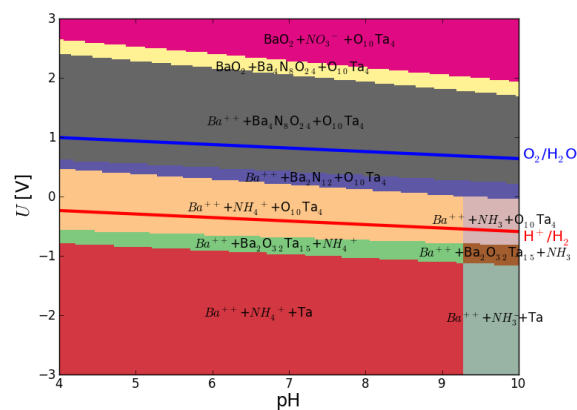
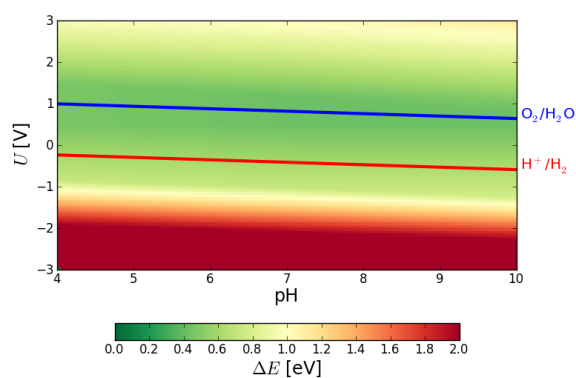
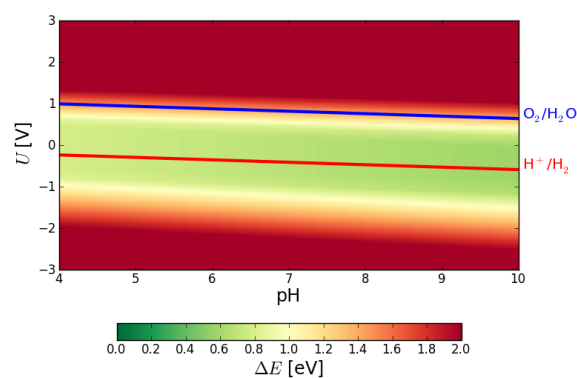
(a) AgNbO_3 - DFT(b) BaTaO_2N - DFT(c) AgNbO_3 - Energy difference(d) BaTaO_2N - Energy difference

Fig. 6 Calculated Pourbaix diagrams for AgNbO_3 ((a)) and BaTaO_2N ((b)). The diagrams are drawn for a concentration of 10^{-6} M at 25°C . The chemical formula in *italic* indicates an aqueous compound. Figs. (c) and (d) show the energy differences between the cubic perovskite phases and the most stable phases for AgNbO_3 and BaTaO_2N , respectively.

Paper VI

Stability and Bandgaps of Layered Perovskites for One- and Two-photon Water Splitting

Ivano E. Castelli, Juan María García-Lastra, Falco Hüser, Kristian S. Thygesen, and Karsten W. Jacobsen.

To be submitted, 2013.

Stability and Bandgaps of Layered Perovskites for One- and Two-photon Water Splitting

Ivano E. Castelli, Juan María García-Lastra, Falco Hüser,
Kristian S. Thygesen, and Karsten W. Jacobsen

Center for Atomic-scale Materials Design, Department of Physics, Technical
University of Denmark, DK - 2800 Kongens Lyngby, Denmark.

E-mail: ivca@fysik.dtu.dk

Abstract. Direct production of hydrogen from water and sun light requires stable and abundantly available semiconductors with well positioned band edges relative to the water red-ox potentials. We have used density functional theory (DFT) calculations to investigate 300 oxides and oxynitrides in the Ruddleson-Popper phase of the layered perovskite structure. Based on screening criteria for the stability, bandgaps and band edge positions, we suggest 20 new materials for the light harvesting photo-electrode of a one-photon water splitting device and 5 anode materials for a two-photon device with silicon as photo anode. In addition, we explore a simple rule relating the bandgap of the perovskite to the number of octahedra in the layered structure and the B-metal ion. Finally, the quality of the GLLB-SC potential used to obtain the bandgaps is validated against $G_0W_0@LDA$ gaps for 20 previously identified oxides and oxynitrides in the cubic perovskite structure.

PACS numbers: 71.20.Mq, 71.20.Nr, 82.47.Jk

Submitted to: *New J. Phys.*

1. Introduction

The direct conversion of solar light into chemical fuels through electrochemical reactions represents a clean, sustainable and potentially cheap alternative to fossil fuels. The simplest reaction of this kind is the water splitting reaction in which water is split into hydrogen and oxygen. In the most basic photo-electrochemical device, each photon is harvested by a single semiconductor and the created electron-hole pair is used to evolve hydrogen and oxygen. The maximum efficiency of such a one-photon device is only around 7% when overpotential of the reactions and losses are accounted for [1]. Significantly higher energy conversion efficiencies of up to 27% [2] can be achieved using a combination of two or more semiconductors with appropriately aligned band edges.

First attempts of photocatalytic water splitting were made in the 70s using TiO_2 as the light harvesting and hydrogen evolving material [3]. Due to the large bandgap of TiO_2 and its poor catalytic properties the devices had extremely low efficiencies. Since then several materials have been proposed as light harvesting photo-electrodes for water splitting both in the UV and in the visible range REFS to review. Still, the efficiencies of the water splitting devices are significantly lower than the alternative combination of electrolysis driven by standard photovoltaic cells.

The search for new materials can be guided by *ab-initio* quantum mechanical calculations, avoiding expensive “trial and error” experimental processes. Recently, high-throughput materials design of stable binary and ternary alloys [4], carbon capture and storage [5], batteries [6], photovoltaic [7, 8] and water splitting materials [9, 2] have been reported. A number of databases have been also implemented to store and to analyze the huge amount of computed data generated. Some examples are the Materials Project database [10], the AFLOWLIB consortium [4] and the Computational Materials Repository [11].

In previous studies [9, 2], we have investigated the cubic perovskite structure and proposed 20 materials for the one-photon water splitting process and 12 others for the anode in a two-photon device with a Si cathode. Several of those were unknown in the water splitting community, but some of them have been already successfully tested. In particular the oxynitrides, like BaTaO_2N , SrTaO_2N , CaTaO_2N , LaTiO_2N , and LaTaON_2 , gives good results in term of oxygen and/or hydrogen evolution in presence of sacrificial agent [12].

The perovskite is a very versatile structure with a large variety of properties and applications [13]. In addition to the standard cubic and low-symmetry perovskites, two cubic perovskites with general formula ABO_3 can be combined together in the so-called double perovskite [14]. The double perovskite structure was recently explored with the focus of finding new materials for water splitting and engineering of the bandgap by combining two perovskites with different electronic properties [15].

In the present work, we investigate the layered perovskite structure. A layered perovskite is composed of 2D slabs of ABO_3 cubic perovskite separated by a motif of metal atoms. There are several phases of layered perovskites which differ in the thickness

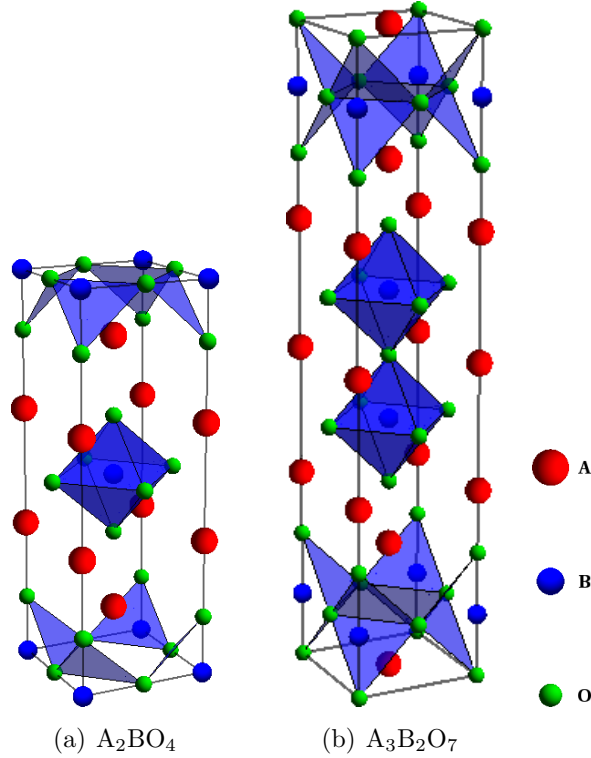


Figure 1. Crystal structure of the Ruddlesden-Popper phase with $n = 1$ (a) and $n = 2$ (b).

and the relative displacement of the cubic perovskite slabs and in the motifs. The phase studied here is the Ruddlesden-Popper with general formula $A_{n-1}B_nO_{3n+1}$, where n is the number of BO_6 octahedra forming the 2D slabs. We consider the cases of $n = 1$ and $n = 2$ (A_2BO_4 and $A_3B_2O_7$, respectively) and one oxygen replacement in favor of nitrogen in the case of $n = 1$ (A_2BO_3N).

2. Method

In the one-photon water splitting device, one material is responsible for the evolution of both oxygen and hydrogen. First a photon is harvested creating an electron-hole pair. Next, the electron and hole reach two different points on the surface where the evolution of O_2 and H_2 takes place. Any material that should function as photo-electrode for water splitting should meet a number of criteria: (i) chemical and structural stability (ii) a bandgap in the visible range (iii) well positioned band edges with respect to the red-ox levels of water (iv) high mobility for electrons and holes. In addition, low cost and non-toxicity are required. Here we focus on the criteria (i)-(iii).

The stability of a material is evaluated with respect to around 2000 reference systems. The reference systems constitute stable phases of the possible materials into which the considered layered perovskite can be decomposed, and are taken from the experimental ICSD database [16] and the Materials Project database [10]. A

material is considered stable only if the energy difference between the layered perovskite phase and the most stable alternative combination of reference systems is below 0.2 eV/atom. We use this finite threshold energy in order not to exclude potential candidates due to inaccuracies in the calculations and the possible metastability of the investigated structure. Each combination is fully relaxed using the RPBE functional [17] implemented in the DFT-GPAW code [18, 19].

As an example, the stability of the $\text{Ba}_2\text{TaO}_3\text{N}$ compound is given by:

$$\Delta E = \text{Ba}_2\text{TaO}_3\text{N} - \min_{c_i} \left\{ c_1 \text{Ba}_2 + c_2 \text{Ta}_2 + c_3 \text{BaO} + c_4 \text{BaO}_2 + c_5 \text{Ta}_2\text{O}_5 + c_6 \text{BaN}_6 + c_7 \text{Ta}_3\text{N}_5 + c_8 \text{Ba}_2\text{Ta}_3\text{N}_3 + c_9 \text{BaTaO}_2\text{N} + c_{10} \text{N}_2 + c_{11} \text{O} \right\}, \quad (1)$$

where c_i are positive and sum up to assure the correct stoichiometry of the $\text{A}_2\text{BO}_3\text{N}$ layered structure and the chemical formulas indicate the DFT total energies of the references. All the references are in their solid state phase except for N_2 and O which are in the gas phase. Note that the energy of oxygen is calculated from H_2 and H_2O due to the well problems associated with the DFT description of the O_2 triplet ground-state.

We note that the present stability analysis does not include corrosion of the materials. Extended stability analysis including this effect were recently found to be of some importance [20, 21]. However, we leave this to a future study.

It is well known that the Kohn-Sham eigenvalues from DFT systematically underestimate bandgaps of extended semiconductors due to the approximate nature of the exchange-correlation functionals and the missing derivative discontinuity [22, 23]. On the other hand, many-body methods like the GW approximation give better bandgaps, but are computationally too expensive to be used in a screening project of several hundred materials. Here, we used the GLLB-SC potential [24, 25], which includes an explicit estimation of the derivative discontinuity. In a previous work [9], the GLLB-SC bandgaps of around 40 metal oxides were compared to experiments. On average the GLLB-SC band gaps were found to lie within 0.5 eV of the experimental gaps.

Figure 2 shows the bandgaps of the 20 identified cubic perovskites for one-photon water splitting [2] obtained using different methods and xc-functionals. Standard DFT functionals, like LDA and PBE (not shown in the figure), seriously underestimate the bandgap, while the hybrid PBE0 (not shown) tend to overestimate the gaps. We have performed G_0W_0 [26] calculations using a recent implementation in the GPAW code. In these calculations the G_0W_0 self-energy is evaluated using LDA energies and wave functions and the frequency dependence of the dielectric function is fitted to a plasmon pole model. We use a 150 eV plane wave cut off for the representation of the dielectric matrix and include empty bands up to the same energy cut off. A $7 \times 7 \times 7$ k-point mesh is used for both DFT and G_0W_0 calculations.

The GLLB-SC and G_0W_0 bandgaps are quite similar with a mean absolute difference of 0.3 eV. This is consistent with the results of a similar comparison made for

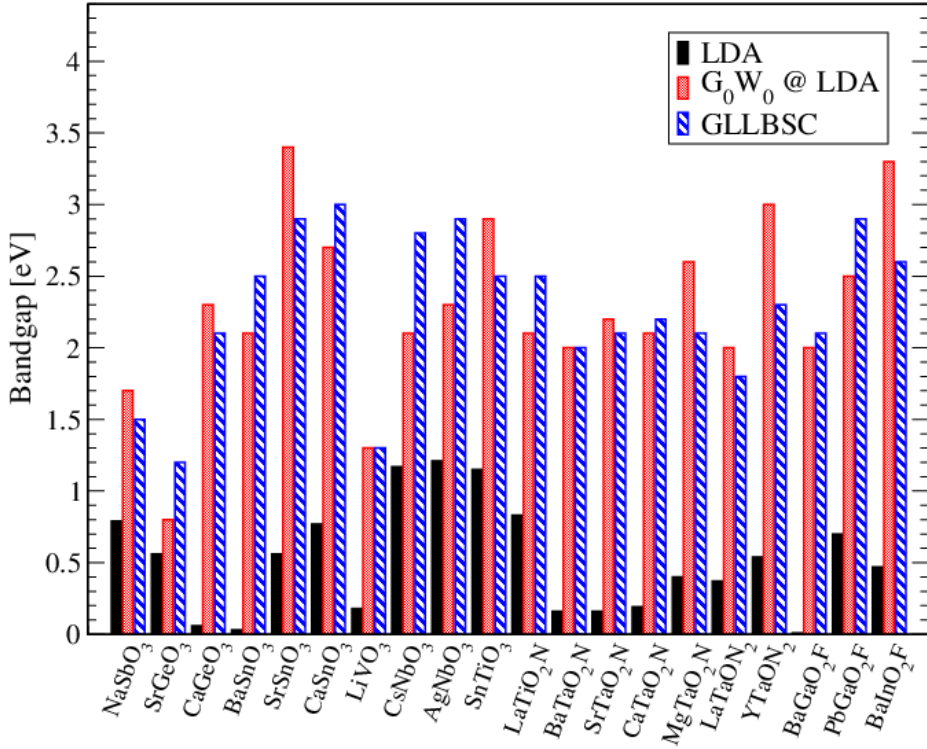


Figure 2. The bandgaps of the 20 identified candidates for one-photon water splitting calculated with the GLLB-SC potential (in blue) $G_0W_0@LDA$ (in red), and LDA (in black). The agreement between the GLLB-SC potential and G_0W_0 is very good.

a set of ten well characterized simple semiconductors and insulators [26]. Based on this we conclude that the bandgaps obtained with the GLLB-SC are sufficiently accurate for the purpose of materials screening.

In addition to the bandgap, the position of the conduction and valence band edges with respect to the water red.ox levels is crucial: The energy of electrons at the surface should be above the hydrogen evolution potential and the energy of holes must be below the oxygen evolution level. It is not trivial to calculate the band edge positions at a semiconductor-water interface from first principles. Although some methods have been proposed [27, 28], they are computationally rather demanding and not suited for screening studies. Instead we obtain the position of the band edges simply using an empirical equation [29, 30] that gives the center of the bandgap in terms of the geometrical average of the electronegativities in the Mulliken scale of the pure chemical elements, χ_M , forming the compound. The band edge positions are then calculated by adding and subtracting half of the bandgap, E_{gap} . In formula, for the A_2BO_4 layered perovskite:

$$E_{\text{VB, CB}} = E_0 + (\chi_A^2 \chi_B \chi_O^4)^{1/7} \pm E_{\text{gap}}/2, \quad (2)$$

where E_0 is the difference between the normal hydrogen electrode (NHE) and the vacuum ($E_0 = -4.5$ eV). More details about the method and its validation are available

in refs. [9, 2].

It has been recently shown for the cubic perovskite structure [31], that the search for new materials can be guided using chemical-based rules. The three chemical rules used here are:

- Valence balance rule: in a realistic material, the sum of the possible oxidation states of its element must be zero.
- Even-odd electrons rule: a material with an odd number of electrons has partially-occupied bands at the Fermi level and is thus a metal. There are some exceptions to this rule, but they correspond to magnetic and/or strongly correlated materials which require more advanced theoretical descriptions than the one used here.
- Ionic radii of the atoms: the metals that can occupy the A- and B-ion position in the perovskite depends on the ionic radii of the neutral atom. Usually alkali and alkaline earth metals occupy the A-ion side, and post-transition metals the B-ion position [13].

The use of these rules drastically reduce the number of calculations (up to 60% in the already mentioned case of the oxo-perovskites) since only materials that fulfill the first two rules needs to be considered. The last rule determine which metals from the periodic table can occupy the A and B sites[‡]. With these constrains, it is possible to reduce the search space from around 8000 to 300 different materials.

Criterion	One-photon WS	Two-photon WS
Stability (ΔE)	0.2 eV/atom	0.2 eV/atom
Bandgap (E_{gap})	$1.7 \leq E_{\text{gap}} \leq 3$	$1.3 \leq E_{\text{gap}} \leq 3$
Band edges	$\text{VB}_{\text{edge}} > 1.6$	$\text{VB}_{\text{edge}}^{\text{anode}} > 1.6$
($\text{VB}_{\text{edge}}, \text{CB}_{\text{edge}}$)	$\text{CB}_{\text{edge}} < -0.1$	$\text{CB}_{\text{edge}}^{\text{cathode}} < -0.1$
		$\text{CB}_{\text{edge}}^{\text{anode}} < \text{VB}_{\text{edge}}^{\text{cathode}}$

Table 1. Screening parameters (in eV) used for the one- and two-photon water splitting (WS) devices. The red-ox levels of water with respect to the Normal Hydrogen Electrode (NHE) are 0 and 1.23 eV for the hydrogen and oxygen evolution, respectively. The criterion for the position of the band edges include also the overpotentials for hydrogen (0.1 eV) and for oxygen (0.4 eV) [32]. Silicon is used as cathode in the two-photon water splitting device ($\text{VB}_{\text{edge}}^{\text{Si}} = 0.86$ eV).

The screening parameters for the one-photon water splitting device are summarized in Table 1. In addition to stability and a band gap in the visible range, the band edges should straddle the red-ox levels of water plus the required overpotentials (0.1 eV for hydrogen and 0.4 eV for oxygen [32]).

[‡] The metals used in the A-ion position are: Li, Na, Mg, K, Ca, Ga, Ge, Rb, Sr, Y, Ag, Cd, In, Sn, Cs, Ba, La, Tl, and Pb. The B-metals are Al, Sc, Ti, V, Cr, Mn, Fe, Co, Ni, Cu, Zn, Ga, Ge, Zr, Nb, Mo, Ru, Rh, Pd, In, Sn, Sb, Te, Hf, Ta, W, Re, Os, Ir, Pt, and Bi.

The ideal efficiency of the one-photon device can be up to 7% [1]. Higher efficiencies can be achieved using a two-photon, or tandem, device, consisting of two semiconductors forming a pn-junction. Electrons generated in the anode move to the surface and evolve hydrogen while the holes move towards the pn-junction and recombine with electrons from the cathode. Similarly, the holes generated in the cathode move towards the surface and evolve oxygen. Thus it takes two photons to generate one H_2 . The efficiency of the device depends strongly on the relative sizes of the bandgaps of the two materials. Assuming ideal band edge line up, the best performance (around 25%) is obtained by combining two materials with bandgaps of 1.1 eV and 1.7 eV, respectively [2]. The sum of the two bandgaps should not be smaller than 2.8 eV: 1.23 eV is the energy required per electron to split water and approximately 0.5 eV is required to account for the overpotentials of the oxidation and reduction reactions. In addition, the relevant quasi Fermi levels are located 0.25 eV below (above) the conduction (valence) bands. Finally, the quasi Fermi level corresponding to the conduction band of the cathode should be at least 0.1 eV above the quasi Fermi level corresponding to the valence band of the anode to ensure efficient charge recombination at the interface. As it turns out, silicon is an ideal photo-cathode for water splitting since it has a bandgap of 1.1 eV well positioned with respect to the reduction potential of hydrogen and because of the mature fabrication technology. In the case of two-photon devices we therefore limit our search to photo-anode materials assuming a silicon anode and use the screening criteria summarized in Table. 1.

3. Trends in Stability and Bandgaps

The simplest layered perovskite is the Ruddleson-Popper phase. The two phases studies here have the general formula A_2BO_4 and $A_3B_2O_7$. The former is composed of slabs of cubic perovskite ABO_3 offset by a translation of $(1/2, 1/2)$ with respect to each other and separated by a layer of A metal atoms. In the latter structure each slab of perovskite is formed by two octahedra BO_6 units. The unit cells of the two phases contain 14 and 24 atoms, respectively. The A-ion position is generally occupied by a alkali and alkali-earth metal, and the B-ion by a transition or post-transition metal. Materials of the form A_2BO_3N , in which an oxygen atom has been replaced by nitrogen, have been considered. In general, oxides tend to have valence band edges that are somewhat deep compared to the oxidation potential of water. Nitrogen is slightly less electronegative compared to oxygen and the valence bands of the oxynitrides are consequently shifted up compared to the oxides [33]. The smaller electronegativity of nitrogen leads also to a reduction in the size of the bandgaps. In addition, a nitrogen replacement breaks the symmetry of the cubic perovskite and creates an excess of charge in one of the corners of the octahedron. This leads to a reduction in the stability of the obtained materials, as shown in Fig. 3.

Fig. 3 shows the calculated heat of formation for the A_2BO_4 , A_2BO_3N , and $A_3B_2O_7$ perovskites plotted against the GLLB-SC bandgap. The bandgaps of both types of

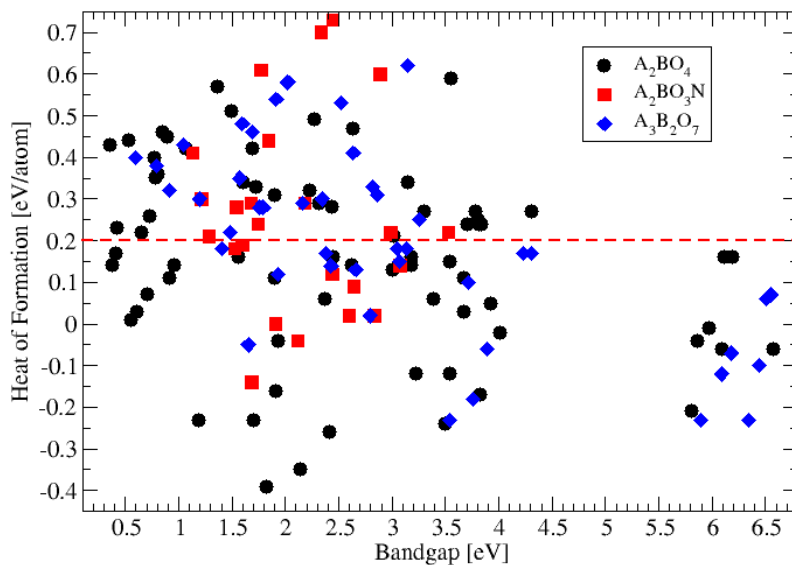


Figure 3. Calculated heat of formation plotted versus bandgap for the A_2BO_4 (black circles), A_2BO_3N (red squares), and $A_3B_2O_7$ (blue diamonds). The oxides show high stability and a wide range of bandgaps. The oxynitrides are overall less stable and have smaller bandgaps than the oxides.

oxides range from zero to above 6 eV. The oxides are in general highly stable especially the materials with larger bandgaps. As expected, the oxynitrides are less stable and show smaller gaps. Despite of this, around 8 oxynitrides are found to fulfill the criteria on bandgap and stability for the one-photon water splitting device. A further nitrogen replacement is likely to lower the band gaps and reduce the stability even further [2], and therefore has not been investigated here.

All the bandgaps of the stable A_2BO_4 layered perovskites are plotted in Fig. 4. There is some degree of correlation between the chemical elements and the size of the band gaps. First of all it can be seen that the gap is mainly determined by the B-ion while the A-ion has little influence. Hf and Zr in the B-ion position generate large bandgap insulators with a gaps above 6 eV. Ti, Ge, and Sn lead to structures with gaps above 3 eV while W and Zn produce structures with gaps around 2 eV.

Most of the oxides investigated have valence bands formed by the 2p levels of the O^{2-} ions. Since the nature of the bonds in these materials is highly ionic, this implies that the top of the valence band is roughly the same for all the oxides[§]. The conduction

[§] There are some exceptions to these rule, e.g those compounds that contain carbon group ions with valence 2+ (Ge^{2+} , Sn^{2+} and Pb^{2+}), in which the valence band is a mix between the 2p levels of the O^{2-} ions and the s levels of the carbon group ion.

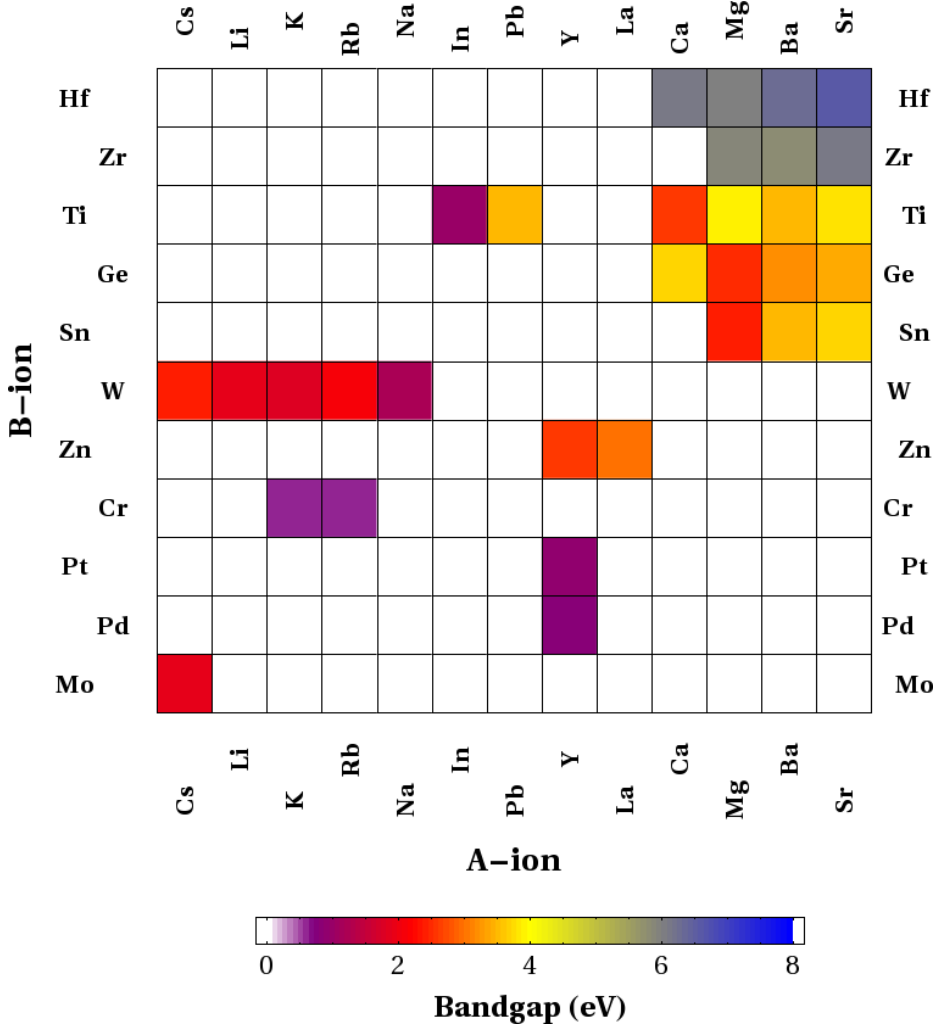


Figure 4. Bandgaps of the stable compounds in the A_2BO_4 structure. The gaps range from zero to more than 6 eV. The chemical elements are sorted for similarity so that atoms that generate layered perovskites with similar bandgaps are close together.

bands are mainly composed of the lowest unoccupied molecular orbitals (LUMO) of the A and B metal ions. This means that the size of the bandgap should correlate with the lowest lying LUMO level of the A and B cations. The relevant LUMO level is, however, not that of the cations in vacuum, but rather a cation sitting in the electrostatic field from the rest of lattice, V_R . This is done following an Ewald-Evjen scheme, assuming that all the ions keep their nominal charges. This scheme is described elsewhere in the literature [34].

Table 2 shows how the LUMO energies change drastically passing from the free cations to the cations under the effect of V_R . V_R destabilizes much more the energies of the B site ions than the ones of A site ions. This is due to the short distance between the O^{2-} and A ions (usually in a range from 1.9 to 2.3 Å) in comparison with the B- O^{2-} distances (in a range from 2.5 to 3.0 Å). The table shows the correlation between

B-ion	In vacuum	V_R	Bandgap		
			Ca ₂ BO ₄	Sr ₂ BO ₄	Cd ₂ BO ₄
Ti ⁴⁺ (d)	-56.13	-3.35	4.01	3.82	0.78
Zr ⁴⁺ (d)	-42.30	-1.24	6.19	6.09	1.90
Hf ⁴⁺ (d)	-39.90	-1.10	6.11	6.57	1.60
Ge ⁴⁺ (s)	-52.28	-3.64	3.67	3.39	0.36
Sn ⁴⁺ (s)	-45.45	-3.82	3.70	3.67	0.54

Table 2. LUMO energies (in eV) of several B⁴⁺ ions in vacuum and in the presence of the crystal electrostatic field V_R , respectively. V_R is calculated for ASnO₄ and CaBO₄ for the A²⁺ and B⁴⁺ ions respectively (similar results are obtained for other lattices). The LUMO energies of the A²⁺ ions in vacuum and under the effect of V_R are for Ca²⁺ (s): -14.65 and -0.58; for Sr²⁺ (s): -13.58 and -1.02; for Cd²⁺ (s): -20.35 and -4.91. The bandgaps of the compounds containing these ions are also shown for comparison.

the lowest LUMO energy from A and B (under the effect of V_R) ions and the bandgap for the particular case of (A²⁺)₂B⁴⁺(O²⁻)₄ perovskites. The LUMO of the B⁴⁺ ions is more stable than the LUMO of the A²⁺ ions when the A position is occupied by an alkaline-earth ion (in the table only the results for Ca²⁺ and Sr²⁺ are shown, but similar features are observed for Mg²⁺ and Ba²⁺). Thus, in these cases the bandgap is correlated with the LUMO of the B ion. This explains why Zr⁴⁺ and Hf⁴⁺ compounds have similar gaps, whereas Ti⁴⁺ shows a smaller gap. This could be understood even just by looking at the energies of the ions in vacuum, since the d-levels of Ti⁴⁺ are much deeper in energy than those of Zr⁴⁺ and Hf⁴⁺. This difference is strongly reduced when V_R is considered due to the smaller ionic radius of Ti⁴⁺ (10 pm smaller than Zr⁴⁺ of Hf⁴⁺ ionic radii [35]), which has O²⁻ ions closer. In the case of the carbon group (Ge⁴⁺ and Sn⁴⁺), their compounds have similar bandgaps due to a compensation of effects: Ge⁴⁺ s level in vacuum is lower in energy than Sn⁴⁺ s level (by ≈ 7 eV), but Ge⁴⁺ ionic radii is 16 pm smaller than that of Sn⁴⁺.

When Cd²⁺ occupies the A site, its LUMO (the s level) is more stable than the LUMO of B⁴⁺ ions, contrary to the case of an alkaline-earth on A position. This leads to compounds with a conduction band dominated by the Cd²⁺ s level and consequently to a small bandgap. A similar investigation has been performed also for the A₃B₂O₇ layered perovskites with similar results. Since nitrogen has an electronegativity very close to the one of oxygen, we expect that these results are still valid for the oxynitrides. The main difference will be that the valence band is formed by an hybridization of the oxygen and nitrogen 2p orbitals.

A couple of A- and B-ions can be used for both the A₂BO₄ and the A₃B₂O₇ perovskites. For these cases, we have investigated the changes in the size of the bandgaps depending on the number of octahedra forming the 2D slab. There is a weak trend that correlates the bandgaps to the B-ions: when the B-ion position is occupied by a *p*-metal

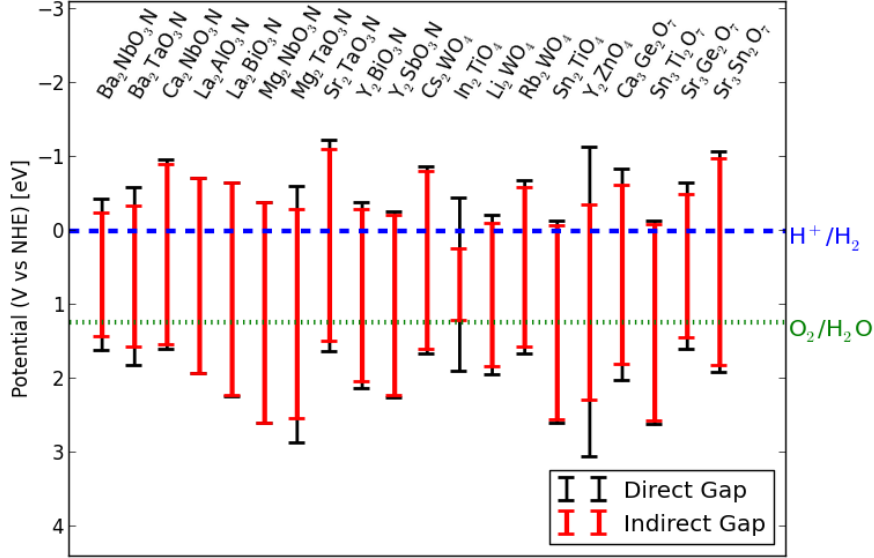


Figure 5. The identified candidates in the Ruddleson-Popper phases for one-photon water splitting. The figure shows the red-ox levels of water and the calculated band edges for the indirect (red) and direct (black) bandgaps.

(e.g. Ge and Sn) the gaps are generally reduced when the slab thickness is increased, while for d -metals (e.g. Ti, Zr, and Hf), the gaps seem to increase with slab thickness. This observation could be used to tune the bandgap by increasing or reducing the number of octahedra within the layers.

4. Candidates for Water Splitting

The screening criteria of Table 1 have been applied to the calculated structures. Out of the 30 investigated materials 20 fulfill the criteria for one-photon water splitting, see Fig. 5. $\text{Ba}_2\text{TaO}_3\text{N}$ and $\text{Sr}_3\text{Sn}_2\text{O}_7$ are known to exist experimentally in the layered perovskite structure. $\text{Ba}_2\text{TaO}_3\text{N}$ has also recently been proposed as a water splitting material by Wu *et al.* [36] who used a computational screening procedure similar to the one proposed here. $\text{Y}_2\text{BiO}_3\text{N}$ and the other $\text{A}_3\text{B}_2\text{O}_7$ compounds are already known in other stoichiometries and most of the A_2BO_4 materials and $\text{Sr}_2\text{TaO}_3\text{N}$ have been synthesized in other crystal structures with the same stoichiometry as the layered perovskite. 8 of the identified perovskites have not been investigated experimentally to our knowledge. In particular, the oxynitrides are interesting candidates for water splitting. In fact, the cubic perovskites ABO_2N with $\text{A} = \text{Ba}, \text{Sr}, \text{and Ca}$, and $\text{B } x = \text{Ta, and Nb}$ are known to evolve hydrogen and/or oxygen in the presence of a sacrificial agent [12, 37]. We expect that the layered perovskites containing these elements conserve

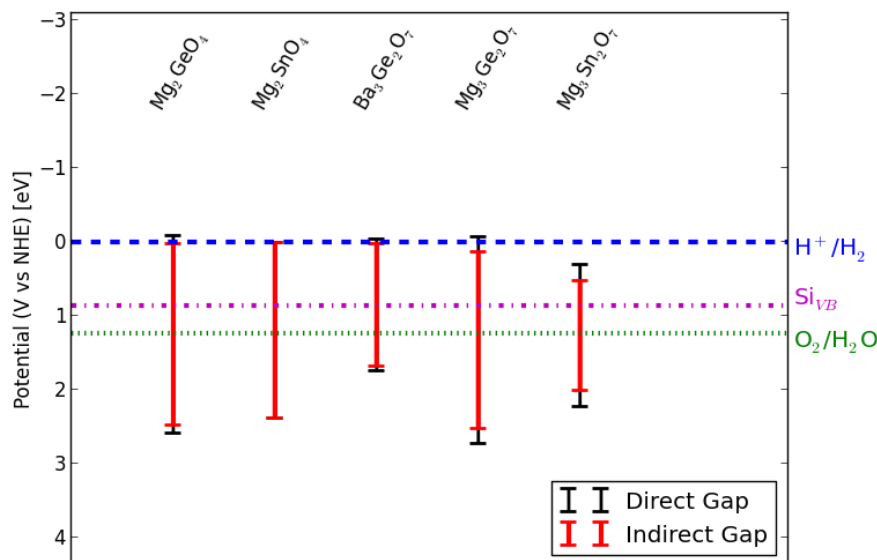


Figure 6. The identified candidates in the Ruddleson-Popper phases for two-photon water splitting device. The figure shows the red-ox levels of water and the valence band of silicon. The calculated band edges for the indirect (red) and direct (black) bandgaps are drawn.

the good properties in terms of activity already present in the cubic phase.

For the two-photon device with a silicon anode, our screening identifies five layered perovskites as candidates for cathode material. All five are experimentally known in other structures/stoichiometry, but none of them has been used so far as photocatalyst.

5. Conclusions

With the aim of identifying stable and abundantly available semiconductors for light harvesting photo-electrodes for water splitting, we have screened 300 oxides and oxynitrides in the layered perovskite structure with stoichiometry A_2BO_4 , $A_3B_2O_7$, and A_2BO_3N . The stability and bandgaps were calculated using density functional theory and the band edge alignment relative to the water red-ox potentials was estimated using an empirical formula. The accuracy of the calculated bandgaps, which were obtained with the GLLB-SC potential, was validated by comparing with state of the art G_0W_0 calculations for 20 oxides in the cubic perovskite structure.

We have identified 20 candidate materials for one-photon water splitting, and additional 5 materials for photo-cathode in a two-photon device with a silicon anode. A few of these materials are already experimentally known, but none of them have been used so far for photoelectrocatalysis.

The trends in stability and bandgap has been studied in some detail. We have found that the bandgap of the layered perovskites is mainly determined by the position of the most stable LUMO of the A- and B-ion. Furthermore, our results indicate that the bandgap can be tuned to some extent by varying the number of octahedra forming the layered structure. Specifically, for a *d*-metal (*p*-metal) at the B-ion position the effect is to increase (decrease) the gap with the number of octahedra within a layer.

Acknowledgments

The authors acknowledge support from the Catalysis for Sustainable Energy (CASE) initiative funded by the Danish Ministry of Science, Technology and Innovation, and from the Center on Nanostructuring for the Efficient Energy Conversion (CNEEC) at Stanford University.

References

- [1] M. R. Weber and M. J. Dignam. Splitting water with semiconducting photoelectrodes - efficiency considerations. *Int. J. Hydrogen Energy*, 11(4):225–232, 1986.
- [2] Ivano E. Castelli, David D. Landis, Kristian S. Thygesen, Soren Dahl, Ib Chorkendorff, Thomas F. Jaramillo, and Karsten W. Jacobsen. New cubic perovskites for one- and two-photon water splitting using the computational materials repository. *Energy Environ. Sci.*, 5:9034–9043, 2012.
- [3] A Fujishima and K Honda. Electrochemical photolysis of water at a semiconductor electrode. *Nature*, 238(5358):37–38, July 1972.
- [4] Stefano Curtarolo, Wahyu Setyawan, Gus L.W. Hart, Michal Jahnatek, Roman V. Chepulskii, Richard H. Taylor, Shidong Wang, Junkai Xue, Kesong Yang, Ohad Levy, Michael J. Mehl, Harold T. Stokes, Denis O. Demchenko, and Dane Morgan. Aflow: An automatic framework for high-throughput materials discovery. *Computational Materials Science*, 58(0):218 – 226, 2012.
- [5] Li-Chiang Lin, Adam H. Berger, Richard L. Martin, Jihan Kim, Kuldeep Swisher, Joseph A. and Jariwala, Chris H. Rycroft, Michael W. Bhowm, Abhoyjit S. and Deem, Maciej Haranczyk, and Berend Smit. In silico screening of carbon-capture materials. *Nat Mater*, 11(7):633–641, 2012.
- [6] G Ceder, Y-M Chiang, D R Sadoway, M K Aydinol, Y-I Jang, and B Huang. Identification of cathode materials for lithium batteries guided by first-principles calculations. *Nature*, 392:694, April 1998.
- [7] Johannes Hachmann, Roberto Olivares-Amaya, Sule Atahan-Evrenk, Carlos Amador-Bedolla, Roel S. Sanchez-Carrera, Aryeh Gold-Parker, Leslie Vogt, Anna M. Brockway, and Alan Aspuru-Guzik. The harvard clean energy project: Large-scale computational screening and design of organic photovoltaics on the world community grid. *The Journal of Physical Chemistry Letters*, 2(17):2241–2251, 2011.
- [8] Mayeul d’Avezac, Jun-Wei Luo, Thomas Chanier, and Alex Zunger. Genetic-algorithm discovery of a direct-gap and optically allowed superstructure from indirect-gap si and ge semiconductors. *Phys. Rev. Lett.*, 108:027401, Jan 2012.
- [9] Ivano E. Castelli, Thomas Olsen, Soumendu Datta, David D. Landis, Soren Dahl, Kristian S. Thygesen, and Karsten W. Jacobsen. Computational screening of perovskite metal oxides for optimal solar light capture. *Energy Environ. Sci.*, 5:5814, 2012.
- [10] Materials Project - A Materials Genome Approach. <http://materialsproject.org/>.

- [11] Computational Materials Repository. <https://wiki.fysik.dtu.dk/cmr/> (Documentation) and <https://cmr.fysik.dtu.dk/> (Database).
- [12] D Yamasita, T Takata, M Hara, JN Kondo, and Kazunari Domen. Recent progress of visible-light-driven heterogeneous photocatalysts for overall water splitting. *Solid State Ionics*, 172:591–595, 2004.
- [13] Tatsumi Ishihara. *Perovskite Oxide for Solid Oxide Fuel Cells*. Springer Verlag, June 2009.
- [14] K.-I. Kobayashi, T. Kimura, H. Sawada, K. Terakura, and Y. Tokura. Room-temperature magnetoresistance in an oxide material with an ordered double-perovskite structure. *Nature*, 395:677–680, 1998.
- [15] Ivano E. Castelli, Kristian S. Thygesen, and Karsten W. Jacobsen. Bandgap engineering of double perovskites for one- and two-photon water splitting. *MRS Online Proceedings Library*, 1523, 0 2013.
- [16] ICSDWeb. http://www.fiz-karlsruhe.de/icsd_web.html.
- [17] Bjørk Hammer, L B Hansen, and J K Nørskov. Improved adsorption energetics within density-functional theory using revised Perdew-Burke-Ernzerhof functionals. *Physical Review B (Condensed Matter and Materials Physics)*, 59(1):7413–7421, March 1999.
- [18] J J Mortensen, L B Hansen, and K W Jacobsen. Real-space grid implementation of the projector augmented wave method. *Physical Review B*, 71(3):35109, January 2005.
- [19] J. Enkovaara, C Rostgaard, J J Mortensen, J Chen, M. Dulak, L Ferrighi, J Gavnholt, C Glinsvad, V Haikola, H A Hansen, H H Kristoffersen, M. Kuisma, A H Larsen, L Lehtovaara, M Ljungberg, O Lopez-Acevedo, P G Moses, J Ojanen, T Olsen, V Petzold, N A Romero, J Stausholm-Møller, M Strange, G A Tritsarlis, M Vanin, M Walter, Bjørk Hammer, H. Hakkinen, G K H Madsen, R M Nieminen, J K Nørskov, M Puska, T T Rantala, J Schiotz, K S Thygesen, and K W Jacobsen. Electronic structure calculations with GPAW: a real-space implementation of the projector augmented-wave method. *Journal of Physics Condensed Matter*, 22(25):253202, 2010.
- [20] Kristin A. Persson, Bryn Waldwick, Predrag Lazic, and Gerbrand Ceder. Prediction of solid-aqueous equilibria: Scheme to combine first-principles calculations of solids with experimental aqueous states. *Phys. Rev. B*, 85:235438, Jun 2012.
- [21] Ivano E. Castelli, Kristian S. Thygesen, and Karsten W. Jacobsen. Calculated pourbaix diagrams of cubic perovskites for water splitting: A critical stability analysis. *Submitted*, 2013.
- [22] John P. Perdew and Mel Levy. Physical content of the exact kohn-sham orbital energies: Band gaps and derivative discontinuities. *Phys. Rev. Lett.*, 51:1884–1887, Nov 1983.
- [23] R. W. Godby, M. Schlüter, and L. J. Sham. Accurate exchange-correlation potential for silicon and its discontinuity on addition of an electron. *Phys. Rev. Lett.*, 56:2415–2418, Jun 1986.
- [24] Oleg Gritsenko, Robert van Leeuwen, Erik van Lenthe, and Evert Jan Baerends. Self-consistent approximation to the Kohn-Sham exchange potential. *Physical Review A (Atomic*, 51:1944, March 1995.
- [25] M. Kuisma, J Ojanen, J. Enkovaara, and T T Rantala. Kohn-Sham potential with discontinuity for band gap materials. *Physical Review B*, 82(1):115106, September 2010.
- [26] Falco Hüuser, Thomas Olsen, and Kristian S. Thygesen. The gw approximation in the projector augmented wave method applied to solids, molecules and 2d materials. *Accepted*, 2013.
- [27] Yabi Wu, M. K. Y. Chan, and G. Ceder. Prediction of semiconductor band edge positions in aqueous environments from first principles. *Phys. Rev. B*, 83:235301, Jun 2011.
- [28] Poul Georg Moses and Chris G. Van de Walle. Band bowing and band alignment in ingan alloys. *Applied Physics Letters*, 96(2):021908, 2010.
- [29] M. A. Butler and D. S. Ginley. Prediction of Flatband Potentials at Semiconductor-Electrolyte Interfaces From Atomic Electronegativities. *Journal of The Electrochemical Society*, 125(2):228–232, 1978.
- [30] Yong Xu and Martin A.A. Schoonen. The absolute energy positions of conduction and valence bands of selected semiconducting minerals. *American Mineralogist*, 85(3–4):543–556, March 2000.

- [31] Anubhav Jain, IvanoE. Castelli, Geoffroy Hautier, DavidH. Bailey, and KarstenW. Jacobsen. Performance of genetic algorithms in search for water splitting perovskites. *Journal of Materials Science*, pages 1–16, 2013.
- [32] S. Trasatti. *Croat. Chem. Acta*, 63:313–329, 1990.
- [33] Rosiana Aguiar, Dmitry Logvinovich, Anke Weidenkaff, Anita Rachel, Armin Reller, and Stefan G Ebbinghaus. The vast colour spectrum of ternary metal oxynitride pigments. *Dyes and Pigments*, 76(1):70–75, 2008.
- [34] A. G. Piken and W. Van Gool. Ewald program v1.1 (v3.4 modified by j a aramburu). 1968.
- [35] R. D. Shannon. Revised effective ionic radii and systematic studies of interatomic distances in halides and chalcogenides. *Acta Crystallographica Section A*, 32(5):751–767, Sep 1976.
- [36] Yabi Wu, Predrag Lazic, Geoffroy Hautier, Kristin Persson, and Gerbrand Ceder. First principles high throughput screening of oxynitrides for water-splitting photocatalysts. *Energy Environ. Sci.*, 6:157–168, 2013.
- [37] Bhavin Siritanaratkul, Kazuhiko Maeda, Takashi Hisatomi, and Kazunari Domen. Synthesis and photocatalytic activity of perovskite niobium oxynitrides with wide visible-light absorption bands. *ChemSusChem*, 4(1):74–78, 2011.

